Swansea University

Doctoral Thesis

Non-perturbative dynamics and compositeness in symplectic groups and beyond

by:
Niccolò Forzano

A thesis submitted in fulfillment of the requirements for the Doctor of Philosophy

of the

Department of Physics,
Faculty of Science and Engineering,
Swansea University

November 12, 2025

Declaration of Authorship

I, Niccolò Forzano, declare that this thesis titled, "Non-perturbative dynamics and compositeness in symplectic groups and beyond" and the work presented in it are my own. I confirm that:

- This work has not previously been accepted in substance for any degree and is not being concurrently submitted in candidature for any degree.
- This thesis is the result of my own investigations, except where otherwise stated. Other sources are acknowledged by giving explicit references. A bibliography is appended. Especially, this thesis is based on the following publications:
  - N. Forzano *et al.*, "Symplectic lattice gauge theories in the grid framework: Approaching the conformal window", *Phys. Rev. D* 108 (2023) no.9, 094508 [arXiv:2306.11649].
  - N. Forzano *et al.*, "Lattice studies of $Sp(2N)$ gauge theories using GRID", *PoS* (2024), 097 [arXiv:2310.02111].
  - N. Forzano *et al.*, "Meson spectroscopy from spectral densities in lattice gauge theories", *Phys. Rev. D* 110 (2024) no.7, 074509 [arXiv:2405.01388].
  - N. Forzano *et al.*, "Progress on the spectroscopy of lattice gauge theories using spectral densities", *PoS* (2025), 137 [arXiv:2410.11386].
  - N. Forzano *et al.* "Chimera baryons and mesons on the lattice: a spectral density analysis," [arXiv:2506.19804].
- I hereby give consent for my thesis, if accepted, to be available for electronic sharing.
- The University's ethical procedures have been followed and, where appropriate, that ethical approval has been granted.

Signed: N. Forzano

Date: November 12, 2025

Acknowledgements

I would like to thank my advisors, Maurizio Piai, Biagio Lucini, and Ed Bennett, for their help throughout this journey. I also thank my collaborators in the TELOS collaboration, whose insight shaped much of this work. Thanks to Luigi del Debbio and Peter Boyle for continuous support. A special thanks to my collaborators Alessandro Lupo, Fabian Zierler, and Ho Hsiao, for enduring both my temper and my enthusiasm, for sharing not only the challenges but also the joys of this path. My heartfelt thanks go to my friends Cristian, Mattia, Sara, and Andrea, who kept me grounded and alive–checking in, lifting my spirits, and even crossing overseas lands to visit me more times than I could ever deserve. Many others made this journey lighter: Chanju, Ali, David (I never made it to Talking Research — sorry, David), Dimitrios, Antonio, Matteo, Federico, Karol, Mohammad Naeem, Neil, Lewis, Lucas, Luke, Ricardo, Alexis, and Nicolò. To my brother Gianmarco, one of the kindest souls I've known—thank you for your endless support and quiet strength. To my parents, Luca and Sabrina, who have believed in me without hesitation–your faith has been my anchor.

And finally, to the love of my life, Aya—your love has been boundless, your support unwavering. You have stood by me through every struggle and triumph, and given me the courage to go on. For that, and for so much more, you have my most profound gratitude.

Research Data Access Statement– Analysis and simulation code and data for research papers on related work can be found in Ref. [1], [2], [3], [4], [5], [6].

Abstract

This thesis presents an in-depth, non-perturbative investigation of symplectic gauge theories, focusing on the $Sp(4)$ gauge group coupled to fermions in both the fundamental and two-index antisymmetric representations. These models are particularly relevant to Beyond the Standard Model (BSM) physics, including scenarios such as composite Higgs models (CHM), top partial compositeness (TPC) and dark matter. To support this study, the thesis advances lattice gauge theory methods by developing a flexible and efficient numerical framework built upon the `GRID` library that enables simulations of $Sp(2N)$ gauge groups with multiple fermion representations. This framework is optimised for scaling on modern high-performance computing architectures. A central focus is the computation of hadronic observables using spectral density methods, specifically the Hansen-Lupo-Tantalo (HLT) approach, which is validated against the conventional variational Generalised Eigenvalue Problem (GEVP) technique. Comprehensive numerical results are presented, including meson spectra, chimera baryon ones, and renormalised matrix elements. Careful attention is given to smearing techniques and ensemble selection. Beyond the novel non-perturbative results obtained, this work provides a robust computational framework to support future explorations of strongly coupled dynamics relevant to BSM physics.

Keywords: lattice gauge theories, `GRID`, spectral densities, composite Higgs models, top partial compositeness

Contents

Chapter 1

Introduction

Understanding strongly coupled non-Abelian gauge theories, such as quantum chromodynamics (QCD), remains a central challenge in theoretical physics. In regimes where the coupling becomes large, the tools of perturbation theory are no longer effective, requiring alternative, non-perturbative approaches. A major development came in 1974, when Kenneth Wilson introduced the lattice formulation of quantum field theory [7]. By discretising Euclidean spacetime, Wilson provided a practical regularisation scheme and established a framework for the numerical study of gauge theories from first principles. This approach laid the groundwork for what is now known as lattice field theory, a method that allows for systematic investigations of complex, strongly interacting systems that are otherwise inaccessible through analytic methods. With continued improvements in computational resources and advances in numerical techniques, lattice gauge theory has become an increasingly precise tool for exploring non-perturbative aspects of quantum field theories.

In the search for physics beyond the Standard Model, strongly coupled non-Abelian gauge theories have drawn increasing attention, particularly those based on symplectic groups in four-dimensional spacetime. Among these, $Sp(2N)$ gauge theories have emerged as promising candidates for new physics scenarios due to their elegance and simplicity. These models have been extensively studied using lattice field theory techniques, to quantitatively explore their strongly coupled dynamics [8–26].

Within this framework, numerical methods have been used in $Sp(2N)$ Yang-Mills theories to calculate glueball and string spectra [27–36], as well as topological charge and susceptibility [37–53]. These results allow comparisons with other gauge groups, such as $SU(N)$, to better understand important aspects of gauge theories such as the behaviour of the theory in the large-N limit [12, 17, 54–56].

A particularly compelling case emerges when introducing fermionic content matter. The $Sp(4)$ gauge theory with $N_\mathrm{f} = 2$ fundamental fermions presents a framework for investigating non-perturbative dynamics that are reminiscent of traditional QCD-like theories, but realised in a distinct theoretical setting. Lattice studies of this theory provide a valuable framework

for understanding confinement and chiral dynamics, and the spectrum of bound states in strongly interacting systems. Recent lattice studies of $Sp(4)$ have yielded detailed insights into meson and baryon spectroscopy, decay constants, and other observables [57–64].

One promising application for this gauge theory lies in the study of strongly interacting dark sectors. Despite extensive searches, a dark sector with strong self-interactions and weak couplings to the Standard Model could have evaded detection [65–71]. This idea underpins many models, including composite dark matter [72–81] and strongly interacting massive particles (SIMP) [82–90]. The minimal SIMP model [83] is based on the aforementioned $Sp(4)$ gauge theory with $N_{\mathrm{f}} = 2$ fundamental fermions.

A first-order phase transition in such a dark sector could generate a stochastic gravitational wave (GW) background [91–96], potentially detectable by future GW detectors. [97–115]. Exploring this possibility in strongly coupled theories requires thermodynamic information near the transition, obtainable via lattice simulations and effective models [116–121], such as Polyakov-loop [122–130] and matrix models [131–139].

Another recent and important focus is the $Sp(4)$ theory with $N_{\mathrm{f}} = 2$ fermions transforming in the fundamental representation, and $N_{\mathrm{as}} = 3$ fermions in the two-index antisymmetric representation. This theory forms the basis of the effective field theory behind the minimal Composite Higgs Model [140], and of top partial compositeness [141–143], providing a microscopic explanation for the origin of the top quark and Higgs boson. Its relevance to beyond the Standard Model physics motivates the numerical study presented in Chapter 5.

To support the exploration of these theories, new software tools have been developed [144], extending previous versions of the `GRID` library [145–148] with specific functionalities for handling $Sp(2N)$ gauge theories featuring matter fields in multiple representations. These tools leverage the flexibility of `GRID` to enable efficient deployment on both CPU and GPU architectures. In Chapter 4, the $Sp(4)$ theory coupled to a variable number N_{as} of Wilson-Dirac fermions in the two-index antisymmetric representation is used to benchmark the implementation. This setup provides insights that are broadly applicable to the field.

One key focus of this work is the study of symplectic gauge theories observables under the prism of spectral densities. Defined as inverse Laplace transforms of Euclidean correlators, spectral densities have become a powerful tool for analysing strongly coupled field theories. They enable the computation of high-precision spectral observables, which are difficult to access using traditional techniques. Spectral densities also capture off-shell physics and provide alternative methods for computing scattering amplitudes [149, 150] and inclusive decay rates [151–157]. Their utility extends beyond QCD to new physics models, such as those exploring composite Higgs and partial top compositeness [158–160] and theories of electroweak symmetry breaking [161–163].

This thesis is organised as follows: Chapter 2 provides a theoretical introduction to

gauge theories, flavour symmetry breaking patterns, composite Higgs models and defines symplectic gauge groups and the deriving gauge theories. Appendix A provides details about the generators of the $Sp(4)$ gauge groups algebra in `GRID`, whereas Appendix B gives a possible choice of $SU(4)$ generators, used to discuss the $SU(4)/Sp(4)$ composite Higgs coset. Chapter 3 describes how to discretise a gauge theory on the lattice, pointing out potential problems involving the presence of doublers. A description of numerical simulations on the lattice is provided. An introduction to meson and baryon interpolators and fitting techniques is outlined as well. In Chapter 4, a description of the development of the `GRID` framework is given, and subsequent sanity checks are reported. Chapter 5 introduces the open-source code `LSDensities` [164], developed to compute spectral densities using the Hansen-Tantalo-Lupo (HLT) algorithm. Furthermore, numerical results for the spectrum and matrix elements of bound states in this class of theories are presented, employing advanced techniques for spectral density reconstruction and fitting. A comprehensive collection of fit results is provided in Appendix F. Chapter 5 also explores the impact of different smearing kernels, correlation function smearing methods (APE and Wuppertal), and reconstruction parameters. Technical details on APE and Wuppertal smearing are given in Appendix C, while Appendix D discusses details of the renormalisation of matrix elements. Further information on the `LSDensities` code and relevant formulae can be found in Appendix E. Finally, Chapter 6 presents the main conclusions and summarises the findings of this work.

Chapter 2

Gauge theories in continuous space-time

2.1 Building a gauge theory

A gauge theory is formulated by enforcing local invariance of internal degrees of freedom under transformations belonging to a given gauge group G. For connected Lie groups, G is generated through exponentiation of its associated algebra, $\mathcal{G}$, whose generators in the representation R are denoted as $T^a_{\mathrm{R}} \in \mathcal{G}$. The fundamental components of a renormalisable gauge theory in the continuum include:

1. Selection of a gauge group, G, and construction of an invariant action in the Minkowski space, $S = \int d^4x\, \mathcal{L}$, under gauge transformations, where $x = (t, \vec{x})$ are the 4-dimensional space-time coordinates in a Minkowski space with metric $\eta_{\mu\nu}$ and $\mathcal{L}$ is the Lagrangian density.

2. Definition of the fields in the theory and their transformation properties under the group G.

3. In the traditional sense, one can ensure renormalisability by restricting terms in the Lagrangian to have a canonical energy dimension no greater than 4. However, this condition can be relaxed in the context of effective field theories, where higher-dimensional operators suppressed by a cutoff scale are systematically included, or in strongly coupled theories where large anomalous dimensions can make classically irrelevant operators effectively relevant or marginal [165–167].

To properly define gauge fields, it is useful to first consider a theory with matter content. In a gauge theory, each type of fermionic matter field is represented:

$$\psi^{\mathrm{R}}_{\{a\},\alpha,k}(x) \tag{2.1.1}$$

where $\{a\}$ represents the colour index structure, depending on the representation R that the Dirac spinor transforms under, $\alpha = 1, \ldots, 4$ and $k = 1, \ldots, N_{\mathrm{R}}$ are Dirac and flavour indices, respectively. Let us restrict to the simplest case where we consider fermions transforming in the fundamental representation of the gauge group G [168, 169], flavour number to be set to $N_{\mathrm{R=f}} = 1$, and we omit the indices. The action describing fermionic matter fields of mass m in four-dimensional spacetime is given by

$$S_F[\psi, \bar{\psi}] = \int d^4x\, \bar{\psi}(x)[i\gamma_\mu \partial_\mu - m]\psi(x)\,, \tag{2.1.2}$$

where $\bar{\psi}(x) = \psi^\dagger(x)\gamma_0$, and the γ_μ matrices satisfy the Clifford algebra $\{\gamma_\mu, \gamma_\nu\} = 2\eta_{\mu\nu}\mathbb{I}$. A key principle in gauge theory is requiring invariance of the action S_F under local gauge transformations:

$$\psi(x) \to \psi'(x) = U(x)\psi, \quad \bar{\psi}(x) \to \bar{\psi}'(x) = \bar{\psi}(x)U^\dagger(x)\,, \tag{2.1.3}$$

where $U(x) \equiv e^{i\alpha_a(x)T^a} \in G$ (with $a = 1, \ldots, \dim(G)$). Enforcing invariance under these transformations,

$$S_F[\psi, \bar{\psi}] = S_F[\psi', \bar{\psi}']\,, \tag{2.1.4}$$

reveals that the standard derivative ∂_μ alone does not preserve this property. To construct an invariant action, we introduce the covariant derivative:

$$\partial_\mu \to D_\mu = \partial_\mu + iA_\mu\,, \tag{2.1.5}$$

where the gauge field A_μ is expanded as

$$A_\mu = A_\mu^a T^a, \quad a = 1, \ldots, \dim(G)\,, \tag{2.1.6}$$

and the components A_μ^a define the gauge fields. Imposing the property (2.1.4), is equivalent to imposing:

$$D_\mu\psi(x) \to \Omega(x) D_\mu\psi(x)\,, \tag{2.1.7}$$

which implies, by applying Eq. (2.1.5),

$$D'_\mu\psi'(x) = (\partial_\mu + iA'_\mu)\Omega(x)\psi(x) = \tag{2.1.8}$$

and by applying the derivative, ∂_μ, and multiplying by a $\Omega^{-1}\Omega = \mathbb{I}$ term,

$$= \Omega(\partial_\mu + \Omega^{-1}\partial_\mu\Omega + i\Omega^{-1}A'_\mu\Omega)\psi\,. \tag{2.1.9}$$

Therefore, imposing the key property of covariant derivatives in Eq. (2.1.7):

$$D'_\mu \psi'(x) \equiv \Omega D_\mu \psi = \Omega(\partial_\mu + iA_\mu)\psi\,, \tag{2.1.10}$$

and comparing to Eq. (2.1.9), one gets the transformation property

$$A'_\mu(x) = \Omega(x) A_\mu(x) \Omega^{-1}(x) + i\partial_\mu \Omega(x) \cdot \Omega^{-1}(x)\,. \tag{2.1.11}$$

The action for a pure Yang-Mills theory, containing only gauge fields, must also satisfy invariance:

$$S_G[A'] = S_G[A]\,. \tag{2.1.12}$$

To introduce a kinetic term, we define the field strength tensor as

$$F_{\mu\nu}(x) = -i[D_\mu(x), D_\nu(x)] = \partial_\mu A_\nu(x) - \partial_\nu A_\mu(x) + i[A_\mu(x), A_\nu(x)]\,, \tag{2.1.13}$$

Under gauge transformations, the field strength tensor transforms as follows:

$$F_{\mu\nu}(x) \to F'_{\mu\nu}(x) = \Omega(x) F_{\mu\nu}(x) \Omega^\dagger(x)\,. \tag{2.1.14}$$

Thus, an invariant gauge action is formulated as

$$S_G[A] = -\frac{1}{2g^2} \int d^4x \,\mathrm{tr}\left(F_{\mu\nu}(x) F^{\mu\nu}(x)\right)\,, \tag{2.1.15}$$

which generalises the electrodynamic action. The representation (2.1.6) allows rewriting the field strength tensor in component form, $F_{\mu\nu}(x) \equiv F^a_{\mu\nu}(x)\, T^a$, and therefore:

$$F^a_{\mu\nu}(x) = \partial_\mu A^a_\nu(x) - \partial_\nu A^a_\mu(x) - f^{abc} A^b_\mu A^c_\nu\,, \tag{2.1.16}$$

(f^{abc} are the structure constants of the Lie algebra, $\mathcal{G}$) which leads to

$$S_G[A] = -\frac{1}{4g^2} \int d^4x \,[F^a_{\mu\nu}(x) F^{\mu\nu a}(x)]\,, \tag{2.1.17}$$

where repeated indices imply summation over $a = 1, \ldots, \dim(G)$. Finally, the quantum theory is non-perturbatively defined via the path integral,

$$Z = \int \mathcal{D}A\, \mathcal{D}\psi\, \mathcal{D}\bar{\psi}\, e^{iS_G + iS_F + iS_{GF}}\,. \tag{2.1.18}$$

The gauge symmetry introduces redundant degrees of freedom—many physically equivalent field configurations are related by gauge transformations. Therefore, one introduces a term

S_{GF} in the action to operate gauge-fixing, and remove the redundant degrees of freedom due to overcounting.

After gauge fixing, the functional integral in Eq. (2.1.18) still contains divergences that are typical of a quantum field theory. In order to show the predictive power of quantum field theories, we need to perform a procedure of matching between physical observables, computed in field theory, and their experimental counterparts. This mechanism is called renormalisation. The power of quantum field theories consists in the prediction that can be done in the renormalised theory, by finding observables other than those fixed by the procedure of renormalisation.

The integral in Eq. (2.1.18) contains divergences, therefore the starting point for renormalisation is to choose a regularisation, which corresponds to the introduction of an ultraviolet cutoff Λ. In the next chapter, we discuss a possible regularisation scheme: the lattice. By defining a hypercubic lattice of finite spatial volume L^3 and temporal volume T, an infrared cutoff is introduced in the momentum space, $2\pi/L$. The lattice will present a spacing a, and therefore the momentum components are bounded by the value π/a in the ultraviolet regime. At fixed Λ, one then computes the desired physical observable and matches the theory prediction to related experimental values at a certain energy scale μ.

Following the discussions in Refs. [170, 171], let $C\left(\{x_i\}, m, g, \Lambda\right)$ be a n-point correlation function ($i = 1, \ldots, n$), that is computed within the bare theory with UV cutoff Λ, and $C^{\text{ren}}(\{x_i\}, m^{\text{ren}}, g^{\text{ren}}, \mu)$ the renormalised n-point correlation function. Assuming multiplicative renormalisation, one can write

$$Z^n\left(g^{\text{ren}}, \frac{m^{\text{ren}}}{\Lambda}, \frac{\mu}{\Lambda}\right) C^{\text{ren}}(\{x_i\}, m^{\text{ren}}, g^{\text{ren}}, \mu) = C\left(\{x_i\}, m, g, \Lambda\right) , \tag{2.1.19}$$

where Z is the renormalisation constant, and the independence of the bare n-point correlation function $C\left(g, m, \Lambda\right)$ from the renormalisation scale μ leads to the Callan-Symanzik equation [172, 173]

$$\left(\mu\frac{\partial}{\partial\mu} + \beta\frac{\partial}{\partial g^{\text{ren}}} + \gamma_m m^{\text{ren}}\frac{\partial}{\partial m^{\text{ren}}} + n\gamma\right) C^{\text{ren}}(\{x_i\}, m^{\text{ren}}, g^{\text{ren}}, \mu) = 0\,, \tag{2.1.20}$$

where $\gamma \equiv \mu\frac{\partial \log Z}{\partial\mu}$ is defined anomalous field dimension, $\gamma_m \equiv \mu\frac{\partial \log m^{\text{ren}}}{\partial\mu}$ is the anomalous mass dimension and $\beta \equiv \mu\frac{\partial g^{\text{ren}}}{\partial\mu}$ is called beta function. The procedure of renormalisation introduces a dependence of the bare parameters of the theory with the renormalisation scale μ and the relation is fixed by Eq. (2.1.20).

2.2 Flavour symmetry and symmetry breaking patterns

In this section, definitions of flavour symmetry and chiral symmetry breaking pattern are provided.

Let us consider a gauge theory with N_f flavours of quarks and suppress colour and spin indices. This differs from the Lagrangian in Section 2.1 where the number of flavours is assumed to be one. In the present case, the fermion fields $\psi, \bar{\psi}$ carry also a flavour index, therefore

$$\psi = (\psi_1, \ldots, \psi_{N_\mathrm{f}})_T \,. \tag{2.2.1}$$

In this notation, the fermion action reads

$$S_F[\psi, \bar{\psi}, A] = \int \mathrm{d}^4x \bar{\psi} \left(i\gamma_\mu \left(\partial_\mu + iA_\mu\right) - m\right) \psi \,, \tag{2.2.2}$$

where a mass matrix is introduced

$$m = \mathrm{diag}\left(m_1, m_2, \ldots, m_{N_\mathrm{f}}\right) \,, \tag{2.2.3}$$

acting in flavour space.

One defines the following projectors

$$P_{L/R} = \frac{1 \mp \gamma_5}{2} \quad \text{such that} \quad \psi_{L/R} = P_{L/R}\,\psi \,, \tag{2.2.4}$$

and, accordingly, the Lagrangian will be rewritten as follows:

$$\mathcal{L} = i\bar{\psi}_L D\psi_L + i\bar{\psi}_R D\psi_R - m(\bar{\psi}_L\psi_R + \bar{\psi}_R\psi_L) \,, \tag{2.2.5}$$

where the massless Dirac operator is defined as $D = \gamma^\mu\partial_\mu + i\gamma^\mu A_\mu$.
One can show that the Lagrangian in Eq. (2.2.5) is invariant under the chiral transformations, defined as:

$$\psi_L \to \psi'_L = U_L\psi_L, \quad U_L \in U(N_\mathrm{f})_L \,, \tag{2.2.6}$$

and

$$\psi_R \to \psi'_R = U_R\psi_R, \quad U_R \in U(N_\mathrm{f})_R, \tag{2.2.7}$$

for null mass term. For this reason, the massless limit is called the chiral limit. One can summarise the concept of chiral symmetry as follows:

$$D\gamma_5 + \gamma_5 D = 0 \,, \tag{2.2.8}$$

which expresses the fact that the massless Dirac operator anticommutes with γ_5 and this

means that symmetry induced by the chiral rotation (chiral symmetry) is unbroken.
Usually, these transformations are re-arranged in vector and axial transformations, and the massless action has the symmetry $\mathrm{SU}(N_\mathrm{f})_L \times \mathrm{SU}(N_\mathrm{f})_R \times \mathrm{U}(1)_V \times \mathrm{U}(1)_A$. However, when one considers the fully quantised theory one finds that the fermion determinant is not invariant under the axial transformations and the corresponding axial symmetry $\mathrm{U}(1)_A$ is broken explicitly by a non-invariance of the fermion integration measure. This is called the Adler–Bell–Jackiw anomaly [174, 175]. Therefore, in the quantised massless theory, the symmetry is broken explicitly to the remaining symmetry

$$G \equiv \mathrm{SU}(N_\mathrm{f})_L \times \mathrm{SU}(N_\mathrm{f})_R \times \mathrm{U}(1)_V . \tag{2.2.9}$$

Following Refs. [176], we are interested in understanding what is the symmetry breaking pattern, i.e. which subgroup H is left unbroken when such symmetry is broken

$$G \to H , \tag{2.2.10}$$

either spontaneously or explicitly. To do so, it is relevant to mention that even in the massless limit, where the action is invariant under chiral rotations, the bilinear operator dynamically assumes a non-vanishing vacuum expectation value,

$$\left\langle \bar{\psi}^{\bar{\mathrm{R}}} \psi^{\mathrm{R}} \right\rangle , \tag{2.2.11}$$

where ψ^{R} is a Dirac fermion field in the representation R ($\bar{\mathrm{R}}$ is the conjugate representation) of the gauge group G and different scenarios can arise depending on R. The bilinear in (2.2.11) is called chiral condensate, and it can be expressed in terms of Weyl left-handed spinors ψ_L

$$\left\langle i\epsilon_{\alpha\beta} \psi_L^{\mathrm{R},\alpha,i} \psi_L^{\bar{\mathrm{R}},\beta,i} + \mathrm{h.c.} \right\rangle , \tag{2.2.12}$$

where α, β are spinor indices, i is the flavour index, and ϵ is the antisymmetric Levi-Civita tensor. There are two scenarios that differ from the QCD case and are particularly relevant for this thesis:

- When the representation R is pseudoreal, its conjugate $\bar{\mathrm{R}}$ is related to R through a similarity transformation involving an antisymmetric form $\Omega_{ab} = -\Omega_{ba}$, where a, b are colour indices. The condensate takes the form $\left\langle \epsilon_{\alpha\beta} (\psi_L^{\mathrm{R},\alpha})_{a\,i}\, \Omega^{ab} \Omega^{ij}\, (\psi_L^{\mathrm{R},\beta})_{b\,j} + \mathrm{h.c.} \right\rangle$. In this thesis, this applies when R corresponds to the fundamental representation of the gauge group $Sp(2N)$ and it will be shown in the next section that due to the pseudoreal structure, the $SU(N_\mathrm{f})_L \times SU(N_\mathrm{f})_R$ global symmetry is enhanced to $SU(2N_\mathrm{f})$.

Therefore, the flavour symmetry breaking pattern will be

$$SU(2N_{\rm f}) \longrightarrow Sp(2N_{\rm f}). \tag{2.2.13}$$

- When the representation R is real, its conjugate $\bar{\rm R}$ is related to R through a similarity transformation involving a symmetric form δ_{ab}. The condensate in this case is $\left\langle \epsilon_{\alpha\beta}(\psi_L^{{\rm R},\alpha})_{ai}\delta^{ab}(\psi_L^{{\rm R},\beta})_{bi} + \text{h.c.}\right\rangle$, which is invariant under the subgroup $H = SO(2N_{\rm f})$. Also in the real representation case, the enhancement occurs, and this leads to the symmetry breaking pattern:

$$SU(2N_{\rm f}) \longrightarrow SO(2N_{\rm f}). \tag{2.2.14}$$

  In this thesis, this applies when R is the two-index antisymmetric representation, and the gauge group is $Sp(2N)$.

2.3 Symplectic gauge theories

Before entering into the details of the lattice discretisation and of the various numerical studies performed in this thesis, it is interesting to introduce the concept of gauge theories based on the invariance under transformations of gauge groups that differ from $SU(N)$. In particular, this subsection is devoted to give a definition to the symplectic gauge group $Sp(2N)$ [177], and to symplectic gauge theories of interest.

2.3.1 Group theoretical definition

The group $Sp(2N)$ is a subgroup of $SU(2N)$, a set of $2N \times 2N$ unitary matrices $U \in SU(2N)$ with complex elements satisfying the relations

$$U^* = \Omega U \Omega^\dagger\,, \tag{2.3.1}$$

and

$$U^\dagger U = \mathbb{I}_{2N\times 2N}\,, \tag{2.3.2}$$

where Ω is the symplectic form, written as

$$\Omega = \begin{pmatrix} 0 & \mathbb{I}_{N\times N} \\ -\mathbb{I}_{N\times N} & 0 \end{pmatrix}. \tag{2.3.3}$$

Eq. (2.3.1) can be rewritten in a equivalent form:

$$U^T \Omega U = \Omega\,. \tag{2.3.4}$$

Consequently, U and U^* are related by the unitary transformation Ω, hence the $2N$-dimensional fundamental representation of $Sp(2N)$ is pseudoreal.
Matrices obeying the constraint (2.3.4) form a group: indeed the unit matrix also belongs to $Sp(2N)$ and considering $U, V \in Sp(2N)$

$$(UV)^* = U^*V^* = \Omega U \Omega^\dagger \Omega V \Omega^\dagger = \Omega(UV)\Omega^\dagger \,.$$

Finally, the inverse $U^\dagger$ also obeys the constraint

$$(U^{-1})^* = (U^\dagger)^* = (U^*)^\dagger = (\Omega U \Omega^\dagger)^\dagger = \Omega U^\dagger \Omega^\dagger = \Omega U^{-1} \Omega^\dagger \,.$$

Moreover, these types of matrices have a particular structure: considering a general $2N \times 2N$ matrix in the block form

$$U = \begin{pmatrix} A & B \\ C & D \end{pmatrix}, \tag{2.3.5}$$

(where A, B, C, D are $N \times N$ matrices) and imposing constraints (2.3.1) and (2.3.2) the matrix (2.3.5) can be written in block form as

$$U = \begin{pmatrix} A & B \\ -B^* & A^* \end{pmatrix}, \tag{2.3.6}$$

where A and B satisfy the constraints

$$A^\dagger A + B^\dagger B = \mathbb{I}_{N\times N} \,, \tag{2.3.7}$$

and

$$A^T B = B^T A \,. \tag{2.3.8}$$

This can be demonstrated as follows.
Unitarity of matrix U in (2.3.5) gives the conditions

$$A^\dagger A + C^\dagger C = \mathbb{I}_{N\times N} \tag{2.3.9}$$

$$B^\dagger B + D^\dagger D = \mathbb{I}_{N\times N} \tag{2.3.10}$$

$$A^\dagger B + C^\dagger D = 0 \tag{2.3.11}$$

and the symplectic condition of eq. (2.3.4) gives

$$AB^T = BA^T \tag{2.3.12}$$

$$CD^T = DC^T \tag{2.3.13}$$

$$AD^T - BC^T = \mathbb{I}_{N\times N} \tag{2.3.14}$$

The condition of (2.3.14) gives

$$AD^T - BC^T = \mathbb{I}_{N\times N}$$

$$\Rightarrow A^* D^\dagger - B^* C^\dagger = \mathbb{I}_{N\times N}$$

$$\Rightarrow A^* D^\dagger D - B^* C^\dagger D = D$$

$$\Rightarrow A^*(\mathbb{I}_{N\times N} - B^\dagger B) - B^*(-A^\dagger B) = D$$

$$\Rightarrow A^* - A^* B^\dagger B + B^* A^\dagger B = D$$

$$\Rightarrow A^* - (A^* B^\dagger - B^* A^\dagger)B = D$$

$$\Rightarrow A^* - (AB^T - BA^T)^* B = D$$

For (2.3.12) we have

$$\Rightarrow A^* = D \tag{2.3.15}$$

Moreover

$$A^\dagger A + C^\dagger C = \mathbb{I}_{N\times N}$$

$$\Rightarrow A^\dagger AB^T + C^\dagger CB^T = B^T$$

$$\Rightarrow A^\dagger AB^T + C^\dagger (BC^T)^T = B^T$$

$$\Rightarrow A^\dagger AB^T + C^\dagger (AD^T - \mathbb{I}_{N\times N})^T = B^T$$

$$\Rightarrow A^\dagger AB^T + C^\dagger DA^T - C^\dagger = B^T$$

$$\Rightarrow A^\dagger BA^T + C^\dagger DA^T - C^\dagger = B^T$$

$$\Rightarrow (A^\dagger B + C^\dagger D)A^T - C^\dagger = B^T$$

Being $(A^\dagger B + C^\dagger D) = 0$ for (2.3.11) we obtain

$$C = -B^* \tag{2.3.16}$$

so the block structure (2.3.6) is proven.

The properties of $Sp(2N)$ matrices and their algebra follow directly from the defining constraints, (2.3.7) and (2.3.8). These relations lead to several important structural insights:

1. The condition of unit determinant ensures that $Sp(2N)$ forms a compact and simply connected subgroup of $SU(2N)$.

2. The centre of $Sp(2N)$ consists of scalar multiples of the identity matrix. Since eq. (2.3.4) requires $A = A^*$, it follows that the centre of $Sp(2N)$ is isomorphic to $\mathbb{Z}(2)$.

3. The algebra of $Sp(2N)$ emerges naturally by considering the exponential representation of group elements,

$$U = \exp(iH), \tag{2.3.17}$$

where H satisfies the structural constraints of the group. Specifically, H must be a Hermitian traceless matrix that respects the relation

$$H^* = \Omega H \Omega^\dagger. \tag{2.3.18}$$

This condition enforces a block structure of the form

$$H = \begin{pmatrix} A & B \\ B^* & A^* \end{pmatrix}, \tag{2.3.19}$$

with A and B as $N \times N$ matrices. Requiring H to be Hermitian ($H = H^\dagger$) leads to the constraints

$$A = A^\dagger, \quad B = B^T. \tag{2.3.20}$$

Since U belongs to $SU(2N)$, its determinant must satisfy

$$\det U = \det\left[\exp(iH)\right] = \exp(i\,\mathrm{tr} H) = 1, \tag{2.3.21}$$

which implies that H is traceless. Therefore, the generators of $Sp(2N)$ are Hermitian and traceless, similar to those of $SU(N)$.

The counting of degrees of freedom follows from the properties of A and B:

- The Hermitian matrix A contributes N^2 real parameters.
- The symmetric complex matrix B contributes $(N+1)N$ independent components.

Thus, the total dimension of $Sp(2N)$ is

$$\dim Sp(2N) = N^2 + (N+1)N = (2N+1)N. \tag{2.3.22}$$

4. It can be shown that from Eq. (2.3.4), the following

$$\Omega H + H^T \Omega = 0, \tag{2.3.23}$$

is verified.

5. The rank of $Sp(2N)$ is N, corresponding to the number of independent diagonal generators in the maximal Abelian Cartan subgroup. Additionally, $Sp(2N)$ contains N independent $SU(2)$ subgroups.

Explicit realisations of the generators of the $Sp(2N)$ algebra can be built by using the constraint in Eq. (2.3.23), and requiring a normalisation factor, N_{R} ($\mathrm{Tr}\left[T^a_{\mathrm{R}}T^b_{\mathrm{R}}\right] = N_{\mathrm{R}}\delta^{ab}$). Two explicit realisations of the $Sp(4)$ generators in the fundamental representations are presented in Appendices A and B. The generators in higher-dimensional representations can also be relevant. For the purposes of our thesis, the ones in the 2-index antisymmetric representation are discussed in Sec. 3.3.

2.3.2 Symplectic gauge theories in the continuum

Throughout this thesis, we consider $Sp(2N)$ ($N > 1$) gauge theories with N_{f} fermions transforming in the fundamental representation and N_{as} in the two-index antisymmetric representation [16, 178–181]. The theory in the continuum formulated in Minkowski spacetime, is described by the following action:

$$\begin{aligned} S = \int d^4x \Big[&-\frac{1}{2}\mathrm{Tr}\, G_{\mu\nu}G^{\mu\nu} + \frac{1}{2}\sum_{i=1}^{N_{\mathrm{f}}}\left(i\overline{Q^i}_a\gamma^\mu\left(D_\mu Q^i\right)^a - i\overline{(D_\mu Q^i)}_a\gamma^\mu Q^{i\,a}\right) \\ &- m^{\mathrm{f}}\sum_{i=1}^{N_{\mathrm{f}}}\overline{Q^i}_a Q^{i\,a} + \frac{1}{2}\sum_{k=1}^{N_{\mathrm{as}}}\left(i\overline{\Psi^k}_{ab}\gamma^\mu\left(D_\mu\Psi^k\right)^{ab} - i\overline{(D_\mu\Psi^k)}_{ab}\gamma^\mu\Psi^{k\,ab}\right) \\ &- m^{\mathrm{as}}\sum_{k=1}^{N_{\mathrm{as}}}\overline{\Psi^k}_{ab}\Psi^{k\,ab}\Big]. \end{aligned} \tag{2.3.24}$$

where $Q^{i\,a}$ are Dirac fermion fields, where $i = 1,\ldots,N_{\mathrm{f}}$ labels the flavour index and $a = 1,\ldots,2N$ represents the fundamental representation of $Sp(2N)$. Similarly, $\Psi^{k\,ab}$ are Dirac fermions in the two-index antisymmetric representation, where $k = 1,\ldots,N_{\mathrm{as}}$.

The covariant derivatives reflect the transformation properties of fermions under the $Sp(2N)$ gauge group. For an element $U \in Sp(2N)$, the transformations are:

$$Q \to UQ, \quad \Psi \to U\Psi U^{\mathrm{T}}. \tag{2.3.25}$$

The covariant derivatives, involving the gauge field $A_\mu = A^a_\mu T^a_{\mathrm{R}}$ (with T^a_{R} as the generators of

$Sp(2N)$), are given by:

$$\begin{aligned} D_\mu Q^i &= \partial_\mu Q^i + igA_\mu Q^i, \\ D_\mu \Psi^j &= \partial_\mu \Psi^j + igA_\mu \Psi^j + ig\Psi^j A_\mu^{\mathrm{T}}, \end{aligned} \tag{2.3.26}$$

where g is the gauge coupling. The field-strength tensor $G_{\mu\nu}$ is:

$$G_{\mu\nu} = \partial_\mu A_\nu - \partial_\nu A_\mu + ig\left[A_\mu, A_\nu\right]. \tag{2.3.27}$$

This framework reveals the flavour symmetries of the fermions: $SU(N_\mathrm{f})_L \times SU(N_\mathrm{f})_R$ for Q^i and $SU(N_\mathrm{as})_L \times SU(N_\mathrm{as})_R$ for Ψ^k. For this pseudoreal theory, these are enhanced to $SU(2N_\mathrm{f})$ and $SU(2N_\mathrm{as})$, respectively. Adopting a two-component spinor notation, as in Refs. [11, 182], makes these enhanced symmetries explicit. The fermions are rewritten as:

$$\begin{aligned} Q^{i\,a} &= \begin{pmatrix} q^{i\,a} \\ \Omega^{ab}\left(-\tilde{C}q^{i+2,*}\right)_b \end{pmatrix}, \\ \Psi^{k\,ab} &= \begin{pmatrix} \psi^{k\,ab} \\ \Omega^{ac}\Omega^{bd}\left(-\tilde{C}\psi^{k+3,*}\right)_{cd} \end{pmatrix}, \end{aligned} \tag{2.3.28}$$

where $\tilde{C} = -i\tau^2$ (with τ^2 as the second Pauli matrix), and Ω is an antisymmetric matrix. The resulting two-component action is [11]:

$$\begin{aligned} S = \int d^4x \Big[&-\frac{1}{2}\mathrm{Tr}\, G_{\mu\nu}G^{\mu\nu} + \frac{1}{2}\sum_{j=1}^{2N_\mathrm{f}}\left(i\left(q^j\right)_a^\dagger \bar{\sigma}^\mu\left(D_\mu q^j\right)^a - i\left(D_\mu q^j\right)_a^\dagger \bar{\sigma}^\mu\left(q^j\right)^a\right) \\ &- \frac{1}{2}m^\mathrm{f}\sum_{j,k=1}^{2N_\mathrm{f}}\Omega_{jk}\left(q^{j\,a\,T}\Omega_{ab}\tilde{C}q^{k\,b} - \left(q^j\right)_a^\dagger\Omega^{ab}\tilde{C}\left(q^{k\,*}\right)_b\right) \\ &+ \frac{1}{2}\sum_{k=1}^{2N_\mathrm{as}}\left(i\left(\psi^k\right)_{ab}^\dagger\bar{\sigma}^\mu\left(D_\mu\psi^k\right)^{ab} - i\left(D_\mu\psi^k\right)_{ab}^\dagger\bar{\sigma}^\mu\left(\psi^k\right)^{ab}\right) \\ &- \frac{1}{2}m^\mathrm{as}\sum_{j,k=1}^{2N_\mathrm{as}}\omega_{jk}\left(\psi^{j\,ab\,T}\Omega_{ac}\Omega_{bd}\tilde{C}\psi^{k\,cd} - \left(\psi^j\right)_{ab}^\dagger\Omega^{ac}\Omega^{bd}\tilde{C}\left(\psi^{k\,*}\right)_{cd}\right)\Big], \end{aligned} \tag{2.3.29}$$

where $\bar{\sigma}_\mu = (\mathbb{1}_{2\times2}, \tau^i)$ and $\omega_{jk} = \begin{pmatrix} \mathbb{O} & \mathbb{I}_{N_\mathrm{as}} \\ \mathbb{I}_{N_\mathrm{as}} & \mathbb{O} \end{pmatrix}$. The indices are $a = 1, \ldots, 2N$ and $j = 1, \ldots, 2N_\mathrm{f}$.

The mass terms explicitly break the flavour symmetries to the subgroups $Sp(2N_\mathrm{f})$ and $SO(2N_\mathrm{as})$. As explained in Section 2.2, non-perturbative dynamics generates fermion bilinear condensates that break the symmetries spontaneously, following the same pattern, leading to the appearance of pseudo-Nambu-Goldstone bosons. Specifically, there are $N_\mathrm{f}(2N_\mathrm{f}-1)-1$ pseudo Nambu-Goldstone bosons in the fundamental sector (for $N_\mathrm{f} > 1$) and $N_\mathrm{as}(2N_\mathrm{as}+1)-1$

in the antisymmetric sector.

2.4 Composite Higgs models (CHMs) and top partial compositeness (TPC)

Despite its remarkable predictive power, the Standard Model (SM) of particle physics is widely regarded as an incomplete description of nature. It lacks a framework for quantum gravity, and its couplings become non-perturbative at high energies, indicating the need for a more fundamental theory beyond a certain cutoff scale Λ. Phenomenologically, the SM does not account for key cosmological observations: it offers no explanation for dark energy, lacks a viable dark matter candidate, and fails to generate the observed matter–antimatter asymmetry. These deficiencies suggest that the SM should be viewed as an effective field theory, valid only below some high-energy threshold.

A compelling class of extensions involves new strongly coupled sectors, where composite bound states emerge dynamically. Such frameworks can preserve the low-energy successes of the SM while simultaneously addressing its unresolved questions. Compositeness has been proposed to underlie various phenomena, including electroweak symmetry breaking (EWSB), the origin of the Higgs boson, the mass of the top quark, dark matter, and even primordial phase transitions potentially observable through gravitational waves.

In composite Higgs models (CHMs), the Higgs field is reinterpreted as a pseudo Nambu Goldstone boson (pNGB) arising from the spontaneous breaking of a global symmetry in a new strong sector. The Higgs mass is naturally suppressed due to an approximate symmetry, and EWSB is triggered by vacuum misalignment. These ideas and their concrete realisations are reviewed in Refs. [75, 181, 183, 184], with symmetry-based classifications and model-building guidance provided therein.

Additionally, the large top-quark mass can be accommodated through the mechanism of top partial compositeness (TPC) [141], where SM top quarks couple linearly to baryonic operators in the strong sector. This interplay between symmetry, dynamics, and phenomenology provides the foundation for the models and numerical studies explored in this work.

2.4.1 Hierarchy problem of the Standard Model and composite Higgs

As discussed, the Standard Model (SM) of particle physics describes the strong and electroweak (EW) interactions with remarkable accuracy. Nonetheless, several open problems suggest that the SM is only an effective theory valid up to a cutoff energy scale Λ_{SM}, located at least in the TeV range. One of the most prominent issues is the so-called hierarchy problem, or naturalness problem, which arises in the Higgs sector.

Quantum corrections tend to drive the Higgs boson mass towards the cutoff scale Λ_{SM}, while experimentally its mass is observed to be around 125 GeV [185, 186], well within the EW range. In the absence of new physics, this value can only be maintained through finely

tuned cancellations between bare parameters and quantum corrections, a situation that is theoretically unsatisfactory [183].

The hierarchy problem can be analysed quantitatively by considering one-loop corrections to the Higgs mass. If the SM is valid up to Λ_{SM}, the Higgs mass receives quadratically divergent corrections from top quark loops, electroweak gauge bosons, and the Higgs self-interaction itself. These corrections are illustrated in Fig. 2.1.

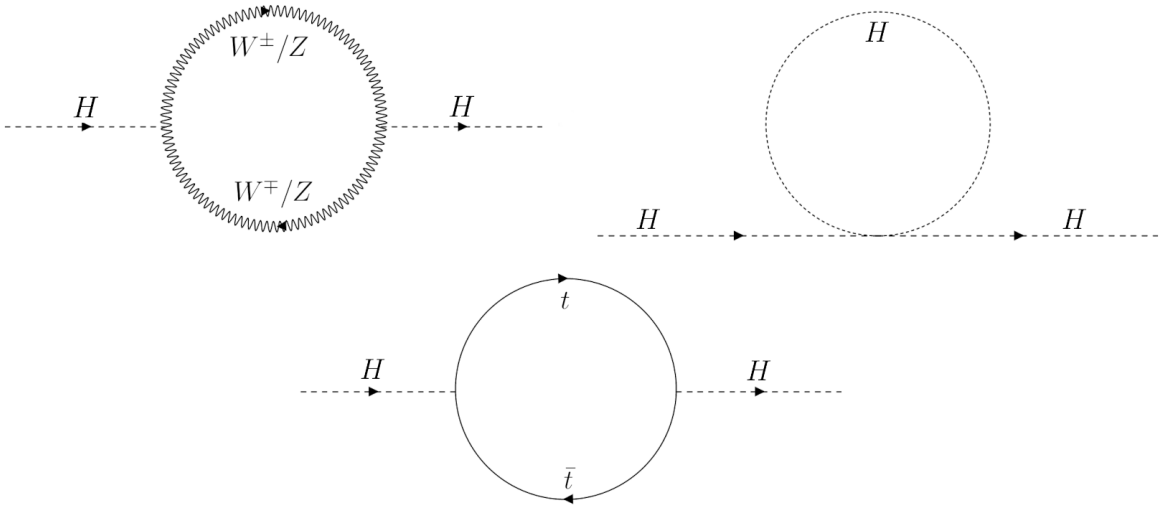

Figure 2.1. One-loop corrections to the Higgs boson mass.

Following [183], the one-loop correction to the squared Higgs mass is

$$\delta m_H^2 = \frac{3y_t^2}{8\pi^2}\Lambda_{\text{SM}}^2 - \frac{3g^2}{8\pi^2}\left(\frac{1}{4} + \frac{1}{8\cos^2\theta_W}\right)\Lambda_{\text{SM}}^2 - \frac{3\lambda}{8\pi^2}\Lambda_{\text{SM}}^2, \tag{2.4.1}$$

where y_t is the top-quark Yukawa coupling, g is the weak coupling constant, θ_W is the Weinberg angle, and λ is the Higgs self-coupling. Among these contributions, the top-quark loop dominates due to the large top mass and Yukawa coupling, $y_t \sim \mathcal{O}(1)$, with the Higgs-quark-quark vertex proportional to m_{quark}/v.

The absence of new physics up to the multi-TeV scale at the LHC implies that Λ_{SM} must be large, which in turn exacerbates the fine-tuning problem. The required counterterm to yield the observed Higgs mass becomes increasingly unnatural. A measure of this tuning can be expressed via the fine-tuning parameter Δ, defined as

$$\Delta \geqslant \frac{\delta_{\text{SM}} m_H^2}{m_H^2} = \frac{3y_t^2}{8\pi^2}\left(\frac{\Lambda_{\text{SM}}}{m_H}\right)^2 \approx \left(\frac{\Lambda_{\text{SM}}}{450\ \text{GeV}}\right)^2. \tag{2.4.2}$$

Even for $\Lambda_{\text{SM}} \sim 10$ TeV, one finds a tuning of better than 1 part in 500, which is often deemed

unnatural and has motivated numerous extensions of the SM that address the hierarchy problem.

Thus, we must either accept this extreme coincidence or seek an alternative framework. A natural solution would require new physics at the TeV scale, ensuring a reasonable fine-tuning parameter Δ in Eq. (2.4.2).

Given these limitations of the Standard Model, despite its experimental successes, it is compelling to explore beyond Standard Model theories. An intriguing solution to the hierarchy problem is the composite Higgs scenario, in which the Higgs boson acquires its mass through Goldstone dynamics. This scenario postulates the existence of a new strongly interacting sector, described by an underlying gauge theory. The global flavour symmetry of this theory depends on its fermionic content. If the fermions condense, the spontaneous breaking of this symmetry generates Goldstone bosons, among which the Higgs doublet can be identified. In the absence of interactions with the Standard Model, the Higgs would remain massless. However, explicit symmetry breaking arises from the couplings to the Standard Model. Consequently, the Higgs is interpreted as a pseudo-Nambu-Goldstone boson: its mass remains nonzero but relatively small, as it is protected by an approximate symmetry that is broken only through interactions with the Standard Model.

This idea finds a well-established analogue in two-flavour QCD, where the up and down quarks form a flavour doublet with an approximate chiral symmetry, $SU(2)_L \times SU(2)_R$. When spontaneously broken by quark condensation, this symmetry yields three pions as the associated Nambu–Goldstone bosons. Small quark masses break the symmetry explicitly, making the pions light but massive.

2.4.2 Necessary requirements for Composite Higgs models

This section elaborates on gauge theories that have the potential to produce a pseudo-Nambu-Goldstone Higgs boson. Refs. [181] and [184] discuss possible ultraviolet completions for composite Higgs models, by leveraging symmetry considerations and empirical constraints.

In order to build a microscopic theory for this type of model, a key assumption is that the colour group is a simple group G_C and the fermions are only left-handed Weyl fermions denoted as $\psi \in n_1 R_1 + \cdots + n_p R_p$, R_i is an irreducible representation of G_C, n_i denotes the number of copies of each irreducible representation, for $i \neq j$, it holds that $R_i \neq R_j$, p counts the different irreducible representations in the model. Restricting the colour group to be simple ensures minimality of the model. The global symmetry group

$$G_F = SU(n_1) \times \cdots \times SU(n_p) \times U(1)^{p-1}. \tag{2.4.3}$$

is required to be chosen in such a way that the following conditions are met:

- The Standard Model fermions are neutral under transformations belonging to G_{C}.
- The fermions ψ are charged appropriately under G_{SM} to form bound states acting as composite Higgs and top-quark partners.
- The model must exhibit asymptotic freedom, ensuring that the theory becomes strongly coupled in the infrared regime. This property typically arises in asymptotically free theories when starting with a small coupling in the ultraviolet regime and without additional perturbative fixed points.

In order to be built, a CHM needs to fulfil several additional necessary requirements:

- Gauge and global anomaly cancellation: the model requires gauge anomaly freedom, for $G_{\mathrm{C}} = SU(N)$, and global anomaly freedom, for $G_{\mathrm{C}} = Sp(2N)$.

- Custodial symmetry: the desired symmetry breaking pattern is

$$G_F \to H_F \supset G_{\mathrm{cus.}} \supset G_{\mathrm{SM}}. \tag{2.4.4}$$

  where H_F must contain the custodial symmetry group $G_{\mathrm{cus.}}$ defined as

$$G_{\mathrm{cus.}} = SU(3)_c \times SU(2)_L \times SU(2)_R \times U(1)_X. \tag{2.4.5}$$

  and the Standard Model gauge group G_{SM}, defined as

$$G_{\mathrm{SM}} = SU(3)_c \times SU(2)_L \times U(1)_Y. \tag{2.4.6}$$

  This custodial symmetry mirrors the structure of the Standard Model, where the electroweak symmetry breaking happens, giving the W and Z bosons their masses [187]. One way to capture its influence is through the definition of the ρ-parameter [188], given by

$$\rho = \frac{m_W^2}{m_Z^2 \cos^2 \theta_{\mathrm{W}}}, \tag{2.4.7}$$

  where θ_{W} represents the Weinberg angle. In the Standard Model, $\rho_{\mathrm{SM}} = 1$ at tree level, aligning with experimental observations. This custodial $SU(2)$ symmetry also suppresses significant loop corrections. The extension involving an additional $SU(2)_R$ symmetry serves to minimise large tree-level corrections to the ρ-parameter, thereby safeguarding key electroweak precision measurements.

- Presence of a composite Higgs candidate: The coset space G_F/H_F must contain a Nambu-Goldstone boson transforming as $(\mathbf{1}, \mathbf{2}, \mathbf{2})_0$ under $G_{\mathrm{cus.}}$. This field, denoted

by H, serves as the composite Higgs candidate. The Higgs field should condense via misalignment, likely induced by interactions with the top-quark, consistent with effective field theory expectations.

Although not strictly necessary, a possibility is to seek models that produce a composite state with the same Standard Model quantum numbers as the heavy quarks. Such a property could provide insight into the hierarchical structure of quark masses: if the composite partner of the top-quark possesses a sufficiently large anomalous dimension, the mass hierarchy emerges naturally. This mechanism is known as partial compositeness [183]. The guiding principle for such models can be expressed as follows:

- Formation of a top-quark: the model must enable the formation of fermionic bound states ψ^3 that can serve as top-quark partners. The left-handed components of these spinors should transform with the same quantum numbers as the SM third-generation quarks. As shown in Ref. [183], requiring large Yukawa couplings–and therefore large masses–for the heavy quarks in effective field theory formalism, involves trilinear operators that require a large anomalous dimension, shifting from the perturbative value 9/2 to approximately 5/2.

Ref. [181] identified the $Sp(4)$ theory with $N_{\rm f} = 2$ fundamental fermions and $N_{\rm as} = 3$ two-index antisymmetric fermions as one of the models that satisfy all the requirements. In this context, Ref [16] devises how the baryonic ψ^3 states (called "chimera baryons") can be associated with possible top-quark partner candidates. This is possible as the symmetry breaking pattern in both the fundamental and antisymmetric fermion sectors are described by the cosets $SU(4)/Sp(4)$ and $SU(6)/SO(6)$: the Standard Model gauge groups can be shown to be embedded within the unbroken groups of the cosets. More details are provided in the next subsection. This allows some of the chimera baryons to carry the same quantum numbers as the top-quark. For these reasons, it is interesting to study the dynamics of this theory in Chapter 5.

Giving up on the last requirement, and therefore on the possibility of bound states ψ^3, amounts to giving up on the top-quark partner candidate but keeps the possibility of a composite Higgs scenario. This is the case in which the $Sp(4)$ gauge theory with $N_{\rm f} = 2$ fundamental fermions falls into. In fact, one of the minimal composite Higgs models amenable to lattice studies was presented in Ref. [140], and it proposes that the Higgs fields arise from the pseudo-Nambu-Goldstone bosons describing the $SU(4)/Sp(4)$ coset in this latter gauge theory. We still stress that, once the Higgs compositeness is ensured, top partial compositeness can be implemented by adding further fermionic content to the theory.

2.4.3 CHM and TPC in the $Sp(4)$, $N_{\rm f} = 2$, $N_{\rm as} = 3$ gauge theory

Let us consider the $Sp(4)$ gauge theory with $N_{\rm f} = 2$ fundamental Dirac fermions and $N_{\rm as} = 3$ 2-index antisymmetric ones. We wrote the Lagrangian density in this theory in two-components notation in Eq. (2.3.29). This makes the global symmetry breaking pattern apparent: the Lagrangian density has a global $SU(4)$ symmetry on the fundamental sector, and a global $SU(6)$ symmetry from the 2-index antisymmetric sector. The mass term breaks these to $Sp(4)$ and $SO(6)$, respectively. The unbroken global symmetry groups $SU(4)$ and $SU(6)$ of the theory possess 15 and 35 generators. Following the discussions in Refs. [8, 11, 16, 26], in the spontaneous breaking pattern, the unbroken subgroups $Sp(4)$ and $SO(6)$ are characterised by the relations (see e.g. Eq. (2.3.23)):

$$\Omega T^a_{\rm f} + T^a_{\rm f}{}^{\rm T}\Omega = 0, \quad \omega T^b_{\rm as} + T^b_{\rm as}{}^{\rm T}\omega = 0, \tag{2.4.8}$$

with $a = 6, \dots, 15$ and $b = 21, \dots, 35$. Instead, the broken directions, $T^a_{\rm f}$ with $a = 1, \dots, 5$ for $SU(4)$ and $T^b_{\rm as}$ with $b = 1, \dots, 20$ for $SU(6)$, obey

$$\Omega T^a_{\rm f} - T^a_{\rm f}{}^{\rm T}\Omega = 0, \quad \omega T^b_{\rm as} - T^b_{\rm as}{}^{\rm T}\omega = 0, \tag{2.4.9}$$

(ω is defined below Eq. (2.3.29)).

The Standard Model Higgs sector has an approximate custodial symmetry, $SU(2)_L \times SU(2)_R \simeq SO(4)$, which can be embedded into the unbroken global symmetry $Sp(4)$. Similarly, the QCD gauge group $SU(3)_c$ is naturally a subgroup of the unbroken $SO(6)$. The hypercharge $U(1)_Y$ arises as a specific linear combination of an $SU(2)_R$ generator and an additional $U(1)_X$ from $SO(6)$ that commutes with $SU(3)_c$. This can be shown explicitly. Let us start from the Higgs sector of the Standard Model: the symmetry breaking structure of the $SU(4)/Sp(4)$ coset encapsulates this sector. In the vacuum aligned with the symplectic form Ω as defined in Eq. (2.3.3), the subgroup $SO(4) \simeq SU(2)_L \times SU(2)_R$ emerges as part of the unbroken global symmetry $Sp(4) \subset SU(4)$. This can be seen in further detail, by starting from the choice of generators for $SU(4)$ and $Sp(4)$ designed in Ref. [189] (and listed in Appendix B). The maximal subgroup is generated of the unbroken $Sp(4)$ group is generated

by the following six elements:

$$
\begin{aligned}
T_L^1 &= \frac{1}{2}\begin{pmatrix} 0&0&1&0\\ 0&0&0&0\\ 1&0&0&0\\ 0&0&0&0 \end{pmatrix}, \quad T_L^2 = \frac{1}{2}\begin{pmatrix} 0&0&-i&0\\ 0&0&0&0\\ i&0&0&0\\ 0&0&0&0 \end{pmatrix}, \quad T_L^3 = \frac{1}{2}\begin{pmatrix} 1&0&0&0\\ 0&0&0&0\\ 0&0&-1&0\\ 0&0&0&0 \end{pmatrix}, \\
T_R^1 &= \frac{1}{2}\begin{pmatrix} 0&0&0&0\\ 0&0&0&1\\ 0&0&0&0\\ 0&1&0&0 \end{pmatrix}, \quad T_R^2 = \frac{1}{2}\begin{pmatrix} 0&0&0&0\\ 0&0&0&-i\\ 0&0&0&0\\ 0&i&0&0 \end{pmatrix}, \quad T_R^3 = \frac{1}{2}\begin{pmatrix} 0&0&0&0\\ 0&1&0&0\\ 0&0&0&0\\ 0&0&0&-1 \end{pmatrix}.
\end{aligned}
\tag{2.4.10}
$$

These satisfy the expected $\mathfrak{su}(2)$ commutation relations: $[T_L^i, T_L^j] = i\epsilon^{ijk}T_L^k$ and $[T_R^i, T_R^j] = i\epsilon^{ijk}T_R^k$, with all mixed commutators vanishing, $[T_L^i, T_R^j] = 0$. This defines a canonical embedding of the custodial $SO(4)$ symmetry within $Sp(4)$ in the vacuum state.

Following Ref. [189], the five pseudo-Nambu–Goldstone bosons associated with the $SU(4)/Sp(4)$ coset are organised into a matrix $\pi(x) \equiv \sum_{a=1}^{5} \pi^a(x)T^a$, explicitly given by

$$
\pi(x) = \frac{1}{2\sqrt{2}}\begin{pmatrix} \pi^3(x) & \pi^1(x) - i\pi^2(x) & 0 & -i\pi^4(x) + \pi^5(x) \\ \pi^1(x) + i\pi^2(x) & -\pi^3(x) & i\pi^4(x) - \pi^5(x) & 0 \\ 0 & -i\pi^4(x) - \pi^5(x) & \pi^3(x) & \pi^1(x) + i\pi^2(x) \\ i\pi^4(x) + \pi^5(x) & 0 & \pi^1(x) - i\pi^2(x) & -\pi^3(x) \end{pmatrix}. \tag{2.4.11}
$$

Here, the real scalar fields π^1, π^2, π^4, and π^5 correspond to the components of the Higgs doublet, while π^3 is an additional singlet under $SU(2)_L \times SU(2)_R$.

In contrast, the $SU(6)/SO(6)$ coset is relevant for the dynamics of top compositeness. With $N_{\text{as}} = 3$ Dirac fermions in the two-index antisymmetric representation of $Sp(4)$, the model accommodates a global $SU(6)$ symmetry, which naturally contains $SU(3)_L \times SU(3)_R$ as a subgroup. This subgroup is generated by:

$$
T_L^b = \frac{1}{2}\begin{pmatrix} \lambda^b & \mathbb{O}_3 \\ \mathbb{O}_3 & \mathbb{O}_3 \end{pmatrix}, \quad T_R^b = \frac{1}{2}\begin{pmatrix} \mathbb{O}_3 & \mathbb{O}_3 \\ \mathbb{O}_3 & -\lambda^{b*} \end{pmatrix}, \tag{2.4.12}
$$

where λ^b are the eight Gell-Mann matrices, normalised such that $\mathrm{Tr}(\lambda^a\lambda^b) = 2\delta^{ab}$, implying $\mathrm{Tr}(T_L^a T_L^b) = \frac{1}{2}\delta^{ab}$.

Defining the combinations $T_c^b = T_L^b + T_R^b$, and employing the choice of ω as below of Eq. (2.3.29), one verifies that these satisfy

$$
\omega T_c^b + T_c^{b\ \mathrm{T}}\omega = 0, \quad [T_c^a, T_c^b] = if^{abd}T_c^d, \tag{2.4.13}
$$

where the f^{abd} are the structure constants of the $\mathfrak{su}(3)_c$ algebra. The trace relation $\mathrm{Tr}(T_c^a T_c^b) = \delta^{ab}$ further confirms that these are generators of $SU(3)_c$, albeit written in a 6×6 representation acting on the six-dimensional space of antisymmetric fermion bilinears.

There is also a residual unbroken $U(1)$ generator in $SU(6)$, orthogonal to $SU(3)_c$, given by

$$X = \begin{pmatrix} \mathbb{1}_3 & \mathbb{0}_3 \\ \mathbb{0}_3 & -\mathbb{1}_3 \end{pmatrix}. \tag{2.4.14}$$

This $U(1)_X$ commutes with all $SU(3)_c$ generators. In the Standard Model, the hypercharge $U(1)_Y$ is embedded as a linear combination of this X and the T_R^3 generator from the custodial $SU(2)_R$ subgroup [11]. Using these assignments of quantum numbers, composite fermion operators can be formulated by combining two fundamental fermions Q (and therefore transforming as a $(2,2)$ of $SU(2)_L \times SU(2)_R$) and a 2-index antisymmetric one Ψ (this corresponds to a triplet of $SU(3)_c$) [16]. Therefore, the resulting composite ψ^3 ($\sim Q^2\Psi$) chimera baryons states[1] can be coupled to the heavy SM quarks and used in the TPC context.

To describe the low-energy degrees of freedom, one constructs an effective field theory for the pseudo Nambu–Goldstone bosons (pNGBs) arising from the coset space $(SU(4) \times SU(6))/(Sp(4) \times SO(6))$. The pNGB content is encoded in matrix fields Σ_6 and Σ_{21}, defined through composite operators formed from the underlying fermions:

$$\begin{aligned} \Sigma_6^{nm} &\sim \Omega_{ab}\, q^{na\ \mathrm{T}} \tilde{C} q^{mb}, \\ \Sigma_{21}^{nm} &\sim -\Omega_{ab}\Omega_{cd}\, \psi^{nac\ \mathrm{T}} \tilde{C} \psi^{mbd}. \end{aligned} \tag{2.4.15}$$

These composite operators transform as antisymmetric (Σ_6 under $SU(4)$) and symmetric (Σ_{21} under $SU(6)$) tensor representations. They are parameterised nonlinearly as

$$\Sigma_6 = e^{\frac{2i\pi_6}{f_6}}\Omega = \Omega e^{\frac{2i\pi_6^{\mathrm{T}}}{f_6}}, \quad \Sigma_{21} = e^{\frac{2i\pi_{21}}{f_{21}}}\omega = \omega e^{\frac{2i\pi_{21}^{\mathrm{T}}}{f_{21}}}, \tag{2.4.16}$$

where $\pi_6 = \pi_6^a T_{\mathrm{f}}^a$ and $\pi_{21} = \pi_{21}^b T_{\mathrm{as}}^b$ with $a = 1, \ldots, 5$ and $b = 1, \ldots, 20$. The fields π_6 and π_{21} are Hermitian, and the generators are normalised via $\mathrm{Tr}(T_{\mathrm{f}}^a T_{\mathrm{f}}^b) = \frac{1}{2}\delta^{ab} = \mathrm{Tr}(T_{\mathrm{as}}^a T_{\mathrm{as}}^b)$. The constants f_6 and f_{21} serve as the decay constants for the pNGBs and are defined in analogy with the QCD value $f_\pi \simeq 93\,\mathrm{MeV}$.

Mass terms for the fermions explicitly break the global symmetry. These are incorporated as spurion fields transforming appropriately: $M_6 = M\Omega$ and $M_{21} = -m\omega$ so that the field content of the theory is the one in Tab. 2.1.

The leading-order effective Lagrangian for each sector ($i = 6, 21$) includes both kinetic

[1] The exact form of these operators in the $Sp(4)$, $N_{\mathrm{f}} = 2$, $N_{\mathrm{as}} = 3$ continuum theory is discussed in Ref. [16] and reported in Eqs. (21) and (22) of this reference. The lattice interpolating operators for the chimera baryons are presented in Chapter 3 of this thesis.

Fields	$Sp(4)$	$SU(4)$	$SU(6)$
G_μ	10	1	1
q	4	4	1
ψ	5	1	6
Σ_6	1	6	1
M_6	1	$\overline{6} \sim 6$	1
Σ_{21}	1	1	21
M_{21}	1	1	$\overline{21}$

Table 2.1. Table from Ref. [11], field content of the microscopic theory, described in Eq. (2.3.29), and of the low-energy EFT described the pseudo Nambu Goldstone bosons, Σ_i and M_i. The gauge symmetry is $Sp(4)$, while $SU(4)$ and $SU(6)$ are the global symmetries.

and mass terms, and can be written as:

$$\begin{aligned}\mathcal{L}_i &= \frac{f_i^2}{4}\,\mathrm{Tr}\left(\partial_\mu \Sigma_i \left(\partial^\mu \Sigma_i\right)^\dagger\right) - \frac{v_i^3}{4}\,\mathrm{Tr}(M_i \Sigma_i) + \text{h.c.} \\ &= \mathrm{Tr}(\partial_\mu \pi_i \partial^\mu \pi_i) + \frac{1}{3 f_i^2}\,\mathrm{Tr}\left([\partial_\mu \pi_i, \pi_i][\partial^\mu \pi_i, \pi_i]\right) + \cdots \\ &\quad + \frac{1}{2} m_i v_i^3\,\mathrm{Tr}(\Sigma_i \Sigma_i^\dagger) - \frac{m_i v_i^3}{f_i^2}\,\mathrm{Tr}(\pi_i^2) + \frac{m_i v_i^3}{3 f_i^4}\,\mathrm{Tr}(\pi_i^4) + \cdots\end{aligned} \tag{2.4.17}$$

with $m_6 = M$ and $m_{21} = m$. The condensates v_6 and v_{21} set the symmetry breaking scales and have dimensions of mass. For consistency, one has $\mathrm{Tr}(\Sigma_6 \Sigma_6^\dagger) = 4$ and $\mathrm{Tr}(\Sigma_{21} \Sigma_{21}^\dagger) = 6$.

To relate the EFT to Standard Model observables, appropriate subgroup embeddings are chosen for $SU(2)_L \times SU(2)_R$ and $SU(3)_c \times U(1)_X$. The derivatives in the Lagrangian are promoted to covariant ones.

In the $SU(4)/Sp(4)$ sector, the five pNGBs furnish a fundamental representation of $SO(5) \simeq Sp(4)$. Decomposing under $SO(4) \simeq SU(2)_L \times SU(2)_R$, we obtain $5 = 4 \oplus 1$. The four components form a Higgs doublet, while the fifth is an $SU(2)_L \times SU(2)_R$ singlet.

The analysis extends similarly to the $SU(6)/SO(6)$ coset. Recognising that $SO(6) \simeq SU(4)$, the twenty pNGBs transform in the self-conjugate $20'$ representation of $SU(4)$. This irreducible representation decomposes under the subgroup $SU(3)_c \times U(1)_X$ as:

$$20' = 8 \oplus 6_{\mathbb{C}}. \tag{2.4.18}$$

Chapter 3

Gauge theories on the lattice

In this chapter, methodologies for discretising gauge theories on the lattice are discussed, and details on numerical simulations through Monte-Carlo algorithms are provided. Moreover, the methodologies for the evaluation of hadronic observables as average values are presented, together with the action on the lattice used throughout the thesis for numerical simulations of $Sp(2N)$ gauge theories.

3.1 Discretisation of spacetime and introduction of link variables

As previously discussed, the functional integral in Eq. (2.1.18) presents divergences typical of quantum field theories, and therefore it requires renormalisation. To make the computation of such functional integrals feasible, we first perform a Wick rotation [190] to Euclidean space by redefining the space-time variables:

$$x^0 = -ix_0^E, \quad x^k = x_k^E, \tag{3.1.1}$$

$$\partial_0 = i\partial_0^E, \quad \partial_k = \partial_k^E, \tag{3.1.2}$$

The Minkowski metric is then replaced by the Euclidean metric in four dimensions:

$$\eta_{\mu\nu} \to \delta_{\mu\nu}, \tag{3.1.3}$$

and there is no longer a distinction between upper and lower Lorentz indices. We can also define a Euclidean action as:

$$S_E = -iS, \tag{3.1.4}$$

so that the pure gauge action in Eq. (2.1.15) becomes

$$S_G[A] = \frac{1}{2g^2} \int d^4x_E \, \mathrm{Tr}[F_{\mu\nu}^E(x) F_{\mu\nu}^E(x)], \tag{3.1.5}$$

the fermion action becomes

$$S_F[\psi,\bar{\psi}] = \int d^4x_E \left[\bar{\psi}_E(\gamma_\mu^E D_\mu^E + m)\psi_E\right], \tag{3.1.6}$$

and the partition function of interest transforms into

$$Z_E = \int \mathcal{D}A\mathcal{D}\psi\mathcal{D}\bar{\psi}\, e^{-S_G[A]-S_F[\psi,\bar{\psi}]}. \tag{3.1.7}$$

where due to their spin-statistics the fermionic degrees of freedom are Grassmann variables. This form ensures exponential suppression of configurations with large action, allowing for rapid convergence in numerical computations. From now on, we drop the subscript E, assuming that all expressions are in a Euclidean space.

Even after Wick rotation, the theory still involves an infinite number of degrees of freedom. To define the gauge theory non-perturbatively, following Ref. [191], we introduce a finite hypervolume and discretise the four-dimensional space-time using a regular hypercubic lattice Ξ:

$$\Xi = \{x = (x_0, x_1, x_2, x_3)\,|\,x_0 = 0, 1, \ldots, N_t - 1\,;\, x_1, x_2, x_3 = 0, 1, \ldots, N_s - 1\}. \tag{3.1.8}$$

The lattice coordinates are expressed in units of the lattice spacing, a, such that $N_s \cdot a \equiv L$ is the spatial extent of the lattice, and $N_t \cdot a \equiv T$ is the temporal extent. The spatial lattice lengths in different directions may differ, but not in this thesis.

To illustrate the discretisation process, Fig. 3.1 presents a three-dimensional slice of Euclidean lattice.

Focussing, once again, on fermions transforming in the R = f fundamental representation of G, spinors are defined on the lattice nodes, meaning our fermionic degrees of freedom are

$$\psi(x), \bar{\psi}(x) \quad \text{for } x \in \Xi. \tag{3.1.9}$$

In this framework, gauge transformations take the same form as in Eq. (2.1.3), but with an independent element $M(x) \in G$ at each lattice site, x. The transformations then take the form:

$$\psi(x) \to \psi'(x) = M(x)\psi(x). \tag{3.1.10}$$

A naive symmetric discretisation of the free-fermion derivative is given by

$$\partial_\mu \psi(x) \to \frac{1}{2a}(\psi(x + \hat{\mu}) - \psi(x - \hat{\mu})), \tag{3.1.11}$$

where $\hat{\mu}$ denotes the unit vector in direction μ. This leads to the lattice version of the free

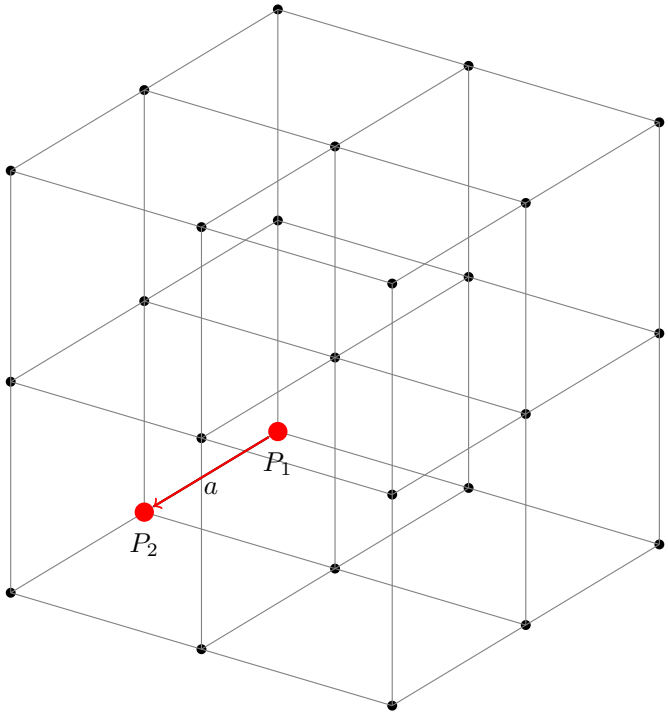

Figure 3.1. A three-dimensional slice of a four-dimensional Euclidean lattice. The red-arrowed line connecting points P_1 and P_2 represents a lattice link. a indicates the lattice spacing.

(massless) fermion action from Eq. (2.1.2):

$$S_F^0[\psi,\bar{\psi}] = a^4 \sum_{x\in\Xi} \bar{\psi}(x) \sum_{\mu=0}^{3} \gamma_\mu \frac{\psi(x+\hat{\mu}) - \psi(x-\hat{\mu})}{2a}. \tag{3.1.12}$$

However, under a gauge transformation

$$\bar{\psi}(x)\psi(x+\hat{\mu}) \to \bar{\psi}'(x)\psi'(x+\hat{\mu}) = \bar{\psi}(x)M^\dagger(x)M(x+\hat{\mu})\psi(x+\hat{\mu})\,, \tag{3.1.13}$$

is not gauge-invariant. To enforce gauge invariance in the discretised kinetic term of the fermionic action, we introduce a field, $U_\mu(x)$, that transforms as:

$$U_\mu(x) \to U'_\mu(x) = M(x)U_\mu(x)M^\dagger(x+\hat{\mu}). \tag{3.1.14}$$

This ensures that

$$\bar{\psi}(x)U_\mu(x)\psi(x+\hat{\mu}) = \bar{\psi}'(x)U'_\mu(x)\psi'(x+\hat{\mu}), \tag{3.1.15}$$

preserving gauge invariance.

Thus, we introduce the gauge fields $U_\mu(x)$ as elements of the gauge group G, which transform as in Eq. (3.1.14). These matrix-valued variables are oriented along the lattice links and are therefore referred to as link variables. In particular, $U_\mu(x)$ represents the link connecting sites x and $x+\hat{\mu}$.

A direct connection between the continuum and lattice formulations can be established. In the continuum, an analogous object that transforms as Eq. (3.1.14) is the Wilson line:

$$G(x,y) = \mathcal{P}\exp\Big(i\int_{\mathcal{C}_{xy}} A\cdot ds\Big), \tag{3.1.16}$$

where $\mathcal{P}$ is the path-ordering operator, A_μ is the gauge field, and $\mathcal{C}_{xy}$ is a curve connecting x and y. It satisfies

$$G(x,y) \to M(x)G(x,y)M^\dagger(y). \tag{3.1.17}$$

We thus interpret the link variable, $U_\mu(x)$, as the lattice analogue of the gauge transporter connecting x and $x+\hat{\mu}$:

$$U_\mu(x) = G(x, x+\hat{\mu}) + \mathcal{O}(a), \tag{3.1.18}$$

and introduce the algebra-valued lattice gauge field $A_\mu(x)$ such that

$$U_\mu(x) = \exp\Big(iaA_\mu(x)\Big). \tag{3.1.19}$$

One can show that the introduction of gauge transporters on the links guarantees exact gauge invariance for the lattice theory. Indeed one can prove that considering the expression (3.1.16) with x and $y = x+\epsilon$ (ϵ being infinitesimal) one can write

$$\bar{\psi}(x)G(x,y)\psi(y) = \bar{\psi}(x)\Big\{1 + i\int ds\cdot A_\mu\Big\}\psi(x) + \epsilon\partial_\mu\psi + \mathcal{O}(\epsilon^2) =$$

$$= \bar{\psi}(x)\psi(x) + \epsilon\bar{\psi}(x)\{\partial_\mu + iA_\mu\}\psi(x) + \mathcal{O}(\epsilon^2)$$

so

$$\bar{\psi}(x)G(x,y)\psi(y) = \bar{\psi}(x)\psi(x) + \epsilon\bar{\psi}(x)D_\mu\psi(x) + \mathcal{O}(\epsilon^2)\,. \tag{3.1.20}$$

3.1.1 Pure gauge case: the Wilson action

If we define the shortest nontrivial closed loop on the lattice, known as the plaquette (illustrated in Fig. 3.2), it is given by

$$U_{\mu\nu}(x) = U_\mu(x)U_\nu(x+\hat{\mu})U_\mu^\dagger(x+\hat{\nu})U_\nu^\dagger(x). \tag{3.1.21}$$

From this object, one can construct a gauge-invariant quantity under transformations of the gauge group, G. Using the transformation property of a single link (3.1.14), the gauge

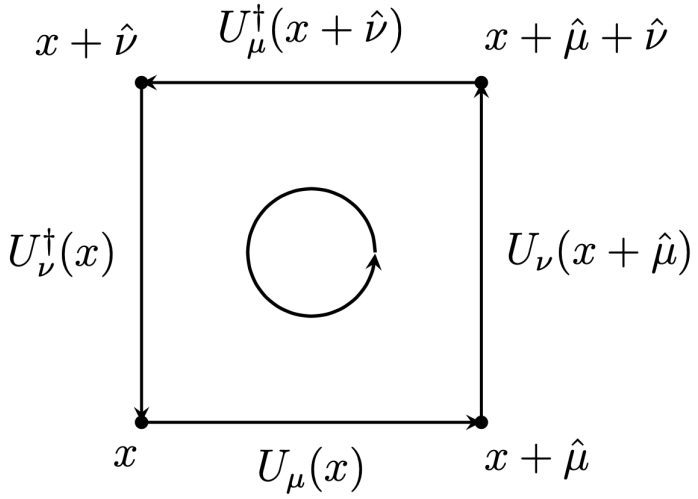

Figure 3.2. The four link variables forming the plaquette, $U_{\mu\nu}(x)$. The circle indicates the order in which the links are traversed.

transformation of a product of links along a path $\mathcal{P}$ connecting the points x_0 and x_1 is

$$P[U] = \prod_{(x,\mu)\in\mathcal{P}} U_\mu(x)\,, \tag{3.1.22}$$

where all gauge factors in the product cancel except at the endpoints x_0 and x_1, leading to

$$P[U] \to P[U'] = M(x_0)P[U]M^\dagger(x_1). \tag{3.1.23}$$

If the path is closed ($x_0 = x_1$), then by the cyclic property of the trace, $\mathrm{tr}(P[U])$ remains gauge-invariant.

This leads to the definition of the simplest lattice action for a purely gluonic theory: the Wilson gauge action. It is obtained by taking the trace of the plaquette and summing over all lattice points x and directions $0 \le \mu < \nu \le 3$,

$$S_G[U] = \frac{2}{g^2}\sum_{x\in\Xi}\sum_{\mu<\nu}\mathrm{Re}\Big\{\mathrm{tr}\,[\mathbb{I} - U_{\mu\nu}(x)]\Big\}. \tag{3.1.24}$$

Here, g^2 is the coupling constant of the gauge theory based on the group G, and the prefactor $\frac{2}{g^2}$ ensures consistency with the continuum action (3.1.5) in the limit $a \to 0$. This can be shown using the Campbell-Baker-Hausdorff formula for the product of exponentials of matrices A and B

$$e^A \cdot e^B = \exp\Big(A + B + \frac{1}{2}[A,B] + \dots\Big), \tag{3.1.25}$$

where dots indicate that terms involving products of more than two matrices are omitted. Inserting (3.1.19) into (3.1.21) and applying (3.1.25) iteratively, one obtain

$$U_{\mu\nu}(x) = \exp\Big(iaA_\mu(x) + iaA_\nu(x+\hat{\mu}) - \frac{a^2}{2}[A_\mu(x), A_\nu(x+\hat{\mu})]$$

$$-iaA_\mu(x+\hat{\nu}) - iaA_\nu(x) - \frac{a^2}{2}[A_\mu(x+\hat{\nu}), A_\nu(x)]$$

$$+\frac{a^2}{2}[A_\nu(x+\hat{\mu}), A_\mu(x+\hat{\nu})] + \frac{a^2}{2}[A_\mu(x), A_\nu(x)]$$

$$+\frac{a^2}{2}[A_\mu(x), A_\mu(x+\hat{\nu})] + \frac{a^2}{2}[A_\nu(x+\hat{\mu}), A_\nu(x)] + \mathcal{O}(a^3)\Big),$$

If we now perform a Taylor expansion

$$A_\nu(x+\hat{\mu}) = A_\nu(x) + a\partial_\mu A_\nu(x) + \mathcal{O}(a^2)\,, \tag{3.1.26}$$

we obtain

$$U_{\mu\nu}(x) = \exp\Big(ia^2(\partial_\mu A_\nu(x) - \partial_\nu A_\nu(x) + i[A_\mu(x), A_\nu(x)]) + \mathcal{O}(a^3)\Big)\,.$$

Using the continuum definition of field strength (2.1.13), we can write

$$U_{\mu\nu}(x) = \exp\Big(ia^2 F_{\mu\nu}(x) + \mathcal{O}(a^3)\Big)\,. \tag{3.1.27}$$

If we insert eq. (3.1.27) in the Wilson action (3.1.24), we find

$$S_G[U] = \frac{2}{g^2}\sum_{x\in\Xi}\sum_{\mu<\nu}\mathrm{Re}\Big\{\mathrm{tr}\,[\mathbb{I} - U_{\mu\nu}(x)]\Big\} = \frac{a^4}{2g^2}\sum_{x\in\Xi}\sum_{\mu<\nu}\mathrm{tr}[F_{\mu\nu}(x)^2] + \mathcal{O}(a^2)\,. \tag{3.1.28}$$

The $\mathcal{O}(a^2)$ terms that appear in the expansion of the exponential in Eq. (3.1.27) cancel when taking the real part of $\mathrm{tr}[\mathbb{I} - U_{\mu\nu}(x)]$. Similarly, the $\mathcal{O}(a^3)$ terms in the expansion of Eq. (3.1.27) also cancel, such that the Wilson action approximates the continuum form up to $\mathcal{O}(a^2)$, as shown in Eq. (3.1.28).

Note that the factor of a^4, together with the sum over Ξ, is simply the discretisation of the space-time integral. Thus, we have

$$\lim_{a\to 0}, S_G[U] = S_G[A]. \tag{3.1.29}$$

We can now define a non-perturbative, purely gluonic theory on the lattice through the partition function

$$Z = \int \mathcal{D}U\, e^{-S_G[U]}. \tag{3.1.30}$$

The corresponding measure is

$$\mathcal{D}U = \prod_{x\in\Xi}\prod_{\mu=0}^{3} dU_\mu(x), \tag{3.1.31}$$

where $dU_\mu(x)$ denotes the Haar measure for the link variable $U_\mu(x)$. Eqs. (3.1.30) and (3.1.24) are the lattice analogues of the pure gauge part of the continuum partition function (3.1.7) and the continuum action (3.1.5). In this context, the expectation value of observables O (which can also be a composite operator) is given by

$$\langle O\rangle = \frac{1}{Z}\int \mathcal{D}U e^{-S_G[U]} O[U]. \tag{3.1.32}$$

Finally, for the gauge group $Sp(2N)$ on the lattice, the Wilson action is written as

$$S_G[U] = \beta \sum_{x\in\Xi}\sum_{\mu<\nu}\left\{\mathrm{tr}\left[\mathbb{I} - \frac{1}{2N}U_{\mu\nu}(x)\right]\right\}, \tag{3.1.33}$$

where $\beta = \dfrac{4N}{g^2}$, since in this case, the trace of each group element is real.

3.1.2 Introducing fermions on the lattice and Wilson-Dirac action

The discretisation procedure for fermions, discussed in Section 3.1, involves some non-trivial challenges. In particular, we must account for the correct fermionic statistics, which differ from the bosonic one. Moreover, following the reasoning of Ref. [191], we will demonstrate in the following section that the lattice formulation of fermions, as presented so far, still suffers from certain lattice artefacts known as "doublers".

The naive free fermion action (3.1.12) is bilinear in $\bar\psi$ and ψ and can be expressed as

$$S_F[\psi,\bar\psi] = a^4 \sum_{x,y\in\Xi}\sum_{a,b,\alpha,\beta} \bar\psi(x)_{\alpha a}\, D_{m,\,\alpha\beta ab}(x,y)\,\psi(y)_{\beta b}\,, \tag{3.1.34}$$

where a,b indices refer to colour, α,β are spinor indices, and the naive Dirac operator on the lattice[1] is given by

$$D_{m,\,\alpha\beta\,ab}(x,y) = \sum_{\mu=0}^{3}(\gamma_\mu)_{\alpha\beta}\frac{\delta_{x+\hat\mu,y} - \delta_{x-\hat\mu,y}}{2a}\delta_{ab} + m\,\delta_{\alpha\beta}\delta_{ab}\delta_{xy}\,. \tag{3.1.35}$$

[1]The subscript m is to indicate the non-zero mass term in the Dirac operator. When not present, the Dirac operator is assumed to be massless.

The Fourier transform of the Dirac operator (3.1.35) reads

$$\begin{aligned}\tilde{D}_m(p,q) &= \frac{1}{|\Xi|}\sum_{x,y\in\Xi} e^{-ip\cdot xa} D(x,y) e^{iq\cdot ya} = \frac{1}{|\Xi|}\sum_{x,y\in\Xi} e^{-i(p-q)\cdot xa}\Big(\sum_{\mu=0}^{3}\gamma_\mu \frac{e^{iq_\mu a}-e^{-iq_\mu a}}{2a} + m\mathbb{I}\Big) \\ &= \delta(p-q)\Big(m\mathbb{I} + \frac{i}{a}\sum_{\mu=0}^{3}\gamma_\mu \sin(p_\mu a)\Big) = \delta(p-q)\tilde{D}_m(p)\,,\end{aligned} \tag{3.1.36}$$

where $|\Xi| = N_t \cdot N_s^3$ is the total number of lattice points, and the Fourier transform of the lattice Dirac operator is defined by

$$\tilde{D}_m(p) = m\mathbb{I} + \frac{i}{a}\sum_{\mu=0}^{3}\gamma_\mu \sin(p_\mu a)\,. \tag{3.1.37}$$

Using the standard formula for the inverse of linear combinations of gamma matrices ($c, b_\mu \in \mathbb{R}$),

$$\Big(c\mathbb{I} + i\sum_{\mu=0}^{3}\gamma_\mu b_\mu\Big)^{-1} = \frac{c\mathbb{I} - i\sum_{\mu=0}^{3}\gamma_\mu b_\mu}{c^2 + \sum_{\mu=0}^{3} b_\mu^2}\,, \tag{3.1.38}$$

(which can be verified by multiplying both sides by $c\mathbb{I} + i\sum_\mu \gamma_\mu b_\mu$), we find the matrix $\tilde{D}(p)^{-1}$:

$$\tilde{D}_m(p)^{-1} = \frac{m\mathbb{I} - ia^{-1}\sum_\mu \gamma_\mu \sin(p_\mu a)}{m^2 + a^{-2}\sum_\mu \sin(p_\mu a)^2}\,. \tag{3.1.39}$$

This is the free quark propagator in Fourier space. By Wick's theorem, the quark propagator governs the behaviour of n-point functions. Setting $m = 0$ in (3.1.39), we find that at fixed p, the propagator has the correct naive continuum limit:

$$\tilde{D}_m(p)^{-1} = \frac{-ia^{-1}\sum_\mu \gamma_\mu \sin(p_\mu a)}{a^{-2}\sum_\mu \sin(p_\mu a)^2} \tag{3.1.40}$$

$$\xrightarrow[a\to 0]{} \frac{-i\sum_\mu \gamma_\mu p_\mu}{p^2}\,. \tag{3.1.41}$$

In the continuum limit, the momentum space propagator (3.1.41) for massless fermions has a pole at

$$p = (0,0,0,0)\,. \tag{3.1.42}$$

This pole corresponds to the single fermion described by the continuum Dirac operator. However, on the lattice, the propagator for free fermions (3.1.40) has 15 additional unphysical poles at $p = \left(\frac{\pi}{a},0,0,0\right), \left(0,\frac{\pi}{a},0,0\right), \ldots, \left(0,0,0,\frac{\pi}{a}\right)$. These poles are the so-called doublers, which arise from the high momentum components of the lattice Dirac operator. They are

artefacts of the discretisation of the fermion field on a finite lattice. These doublers are problematic because they correspond to unphysical degrees of freedom in the theory.

We need to distinguish the proper pole from the doublers. For $m = 0$, a solution was proposed by Wilson, which is based on the Nielsen-Ninomiya theorem [192–194].

Nielsen-Ninomiya Theorem The Nielsen-Ninomiya theorem states that there does not exist a function $\tilde{D}(p)$ satisfying simultaneously the following conditions:

1. $\tilde{D}(p)$ is a smooth function of p_μ with period $\frac{2\pi}{a}$,
2. For small momenta ($p_\mu \ll \frac{\pi}{a}$), the function has the limit $\tilde{D}(p) = i\gamma_\mu p_\mu + \mathcal{O}(ap^2)$,
3. $\tilde{D}(p)$ is invertible for all non-vanishing momenta, modulo $\frac{2\pi}{a}$,
4. The Dirac operator anticommutes with the γ_5 matrix: $\{\gamma_5, \tilde{D}(p)\} = 0$.

Since the Dirac operator in Equation (3.1.37) is smooth and periodic, has the correct continuum limit $i\gamma_\mu p_\mu$, and anticommutes with γ_5, it necessarily has doublers. Therefore, historically, the way to proceed was to choose a Dirac operator that satisfies the first three conditions but gives up on the chirality property.

To avoid doublers and describe the fermionic theory correctly, Wilson added an additional term, called the Wilson term, and obtained:

$$\tilde{D}_m(p) = m\mathbb{I} + \frac{i}{a}\sum_{\mu=0}^{3}\gamma_\mu \sin(p_\mu a) + \mathbb{I}\frac{1}{a}\sum_{\mu=0}^{3}\left(1 - \cos(p_\mu a)\right) . \tag{3.1.43}$$

The Wilson term has the desired properties: even if $m = 0$, the fourth condition of the Nielsen-Ninomiya theorem is violated, enabling us to avoid the doublers. Furthermore, for components with $p_\mu = 0$, the term vanishes. For each component where $p_\mu = \frac{\pi}{a}$, it contributes an extra mass term:

$$m + \frac{2l}{a} , \tag{3.1.44}$$

where l is the number of momentum components with $p_\mu = \frac{\pi}{a}$. In the continuum limit $a \to 0$, the doublers become very heavy and decouple from the theory.

By calculating the momentum space propagator $\tilde{D}^{-1}(p)$, we find that the unwanted poles are removed, leaving only the physical pole as described in Equation (3.1.42). The form of the Wilson term in position space can be derived by inverse Fourier transforming the Wilson term in Equation (3.1.43):

$$-a\sum_{\mu=0}^{3}\frac{\delta_{x+\hat{\mu},y}\delta_{ab} - 2\delta_{ab}\delta_{xy} + \delta_{x-\hat{\mu},y}\delta_{ab}}{2a^2} . \tag{3.1.45}$$

Thus, the complete Wilson-Dirac operator is given by:

$$D_{m,\alpha\beta ab}(x,y) = \left(m + \frac{4}{a}\right)\delta_{\alpha\beta}\delta_{ab}\delta_{xy} - \frac{1}{2a}\sum_{\mu=0}^{3}\left[(\mathbb{I} - \gamma_\mu)_{\alpha\beta}\delta_{x+\hat{\mu},y}\delta_{ab} + (\mathbb{I} + \gamma_\mu)_{\alpha\beta}\delta_{x-\hat{\mu},y}\delta_{ab}\right]. \tag{3.1.46}$$

Note that the Wilson term is a discretisation of a $\left[-\left(\frac{a}{2}\right)\partial_\mu\partial_\mu\right]$ term, i.e.., it is proportional to the Laplace operator (with a minus sign), and the prefactor a shows that the Wilson term vanishes in the naive continuum limit $a \to 0$.

Finally, the action for free fermions in a gauge theory can be written as:

$$S_F[\psi,\bar{\psi}] = \sum_{i=1}^{N_\mathrm{f}} a^4 \sum_{x,y\in\Xi} \bar{\psi}_i(x) D_m(x,y)\psi_i(y)\,, \tag{3.1.47}$$

and the free theory of fermions can be defined non-perturbatively via the path integral:

$$Z_F = \int \mathcal{D}\psi\,\mathcal{D}\bar{\psi}\, e^{-S_F[\psi,\bar{\psi}]}\,, \tag{3.1.48}$$

where

$$\mathcal{D}\psi\,\mathcal{D}\bar{\psi} = \prod_{x\in\Xi}\prod_{i,\alpha,c} d\psi(x)_{i\alpha c}\, d\bar{\psi}(x)_{i\alpha c}\,. \tag{3.1.49}$$

with α, i and c, spin, flavour, and colour indices, respectively. As a final observation, the free fermion theory can be generalised to include interactions between the fermions and the gauge fields. The naive fermionic action (3.1.12) (assuming $m \neq 0$, $N_\mathrm{f} = 1$ for simplicity) can be generalised to:

$$S_F[\psi,\bar{\psi},U] = a^4 \sum_{x\in\Xi} \bar{\psi}(x)\left(\sum_{\mu=0}^{3}\gamma_\mu \frac{U_\mu(x)\psi(x+\hat{\mu}) - U_\mu^\dagger(x-\hat{\mu})\psi(x-\hat{\mu})}{2a} + m\psi(x)\right). \tag{3.1.50}$$

This action is gauge-invariant, as shown using the transformations (3.1.10) and (3.1.14). In the continuum limit, $a \to 0$, using the relation (3.1.19), this becomes equivalent to the continuum covariant derivative coupling between fermions and gauge fields:

$$S_F[\psi,\bar{\psi},A] = \int d^4x\,\bar{\psi}(x)(\gamma_\mu(\partial_\mu + iA_\mu(x)) + m)\psi(x)\,. \tag{3.1.51}$$

Thus, the interacting case can be generalised, and the fermion propagator $D_{m,\alpha\beta ab}(x,y)$ becomes:

$$D_{m,\alpha\beta ab}(x,y) = \sum_{\mu=0}^{3}(\gamma_\mu)_{\alpha\beta}\frac{U_\mu(x)_{ab}\delta_{x+\hat{\mu},y} - U_\mu^\dagger(x-\hat{\mu})_{ab}\delta_{x-\hat{\mu},y}}{2a} + m\delta_{\alpha\beta}\delta_{ab}\delta_{xy}\,, \tag{3.1.52}$$

and the Wilson term becomes:

$$-a\sum_{\mu=0}^{3}\frac{U_\mu(x)_{ab}\delta_{x+\hat{\mu},y}-2\delta_{ab}\delta_{xy}+U_\mu^\dagger(x-\hat{\mu})_{ab}\delta_{x-\hat{\mu},y}}{2a^2}\,. \tag{3.1.53}$$

The final Dirac operator for the interacting theory is:

$$\begin{aligned}D_{m,\alpha\beta ab}(x,y)=&\left(m+\frac{4}{a}\right)\delta_{\alpha\beta}\delta_{ab}\delta_{xy}+\\&-\frac{1}{2a}\sum_{\mu=0}^{3}\left[(\mathbb{I}-\gamma_\mu)_{\alpha\beta}U_\mu(x)_{ab}\delta_{x+\hat{\mu},y}+(\mathbb{I}+\gamma_\mu)_{\alpha\beta}U_\mu^\dagger(x-\hat{\mu})_{ab}\delta_{x-\hat{\mu},y}\right].\end{aligned} \tag{3.1.54}$$

The interacting theory with fermions and gauge fields is described by the path integral:

$$Z=\int\mathcal{D}\psi\,\mathcal{D}\bar{\psi}\,\mathcal{D}U\,e^{-S_F[\psi,\bar{\psi},U]-S_G[U]}\,, \tag{3.1.55}$$

where the fermionic action is given by (3.1.47), the Dirac operator by (3.1.55), and the gauge action by the Wilson action (3.1.24). Compared to the naive action, the discretisation effects here are $\mathcal{O}(a)$ due to the Wilson term.

The Matthews-Salam formula [195] is valid

$$Z_F=\int\mathcal{D}\psi\,\mathcal{D}\bar{\psi}\,e^{-S_F[\psi,\bar{\psi},U]}=\det[D]\,, \tag{3.1.56}$$

and the integration over fermionic variables in the functional integral can be performed according to Wick's theorem as follows

$$\begin{aligned}\langle\bar{\psi}(y_1)\ldots\bar{\psi}(y_n)\,\psi(x_1)\ldots\psi(x_n)\rangle_F&\equiv\frac{1}{Z_F}\int\mathcal{D}\psi\mathcal{D}\bar{\psi}\,e^{-S_F[\psi,\bar{\psi},U]}\left[\bar{\psi}\ldots\bar{\psi}\,\psi\ldots\psi\right]\\&=(-1)^n\sum_{P(1,2,\ldots,n)}\mathrm{sgn}(P)D^{-1}(x_1,y_{P_1})D^{-1}(x_2,y_{P_2})\ldots D^{-1}(x_n,y_{P_n})\,,\end{aligned} \tag{3.1.57}$$

where the sum in the second line runs over all permutations $P(1,2,\ldots,n)$ of the numbers $1,2,\ldots,n$, and $\mathrm{sgn}(P)$ is the sign function of the permutation P. Therefore, given a fermionic action and gauge part, the expectation value of observables O is given by

$$\langle O\rangle=\frac{1}{Z}\int\mathcal{D}U\,\mathcal{D}\psi\,\mathcal{D}\bar{\psi}\,e^{-S_G[U]-S_F[U,\psi,\bar{\psi}]}\,O[U,\psi,\bar{\psi}]\,, \tag{3.1.58}$$

which according to (3.1.56) and (3.1.57) can be rewritten as

$$\langle O\rangle=\frac{1}{Z}\int\mathcal{D}U\,e^{-S_G[U]}\det[D]\,O[U,D^{-1}(U)]\equiv\int dP[U]\,O[U,D^{-1}(U)]\,, \tag{3.1.59}$$

where we identify the probability distribution according to which the gauge links are distributed

$$dP[U] = \frac{1}{Z} e^{-S_G[U]} \mathcal{D}U \, \det\{D\} \, . \tag{3.1.60}$$

3.2 Monte-Carlo simulations

The numerical evaluation of the partition function in Eq. (3.1.55) and the expectation value of observables in Eq. (3.1.58) can be performed using Monte-Carlo methods. Focusing on Eq. (3.1.59), a Monte-Carlo simulation approximates the integral by averaging the observable over N_{conf} gauge field configurations U_n, sampled with probability $dP[U]$ defined as in Eq. (3.1.60):

$$\langle O \rangle = \int dP[U] \, O[U, D^{-1}(U)] \approx \frac{1}{N_{\text{conf}}} \sum_{U_n=1}^{N_{\text{conf}}} O[U_n, D^{-1}(U_n)] + \mathcal{O}\left(\frac{1}{\sqrt{N_{\text{conf}}}}\right). \tag{3.2.1}$$

A precise estimate of an observable requires generating a sufficiently large number of configurations:

$$\langle O \rangle = \lim_{N_{\text{conf}} \to \infty} \frac{1}{N_{\text{conf}}} \sum_{U_n=1}^{N_{\text{conf}}} O[U_n, D^{-1}(U_n)], \tag{3.2.2}$$

and the corrections in Eq. (3.2.1) vanish due to the central limit theorem. The generation of gauge links according to the $dP[U]$ distribution is achieved by the (R)HMC algorithms, whose general principles are outlined in the next section.

As a more general matter, Monte-Carlo sampling is particularly effective for high-dimensional integrals, where traditional numerical quadrature methods become computationally infeasible. Unlike quadrature, where effort scales exponentially with accuracy, Monte-Carlo integration maintains an error proportional to $1/\sqrt{N_{\text{conf}}}$. Comparisons indicate that Monte-Carlo methods surpass quadrature efficiency for integrals involving more than three variables.

Configurations sampled according to the Boltzmann distribution are generated via an update algorithm forming a Markov chain [196]. The principle of importance sampling [191] dictates that configurations should be sampled predominantly from regions of high probability, ensuring efficient exploration of configuration space. To construct a sequence of configurations adhering to the equilibrium distribution $P(U)$ as required in Eq. (3.2.2), a Markov chain is employed:

$$U_0 \to U_1 \to U_2 \to \cdots \to U_n, \tag{3.2.3}$$

where each U_n represents a configuration generated sequentially. Figure 3.3 illustrates a schematic representation of a Markov chain in configuration space. The blob represents the entire configuration space, while dots denote visited configurations. Starting from an initial point, “A”, in the upper left corner, the Markov chain progresses towards the centre, where

lower Euclidean action implies a larger Boltzmann factor $\exp(-S)$ and, consequently, a higher probability density. To formalise this process, consider a stochastic system evolving through

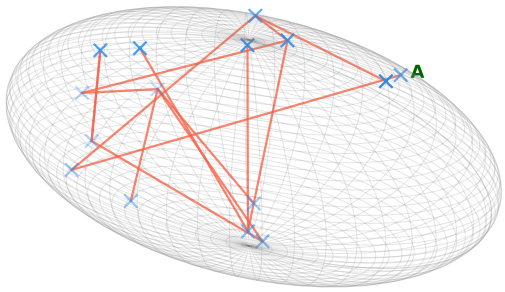

Figure 3.3. Schematic sketch of a Markov chain in the space of configurations, as described in the main text.

a finite set of configurations, transitioning from U_i to U_j with probability $P(U_i \to U_j) \equiv P_{ij}$. Due to its probabilistic nature, the system state at any given time is a random variable. A Markov chain is characterised by the property that its state distribution depends only on the immediately preceding state:

$$P^{(N)}_{i_0 i_n} = a_{i0} P_{i_0 i_1} \dots P_{i_{n-1} i_n}, \tag{3.2.4}$$

where a_{i0} is the probability of initialising the simulation in state i_0.

Following Refs. [196, 197], we consider irreducible and aperiodic Markov chains composed of positive states. These properties are defined as follows:

- Irreducibility: Starting from any configuration U_i, there exists a finite probability of reaching any other configuration U_j in a finite number of steps, i.e., there exists an N such that

$$P^{(N)}_{ij} = \sum i_k P_{i i_1} P_{i_1 i_2} \dots P_{i_{n-1} j} \neq 0. \tag{3.2.5}$$

- Aperiodicity: The probability of transitioning from any configuration to any other configuration is positive.
- Positivity: A state is positive if its mean recurrence time is finite:

$$\tau_i = \sum_{n=1}^{\infty} n p_{ii}^{(n)}, \tag{3.2.6}$$

  where $p_{ii}^{(n)}$ is the probability of returning to state U_i in exactly n steps.

A state satisfying $p_{ii} = \sum_{n=0}^{\infty} p_{ii}^{(n)} = 1$ is called recursive. If it is also positive, it is ergodic, meaning the entire configuration space is accessible in the simulation. For such Markov chains, two fundamental theorems hold:

- Theorem 1: If the chain is irreducible, aperiodic, and composed of positive states, then the limit

$$\lim_{N\to\infty} P_{ij}^{(N)} = \pi_j\,, \tag{3.2.7}$$

  exists and is unique, where π_j satisfies

$$\pi_j > 0, \quad \sum_j \pi_j = 1, \quad \pi_j = \sum_j \pi_j P_{ij}. \tag{3.2.8}$$

- Theorem 2: If the chain is irreducible, composed of positive states, and satisfies

$$\tau_i^{(2)} \equiv \sum_{n=1}^{\infty} n^2 p_{ii}^{(n)} < \infty, \tag{3.2.9}$$

  then the average in Eq. (3.2.1) converges to the ensemble average:

$$\langle O \rangle = \sum_i \pi_i\, O(U_i) + \mathcal{O}\left(\frac{1}{\sqrt{N}}\right). \tag{3.2.10}$$

An essential implication of Theorem 1 is that Eq.(3.2.9) implies stationarity: the probability distribution π_i remains unchanged under the transition probabilities P_{ij}, ensuring equilibrium. Consequently, a Markov process at equilibrium must not introduce probability sinks or sources. This constraint is satisfied by enforcing the detailed balance condition:

$$R(U)P(U \to U') = R(U')P(U' \to U). \tag{3.2.11}$$

The detailed balance condition does not uniquely determine transition probabilities, allowing flexibility in designing efficient update algorithms. While ergodicity ensures full exploration of configuration space, inefficient sampling can hinder convergence. To avoid slow

decorrelation, update schemes must be optimised to ensure efficient exploration and accurate observable estimation.

3.2.1 Simulating a full-dynamics theory: Hybrid Monte-Carlo (HMC)

The Hybrid Monte-Carlo (HMC) algorithm [191, 198, 199] constructs an ergodic Markov process whose equilibrium distribution matches the target probability measure $dP[U]$ from Eq. (3.1.60). This algorithm is widely used for simulating gauge theories with dynamical fermions.

To incorporate the fermionic determinant $\det D^{\mathrm{R}}$, where D^{R} is the Dirac operator in a generic fermion representation R, one introduces complex bosonic pseudofermion fields ϕ and $\phi^\dagger$ to rewrite the determinant as a path integral. Defining the Hermitian Dirac operator as $Q^{\mathrm{R}} = \gamma_5 D^{\mathrm{R}}$, and assuming an even number of fermion flavours N_{f}, the following identity holds:

$$(\det D^{\mathrm{R}})^{N_{\mathrm{f}}} = (\det Q^{\mathrm{R}})^{N_{\mathrm{f}}} = \int \mathcal{D}\phi\mathcal{D}\phi^\dagger \exp\left[-a^4 \sum_x \phi^\dagger(x)(Q^2)^{-N_{\mathrm{f}}/2}\phi(x)\right], \tag{3.2.12}$$

where flavour and colour indices are omitted for brevity.

The HMC algorithm introduces a fictitious Hamiltonian system where the gauge links $U_\mu(x)$ are generalised coordinates, and their conjugate momenta $\pi(x,\mu) = \pi^a(x,\mu)T^a$ lie in the Lie algebra $\mathfrak{sp}(2N)$ for simulations of symplectic gauge theories. The system evolves under the Hamiltonian:

$$H = \frac{1}{2}\sum_{x,\mu,a} \pi^a(x,\mu)\pi^a(x,\mu) + H_G + H_F, \tag{3.2.13}$$

with $H_G = S_G$ and $H_F = S_F$ corresponding to the gauge and fermion actions, respectively. The molecular dynamics (MD) evolution is governed by:

$$\frac{\mathrm{d}U_\mu(x)}{\mathrm{d}\tau} = \pi(x,\mu)U_\mu(x), \quad \frac{\mathrm{d}\pi(x,\mu)}{\mathrm{d}\tau} = F(x,\mu), \tag{3.2.14}$$

where the total HMC force $F(x,\mu)$ decomposes into gauge and fermionic components: $F = F_G + F_F$, each residing in the symplectic gauge group algebra, $\mathfrak{sp}(2N)$. Explicit forms of these terms can be found in Ref. [200].

After operating numerical integration of Eq. (3.2.14), the resulting configuration is accepted or rejected using a Metropolis test to satisfy the detailed balance principle of Eq. (3.2.11):

$$P = \min\left\{1, \exp\left[-(H[U'] - H[U])\right]\right\}. \tag{3.2.15}$$

The HMC algorithm proceeds through the following steps:

- Generate pseudofermion fields ϕ using the Heat Bath algorithm to sample Eq. (3.2.12).
- Draw initial momenta $\pi(x,\mu)$ from a Gaussian distribution and evolve the fields according to Eq. (3.2.14).
- Apply a Metropolis test to accept or reject the new configuration.

By repeating this procedure for N_{conf} trajectories, one obtains a statistically independent set of gauge configurations sampled according to the target probability measure $P[U]$ from Eq. (3.1.60).

3.2.2 Rational Hybrid Monte-Carlo (RHMC)

When simulating theories with an odd number of fermion flavours or requiring fractional powers of the fermion determinant, the identity in Eq. (3.2.12) must be generalised to non-integer exponents. In such cases, the Rational Hybrid Monte-Carlo (RHMC) algorithm [201] is used.

RHMC replaces the inverse fractional power $(Q^2)^{-N_{\text{f}}/2}$ with a rational approximation:

$$(Q^2)^{-N_{\text{f}}/2} \approx \alpha_0 + \sum_{k=1}^{d} \frac{\alpha_k}{Q^2 + \beta_k}, \tag{3.2.16}$$

where the coefficients $\{\alpha_k, \beta_k\}$ are determined using optimal rational approximation techniques (e.g., Remez algorithm [202]), and d is the order of the approximation.

This form enables efficient stochastic evaluation of the fermion action using a multi-shift solver [203]. The pseudofermion action then can be approximated as:

$$\approx a^4 \sum_x \phi^\dagger(x) \left[\alpha_0 + \sum_{k=1}^{d} \frac{\alpha_k}{Q^2 + \beta_k} \right] \phi(x), \tag{3.2.17}$$

and the corresponding fermionic force can be computed by combining the forces from each shifted system.

The RHMC algorithm maintains the same structure as HMC:

- Pseudofermions are generated according to the rational approximation of the action.
- The MD equations are integrated with a suitably chosen step size and integrator.
- A Metropolis accept/reject step ensures exactness and preserves the target measure.

Although RHMC introduces a modest computational overhead due to the use of multi-shift solvers and rational approximations, it is essential for theories requiring fractional powers of the Dirac operator. This makes RHMC the method of choice for lattice simulations with generic (including odd) N_{f} number of fermion flavours.

3.3 $Sp(2N)$ actions on the lattice: Wilson-Dirac action

This section is devoted to defining the lattice action for symplectic gauge theories that have been used in this thesis. The full action consists of two distinct terms:

$$S_{\text{lattice}} \equiv S_G + S_F, \tag{3.3.1}$$

where S_G represents the gauge action and S_F corresponds to the fermionic action. The Wilson gauge action is adopted for S_G, which is expressed as in Eq. (3.1.33). Here, $U_\mu(x) \in Sp(2N)$ is the link variable at the site (x, μ).

In this thesis, the fermionic part of the action uses the Wilson-Dirac formulation as in Eq. (3.1.47) and includes mass terms. Specifically, the action is:

$$S_F^{\text{W}} = a^4 \sum_{j=1}^{N_{\text{f}}} \sum_{x,y} \overline{Q}^j(x) D_{\text{W}}^{(\text{f})}(x,y) Q^j(y) + a^4 \sum_{j=1}^{N_{\text{as}}} \sum_{x,y} \overline{\psi}^j(x) D_{\text{W}}^{(\text{as})}(x,y) \psi^j(y)\,, \tag{3.3.2}$$

where Q^j represents fermions in the fundamental representation, and ψ^j corresponds to fermions in the two-index antisymmetric representation. The index j runs over the flavour space, and we omit spinor and colour indices. The Wilson-Dirac operators for these fields are written as (see, e.g., Ref [191]):

$$\begin{aligned} D_{\text{W}}^{(\text{f})}(x,y) Q^j(y) = &\left(\frac{4}{a} + m^{\text{f}}\right) Q^j(x) \\ &-\frac{1}{2a} \sum_{\mu=0}^{3} \left\{ (1-\gamma_\mu) U_\mu^{(\text{f})}(x) Q^j(x+\hat{\mu}) + (1+\gamma_\mu) U_\mu^{(\text{f}),\dagger}(x-\hat{\mu}) Q^j(x-\hat{\mu}) \right\}, \end{aligned} \tag{3.3.3}$$

and

$$\begin{aligned} D_{\text{W}}^{(\text{as})}(x,y) \psi^j(y) = &\left(\frac{4}{a} + m^{\text{as}}\right) \psi^j(x) \\ &-\frac{1}{2a} \sum_{\mu=0}^{3} \left\{ (1-\gamma_\mu) U_\mu^{(\text{as})}(x) \psi^j(x+\hat{\mu}) + (1+\gamma_\mu) U_\mu^{(\text{as}),\dagger}(x-\hat{\mu}) \psi^j(x-\hat{\mu}) \right\}, \end{aligned} \tag{3.3.4}$$

where m^{f} and m^{as} are the bare masses for the fundamental and antisymmetric fermions, respectively.

The link variables for the fundamental representation are given by $U_\mu^{(\text{f})}(x) = U_\mu(x)$, while the antisymmetric representation link variables are defined as:

$$U_{\mu,(ab)(cd)}^{(\text{as})} = \text{Tr}\left(e^{(ab),T} U_\mu^{(\text{f})} e^{(cd)} U_\mu^{(\text{f}),\text{T}} \right), \tag{3.3.5}$$

where $e^{(ab)}$ is an orthonormal basis in the $(N(2N-1)-1)$-dimensional space of antisymmetric,

Ω-traceless matrices for $2N \times 2N$ matrices. For the indices (ab) with $1 \leq a < b \leq 2N$, the basis elements are defined as:

$$e_{ij}^{(ab)} = \frac{1}{\sqrt{2}} \left(\delta_{aj}\delta_{bi} - \delta_{ai}\delta_{bj} \right) , \tag{3.3.6}$$

except when $b = N + a$ with $2 \leq a \leq N$, in which case the elements are:

$$e_{i,i+N}^{(ab)} = -e_{i+N,i}^{(ab)} = \begin{cases} \frac{1}{\sqrt{2a(a-1)}} & \text{if } i < a, \\ \frac{1-a}{\sqrt{2a(a-1)}} & \text{if } i = a. \end{cases} \tag{3.3.7}$$

The explicit form of the basis elements is given in Appendix A. Each basis element satisfies the condition $\mathrm{Tr}(e^{(ab)}\Omega) = 0$, where Ω is the symplectic matrix from Eq. (2.3.3). Boundary conditions for the link variables are periodic across the entire lattice, while fermion fields follow periodic boundary conditions in the spatial directions and anti-periodic conditions in the temporal direction. In the specific case of interest of this thesis, $Sp(4)$, the representation in the antisymmetric basis is of dimension five ($e^{(13)}$ vanishes by construction), and the multi-index (ab) spans the values (12), (14), (23), (24), and (34), as declared in Ref. [16]. Generators in higher representations of the gauge group can be constructed from those in the fundamental representation [200, 204]. In particular, the generators of the $Sp(2N)$ algebra in the two-index antisymmetric representation can be obtained by Taylor-expanding the group element defined in Eq. (3.3.5) to first order around the identity transformation. This yields:

$$(T^a_{\mathrm{as}})_{(ab)(cd)} = \mathrm{Tr}\left(e^{(ab)\,T}\, T^a_{\mathrm{f}}\, e^{(cd)} + e^{(ab)\,T}\, e^{(cd)}\, T^{a\,T}_{\mathrm{f}} \right) , \tag{3.3.8}$$

where T^a_{f} are the generators in the fundamental representation, and $e^{(ab)}$ is the basis tensor in the antisymmetric two-index space.

3.4 Spectroscopy and matrix elements from two-point correlation functions

This section is designed to describe the observables evaluation on the lattice. A particular focus is devoted to meson and baryon spectroscopy and matrix elements. These quantities are linked to two-point correlation functions. The corresponding interpolating operators are chosen to have the quantum numbers and structures relevant for studying the dynamics of the theories of interest.

As in Sec. 3.3, we denote fundamental fermions as Q and two-index antisymmetric fermions as ψ. To study the non-singlet meson sectors, we utilise fermion bilinears as outlined

Table 3.1. Interpolating operators used to study mesons. The conventions for labelling follow Ref. [179]. The indices assume values $I, J = 1, \dots N_{\rm f}$, $k, l = 1, \dots, N_{\rm as}$ and $i = 1, 2, 3$ refers to spatial directions.

Label	Operator $\mathcal{O}$	J^P	$Sp(4)$	$SO(6)$
PS	$\bar{Q}_I\gamma_5 Q_J$	0^-	5	1
V	$\bar{Q}_I\gamma_i Q_J$	1^-	10	1
T	$\bar{Q}_I\gamma_0\gamma_i Q_J$	1^-	10	1
AV	$\bar{Q}_I\gamma_5\gamma_i Q_J$	1^+	5	1
AT	$\bar{Q}_I\gamma_0\gamma_5\gamma_i Q_J$	1^+	10	1
S	$\bar{Q}_I Q_J$	0^+	5	1
ps	$\bar{\psi}_k\gamma_5\psi_\ell$	0^-	1	20
v	$\bar{\psi}_k\gamma_i\psi_\ell$	1^-	1	15
t	$\bar{\psi}_k\gamma_0\gamma_i\psi_\ell$	1^-	1	15
av	$\bar{\psi}_k\gamma_5\gamma_i\psi_\ell$	1^+	1	20
at	$\bar{\psi}_k\gamma_0\gamma_5\gamma_i\psi_\ell$	1^+	1	15
s	$\bar{\psi}_k\psi_\ell$	0^+	1	20

in Ref. [179]:

$$\mathcal{O}_{\rm f} = \bar{Q}_1(x)\Gamma Q_2(x), \tag{3.4.1}$$

$$\mathcal{O}_{\rm as} = \bar{\psi}_1(x)\Gamma\psi_2(x), \tag{3.4.2}$$

where Γ denotes combinations of Dirac gamma matrices designed to target specific J^P quantum numbers. The meson channels investigated are listed in Table 3.1.

An illustrative example of baryonic interpolating operator can be built in the case of the theory taken into consideration in Chapter 5. These are called chimera baryons [205, 206] and, as discussed in Section 2.4.3, they can couple to the top-quark in the contexts of CHMs and TPC [16]. In this case, the operators are defined as follows:

$$\mathcal{O}_{\rm CB}^{\gamma,\Gamma_1\Gamma_2}(x) = \left(Q_1^{a,\alpha}(x)\,(\mathcal{C}\Gamma_1)^{\alpha\beta}\,Q_2^{b,\beta}(x)\right)\Omega^{ad}\Omega^{bc}\Gamma_2^{\gamma\delta}\psi^{cd,\delta}(x), \tag{3.4.3}$$

where $\mathcal{C}$ is the charge conjugation matrix, and Ω is the symplectic invariant tensor. Spinor and colour indices are represented by Greek and Latin letters, respectively. In this study, we focus on the spin-1/2 and spin-3/2 baryons, setting $\Gamma_2 = \mathbb{I}$ for simplicity. The analysed baryons are summarised in Table 3.2.

The masses and matrix elements are determined from two-point functions, projected to zero momentum:

$$C_{AB}(t) = \frac{1}{N_s^3}\sum_{\vec{x}}\langle\mathcal{O}_A(t,\vec{x})\bar{\mathcal{O}}_B(0,\vec{0})\rangle. \tag{3.4.4}$$

Table 3.2. Summary of chimera baryons studied in this work. Separate analyses are conducted for parity-even and parity-odd states.

Label	Γ_1	J	$Sp(4)$	$SO(6)$
Λ_{CB}	γ_5	1/2	5	6
Σ_{CB}	γ_i	1/2	10	6
Σ^*_{CB}	γ_i	3/2	10	6

For mesons, where $\mathcal{O}_A = \mathcal{O}_B$, the large-time t behaviour is:

$$C_{\mathrm{meson}}(t) \approx A\left(e^{-mt} + e^{-m(T-t)}\right), \tag{3.4.5}$$

with m being the ground-state mass and A encoding ground-state matrix elements.

Chimera baryon correlators are analysed by projecting onto definite parity using $P_\pm = (1 \pm \gamma_0)/2$:

$$C^{\pm}_{\mathrm{CB},\,\alpha\beta}(t) = P_{\pm,\,\alpha\alpha_1} C_{\mathrm{CB},\alpha_1\beta}(t), \tag{3.4.6}$$

asymptotically (large time behaviour) behaving as:

$$C^{\pm}_{\mathrm{CB}}(t) \approx \left(A_\pm e^{-m^\pm t} - A_\mp e^{-m^\mp (T-t)}\right) P_\pm. \tag{3.4.7}$$

For baryons, the interpolating operators with $\Gamma_1 = \gamma_i$ source both spin-1/2 and spin-3/2 baryonic states. To separate these contributions, we decompose the corresponding correlation functions by projecting onto definite spin components. Starting from the zero-momentum two-point function,

$$C^{ij}_{\mathrm{CB},\alpha\beta}(t) \equiv \frac{1}{N_s^3} \sum_{\vec{x}} \left\langle \mathcal{O}^{\gamma_i}_{\mathrm{CB},\alpha}(t,\vec{x})\, \bar{\mathcal{O}}^{\gamma_j}_{\mathrm{CB},\beta}(0,\vec{0}) \right\rangle, \tag{3.4.8}$$

we define the spin-1/2 and spin-3/2 projected correlators as

$$C^{(1/2)}_{\mathrm{CB},\alpha\beta}(t) \equiv P^{(1/2)}_{ij}\, C^{ij}_{\mathrm{CB},\alpha\beta}(t) = \frac{1}{3}\gamma_i\gamma_j\, C^{ij}_{\mathrm{CB},\alpha\beta}(t), \tag{3.4.9}$$

$$C^{(3/2)}_{\mathrm{CB},\alpha\beta}(t) \equiv P^{(3/2)}_{ij}\, C^{ij}_{\mathrm{CB},\alpha\beta}(t) = \left(\delta_{ij} - \frac{1}{3}\gamma_i\gamma_j\right) C^{ij}_{\mathrm{CB},\alpha\beta}(t). \tag{3.4.10}$$

The quantum numbers of the baryonic operators analysed are summarised in Tab. 3.2. By analogy with QCD, we label the state sourced by $\Gamma_1 = \gamma_5$ as Λ_{CB}, the spin-1/2 component of the $\Gamma_1 = \gamma_i$ channel as Σ_{CB}, and the corresponding spin-3/2 partner as Σ^*_{CB}.

3.4.1 Spectroscopy: effective mass and Generalised Eigenvalue Problem

The ground-state energy E_0 in a given channel is determined from the plateau in the effective mass, provided the excited states are sufficiently suppressed. A standard method to isolate the excited states employs multi-exponential fits, minimising the correlated chi-square functional:

$$\chi^2 = \sum_{t,t'} \Big[h^{(k)}(t) - C(t)\Big] \mathrm{Cov}^{-1}_{tt'} \Big[h^{(k)}(t') - C(t')\Big], \tag{3.4.11}$$

where the $\mathrm{Cov}_{tt'}[C]$ is the covariance matrix of the two-point correlation function, $C(t)$, estimated over N bins:

$$\mathrm{Cov}_{tt'}[C] \equiv \frac{1}{N} \sum_{i=1}^{N} \big(C_i(t) - \langle C(t)\rangle\big)\big(C_i(t') - \langle C(t')\rangle\big), \tag{3.4.12}$$

and the fitting function is a sum of exponential states $h^{(k)}(t) = \sum_{n=1}^{k} \mathcal{B}_n\, e^{-tE_n}$.

Alternatively, the exponential behaviour of two-point correlation functions for the lightest state (Eqs. (3.4.5) and (3.4.7)) suggests that, in order to find the ground state, one can define the effective mass as

$$m_{\mathrm{eff}}(t) = -\frac{1}{a} \log\left(\frac{C(t+a)}{C(t)}\right), \tag{3.4.13}$$

or

$$m_{\mathrm{eff}}(t) \equiv \frac{1}{a} \cosh^{-1}\left[\frac{C(t+a) + C(t-a)}{2C(t)}\right], \tag{3.4.14}$$

for a periodic lattice. One can find this quantity for the two-point correlation function in consideration and fitting plateau at large time slices t, expecting the ground state to be isolated $am_{\mathrm{eff}} \to am_0$ at large t.

Increasing the number of excited states E_n introduces computational challenges and reduces the signal-to-noise ratio exponentially. An efficient alternative is the generalised eigenvalue problem (GEVP) [207], applied to a matrix of correlation functions $\mathcal{C}_{ij}(t)$ constructed from a basis of interpolating of N operators $\mathcal{O}_i$:

$$\mathcal{C}_{ij}(t) = \langle \mathcal{O}_i(t) \bar{\mathcal{O}}_j(0)\rangle, \quad i,j = 0,\ldots,N-1. \tag{3.4.15}$$

Assuming non-degenerate energy states, E_n, ordered as $E_n < E_{n+1}$, the GEVP is solved via

$$\mathcal{C}(t) v_n(t,t_0) = \lambda_n(t,t_0) \mathcal{C}(t_0) v_n(t,t_0), \tag{3.4.16}$$

where $\lambda_n(t,t_0)$ and $v_n(t,t_0)$ are the eigenvalues and eigenvectors, respectively. Fixing a reference time t_0, this equation is solved for each $t > t_0$, with the eigenvalues used to define

effective masses:

$$m_n^{\text{eff}}(t,t_0) = -\frac{1}{a}\log\frac{\lambda_n(t+a,t_0)}{\lambda_n(t,t_0)}, \tag{3.4.17}$$

or for periodic lattices:

$$m_n^{\text{eff}}(t,t_0) = \frac{1}{a}\cosh^{-1}\left[\frac{\lambda_n(t+a,t_0)+\lambda_n(t-a,t_0)}{2\lambda_n(t,t_0)}\right]. \tag{3.4.18}$$

In the limit $t\to\infty$, the effective masses converge to the energy levels:

$$aE_n = \lim_{t\to\infty} am_n^{\text{eff}}(t,t_0), \quad n=0,\dots,N-1. \tag{3.4.19}$$

At large t, higher-energy state contributions are exponentially suppressed [208], with corrections scaling as

$$am_n^{\text{eff}}(t,t_0) = aE_n + \mathcal{O}\left(e^{-\Delta(aE_n)t}\right), \quad \Delta(aE_n) = \min_{m\neq n}|aE_m - aE_n|. \tag{3.4.20}$$

Systematic uncertainties are further influenced by terms proportional to $\exp(-E_n t_0)$ [207]. Increasing the lattice time extent, N_t, improves plateau identification and signal quality.

The measurements of the two-point correlation functions described have been supported by Wuppertal [209–211] and APE smearing [212, 213], which are described in Appendix C. An illustrative way to pursue spectroscopy studies (see Chapter 5), is to construct the variational basis using interpolating operators with different Wuppertal smearing levels at the source and sink. The choices adopted are N_{source}, $N_{\text{sink}} = 0$, 40, 80, where the effect of applying the Wuppertal smearing seems to affect the mass plateaus sensibly. For each mesonic channel (pseudoscalar, axial-vector, axial-tensor, scalar), the correlation matrix takes the form:

$$\mathcal{C}^i(t) = \begin{pmatrix} C^i_{0,0}(t) & C^i_{0,40}(t) & C^i_{0,80}(t) \\ C^i_{40,0}(t) & C^i_{40,40}(t) & C^i_{40,80}(t) \\ C^i_{80,0}(t) & C^i_{80,40}(t) & C^i_{80,80}(t) \end{pmatrix}, \tag{3.4.21}$$

where $C^i_{nm}(t) = \langle \mathcal{O}^i(t)\bar{\mathcal{O}}^i(0)\rangle_{nm}$ and i labels the channel (PS, AV, AT, S, etc.).

For the specific case of vector and tensor channels, the operators mix, producing the same spectrum. To account for this, we extend the correlation matrix to include cross-channel

terms:

$$\mathcal{C}^{V,T}(t) = \begin{pmatrix} C^{V}_{0,0} & C^{V}_{0,40} & C^{V}_{0,80} & C^{V/T}_{0,0} & C^{V/T}_{0,40} & C^{V/T}_{0,80} \\ C^{V}_{40,0} & C^{V}_{40,40} & C^{V}_{40,80} & C^{V/T}_{40,0} & C^{V/T}_{40,40} & C^{V/T}_{40,80} \\ C^{V}_{80,0} & C^{V}_{80,40} & C^{V}_{80,80} & C^{V/T}_{80,0} & C^{V/T}_{80,40} & C^{V/T}_{80,80} \\ C^{T/V}_{0,0} & C^{T/V}_{0,40} & C^{T/V}_{0,80} & C^{T}_{0,0} & C^{T}_{0,40} & C^{T}_{0,80} \\ C^{T/V}_{40,0} & C^{T/V}_{40,40} & C^{T/V}_{40,80} & C^{T}_{40,0} & C^{T}_{40,40} & C^{T}_{40,80} \\ C^{T/V}_{80,0} & C^{T/V}_{80,40} & C^{T/V}_{80,80} & C^{T}_{80,0} & C^{T}_{80,40} & C^{T}_{80,80} \end{pmatrix}, \tag{3.4.22}$$

where $C^{V/T}_{nm}(t) = \langle \mathcal{O}^{V}(t)\bar{\mathcal{O}}^{T}(0)\rangle_{nm}$ and $C^{T/V}_{nm}(t) = \langle \mathcal{O}^{T}(t)\bar{\mathcal{O}}^{V}(0)\rangle_{nm}$. This expanded basis enhances resolution for higher-energy states. Energy levels are extracted by fitting eigenvalues at large Euclidean times.

For chimera baryons, we isolate parity-even and parity-odd contributions using the difference of eigenvalues:

$$\tilde{\lambda}^{\pm}_{\mathrm{CB}}(t) = \frac{1}{2}\left[\lambda^{\pm}_{\mathrm{CB}}(t) - \lambda^{\mp}_{\mathrm{CB}}(T-2)\right]. \tag{3.4.23}$$

The effective mass $m_{\mathrm{eff}}(t)$ is then implicitly defined by:

$$\frac{\lambda(t-1)}{\lambda(t)} = \frac{e^{-m_{\mathrm{eff}}(t)(T-t+1)} \pm e^{-m_{\mathrm{eff}}(t)(t-1)}}{e^{-m_{\mathrm{eff}}(t)(T-t)} \pm e^{-m_{\mathrm{eff}}(t)t}}, \tag{3.4.24}$$

with the sign chosen to respect lattice periodicity. The fit range is selected where $m_{\mathrm{eff}}(t)$ exhibits a stable plateau.

3.4.2 Matrix elements and overlap factors

In addition to studying the masses, we investigate the hadron-vacuum matrix elements, commonly known as decay constants. These decay constants appear as factors of the exponential terms in the correlators shown in Eqs. (3.4.5) and (3.4.7). Specifically, these matrix elements are contained in the meson correlation matrix[2], expressed as:

$$C^{\mathrm{M}}_{N_{\mathrm{source}},N_{\mathrm{sink}}}(t) = \sum_{n} \frac{1}{2E_n} \langle 0|\mathcal{O}_{N_{\mathrm{source}}}|e_n\rangle\langle e_n|\bar{\mathcal{O}}_{N_{\mathrm{sink}}}|0\rangle \left[e^{-E_n t} + e^{-E_n(T-t)}\right], \tag{3.4.25}$$

with operators that have been smeared through Wuppertal and APE smearing, by using $N_{\mathrm{source}}, N_{\mathrm{sink}}$ iterations, according to the formulas in Appendix C. The decay constants for the mesons presented in Tab. 3.1 are defined through the matrix elements of local, unsmeared

[2]The states e_n form a complete set characterised by the quantum numbers relevant to the two-point correlation function $C(t)$ under consideration. It is important to note that the lowest-lying state, e_0, is distinct from the vacuum state $|0\rangle$.

operators, as given by:

$$\langle 0|\bar{Q}_1\gamma_5\gamma_\mu Q_2|\mathrm{PS}\rangle = \sqrt{2}f_{\mathrm{PS}}p_\mu, \qquad \langle 0|\bar{\psi}_1\gamma_5\gamma_\mu\psi_2|\mathrm{ps}\rangle = \sqrt{2}f_{\mathrm{ps}}p_\mu, \tag{3.4.26}$$

$$\langle 0|\bar{Q}_1\gamma_\mu Q_2|\mathrm{V}\rangle = \sqrt{2}f_{\mathrm{V}}m_{\mathrm{V}}\epsilon_\mu, \qquad \langle 0|\bar{\psi}_1\gamma_\mu\psi_2|\mathrm{v}\rangle = \sqrt{2}f_{\mathrm{v}}m_{\mathrm{v}}\epsilon_\mu, \tag{3.4.27}$$

$$\langle 0|\bar{Q}_1\gamma_5\gamma_\mu Q_2|\mathrm{AV}\rangle = \sqrt{2}f_{\mathrm{AV}}m_{\mathrm{AV}}\epsilon_\mu, \qquad \langle 0|\bar{\psi}_1\gamma_5\gamma_\mu\psi_2|\mathrm{av}\rangle = \sqrt{2}f_{\mathrm{av}}m_{\mathrm{av}}\epsilon_\mu, \tag{3.4.28}$$

where the polarisation vector, ϵ_μ, satisfies $\epsilon^*_\mu\epsilon^\mu = 1$ and is orthogonal to the momentum p_μ.

Unlike the mass determination process, we refrain from using a variational analysis for the decay constants. Instead, we extract the relevant matrix elements by fitting a selection of the off-diagonal entries of the correlation matrix in Eq. (3.4.25), specifically:

$$C_{80,80}(t) \equiv \langle \mathcal{O}_{80}(t)\,\bar{\mathcal{O}}_{80}(0)\rangle \quad \text{and} \quad C_{80,0}(t) \equiv \langle \mathcal{O}_{80}(t)\,\bar{\mathcal{O}}_{0}(0)\rangle. \tag{3.4.29}$$

The second correlator involves an unsmeared operator, which allows us to extract the matrix elements as defined in Eqs. (3.4.26)–(3.4.28).

To renormalise the decay constants, we use the following relations:

$$f^{\mathrm{ren}}_{\mathrm{PS}} = Z^{\mathrm{f}}_A f_{\mathrm{PS}}, \qquad f^{\mathrm{ren}}_{\mathrm{ps}} = Z^{\mathrm{as}}_A f_{\mathrm{ps}}, \tag{3.4.30}$$

$$f^{\mathrm{ren}}_{\mathrm{V}} = Z^{\mathrm{f}}_V f_{\mathrm{V}}, \qquad f^{\mathrm{ren}}_{\mathrm{v}} = Z^{\mathrm{as}}_V f_{\mathrm{v}}, \tag{3.4.31}$$

$$f^{\mathrm{ren}}_{\mathrm{AV}} = Z^{\mathrm{f}}_A f_{\mathrm{AV}}, \qquad f^{\mathrm{ren}}_{\mathrm{av}} = Z^{\mathrm{as}}_A f_{\mathrm{av}}, \tag{3.4.32}$$

The renormalisation constants in the fermion representation, R are computed by performing the matching between perturbative results in the continuum theory ($\overline{\mathrm{MS}}$ scheme), and the corresponding ones in lattice perturbation theory, as in Refs. [11, 16, 214–216]:

$$Z^{\mathrm{R}}_A = 1 + \frac{C_R g^2}{16\pi^2\langle P\rangle}\left(\Delta_{\Sigma_1} + \Delta_{AV}\right), \tag{3.4.33}$$

$$Z^{\mathrm{R}}_V = 1 + \frac{C_R g^2}{16\pi^2\langle P\rangle}\left(\Delta_{\Sigma_1} + \Delta_{V}\right), \tag{3.4.34}$$

with $\langle P\rangle$ denoting the average plaquette

$$P \equiv \frac{a^4}{6\tilde{V}}\sum_x\sum_{\mu<\nu}\left[\frac{1}{2N}\mathrm{Re}\,\mathrm{Tr}\,U_{\mu\nu}(x)\right], \tag{3.4.35}$$

where $\tilde{V}$ represents the spacetime volume of the lattice, $U_{\mu\nu}$ is defined in Eq. (3.1.21), C_R being the quadratic Casimir (where $C_{\mathrm{f}} = 5/4$ and $C_{\mathrm{as}} = 2$), and the numerical coefficients $\Delta_{\Sigma_1} = -12.82$, $\Delta_{AV} = -3.0$, and $\Delta_V = -7.75$ for $Sp(4)$.

The matrix elements of the chimera baryon operators listed in Eq. (3.4.3) are defined

analogously to those of QCD baryons [217] using local, unsmeared interpolating operators. Specifically, assuming parity-projected states, the matrix elements are given by:

$$\langle 0|O^{\mathcal{C}\gamma_5,\mathbb{1}}_{\mathrm{CB},\alpha}|\Lambda(\vec{p},s)\rangle \equiv K_\Lambda\, u_{s\,\alpha}(\vec{p})\,, \qquad \langle 0|O^{\mathcal{C}\gamma_i,\mathbb{1}}_{\mathrm{CB},\alpha}|\Sigma(\vec{p},s)\rangle \equiv K_\Sigma\, u_{s\,\alpha}(\vec{p})\,, \tag{3.4.36}$$

Here, $u_s(\vec{p})$ denotes an on-shell Dirac spinor with momentum $\vec{p}$ and spin projection s, associated with chimera baryon states of definite parity, $|\Lambda(\vec{p},s)\rangle$ and $|\Sigma(\vec{p},s)\rangle$. The overlap factors K_n characterise the coupling strength between the interpolating operators and the physical states.

The baryon two-point correlation function at finite momentum takes the form [217]:

$$\begin{aligned} C_{\mathrm{CB},\alpha\beta}(t,\vec{p}) &= \frac{1}{N_s^3}\sum_{\vec{x}} e^{-i\vec{p}\cdot\vec{x}}\,\langle \mathcal{O}_{\mathrm{CB},\alpha}(t,\vec{x})\,\bar{\mathcal{O}}_{\mathrm{CB},\beta}(0,0)\rangle \\ &= \sum_n \sum_s \frac{|K_n|^2\, u_{s,\alpha}\bar{u}_{s,\beta}}{2E_n(\vec{p})}\, e^{-E_n(\vec{p})\,t}\,, \end{aligned} \tag{3.4.37}$$

where the momentum dependence and the sums over spin projection s and energy levels n are shown explicitly. In the rest frame, $\vec{p}=0$, we have $E_n \to m_n$, and the spin sum becomes $\sum_s u_s\bar{u}_s = \pm 2m_n P_\pm$, where $P_\pm$ projects onto states of definite parity.

The overlap factors corresponding to spin-projected correlators (Eq. 3.4.9) can be found using the following fit form:

$$C^{\pm}_{\mathrm{CB}}(t) = \pm\sum_n |K_n|^2\, e^{-E_n t} P_\pm\,. \tag{3.4.38}$$

The overlap factors $|K_n|$ are extracted by fitting a matrix of correlation functions constructed from combinations of smeared and local operators, following the same strategy adopted for the mesons in Eq. (3.4.29).

To account for renormalisation for the baryonic operators of Tab. 3.2, we define the renormalised overlap factors as:

$$K^{\mathrm{ren}}_\Lambda = Z_{\mathrm{CB},\mathcal{C}\gamma_5}\,|K_\Lambda|, \qquad K^{\mathrm{ren}}_\Sigma = Z_{\mathrm{CB},\mathcal{C}\gamma_i}\,|K_\Sigma|. \tag{3.4.39}$$

The detailed derivation of the renormalisation factors $Z_{\mathrm{CB},\mathcal{C}\gamma_5}$ and $Z_{\mathrm{CB},\mathcal{C}\gamma_i}$ is provided in Appendix D. They are given by:

$$Z_{\mathrm{CB},\mathcal{C}\gamma_5} = 1 + \frac{g^2}{16\pi^2\langle P\rangle}\left[\left(C_{\mathrm{f}} + \frac{1}{2}C_{\mathrm{as}}\right)\Delta_{\Sigma_1} + \Delta_\Gamma[\mathcal{C}\gamma_5]\right], \tag{3.4.40}$$

$$Z_{\mathrm{CB},\mathcal{C}\gamma_i} = 1 + \frac{g^2}{16\pi^2\langle P\rangle}\left[\left(C_{\mathrm{f}} + \frac{1}{2}C_{\mathrm{as}}\right)\Delta_{\Sigma_1} + \Delta_\Gamma[\mathcal{C}\gamma_i]\right], \tag{3.4.41}$$

where the numerical values of the Dirac structure-dependent constants are:

$$\Delta_\Gamma[\mathcal{C}\gamma_5] = -26.670, \quad \Delta_\Gamma[\mathcal{C}\gamma_i] = 18.123, \tag{3.4.42}$$

and the dependence of Δ_Γ and Δ_{Σ_1} on the lattice spacing, a, and on the renormalisation scale, μ, is shown in Eqs. (D.0.56) and (D.0.58), and it is cancelled here by the convenient choice $\mu = 1/a$.

3.5 Spectral densities on the lattice

Another method to determine observables on the lattice involves solving an inverse problem, finding spectral densities [218–227]. From the latter quantity, one finds spectra and matrix elements of gauge theories on the lattice. Here, we discuss a way to find spectral densities and hadronic observables. This elaborates on the methodology devised in Refs. [218, 227]. We make use of the Hansen-Tantalo-Lupo (HLT) algorithm and introduce a novel fitting technique to find matrix elements from spectral densities. In order to tackle all these points, an open-source `PYTHON` software, called `LSDensities` [164], has been developed. All the studies presented in this thesis have been obtained through this software package.

3.5.1 The Hansen-Lupo-Tantalo (HLT) algorithm

For a given two-point correlation function, $C(t)$, the spectral density, $\rho(E)$, is defined by the equation:

$$C(t) = \int_{E_{\min}}^{\infty} dE\, \rho(E)\, b(t, E), \tag{3.5.1}$$

where $b(t, E)$ is defined for periodic time extensions as

$$b(t, E_n) = e^{-t\,E_n} + e^{-(T-t)E_n}\,, \tag{3.5.2}$$

In the case of infinite time extension, this equation reduces to an inverse Laplace transform when $E_{\min}$ is set to zero. The integration lower bound, $E_{\min}$, is flexible and can be chosen from zero up to the energy associated with the ground state of the theory in the channel defined by the operators creating $C(t)$.

The data we are going to analyse consists of measurements indexed by $k = 1, \ldots, N_m$, where $N_m \leq N_{\text{conf}}$. These correspond to a set of correlation functions, $C_k(t)$. On the lattice, time is discretised, so $t/a \equiv \tau = 1, \ldots, \tau_{\max} \leq N_t/2$. The covariance matrix, $\tau_{\max} \times \tau_{\max}$, similarly to Eq. (3.4.12), is given by:

$$\text{Cov}_{\tau\tau'}[C] \equiv \frac{1}{N_m} \sum_{k=1}^{N_m} \big(C_k(a\tau) - \langle C(a\tau)\rangle\big)\big(C_k(a\tau') - \langle C(a\tau')\rangle\big), \tag{3.5.3}$$

where $\langle C(a\tau)\rangle$ denotes the configuration average of the measurements at a given time slice $t = a\tau$.

The reconstruction of spectral densities from a finite set of noisy correlation measurements, $C(t)$, i.e. the inversion of Eq. (3.5.1) is an ill-posed problem. Several techniques are available to tackle this problem. Among these, the Backus-Gilbert algorithm [228] was refined in Ref. [218] to improve its applicability to lattice simulations. This modified method is known as the Hansen-Lupo-Tantalo (HLT) algorithm.

A crucial element of the HLT algorithm is the introduction of smeared spectral densities[3], defined as:

$$\rho_\sigma(\omega) \equiv \int_{E_{\min}}^{\infty} dE\, \Delta_\sigma(E-\omega)\, \rho(E), \tag{3.5.4}$$

where the spectral density, $\rho(E)$, is convoluted with a smearing kernel, $\Delta_\sigma(E-\omega)$. The parameter σ represents the smearing radius around ω, and, at a non-zero σ, $\rho_\sigma(\omega)$ becomes smooth.

In a finite lattice volume, the spectral density is represented as a sum of Dirac delta functions corresponding to the eigenvalues of the Hamiltonian:

$$\rho(E) = \sum_n k_n\, \delta(E-\omega_n), \tag{3.5.5}$$

where the eigenvalues, ω_n, are dependent on the lattice spatial volume $N_s a$, and k_n are coefficients. A proper smearing kernel must satisfy:

$$\Delta_\sigma(E-\omega) \xrightarrow[\sigma\to 0]{} \delta(E-\omega), \tag{3.5.6}$$

which ensures that the regulator disappears as $\sigma \to 0$:

$$\rho_\sigma(\omega) \xrightarrow[\sigma\to 0]{} \rho(E=\omega). \tag{3.5.7}$$

By introducing energy-smearing techniques, given lattice data in a finite lattice of volume V, a robust infinite-volume limit is well-defined

$$\rho(E=\omega) = \lim_{\sigma\to 0}\left[\lim_{V\to\infty} \rho_\sigma(\omega)\right]. \tag{3.5.8}$$

The order of the limits is relevant (first one has to perform the infinite volume limit, and then remove the regulator, σ), as performing the limit in the converse order would force a connection between a distribution as in Eq. (3.5.5) and the continuum spectral density $\rho(E)$, which above the multi-particle threshold is expected to be a smooth function.

[3]Note that this refers to smearing the spectral densities themselves at the energy level, not to (APE or Wuppertal) smearing of two-point correlation functions.

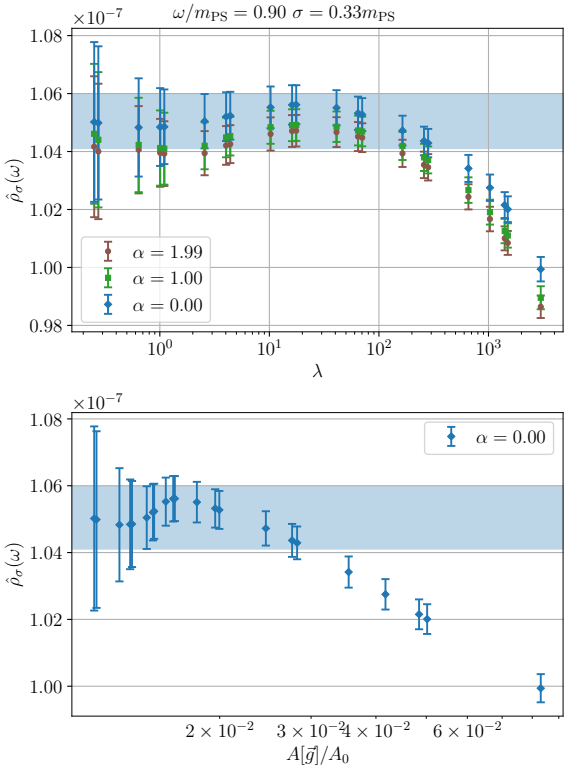

Figure 3.4. Spectral density reconstruction plateaux for a fixed energy value. The top panel shows the variation of the trade-off parameter λ on the x-axis, while $A_0 = A[\vec{g} = 0]$ is varied in the bottom panel. The reconstructed spectral densities, $\hat{\rho}_\sigma(\omega)$ (depicted on both y-axes), show minimal statistical variation for various choices of λ and α. Representative α and λ values are indicated in the figure.

An important aspect is the freedom in choosing the smearing kernel, $\Delta_\sigma(E-\omega)$, whose properties–allowing a well defined continuum limit (3.5.8), being smooth, and approaching a δ-distribution as in Eq. (3.5.5) are met by a wide range of functions. Among those, two typical choices are Gaussian and Cauchy functions.

Although the energy smearing can theoretically be removed and the infinite volume limit can be performed, we prioritise fits of smeared spectral densities to extract finite-volume spectra and matrix elements, as proposed in Ref. [227].

In the HLT framework, the smearing kernel is chosen and fixed as an input of the procedure. If this kernel can be expressed as a sum over basis functions:

$$\Delta_\sigma(E-\omega) = \sum_{\tau=1}^{\infty} g_\tau(\omega,\sigma)\, b(a\tau, E), \tag{3.5.9}$$

which is approximated at a finite $\tau_{\max} \leq N_t/2$ as follows:

$$\bar{\Delta}_\sigma(E-\omega) = \sum_{\tau=1}^{\tau_{\max}} g_\tau(\omega,\sigma)\, b(a\tau, E)\,, \tag{3.5.10}$$

the coefficients g_τ are determined by minimising a functional, $A[\vec{g}]$, which quantifies the difference between the reconstructed smearing kernel, $\bar{\Delta}_\sigma(E-\omega)$, and the target kernel, $\Delta_\sigma(E-\omega)$:

$$A[\vec{g}] \equiv \int_{E_{\min}}^{\infty} dE\, e^{\alpha a E} \left|\bar{\Delta}_\sigma(E-\omega) - \Delta_\sigma(E-\omega)\right|^2, \tag{3.5.11}$$

where α is a parameter controlling the choice of the norm [227]. This minimisation problem is complicated by the presence of uncertainties in the input data, which is regularised by adding a second functional:

$$B[\vec{g}] \equiv \sum_{\tau,\tau'=1}^{\tau_{\max}} g_\tau\, \mathrm{Cov}_{\tau\tau'}[C]\, g_{\tau'}, \tag{3.5.12}$$

where the covariance matrix $\mathrm{Cov}_{\tau\tau'}[C]$ is computed from the available data.

The functional to minimise is:

$$W[\vec{g}] \equiv \frac{A[\vec{g}]}{A[0]} + \lambda \frac{B[\vec{g}]}{B_{\mathrm{norm}}(\omega)}, \tag{3.5.13}$$

where λ is the trade-off parameter, and $B_{\mathrm{norm}}(\omega) = C^2(a)/\omega^2$. The second term, known as the statistical error functional, helps to regularise the reconstruction process. Minimising $W[\vec{g}]$ for a fixed ω provides the coefficients $\vec{g}$, which are used to estimate the smeared spectral density:

$$\hat{\rho}_\sigma(\omega) = \sum_{\tau=1}^{\tau_{\max}} g_\tau(\omega,\sigma) C(a\tau)\,. \tag{3.5.14}$$

Further details on the implementation of these formulas in the `LSDensities` software package are provided in Appendix E. We now discuss the systematic uncertainties arising in the minimisation of $W[\vec{g}]$. The ratio $\sqrt{A[\vec{g}]/A_0}$ serves as a proxy for the systematic error introduced by the HLT method in reconstructing $g_\tau(\omega,\sigma)$ for finite $\tau_{\max}$ and N_m, as it quantifies the deviation between the target kernel, $\Delta_\sigma(E-\omega)$, and its reconstructed counterpart, $\bar{\Delta}_\sigma(E-\omega)$. On the other hand, the term $B[\vec{g}]/B_{\mathrm{norm}}$ in $W[\vec{g}]$ provides an estimate of the statistical uncertainty in the reconstructed spectral density, $\hat{\rho}_\sigma(\omega)$.

In Fig. 3.4, we illustrate the dependence of $A[\vec{g}]/A_0$ on the regularisation parameter λ by using as an example numerical data that are considered in this thesis in Chapter 5 (ensemble M1, pseudoscalar meson channel, fundamental sector). Larger values of $A[\vec{g}]/A_0$ signal unsuppressed systematics, especially when variations in λ or α lead to significant changes in $\hat{\rho}_\sigma(\omega)$. Reducing λ can mitigate these systematics, but at the expense of amplifying statistical uncertainties. Following Ref. [152], we tune λ to ensure that systematic fluctuations are

negligible compared to statistical errors, as demonstrated in Fig. 3.4. This tuning approach ensures that the reconstruction is both stable and unaffected by the unphysical parameters λ and α.

While the plateau analysis should ensure that the error is dominated by its statistical component, as an additional precaution, we evaluate the following terms:

$$\sigma_{1,\mathrm{sys}}(E) \equiv |\rho_{\lambda_*}(E) - \rho_{\lambda_*/10}(E)|, \tag{3.5.15}$$

$$\sigma_{2,\mathrm{sys}}(E) \equiv |\rho_{\lambda_*,\alpha}(E) - \rho_{\lambda_*,\alpha'}(E)|, \tag{3.5.16}$$

where λ_* is determined as above, and α and α' are distinct norm parameters. The total error is then computed as

$$\sigma^2_{\rho_\sigma} = \sigma^2_{\mathrm{stat}} + \sigma^2_{1,\mathrm{sys}} + \sigma^2_{2,\mathrm{sys}}. \tag{3.5.17}$$

3.5.2 Observables evaluation using spectral densities

We explore the use of smeared spectral densities in meson spectroscopy by minimising the correlated χ^2 functional as introduced in Ref. [227]:

$$\chi^2 = \sum_{E,E'} \left(f^{(k)}_\sigma(E) - \hat{\rho}_\sigma(E)\right) \mathrm{Cov}^{-1}_{EE'}[\rho_\sigma] \left(f^{(k)}_\sigma(E') - \hat{\rho}_\sigma(E')\right), \tag{3.5.18}$$

where $\mathrm{Cov}_{EE'}[\rho_\sigma]$ is the covariance matrix for the spectral densities (estimated analogously to the matrix in Eq. (3.5.3)), and $f^{(k)}_\sigma(E)$ represents the fitting function and is a sum of k smearing kernels:

$$f^{(k)}_\sigma(E) = \sum_{n=1}^{k} \mathcal{A}_n \, \Delta_\sigma(E - E_n). \tag{3.5.19}$$

As illustrated in Eq. (3.5.19), fitting spectral densities enables the determination of the energy levels, aE_n, the matrix elements and the overlap factors of the interpolating operators involved in the spectral reconstruction. The amplitudes of the fitted functions, $f^{(k)}(E)$, encode the matrix elements, $\langle 0|\mathcal{O}(0)|e_n\rangle$, for the mesonic observables, and the overlap factors for the baryonic ones. To extract this information, we have developed a method for directly obtaining these matrix elements and overlap factors from spectral density fits.

Firstly, it is relevant to show that the spectral density can be expressed as in Eq. (3.5.19), where the amplitude $\mathcal{A}_n$ contains the matrix elements $\langle 0|\mathcal{O}(0)|e_n\rangle$ and $\langle e_n|\bar{\mathcal{O}}(0)|0\rangle$ for mesons, and the latter determines the relative contributions of each energy level to the spectral density. For chimera baryons the amplitude contains information about the overlap factors $|K_n|^2$.

We begin by considering correlation functions generated with different levels of source and sink smearing, where the two-point correlation functions show visible differences. We observe that this happens, e.g., for the choices N_{source}, $N_{\mathrm{sink}} = 80$ and $N_{\mathrm{sink}} = 0$. This setup results in

two distinct correlation functions: $C^{80,80}(t)$ and $C^{80,0}(t)$, as described in Eq. (3.4.29). From these functions, we compute the spectral densities, which take the following forms for mesons:

$$\rho_\sigma^{80,80}(E) = \sum_{n=0}^{k-1} \frac{|\langle 0|\mathcal{O}^{80}(0)|e_n\rangle|^2}{2E_n}\ \Delta_\sigma(E-E_n)\,, \tag{3.5.20}$$

$$\rho_\sigma^{80,0}(E) = \sum_{n=0}^{k-1} \frac{\langle 0|\mathcal{O}^{80}(0)|e_n\rangle\langle e_n|\bar{\mathcal{O}}^{0}(0)|0\rangle}{2E_n}\ \Delta_\sigma(E-E_n)\,, \tag{3.5.21}$$

and for chimera baryons

$$\rho_\sigma^{80,80}(E) = \sum_{n=0}^{k-1} |K_n^{80}|^2\ \Delta_\sigma(E-E_n)\,, \tag{3.5.22}$$

$$\rho_\sigma^{80,0}(E) = \sum_{n=0}^{k-1} K_n^{80}K_n^{\dagger,0}\ \Delta_\sigma(E-E_n)\,. \tag{3.5.23}$$

By performing simultaneous fits to these two spectral densities, we extrapolate the unsmeared matrix elements and overlap factors associated with the coupling between the vacuum and the n^{th} state of the interpolating operator.

Chapter 4

A numerical framework for symplectic lattice gauge theories: GRID

As anticipated in the previous chapters, symplectic gauge theories coupled to matter fields display intriguing symmetry enhancement phenomena, making them promising candidates for applications in areas such as composite Higgs models [10, 216], top partial compositeness [16, 181, 184], and strongly interacting dark matter [83, 229]. These theories are also interesting to the broader field theory community, because they provide an alternative path to the large-N limit [12, 17, 54–56].

The general strategy is to investigate various symplectic groups, fermion representations, and field contents to explore their features. Although this research holds the potential to uncover deep insights, it poses considerable technical challenges.

Numerical lattice field theory provides a robust method for addressing these difficulties, enabling the precise calculations necessary to advance our understanding. As part of this effort, we have developed specialised software to incorporate symplectic gauge groups into Monte-Carlo simulations using the `GRID` framework [145, 146, 230].

In this chapter, we examine the $Sp(4)$ gauge theories as representative examples, focusing on fermions transforming in the two-index antisymmetric representation. We detail a thorough suite of technical validations for our algorithms, along with preliminary results, which form the foundation for future large-scale computational studies. Moreover, we present a parameter space exploration of $Sp(4)$ lattice gauge theories with varying numbers of fermions in the antisymmetric representation. The results presented in this chapter are taken from those obtained and shown in Refs. [178, 231].

4.1 GRID framework implementation

We use GRID for our computational investigations. This C++ framework provides a sophisticated, platform-independent library specifically designed for lattice gauge theory calculations. Its ability to run identical source code across various exascale architectures makes it particularly valuable for long-term computational research. The framework has demonstrated its versatility through successful applications in studying $SU(N)$ gauge theories with various fermion representations [204, 227]. Here, we detail our modifications to GRID, enabling $Sp(2N)$ gauge field configuration sampling.

Looking ahead to future studies incorporating dynamical fermions in $Sp(2N)$ gauge theories, we concentrated on implementing the HMC algorithm and its variant, the RHMC, which is necessary for odd number of fermion species.

As with the routines for $SU(N)$, our $Sp(2N)$ implementation supports any number of colours, with the Molecular Dynamics process starting from random Lie algebra-valued momenta. The implementation extends GRID's existing $SU(N)$ framework to handle $Sp(2N)$. Key modifications we made include:

1. Generation of random $\mathfrak{sp}(2N)$ Lie algebra-valued conjugated momenta using the generators defined in Appendix A.

2. Implementation of the generators in the 2-index antisymmetric representation of $Sp(2N)$, according to Eq. (3.3.8).

3. In the numerical integration of Eq. (3.2.14), the HMC force must be projected onto the Lie algebra of the gauge group. In GRID, this projection is embedded within the integrator, which requires the forces to be anti-hermitian. Therefore, it is required a projection operation onto the algebra $\mathfrak{sp}(2N)$. To implement it, we follow the procedure for the $\mathfrak{su}(N)$ algebra, where for a generic matrix, M, we project

$$P_{\mathrm{tr}} P_{\mathrm{aH}} M, \tag{4.1.1}$$

with $P_{\mathrm{tr}} M \equiv M - \mathbb{1}_{N\times N}\mathrm{Tr}(M)/N$ and $P_{\mathrm{aH}} M \equiv (M - M^\dagger)/2$ representing projections onto the traceless and anti-hermitian parts, respectively.

For the $\mathfrak{sp}(2N)$ algebra, the projection can be defined as follows:

$$P_{\mathrm{aH}} P^{-}_{\mathrm{Sp}} P_{\mathrm{tr}} M, \tag{4.1.2}$$

where

$$P^{\pm}_{\mathrm{Sp}} M \equiv \frac{M \pm \Omega M^* \Omega}{2}. \tag{4.1.3}$$

Here, P^{-}_{Sp} yields anti-hermitian matrices, while P^{+}_{Sp} projects onto hermitian matrices.

4. Link re-symplecticisation via a modified Gram-Schmidt process [8], where we:

   - Normalise the first column to unit length.
   - Compute the $(N+1)$-th column as $U_{i,j+N} = -\sum_{k=1}^{2N} \Omega_{ik} U^{*}_{kj}$.
   - Compute the second column by orthonormalising with respect to the first and $(N+1)$-th columns.
   - Compute the $(N+2)$-th column from the second column as done in the second passage.
   - Repeat until all the columns are filled.

   This is a modification of the Gram-Schmidt process to take into account the definition of symplectic groups, devised by Eq. (2.3.6), and it is performed after every configuration update. It also automatically ensures that the determinant of gauge links is equal to one, according to Eqs. (2.3.6) and (2.3.7). The re-projection prevents the gauge degrees of freedom from drifting away from the group manifold, which normally would be present due to machine accuracy roundings.

In the next section, following Ref. [200], we verify our implementation through (R)HMC algorithm tests, Molecular Dynamics behaviour analysis, and algorithm comparison studies.

4.1.1 Testing the algorithms

Our molecular dynamics evolution is performed using a second-order Omelyan integrator [232]. We focus on the $Sp(4)$ theory with $N_{\mathrm{f}} = 0$, and $N_{\mathrm{as}} = 4$ in Eq. (3.3.1), conducting a series of initial tests on the algorithms employed. The results are shown in Figs. 4.1, 4.2, 4.3, 4.4, and 4.5, with the lattice parameters set to $\beta = 6.8$, and $am_0 = -0.6$, using an isotropic lattice with volume $\tilde{V} = (8a)^4$.

Firstly, we check whether Creutz's equality [233] is fulfilled. By calculating the difference in Hamiltonian, ΔH, before and after the molecular dynamics evolution, we expect to find that

$$\langle \exp(-\Delta H) \rangle = 1\,. \tag{4.1.4}$$

Figure 4.1 displays the computed values of $\langle \exp(-\Delta H) \rangle$ for five different time-step choices ($\Delta\tau = \tau/n_{\mathrm{steps}}$, with $\tau = 1$) in the molecular dynamics integration. These results are obtained from a thermalised ensemble of 3400 trajectories, with an integrated plaquette autocorrelation

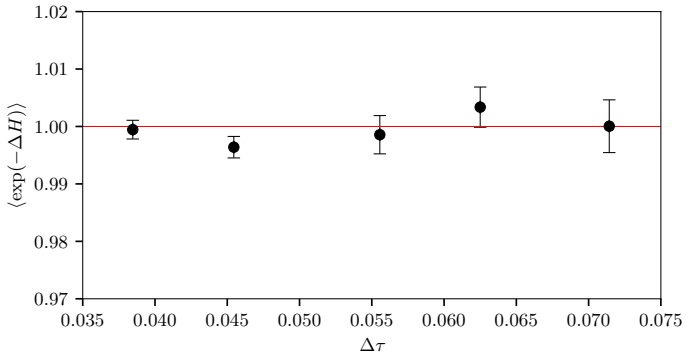

Figure 4.1. Test of Creutz's equality, $\langle \exp(-\Delta H) \rangle = 1$. Dependence of the expectation value $\langle \exp(-\Delta H) \rangle$ on the molecular dynamics (MD) integration time step $\Delta\tau$, for a system with gauge group size $N = 2$, zero fundamental fermions ($N_{\rm f} = 0$), and four antisymmetric-representation fermions ($N_{\rm as} = 4$). The trajectory length is fixed to $\tau = 1$, with the number of integration steps varied as $n_{\rm steps} = 14,\ 16,\ 18,\ 22,\ 26$, corresponding to $\Delta\tau = \tau/n_{\rm steps}$. Simulations are performed on an ensemble with lattice volume $\tilde{V}/a^4 = 8^4$, at gauge coupling $\beta = 6.8$, and antisymmetric bare mass $am_0^{\rm as} = -0.6$.

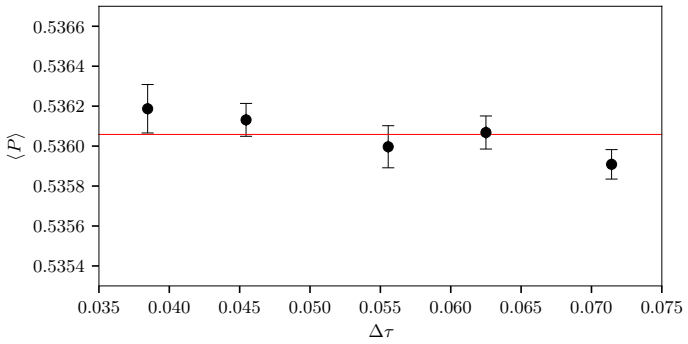

Figure 4.2. Test of the independence of the plaquette on the molecular dynamics (MD) integration time step $\Delta\tau$, for $N = 2$, $N_{\rm f} = 0$, and $N_{\rm as} = 4$. The trajectory length is fixed to $\tau = 1$, and the number of integration steps is varied as $n_{\rm steps} = 14,\ 16,\ 18,\ 22,\ 26$, corresponding to $\Delta\tau = \tau/n_{\rm steps}$. Simulations are performed on an ensemble with lattice volume $\tilde{V}/a^4 = 8^4$, gauge coupling $\beta = 6.8$, and antisymmetric bare mass $am_0^{\rm as} = -0.6$. The horizontal line represents the plaquette value obtained by averaging over all trajectories with different values of $n_{\rm steps}$.

time $\tau_{\rm int}^{\langle P \rangle} = 6.1(2)$, determined using the Madras-Sokal integrated autocorrelation time [234–236], which is defined as

$$\tau_{\rm int}^{X} = \max_{\tau_{\rm max}} \left[\frac{1}{2} + \sum_{t=1}^{\tau_{\rm max}} \Gamma(\tau) \right], \tag{4.1.5}$$

where

$$\Gamma^X(\tau) = \sum_{i=1}^{N-\tau} \frac{\left(X_i - \bar{X}\right)\left(X_{i+\tau} - \bar{X}\right)}{N-\tau}, \tag{4.1.6}$$

and the Monte-Carlo time series, X_i, is assumed fully thermalised.

Alternatively, the exponential autocorrelation time, τ^X_{exp}, can be obtained by fitting the autocorrelation function, $C_X(\tau)$:

$$C_X(\tau) = \sum_{i=1}^{N-\tau} \left(X_i - \bar{X}\right)\left(X_{i+\tau} - \bar{X}\right), \tag{4.1.7}$$

$$\frac{C_X(\tau)}{C_X(0)} \sim \exp\left(-\frac{\tau}{\tau^X_{\text{exp}}}\right), \tag{4.1.8}$$

to an exponential decay. Additionally, Fig. 4.2 demonstrates that the average plaquette value defined as in Eq. (3.4.35) remains unaffected by changing $\Delta\tau$, confirming the stability of the integration.

Our third test evaluates the scaling behaviour of $\langle \Delta H \rangle$ with respect to $\Delta\tau$. For a second-order integrator, $\langle \Delta H \rangle$ is expected to scale as $(\Delta\tau)^4$ [237]. Figure 4.3 shows the measurements alongside a best-fit curve, parameterised as $\log\langle \Delta H \rangle = \mathcal{K}_1 \log(\Delta\tau) + \mathcal{K}_2$. The fit yields $\mathcal{K}_1 = 3.6(4)$, in close agreement with the theoretical value of 4, with a reduced $\chi^2/N_{\text{d.o.f.}} = 0.6$.

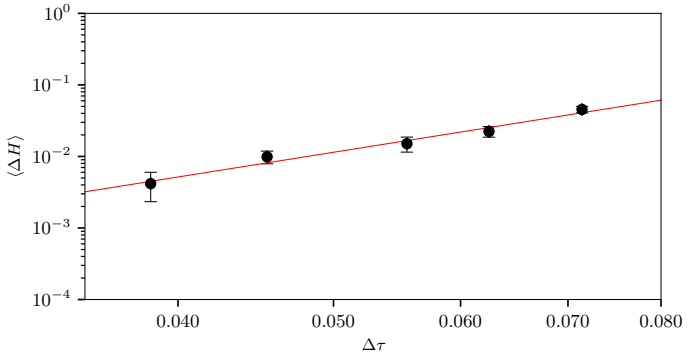

Figure 4.3. Scaling of the energy violation with the MD time step. Dependence of the expectation value $\langle \Delta H \rangle$ on the molecular dynamics (MD) integration time step $\Delta\tau$, for $N = 2$, $N_{\text{f}} = 0$, and $N_{\text{as}} = 4$. The quantity $\langle \Delta H \rangle$ scales proportionally to $(\Delta\tau)^4$, as expected for a second-order integrator. The plot is shown on a log-log scale. The trajectory length is fixed to $\tau = 1$, and the number of integration steps is varied as $n_{\text{steps}} = 14,\ 16,\ 18,\ 22,\ 26$, corresponding to $\Delta\tau = \tau/n_{\text{steps}}$. Simulations are performed on an ensemble with lattice volume $\tilde{V}/a^4 = 8^4$, gauge coupling $\beta = 6.8$, and bare mass $am_0 = -0.6$.

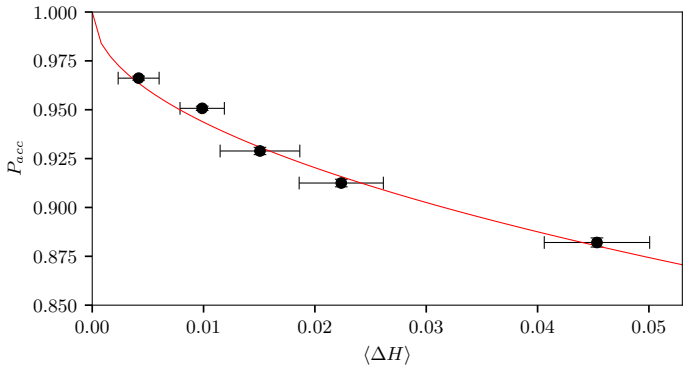

Figure 4.4. Test of the relationship between acceptance probability and ΔH for the theory with $N = 2$, $N_{\rm f} = 0$, and $N_{\rm as} = 4$. The expected behaviour, $P_{\rm acc} = \mathrm{erfc}\left(\frac{\sqrt{\Delta H}}{2}\right)$, is confirmed. The trajectory length is fixed to $\tau = 1$, with the number of integration steps varied as $n_{\rm steps} = 14,\ 16,\ 18,\ 22,\ 26$, corresponding to $\Delta\tau = \tau/n_{\rm steps}$. Simulations are performed on an ensemble with lattice volume $\tilde{V}/a^4 = 8^4$, gauge coupling $\beta = 6.8$, and bare mass $am_0 = -0.6$.

Finally, a related test verifies the acceptance probability, $P_{\rm acc}$, of the algorithm, as illustrated in Fig. 4.4. The measurements are consistent (Fig. 4.5) with the theoretical prediction [238]:

$$P_{\rm acc} = \mathrm{erfc}\left(\frac{1}{2}\sqrt{\langle \Delta H \rangle}\right). \tag{4.1.9}$$

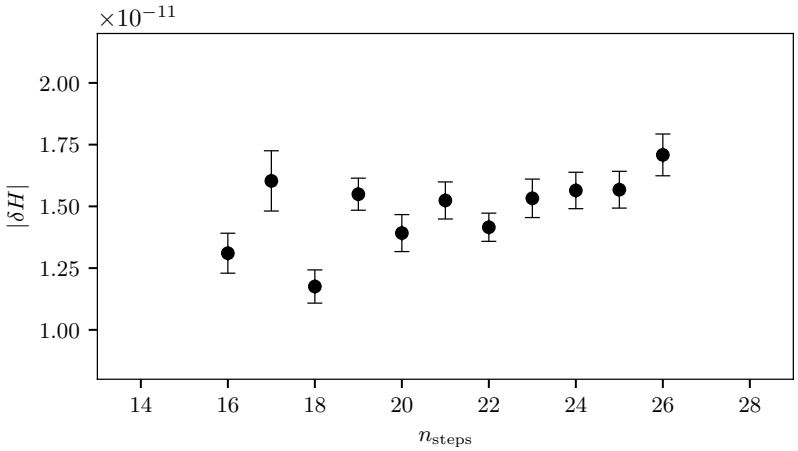

Figure 4.5. Reversibility test displaying $|\delta H|$ for various values of the molecular dynamics time step $\Delta\tau$, in the theory with $N = 2$, $N_{\rm f} = 0$, and $N_{\rm as} = 4$. The trajectory length is fixed at $\tau = 1$, with the number of integration steps varied within $n_{\rm steps} \in [16, 26]$, corresponding to $\Delta\tau = \tau/n_{\rm steps}$. Simulations are performed on an ensemble with lattice volume $\tilde{V}/a^4 = 8^4$, gauge coupling $\beta = 6.8$, and bare mass $am_0 = -0.6$.

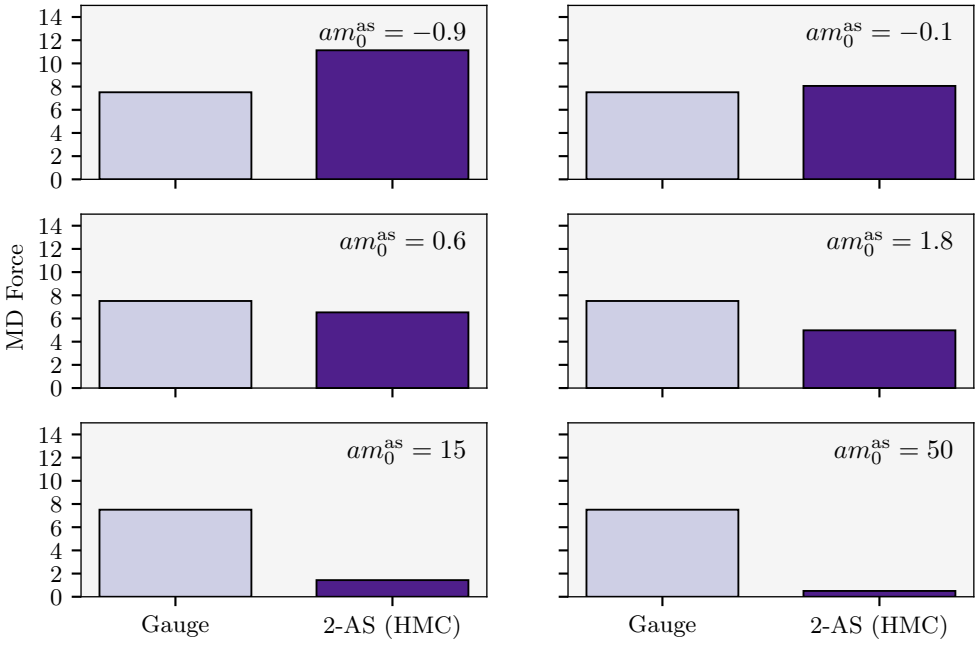

Figure 4.6. Contribution of fields to the molecular dynamics (MD) force in the theory with $N = 2$, $N_{\mathrm{f}} = 0$, and $N_{\mathrm{as}} = 4$, simulated on an isotropic lattice with volume $\tilde{V} = (8a)^4$ and lattice coupling $\beta = 6.8$. The two blocks display the contributions from gauge fields (light shading, left) and fermions (dark shading, right), with fermion forces computed using the Hybrid Monte-Carlo (HMC) algorithm. Fermion contributions are summed over all flavours. The six panels correspond to different bare anti-symmetric masses: $am_0^{\mathrm{as}} = -0.9, -0.1, +0.6, +1.8, +15, +50$, arranged left to right and top to bottom.

As outlined in Refs. [200, 239], ensuring reversibility is essential to validate correct HMC updates. While the leapfrog algorithm is analytically reversible, numerical precision can compromise this property in practical implementations. Finite precision may lead to small deviations from reversibility, potentially introducing biases if left unchecked. To address this, we verify that the key steps in our algorithm uphold approximate reversibility. Specifically, we monitor the difference in Hamiltonian, $|\delta H|$, after evolving the molecular dynamics forward and backward while flipping the momenta at $\tau = 1$. In our simulations, $|\delta H|$ remains negligible, with typical values around $\sim 10^{-11}$, despite the Hamiltonian being of order $\sim 10^{6}$. The entity of the observed violation aligns with the expected precision of double-precision floating-point arithmetic. Additionally, the observed $|\delta H|$ is independent of $\Delta\tau$.

Reversibility violations may arise from the updates to gauge link variables and momenta. To minimise such effects, we update the gauge links via exponentiation, ensuring $U(\pi)U(-\pi) = 1$, and rely on double-precision arithmetic to keep relative momentum violations within machine accuracy. These measures effectively mitigate global reversibility

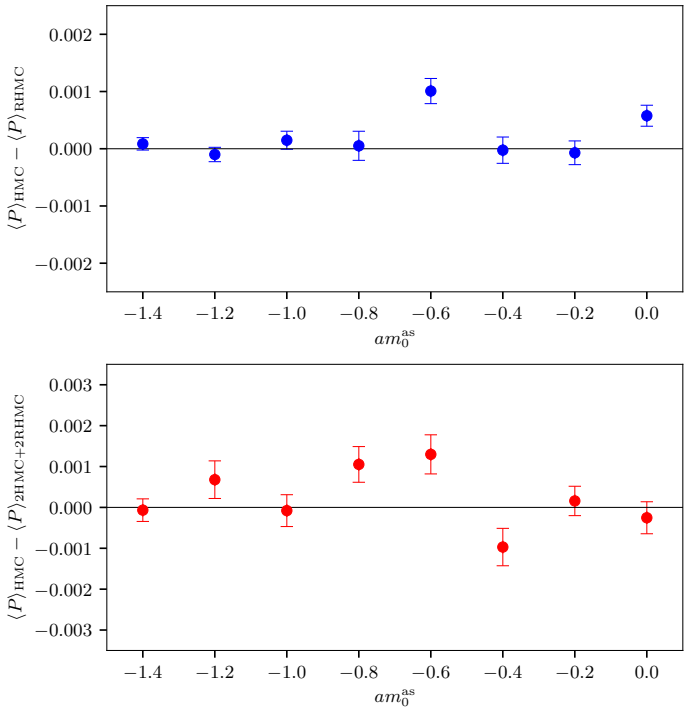

Figure 4.7. Comparison of plaquette averages $\langle P\rangle$ obtained using the HMC and RHMC algorithms for the theory with $N = 2$, $N_{\mathrm{f}} = 0$, and $N_{\mathrm{as}} = 4$. The value $\langle P\rangle_{\mathrm{HMC}}$ is obtained by simulating two pairs of fermions using HMC. For $\langle P\rangle_{\mathrm{RHMC}}$ (top panel), RHMC was applied separately to each fermion. The quantity $\langle P\rangle_{\mathrm{2HMC+2RHMC}}$ (bottom panel) corresponds to simulations where two fermions were evolved with HMC and the other two with RHMC. Simulations are performed at lattice coupling $\beta = 6.8$, with bare mass in the range $-1.4 \leq am_0^{\mathrm{as}} \leq 0.0$ with steps of magnitude 0.2. The lattice is isotropic with volume $\tilde{V} = (8a)^4$.

violations in the algorithm.

To further illustrate the dynamics of the physical system in consideration, we examine the contributions of the fields to the molecular dynamics force, F, as defined in Eq. (3.2.14), under varying lattice parameters. Focusing on the theory with $N = 2$, $N_{\mathrm{f}} = 0$, and $N_{\mathrm{as}} = 4$, we study several ensembles with isotropic lattices of volume $\tilde{V} = (8a)^4$ and lattice coupling $\beta = 6.8$, varying the mass am_0^{as}. Figure 4.6 presents the force decomposed into contributions from the gauge and fermion dynamics. The fermion forces are computed using the HMC algorithm, and the results are normalised such that the gauge contribution remains constant. As shown, for large positive values of am_0^{as}, the fermion contribution is negligible, consistent with the quenched regime. As the mass decreases, the fermion contribution grows, eventually surpassing the gauge contribution for very negative Wilson bare masses near the chiral limit.

While the main focus in this chapter is on the theory with $N = 2$, $N_{\mathrm{f}} = 0$, and $N_{\mathrm{as}} = 4$,

where we can utilise the HMC algorithm, for more general purposes of study it may be necessary to consider odd numbers of fermions. In such cases, we make use of the RHMC algorithm, which is deployable for a generic number of fermions. This method uses a rational approximation to compute the fermion force, but the inclusion of a Metropolis accept-reject step guarantees the exactness of the algorithm. To verify the accuracy of the Remez implementation, one could, in principle, use any function of an arbitrary matrix, M. In particular, choosing diagonal matrices simplifies the comparison. This was a preliminary test employed while developing the code. A further test can be conducted to verify the consistency and accuracy of our implementation, similar to what has been performed for $SU(3)$ theories (see Ref. [240]). To evaluate the numerical precision of the implementation, we compute the average plaquette, $\langle P \rangle$, defined as in Eq. (3.4.35), where the lattice volume is $\tilde{V} = (8a)^4$, and the coupling is set to $\beta = 6.8$. This computation is performed for several representative values of the bare mass, $-1.4 \leq am_0^{\text{as}} \leq 0.0$.

We repeat this analysis under three distinct scenarios:

- All fermions treated with the HMC.
- All fermions treated with the RHMC.
- A mixed approach, where two fermions are treated with the HMC and the remaining two with the RHMC.

The results are summarised in Fig. 4.7, where the differences between the second and third methods relative to the first are shown in the two panels. For most data points, these differences are statistically consistent with zero, well within the uncertainties. Broadly speaking, given the number of observables examined, the probability of observing a deviation greater than 3σ from zero is approximately 12%.

4.1.2 Wilson flow and topology on `GRID`

We study the $Sp(4)$ gauge theory with $N_{\text{f}} = 0$ and $N_{\text{as}} = 4$, focusing on the procedure for setting the lattice scale using the Wilson flow. Additionally, we monitor the evolution of the topological charge with respect to the number of trajectories, to check that topological freezing is avoided. While our analysis is carried out on selected representative cases, the conclusions drawn remain applicable across the full range of parameter sets considered.

The Wilson flow [241, 242] is a versatile tool for lattice studies, serving two essential purposes. First, it offers a robust and theory-independent method for setting the lattice scale, making it particularly valuable for theories lacking direct experimental benchmarks. Second, it smoothens gauge field configurations, suppressing short-distance fluctuations and reducing numerical noise in the computation of observables like the topological charge, Q, which is sensitive to ultraviolet fluctuations.

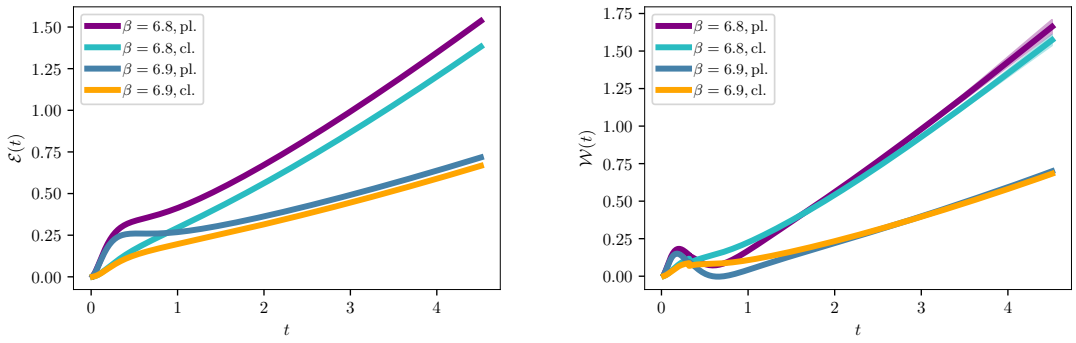

Figure 4.8. Wilson flow [241, 242] energy density $\mathcal{E}(t)$ (left) and its derivative $\mathcal{W}(t)$ (right), computed following the process outline in Refs. [8, 18]. Results are shown for the $Sp(4)$ gauge theory with $N_{\rm as} = 4$ antisymmetric fermions. Calculations use both the standard plaquette (pl) and clover-leaf (cl) discretizations [243, 244]. Simulations are performed on a lattice volume $\tilde{V} = (12a)^4$, at bare couplings $\beta = 6.8$ and 6.9, with a common bare mass $am_0^{\rm as} = -0.8$. The flow time step is set to 0.01, and the maximum flow time $t_{\rm max} = 4.5$ is chosen to suppress finite-volume effects. Errors are estimated using bootstrap resampling. The reference value $\mathcal{W}_0$ is fixed to $\frac{1}{2}C_{\rm f}$ (half of the eigenvalue of the quadratic Casimir operator), resulting in scale-setting parameters $w_{0,\rm pl} = 1.485(3)$ and $w_{0,\rm cl} = 1.495(2)$ at $\beta = 6.8$, and $w_{0,\rm pl} = 2.005(2)$ and $w_{0,\rm cl} = 2.026(2)$ at $\beta = 6.9$. For convenience, the lattice spacing is set to $a = 1$.

Following Refs. [8, 18], the Wilson flow introduces a fictitious flow time t, defined through the evolution equation:

$$\frac{\mathrm{d}B_\mu(x,t)}{\mathrm{d}t} = D_\nu G_{\nu\mu}(x,t)\,, \tag{4.1.10}$$

with boundary condition $B_\mu(x,0) = A_\mu(x)$, where $A_\mu(x)$ is the four-dimensional gauge field, D_μ the corresponding covariant derivative, and $G_{\mu\nu}(t) \equiv [D_\mu, D_\nu]$. The flow smoothens field configurations over a Gaussian kernel with radius $\sqrt{8t}$.

To set the scale, we evaluate flow observables:

$$\mathcal{E}(t) \equiv \frac{t^2}{2}\left\langle \mathrm{Tr}\,[G_{\mu\nu}(t)G_{\mu\nu}(t)]\right\rangle\,, \quad \text{and} \quad \mathcal{W}(t) \equiv t\frac{\mathrm{d}}{\mathrm{d}t}\mathcal{E}(t)\,, \tag{4.1.11}$$

and define reference scales such as t_0, where $\mathcal{E}(t_0) = \mathcal{E}_0$, or w_0, satisfying $\mathcal{W}(t = w_0^2) = \mathcal{W}_0$. The parameter $\mathcal{W}_0$ is typically chosen as $\mathcal{W}_0 = c_w C_{\rm f}$, where $C_{\rm f} = (1+2N)/4$ is the fundamental Casimir for $Sp(2N)$ and there are several choices that have been operated in the literature for c_w. Two examples are $c_w = 0.225$, 0.5 [178, 245]. In this chapter, we make use of $c_w = 0.5$.

On the lattice, gauge fields $A_\mu(x)$ are replaced by link variables $U_\mu(x)$, and $B_\mu(x,t)$ is replaced by $V_\mu(x,t)$ with $V_\mu(x,0) = U_\mu(x)$. The field strength $G_{\mu\nu}$ can be computed using either the standard plaquette ($V_{\mu\nu}(x,t)$, when built through the variables $V_\mu(x,t)$), where, according to Ref. [241],

$$\mathcal{E}(t) = t^2 \sum_{x\in\Xi}\sum_{\mu<\nu} \mathrm{Re}\ \mathrm{Tr}[1 - V_{\mu\nu}(x,t)], \tag{4.1.12}$$

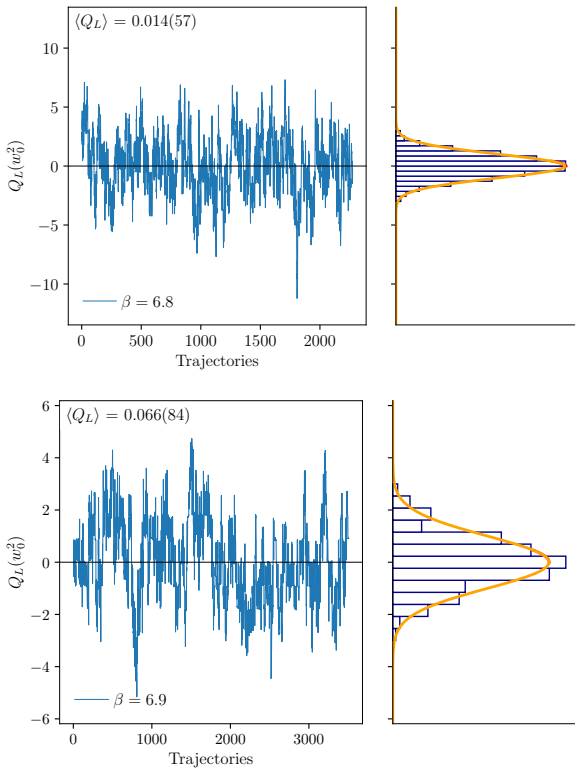

Figure 4.9. Evolution of the topological charge, $Q_L(t = w_0^2) \equiv \sum_x \frac{1}{32\pi^2}\varepsilon^{\mu\nu\rho\sigma}\,\mathrm{Tr}\,[\mathcal{C}_{\mu\nu}(x)\mathcal{C}_{\rho\sigma}(x)]$, evaluated at flow time $t = w_0^2$ for the $Sp(4)$ theory with $N_{\mathrm{as}} = 4$ antisymmetric fermions. Results are shown for lattice volume $\tilde{V} = (12a)^4$, with bare coupling $\beta = 6.8$ (top panel) and $\beta = 6.9$ (bottom panel), and bare mass $am_0^{\mathrm{as}} = -0.8$. The histograms (right) exhibit Gaussian distributions centred at zero, with reduced chi-square values $\tilde{\chi}^2 = \chi^2/N_{\mathrm{d.o.f.}} = 1.1$. Integrated autocorrelation times are $\tau_{\mathrm{int}}^Q = 31(3)$ (top) and $\tau_{\mathrm{int}}^Q = 238(12)$ (bottom), computed using the Madras-Sokal algorithm.

or directly through the clover-leaf operator [243, 244] that is defined as follows:

$$\begin{aligned}\mathcal{C}_{\mu\nu}(x) \equiv \frac{1}{8a^2}\big\{&U_\mu(x)U_\nu(x+\hat{\mu})U_\mu^\dagger(x+\hat{\nu})U_\nu^\dagger(x)+\\ &+U_\nu(x)U_\mu^\dagger(x+\hat{\nu}-\hat{\mu})U_\nu^\dagger(x-\hat{\mu})U_\mu(x-\hat{\mu})+\\ &+U_\mu^\dagger(x-\hat{\mu})U_\nu^\dagger(x-\hat{\nu}-\hat{\mu})U_\mu(x-\hat{\nu}-\hat{\mu})U_\nu(x-\hat{\nu})+\\ &+U_\nu^\dagger(x-\hat{\nu})U_\mu(x-\hat{\nu})U_\nu(x-\hat{\nu}+\hat{\mu})U_\mu^\dagger(x)-\mathrm{h.c.}\big\}\,.\end{aligned} \tag{4.1.13}$$

.

Ideally, the lattice scale should be set in a manner that minimises dependence on microscopic details. In practice, however, scale-setting using the Wilson flow is influenced by the specific lattice discretisation of the flow equation in Eq. (4.1.10) and the observable $\mathrm{Tr}[G_{\mu\nu}G_{\mu\nu}]$ in Eq. (4.1.11). Different discretisation schemes can yield slightly different scale values for a fixed lattice cutoff. Nevertheless, choosing an appropriate flow time, t, significantly mitigates these discretisation effects.

To illustrate this, Fig. 4.8 presents results for the $Sp(4)$ gauge theory with $N_{\rm f} = 0$ and $N_{\rm as} = 4$, for two representative values of β, along with a fixed lattice volume $\tilde{V}$ and bare mass $am_0^{\rm as}$. The plots show the flow observables $\mathcal{E}(t)$ and $\mathcal{W}(t)$ as functions of the flow time, comparing the outcomes for two lattice regularisations of the action: the elementary plaquette (3.1.21), $U_{\mu\nu}$, and the clover-leaf operator (4.1.13), $\mathcal{C}_{\mu\nu}$. We observe that the observable $\mathcal{W}(t)$ shows reduced sensitivity to short-distance discretisation effects compared to $\mathcal{E}(t)$.

Wilson flow observables have also been employed in defining non-perturbative running couplings, as discussed in Refs. [246–250] and reviewed in [251]. While this is a promising avenue for further applications of the Wilson flow, such studies demand extensive computational resources, including large lattices, which are beyond the scope of this introductory work.

The topological charge density is defined as

$$q_L(x,t) \equiv \frac{1}{32\pi^2}\varepsilon^{\mu\nu\rho\sigma}\,\mathrm{Tr}\,[\mathcal{C}_{\mu\nu}(x,t)\mathcal{C}_{\rho\sigma}(x,t)]\,, \tag{4.1.14}$$

and the total topological charge is given by $Q_L(t) \equiv \sum_x q_L(x,t)$, where t denotes the flow time.

We aim to confirm that topological freezing does not occur. To this end, Fig. 4.9 shows the evolution of $Q_L(t = w_0^2)$ for the $Sp(4)$ theory with $N_{\rm f} = 0$ and $N_{\rm as} = 4$, using two values of β and a common bare mass. The trajectories of $Q_L(t)$ are plotted alongside histograms of their distributions. Visual inspection reveals no signs of topological freezing, as this quantity moves freely through different values of opposite signs, and its distribution appears Gaussian, as expected, and centred at the null value. The former conclusion is reinforced by applying the Madras-Sokal windowing algorithm [234], which yields estimates for the integrated autocorrelation time, $\tau_{\rm int}^{Q}$, of the topological charge. In both cases, $\tau_{\rm int}^{Q}$ is orders of magnitude smaller than the number of trajectories, and the histograms are well-fitted by Gaussian distributions centred at $\langle Q_L(t = w_0^2)\rangle = 0$.

The results presented here demonstrate that the Wilson flow and topological charge, computed with a new software implementation based on `GRID` and tested on GPU architectures, perform as expected for the $Sp(4)$ gauge theory with $N_{\rm f} = 0$, and $N_{\rm as} = 4$. These findings are consistent with those reported in the literature for similar theories, confirming that the simulation algorithms and observable calculations are free from systematic artefacts.

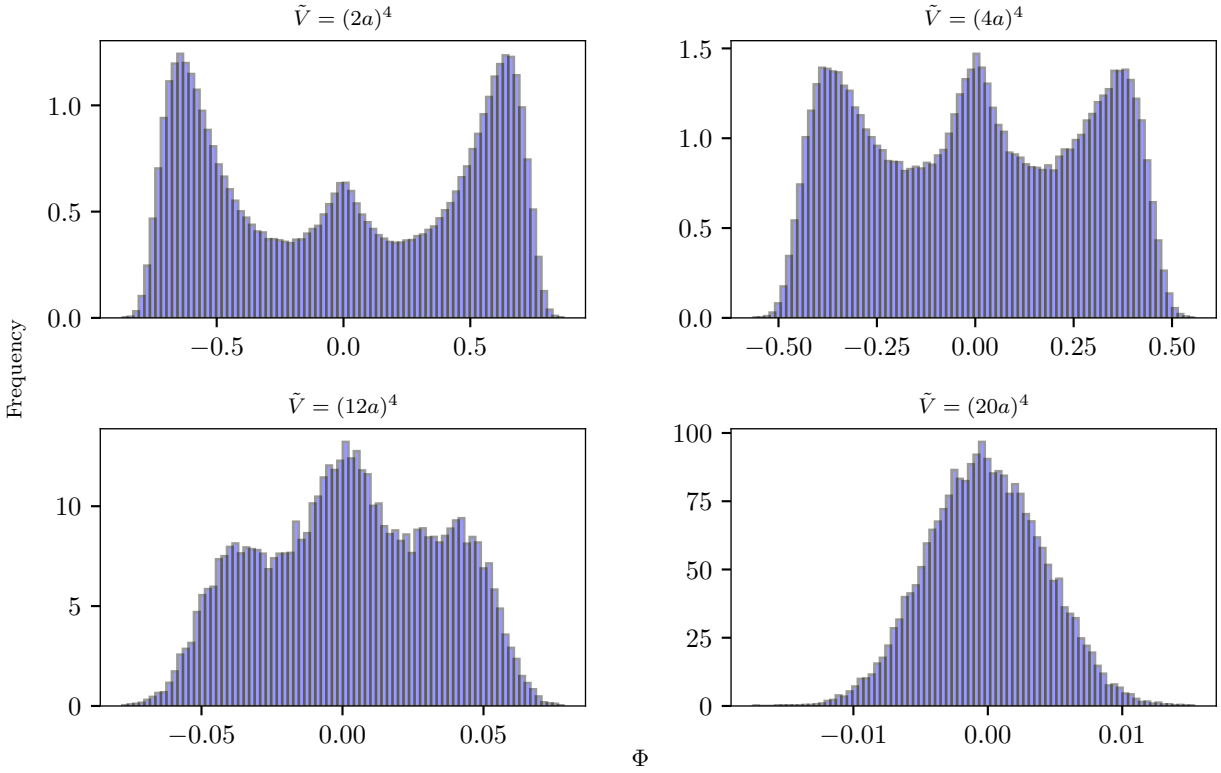

Figure 4.10. Study of finite-size effects in the $Sp(4)$ Yang–Mills theory. The histograms show the distribution of (real) Polyakov loops for ensembles at fixed coupling $\beta = 9.0$ and four different lattice volumes: $\tilde{V} = (2a)^4, (4a)^4, (12a)^4, (20a)^4$. All histograms are normalised such that their areas equal 1.

4.2 $Sp(4)$: centre symmetry and global symmetry breaking

This section aims to show how several symmetry-breaking patterns are respected in our findings. This signals the correct implementation of the symplectic gauge group in the `GRID` code. This study of $Sp(4)$ theories can be done by initially analysing its pure Yang-Mills dynamics, where $N_f = 0$ and $N_{as} = 0$ in Eq. (3.3.1). We begin by examining the behaviour of the centre symmetry, depending on the centre group, $(\mathbb{Z}_2)^4$. This global symmetry is broken at small volumes but restored at sufficiently large volumes. The analysis of the Polyakov loop, follows a methodology similar to Ref. [252]. Subsequently, as in Ref. [204], we explore the spectrum of the Dirac operator in the quenched approximation, for both fundamental and two-index antisymmetric fermions, verifying the anticipated symmetry-breaking pattern predicted by random matrix theory.

The results of the centre symmetry analysis are shown in Fig. 4.10. At a fixed coupling

of $\beta = 9.0$, we generate four ensembles in the pure $Sp(4)$ theory, corresponding to different space-time volumes: $\tilde{V} = (2a)^4$, $(4a)^4$, $(12a)^4$, $(20a)^4$. For each configuration, we compute the spatially averaged real Polyakov loop, defined as:

$$\Phi \equiv \frac{1}{NN_s^3} \sum_{\vec{x}} \mathrm{Tr} \left(\prod_{t=0}^{t=N_t-1} U_0(t, \vec{x}) \right), \tag{4.2.1}$$

where $U_0(t, \vec{x})$ denotes the time-like link variable. The lattices are isotropic, with equal extent in all four directions, $N_t = N_s = L/a$. The frequency histograms of Φ for each ensemble are displayed in Fig. 4.10.

In the zero-temperature limit, the $Sp(4)$ lattice theory is expected to preserve the $(\mathbb{Z}_2)^4$ centre symmetry in four-dimensional Euclidean space-time. This behaviour is confirmed at large volumes, as shown in the bottom-right panel of Fig. 4.10 for $N_t = N_s = 20$, where the distribution of Φ is Gaussian and centred at zero. However, at smaller volumes, this symmetry is broken, as evidenced in the other panels of Fig. 4.10. For these cases, the distribution of Φ becomes non-Gaussian, with two additional peaks emerging symmetrically around zero. At the smallest volume, $N_t = N_s = 2$, the distribution is dominated by two peaks at finite values of Φ, while maintaining overall symmetry around zero.

Polyakov loops are also valuable tools for studying the finite-temperature (de)confinement phase transition. This is operated for symplectic gauge theories in Refs. [253] and [229], and requires lattices with $N_t \neq N_s$, varying the coupling β to locate the critical temperature, and performing continuum and infinite volume extrapolations.

The Wilson-Dirac formulation for mass-degenerate Dirac fermions in Eq. (3.3.2) explicitly breaks the global symmetry G of Eq. (2.2.10). This can be verified on ensembles of gauge configurations in the quenched approximation, to verify the correctness of our implementation of the Dirac operators. Following Ref. [204] (and Ref. [16]), we consider the theory with quenched fermions in either the fundamental or two-index antisymmetric representation and compute the spectrum of eigenvalues of the Hermitian Wilson-Dirac operator, $Q_m = \gamma_5 D_m$. The number of configurations is $N_{\mathrm{conf,f}} = 88$ for fundamental fermions and $N_{\mathrm{conf,as}} = 47$ for antisymmetric fermions, with 3696 eigenvalues for fundamental fermions and 5120 for antisymmetric fermions per configuration. We then compute the distribution of the folded density of spacing, $P(s)$, as in Ref. [16], and compare the results with the predictions from chiral Random Matrix Theory (chRMT) [254, 255].

Since the spectrum reflects the properties of the theory, particularly the pattern of chiral

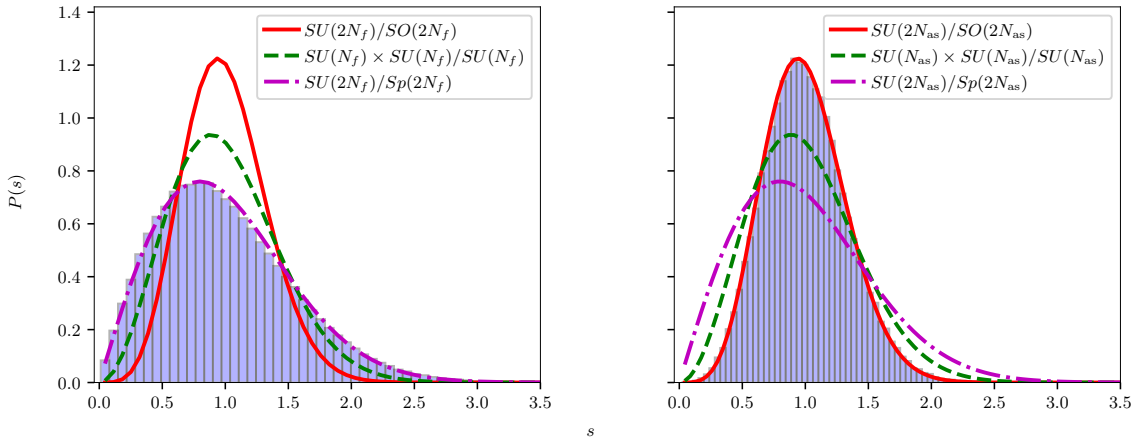

Figure 4.11. Distribution of the folded spacing density between consecutive eigenvalues of the Hermitian Wilson-Dirac operator $Q_m = \gamma_5 D_m$, compared with predictions from chiral Random Matrix Theory (chRMT). Results are computed in the quenched approximation for ensembles with coupling $\beta = 8.0$, bare mass $am_0 = -0.2$, and lattice volume $\tilde{V} = (4a)^4$ in the $Sp(4)$ theory. The left panel corresponds to fermions in the fundamental representation, while the right panel shows fermions in the two-index antisymmetric representation.

symmetry breaking [256], the distribution $P(s)$ varies depending on the expected symmetry-breaking pattern. The folded density of spacing is given by

$$P(s) = N_{\tilde{\beta}} s^{\tilde{\beta}} \exp\left(-c_{\tilde{\beta}} s^2\right), \quad \text{where} \quad N_{\tilde{\beta}} = 2\frac{\Gamma^{\tilde{\beta}+1}\left(\frac{\tilde{\beta}}{2}+1\right)}{\Gamma^{\tilde{\beta}+2}\left(\frac{\tilde{\beta}+1}{2}\right)}, \; c_{\tilde{\beta}} = \frac{\Gamma^2\left(\frac{\tilde{\beta}}{2}+1\right)}{\Gamma^2\left(\frac{\tilde{\beta}+1}{2}\right)}, \tag{4.2.2}$$

where $\tilde{\beta}$ is the Dyson index. This index can take three values: $\tilde{\beta} = 2$ corresponds to the symmetry breaking pattern $SU(N_f) \times SU(N_f) \to SU(N_f)$, $\tilde{\beta} = 1$ to $SU(2N_f) \to Sp(2N_f)$ which is the relevant fundamental representation case, and $\tilde{\beta} = 4$ to $SU(2N_f) \to SO(2N_f)$ which represents the two-index antisymmetric fermions case in the symplectic theory.

To evaluate the consistency of our results with the chiral random matrix theory (chRMT) prediction in Eq. (4.2.2), we calculate the eigenvalues of the operator Q_m for a total of N_{conf} configurations. For each configuration c, indexed as $c = 1, \ldots, N_{\text{conf}}$, the eigenvalues $\lambda_i^{(c)}$ are computed and sorted in ascending order. In the case of fermions in the two-index antisymmetric representation, we discard any degenerate eigenvalues. From this sorted list, we assign a rank $n_i^{(c)}$ to each eigenvalue $\lambda_i^{(c)}$, corresponding to its position in the ordered sequence. The eigenvalue spacings, s, are then defined as:

$$s = \frac{n_{i+1}^{(c)} - n_i^{(c)}}{\mathcal{N}}, \tag{4.2.3}$$

where $\mathcal{N}$ is a normalisation factor ensuring the mean spacing satisfies $\langle s \rangle = 1$. Using these spacings, we construct the unfolded density $P(s)$ by binning the values of s and normalising the resulting histogram.

In Fig. 4.11, we show the numerically computed folded eigenvalue distributions for the Wilson-Dirac operator. For fundamental fermions, the observed distribution matches the symmetry breaking pattern corresponding to the coset $SU(2N_f)/Sp(2N_f)$, while for fermions in the two-index antisymmetric representation, the results align with the coset $SU(2N_f)/SO(2N_f)$. These findings demonstrate excellent agreement with chRMT predictions. Moreover, it is noticeable that, since the Wilson-Dirac fermions discretisation shows the same bilinear form as the mass term of a Lagrangian as in Eq. (2.2.2) and the corresponding chiral condensate (Eq. (2.2.11)), it shows their same symmetry breaking pattern, devised in Section 2.2.

To minimise finite-volume artefacts, we carefully selected the lattice sizes for our study. Such artefacts can distort the spacing distribution, especially for the largest and smallest eigenvalues. In smaller volumes, this leads to unusually large spacings that deviate from the expected chRMT behaviour, an issue we interpret as a finite-size effect. For the two-index antisymmetric representation, we observe that even at a volume of $\tilde{V} = (4a)^4$, the results adhere to the chRMT predictions without requiring any corrections. In contrast, for the fundamental representation, the inclusion of extreme eigenvalues introduces discrepancies. By excluding the 200 smallest and largest eigenvalues, reducing the total count from 4096 to 3696, we eliminate these deviations. This approach allows the fundamental representation to reproduce the chRMT predictions even at relatively small lattice volumes, such as $\tilde{V} = (4a)^4$.

4.3 Bulk phase structure

When exploring a theory on the lattice, it is important to check whether bulk phase transitions are present. The physical region of interest is separated by the bulk region by a (first-order) phase transition[1]. In this section, we present a study of the bulk phase structure for the $Sp(4)$ gauge theory with $N_\mathrm{f} = 0$ (pure gauge theory), and then allowing the system to have dynamical fermions. This involves comprehensive parameter scans and provides preliminary measurements, laying the groundwork for future large-scale numerical studies. We do so, while varying numbers of fermions (N_as) in the antisymmetric representation. The initial focus is on the case $N_\mathrm{as} = 4$.

A preliminary exploration of the lattice parameter space is performed to locate phase transitions in the (β, m_0) plane. This investigation involves analysing the average plaquette, $\langle P \rangle$, its susceptibility, and potential hysteresis phenomena. From this analysis, we estimate

[1] The presence of a sharp cross-over is also a possibility in the context of bulk-to-physical phases separation.

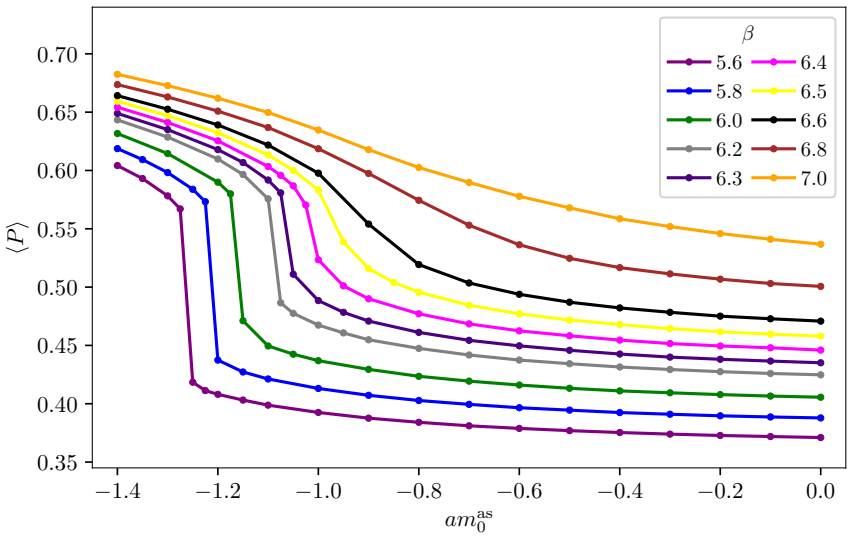

Figure 4.12. Parameter scan of the $Sp(4)$ theory with $N_{\mathrm{as}} = 4$ antisymmetric fermions. Ensembles generated from cold starts using the Hybrid Monte-Carlo algorithm are analysed. The average plaquette, $\langle P \rangle$, is shown as a function of bare mass across a range of lattice couplings β. Simulations use lattices of volume $\tilde{V} = (8a)^4$. Couplings span $\beta = 7.0, 6.8, 6.6, 6.5, 6.4, 6.3, 6.2, 6.0, 5.8, 5.6$ with bare masses between -1.4 and 0.0.

the critical coupling β_*, which defines the upper limit of the bulk phase. Above β_*, the lattice results can be extrapolated to the continuum limit.

Figure 4.12 depicts the average plaquette, $\langle P \rangle$, calculated from ensembles initialised with cold starts. Simulations were carried out on a lattice volume $\tilde{V} = (8a)^4$, with the bare mass spanning $-1.4 \leq am_0^{\mathrm{as}} \leq 0.0$ and β ranging from 5.6 to 7.0. For small β and large negative am_0^{as}, a sharp discontinuity in $\langle P \rangle$ was observed, signalling a first-order bulk phase transition. In other regions of parameter space, $\langle P \rangle$ varied smoothly, consistent with a crossover.

To confirm these findings, simulations with thermalised (hot) and cold starts were compared. Figure 4.13 demonstrates the dependence of $\langle P \rangle$ on am_0^{as} at fixed β, highlighting the hysteresis for $\beta < 6.4$. This behaviour provides strong evidence of a first-order phase transition at a critical mass $am_0^{\mathrm{as}\,*}$.

The plaquette susceptibility, χ_P, defined as

$$\chi_P \equiv \frac{\tilde{V}}{a^4} \left(\langle P^2 \rangle - \langle P \rangle^2 \right), \tag{4.3.1}$$

offers further insights. Figure 4.14 shows χ_P for two lattice volumes, $\tilde{V} = (8a)^4$ and $\tilde{V} = (16a)^4$, at $\beta = 6.2$ (where a first-order transition occurs) and $\beta = 6.5$ (where a smooth crossover is observed). At $\beta = 6.2$, the susceptibility peak height scales with the four-volume, and the

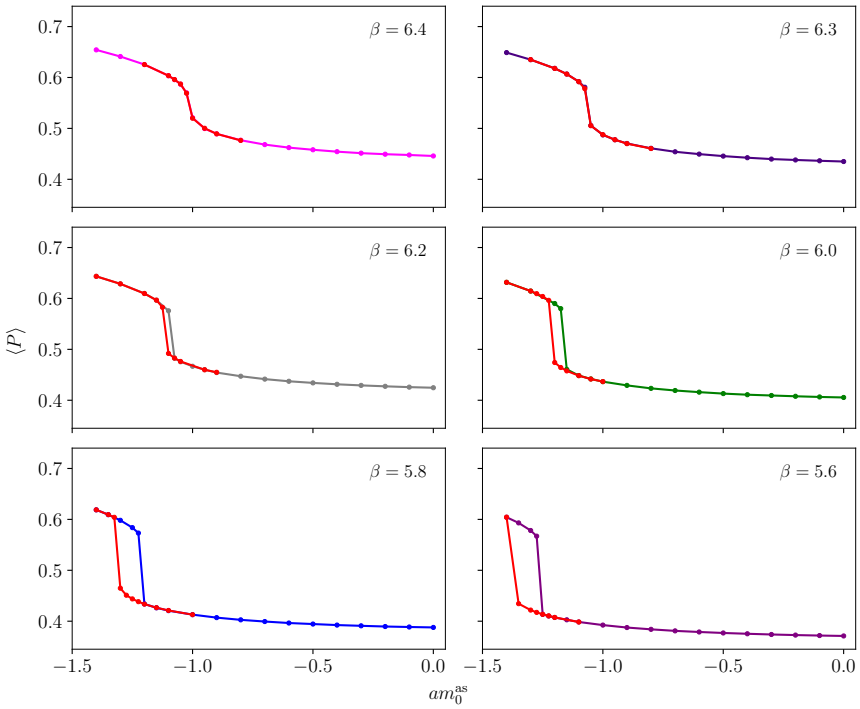

Figure 4.13. Hysteresis between hot (red) and cold (other colours) starts for $N_{as} = 4$ fermions in the antisymmetric representation of the $Sp(4)$ gauge theory. Simulations were performed at lattice couplings $\beta = 6.4, 6.3, 6.2, 6.0, 5.8, 5.6$, displayed left to right, top to bottom, on lattices with volume $\tilde{V} = (8a)^4$. The bare mass was varied over the range $-1.4 \leq am_0^{as} \leq 0.0$.

peak position shifts with volume, consistent with a first-order transition. In contrast, χ_P exhibits no significant scaling at $\beta = 6.5$.

The parameter scan was extended to other values of N_{as}, using the RHMC algorithm for odd N_{as} and HMC for even N_{as}. This allows us to study the variation of β_*, the coupling defining the bulk phase boundary, with N_{as}. Figure 4.15 summarises the results, showing $\langle P \rangle$ as a function of the bare parameters for various N_{as}. For the pure gauge case, our results are consistent with those in Ref. [253], with $\beta_* \simeq 7.2$. For a larger number of fermion species than the case study $N_{as} > 4$, the upper bound of the bulk phase, β, decreases progressively. Specifically, for $N_{as} = 5$, we find $\beta_* \simeq 6.3$. For $N_{as} = 6$, the upper bound is $\beta_* \simeq 6.2$. For $N_{as} = 7$, it is $\beta_* \simeq 6.1$, and for $N_{as} = 8$, we obtain $\beta_* \simeq 6.1$. For a lower number of fermions, $N_{as} < 4$, for $N_{as} = 1$ the upper bound is $\beta_* \simeq 6.7$. For $N_{as} = 2$ the upper bound is $\beta_* \simeq 6.7$, and for $N_{as} = 3$ it is $\beta_* \simeq 6.5$, in agreement with the values found in Ref. [9].

In conclusion, we can assert that increasing the fermion content lowers β_* and raises the critical mass $am_0^{(as)*}$, illustrating the impact of N_{as} on the phase structure.

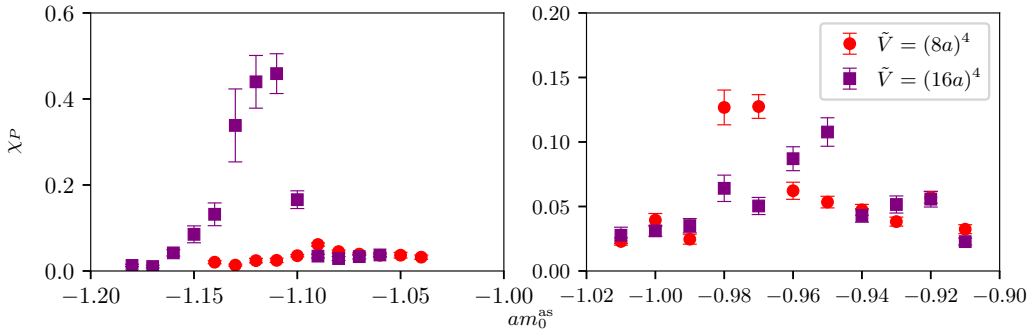

Figure 4.14. Plaquette susceptibility, χ_P, measured in the $Sp(4)$ gauge theory with $N_{\rm as} = 4$ fermions in the antisymmetric representation, evaluated on lattices of size $\tilde{V} = (8a)^4$ and $\tilde{V} = (16a)^4$. Results are presented for two values of the lattice coupling: $\beta = 6.2$ (left panel) and $\beta = 6.5$ (right panel). The corresponding bare mass ranges are $-1.18 \leq am_0^{\rm as} \leq -1.04$ for $\beta = 6.2$, and $-1.01 \leq am_0^{\rm as} \leq -0.91$ for $\beta = 6.5$. The scenario displayed in the left plot is expected for a first-order phase transition, the right one for a cross-over.

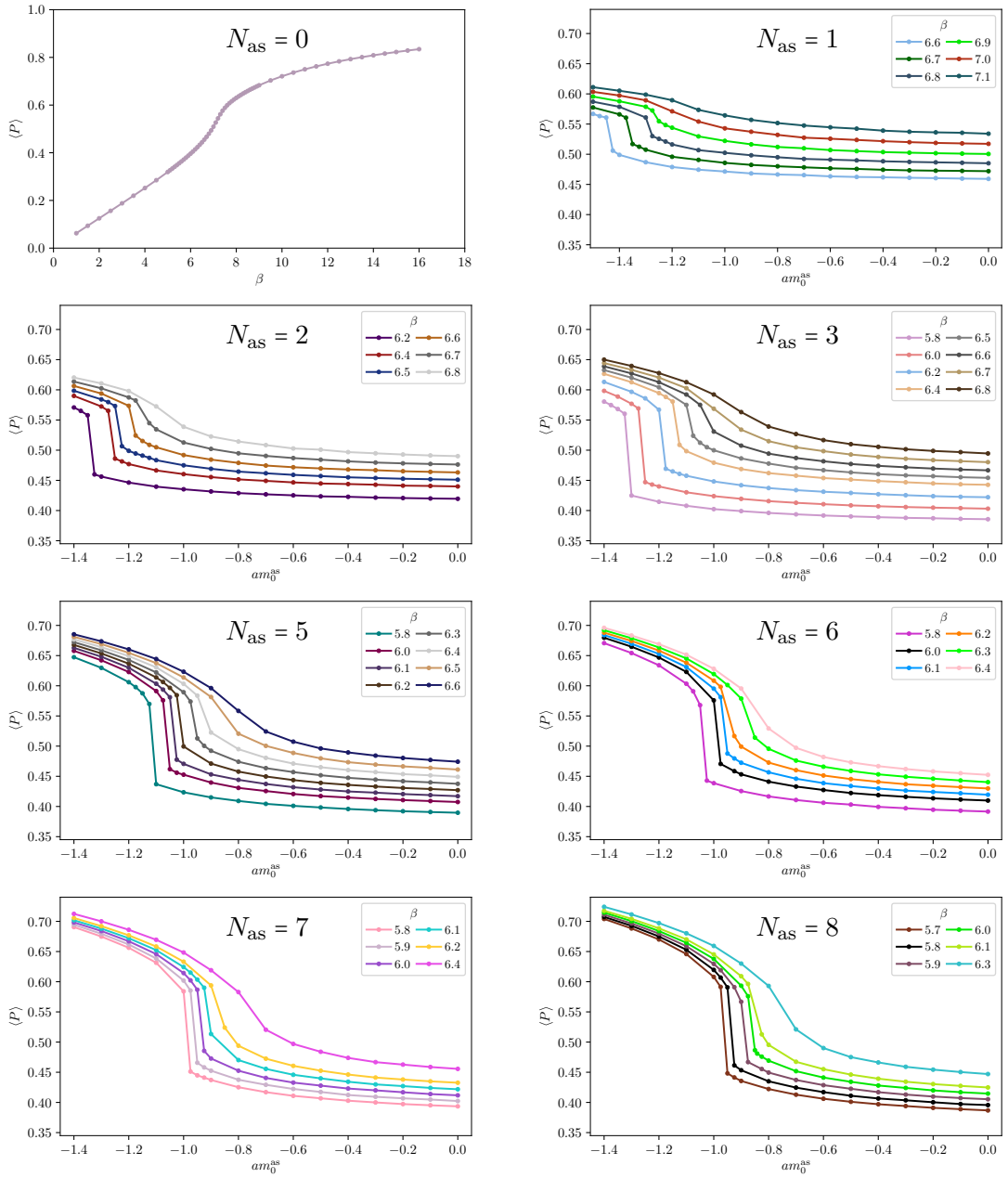

Figure 4.15. Parameter scan of the $Sp(4)$ theory with varying numbers of antisymmetric fermions, $N_{\text{as}} = 0, 1, 2, 3, 5, 6, 7, 8$, shown in panels arranged left to right and top to bottom. All ensembles were generated from a cold start, using HMC/RHMC algorithms for fermions. For $N_{\text{as}} > 0$, the average plaquette $\langle P \rangle$ is plotted as a function of the bare mass over selected values of the gauge coupling β. For the pure gauge case ($N_{\text{as}} = 0$), only β varies. Simulations are performed on lattices with volume $\tilde{V} = (8a)^4$. The bare mass ranges are $-1.4 \leq am_0^{\text{as}} \leq 0.0$ for $N_{\text{as}} \geq 2$, and $-1.5 \leq am_0^{\text{as}} \leq 0.0$ for $N_{\text{as}} = 1$. The gauge couplings explored are: for pure gauge, $1.0 \leq \beta \leq 16.0$; for $N_{\text{as}} = 1$, $\beta = 7.1, 7.0, 6.9, 6.8, 6.7, 6.6$; for $N_{\text{as}} = 2$, $\beta = 6.8, 6.7, 6.6, 6.5, 6.4, 6.2$; for $N_{\text{as}} = 3$, $\beta = 6.8, 6.7, 6.6, 6.5, 6.4, 6.2, 6.0, 5.8$; for $N_{\text{as}} = 5$, $\beta = 6.6, 6.5, 6.4, 6.3, 6.2, 6.1, 6.0, 5.8$; for $N_{\text{as}} = 6$, $\beta = 6.4, 6.3, 6.2, 6.1, 6.0, 5.8$; for $N_{\text{as}} = 7$, $\beta = 6.4, 6.2, 6.1, 6.0, 5.9, 5.8$; and for $N_{\text{as}} = 8$, $\beta = 6.3, 6.1, 6.0, 5.9, 5.8, 5.7$.

Chapter 5

Spectral densities

In Section 3.5, a novel method for extracting spectral densities from lattice correlation functions, called HLT, was described. A software (`LSDensities`) has been specifically designed for spectral density reconstruction, and made available for public use [164], to encourage the usage in broader contexts in lattice field theory research. The results shown in this chapter are the ones presented in Refs. [179, 257, 258].

We study the meson spectra in a $Sp(4)$ gauge theory with fermions transforming in mixed representations, fundamental and two-index antisymmetric, a candidate for ultraviolet completions of Composite Higgs Models [140]. This theory, featuring two Dirac fermions in the fundamental representation and three in the two-index antisymmetric representation, has gained attention [8–18, 20–26, 178, 206, 259, 260]. In this chapter, we show the results for smeared spectral densities for the two-point correlation functions defined in Table 3.1 and Eq. (3.4.3). This study focuses on flavour non-singlet states and chimera baryons.

The analysis reveals improved statistical accuracy, good control of systematic uncertainties. Decay constants are also extracted, complementing the spectral study. These advancements are validated against benchmark observables, laying a solid foundation for future applications, which might include both QCD and other strongly coupled gauge theories. This work demonstrates the potential of spectral densities as a versatile tool for studying both the Standard Model and BSM theories.

5.1 Lattice theory and lattice setup

In this chapter, we make use of the lattice setup described in Eq. (3.3.2). In particular, we consider a $Sp(4)$ gauge theory on the lattice with $N_{\mathrm{f}} = 2$ fermions transforming in the fundamental representation and $N_{\mathrm{as}} = 3$ fermions in the two-index antisymmetric representation.

Gauge configurations are generated using the `GRID` software suite [145–147], which includes functionality for $Sp(2N)$ gauge groups [178], described in the previous chapter. Dynamical fermions in the fundamental representation (f) are simulated using the HMC algorithm [199], while the antisymmetric representation (as) fermions are handled via the RHMC

Table 5.1. Parameters of the $Sp(4)$ ensembles used in the spectral density study. We denote the inverse gauge coupling by β, and the bare mass of the Wilson-Dirac fermions in the fundamental representation by am_0^{f}. The simulations are performed on lattice volumes $N_t N_s^3 a^4$. The antisymmetric bare mass is fixed to be $am_0^{\mathrm{as}} = -1.01$. The number of gauge configurations N_{conf} is also reported, together with the number of thermalisation steps, N_{therm}, and the number of complete sweeps between configurations, n_{skip}. For each ensemble, the average plaquette value, $\langle P \rangle$, the Wilson flow scale, w_0/a, and the average topological charge, $\bar{Q}$, are also reported.

Label	β	am_0^{f}	N_t	N_s	N_{therm}	n_{skip}	N_{conf}	$\langle P \rangle$	w_0/a	τ_{int}^Q	$\bar{Q}$
M1	6.5	-0.71	48	20	3006	14	479	0.585172(16)	2.5200(50)	6.9(2.4)	0.38(12)
M2	6.5	-0.71	64	20	1000	28	698	0.585172(12)	2.5300(40)	7.1(2.1)	0.58(14)
M3	6.5	-0.71	96	20	4000	26	436	0.585156(13)	2.5170(40)	6.4(3.3)	-0.60(19)
M4	6.5	-0.70	64	20	1000	20	709	0.584228(12)	2.3557(31)	10.6(4.8)	-0.31(19)
M5	6.5	-0.72	64	32	3020	20	295	0.5860810(93)	2.6927(31)	12.9(8.2)	0.80(33)

algorithm [261]. The determinant of the Dirac operator for the (as) fermions remains positive and real, ensuring the absence of sign problems [16, 262]. Algorithm tuning achieves acceptance rates of 70%–80%, typically using 27–36 integration steps per unit of Monte-Carlo time. Additionally, resymplecticisation and even-odd preconditioning are applied after each gauge update, as detailed in Ref. [16].

The simulations are performed on hypercubic lattices with spatial extent N_s and temporal extent N_t, yielding a total four-dimensional volume of $V_4 = L^3 \times T$, where $L = N_s a$ and $T = N_t a$. Boundary conditions are periodic for the gauge fields, while the fermion fields employ periodic spatial and anti-periodic temporal boundary conditions.

Three primary parameters define the lattice action: the inverse gauge coupling $\beta = 8/g^2$ and the bare fermion masses, m_0^{f} and m_0^{as}. To avoid the unphysical bulk phase at strong coupling ($\beta \lesssim 6.3$), we fix $\beta = 6.5$ [16]. For the ensembles used in this work, the bare mass of the (as) fermions is set to $am_0^{\mathrm{as}} = -1.01$, while am_0^{f} is varied across a narrow range, as outlined in Table 5.1.

The average plaquette, $\langle P \rangle$, is computed for each ensemble as in Eq. (3.4.35), and serves as an input in determining the tadpole-improved coupling, $\tilde{g}^2 = g^2/\langle P \rangle$ [214, 263], defined in Eq. (3.4.33).

The measurements of the two-point correlation functions have been supported by APE and Wuppertal smearing. More details about the smearing procedures are provided in Appendix C and the smearing parameters choice is consistent with the one in Ref. [179]: $\alpha_{\mathrm{APE}} = 0.4$, $N_{\mathrm{APE}} = 50$ for APE smearing, and $\varepsilon_{\mathrm{f}} = 0.20$, $\varepsilon_{\mathrm{as}} = 0.12$ for Wuppertal smearing.

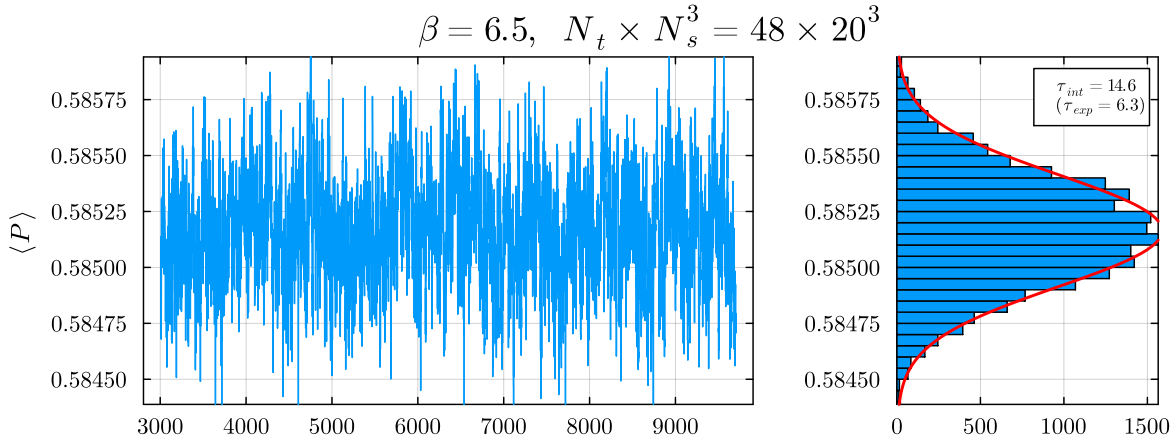

Figure 5.1. Monte-Carlo trajectory (left) and histogram (right) of the average plaquette, $\langle P \rangle$, for ensemble M1 (see Tab. 5.1). Other ensembles exhibit similar behaviour. The red line represents a Gaussian fit to the histogram.

5.1.1 Characterisation of the ensembles

As described in Chapter 4, the Wilson flow [241] plays a central role in two main tasks. The first is the determination of the physical scale for our lattice ensembles [264], and the second is the extraction of topological properties through UV noise suppression. We follow the conventions established in Ref. [18].

We define the quantity $\mathcal{W}(t)$, which evolves with the flow time t, as outlined in Chapter 4. The gradient flow scale, w_0, is introduced via the condition $\mathcal{W}(t)\big|_{t=w_0^2} = \mathcal{W}_0 = c_w C_\mathrm{f}$ (where C_f is the eigenvalue of the quadratic Casimir operator with fundamental fermions), with the choice of $c_w = 0.225$[1]. Dimensionful quantities in this work are normalised to w_0, indicated with a hat notation, such as $\hat{m} = (ma)(w_0/a)$. The extracted values of w_0/a, computed using the clover discretisation for $G_{\mu\nu}$ in Eq. (4.1.11), are provided in Tab. 5.1.
The topological charge, Q, on the lattice is computed using Eq. (4.1.14), with the gradient flow applied to mitigate UV fluctuations. Across all ensembles, no signs of topological freezing are observed. The Monte-Carlo algorithm successfully samples configurations with a broad range of Q values. To confirm this, we analyse the autocorrelation of Q and the average plaquette, $\langle P \rangle$, as functions of Monte-Carlo time.

The gradient flow scale, topological charge, and hadronic correlators are measured using the `HiRep` code [200, 266], extended to support symplectic gauge groups [267]. Configuration files generated via the `GRID` code are translated into the required format using the Gauge Link Utility (`GLU`) library [268].

[1] As mentioned in Ref. [265], the choice of $\mathcal{W}_0 = 0.225 \cdot C_\mathrm{f}$ is determined by initially setting $\mathcal{W}_0 = 0.3$ for the $SU(3)$ Yang-Mills theory and subsequently employing large-N scaling assumptions of the relevant observables to compare with $Sp(4)$.

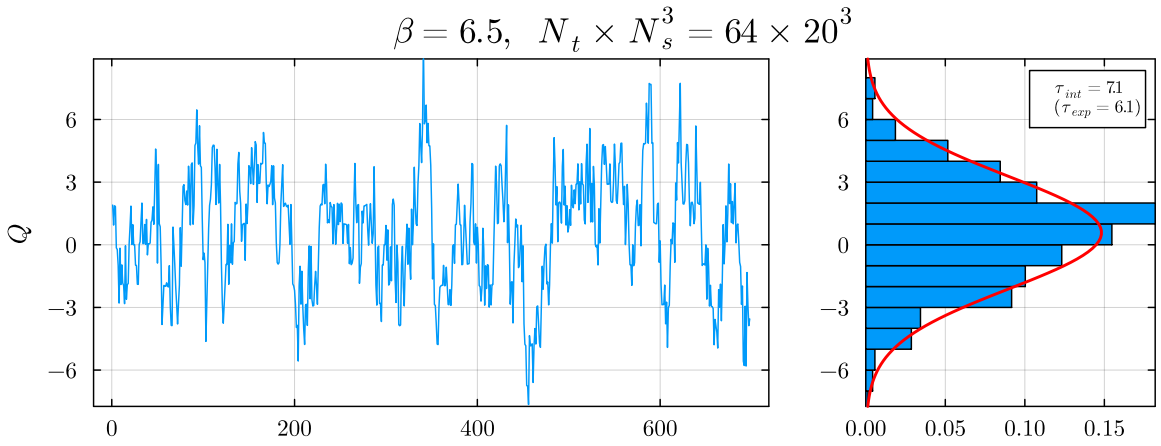

Figure 5.2. Monte-Carlo trajectory (left) and histogram (right) of the topological charge, Q, for ensemble M2. A Gaussian fit is overlaid in red. Modest residual autocorrelations are observed, but the results remain consistent across all ensembles.

To quantify autocorrelations, we analyse the Monte-Carlo time series for an observable X, where $\tau = 1, \ldots, N$ indexes the trajectory, X_i are individual measurements, and $\bar{X}$ is the mean value. The integrated autocorrelation time, τ_{int}^{X}, is computed following the Madras-Sokal definition from Chapter 4, as detailed in Eq. (4.1.5).

In Fig. 5.1, we show a representative trajectory of the average plaquette in Monte-Carlo time. Across our ensembles, we observe that the exponential autocorrelation time, $\tau_{\text{exp}}^{\langle P \rangle}$ (Eq. (4.1.7)), is consistently shorter than the integrated Madras-Sokal autocorrelation time, $\tau_{\text{int}}^{\langle P \rangle}$. To mitigate autocorrelations, we retain one gauge configuration every n_{skip} Monte-Carlo time units, choosing $n_{\text{skip}} \gtrsim \tau_{\text{int}}^{\langle P \rangle}$, where $\tau_{\text{int}}^{\langle P \rangle}$ denotes the integrated autocorrelation time of the average plaquette. Observables are measured on these configurations. This yields N_{conf} total measurements. The values of N_{conf} for each ensemble are listed in Tab. 5.1.

We also compute the topological charge Q on the same N_{conf} configurations used throughout this work. As with the plaquette, we examine the Monte-Carlo history, determine autocorrelation times, and present the distribution of Q in a histogram. An example is shown in Fig. 5.2. The integrated autocorrelation time τ_{int}^{Q} and the ensemble average $\bar{Q}$ are reported in Tab. 5.1. The distributions are qualitatively Gaussian, although $\tau_{\text{int}}^{Q} > 1$ and a nonzero $\bar{Q}$ are observed in all cases. We conclude that the configurations used in this study exhibit a moderate level of residual autocorrelation in the topological charge.[2]

[2] In pure gauge theory, even ensembles with complete topological freezing show no significant effect on the glueball spectrum [36].

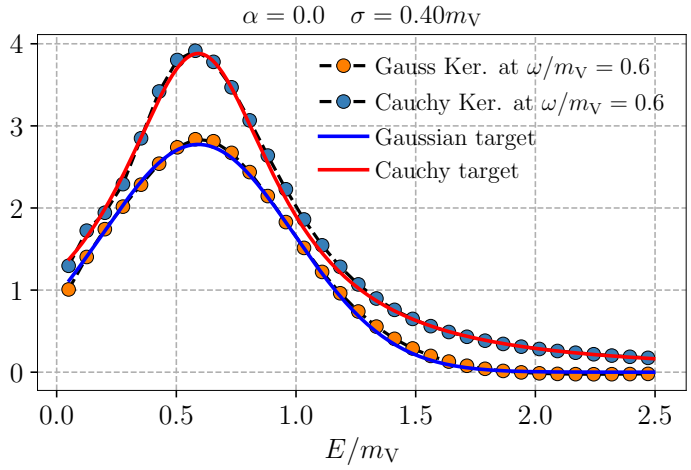

Figure 5.3. Reconstruction of the smearing kernel for the vector meson (V) formed by fermions in the fundamental representation of $Sp(4)$. Data are taken from ensemble M2, with the vector meson mass m_V determined using the GEVP method. The smearing parameters are set to $\tau_{max} = N_t/2$, $\alpha = 0$, and $\sigma = 0.40\, m_V$.

5.2 Spectral densities techniques

In this section, we report several methodological studies on real data (unless stated), and analysed by using the `LSDensities` code [164]. We show how results vary by changing the smearing kernel $\Delta_\sigma(E-\omega)$, the smearing radius σ, the effect of APE and Wuppertal smearings [209–213], and more.

5.2.1 Smearing kernel analysis

As introduced in Chapter 3, the HLT method supports the use of various smearing kernels, $\Delta_\sigma(E-\omega)$, to model the energy distribution. Two widely used forms are:

$$\Delta_\sigma^{(1)}(E-\omega) = \frac{1}{Z(\omega)} \exp\left(-\frac{(E-\omega)^2}{2\sigma^2}\right), \tag{5.2.1}$$

and

$$\Delta_\sigma^{(2)}(E-\omega) = \frac{\sigma}{(E-\omega)^2+\sigma^2}, \tag{5.2.2}$$

where $Z(\omega)$ ensures proper normalisation for the Gaussian kernel and the two kernels ensure the properties described around Eq. (3.5.6).

A direct comparison between the target kernels, $\Delta_\sigma(E-\omega)$, and their reconstructed versions, $\bar{\Delta}_\sigma(E-\omega)$, is presented in Fig. 5.3, showing close agreement (Eq. (3.5.10)) when the parameters λ and σ are carefully tuned. To limit the impact of systematics, we impose

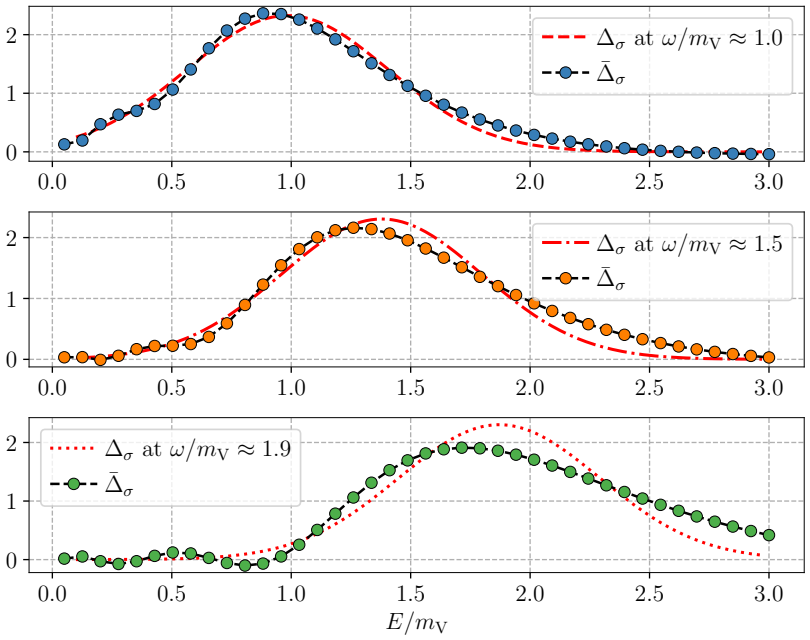

Figure 5.4. Energy dependence of reconstructed kernels for $\sigma = 0.28 m_V$ (ensemble M2). Target (curves) and reconstructed (points) kernels are shown for $\omega/m_V \approx 1.0, 1.5, 1.9$ (top to bottom).

the condition $A[\bar{g}]/A_0 < 0.1$, effectively bounding potential biases in the analysis. The values of other relevant parameters are described in the figure caption. This approach reflects the general trends observed across the datasets used in this study.

As shown in Fig. 5.4, reconstruction accuracy deteriorates progressively at higher energies. This outcome is anticipated due to the inherent limitations of finite lattice volume and statistical noise in the correlation functions. For a successful reconstruction, it is crucial to minimise the deviation between the target kernel, $\Delta_\sigma(E-\omega)$, and the reconstructed kernel, $\bar{\Delta}_\sigma(E-\omega)$, over the entire energy spectrum.

5.2.2 Choice of smearing radius

For convenience, we define the smearing radius, σ, in terms of the ground state mass, m_0, of the mesonic channel under consideration. The value of m_0 can be determined independently, for instance, using the GEVP method. The optimal selection of σ is influenced by the quality of the data, particularly the available statistics for the input two-point correlation functions, which set a practical lower limit for σ. In our ensembles, σ typically falls within the range $0.18 m_0 \leq \sigma \leq 0.35 m_0$, where smaller values of σ are advantageous for resolving closely spaced energy levels in dense spectra.

Figure 5.5 shows the impact of varying σ on the reconstruction of synthetic two-point

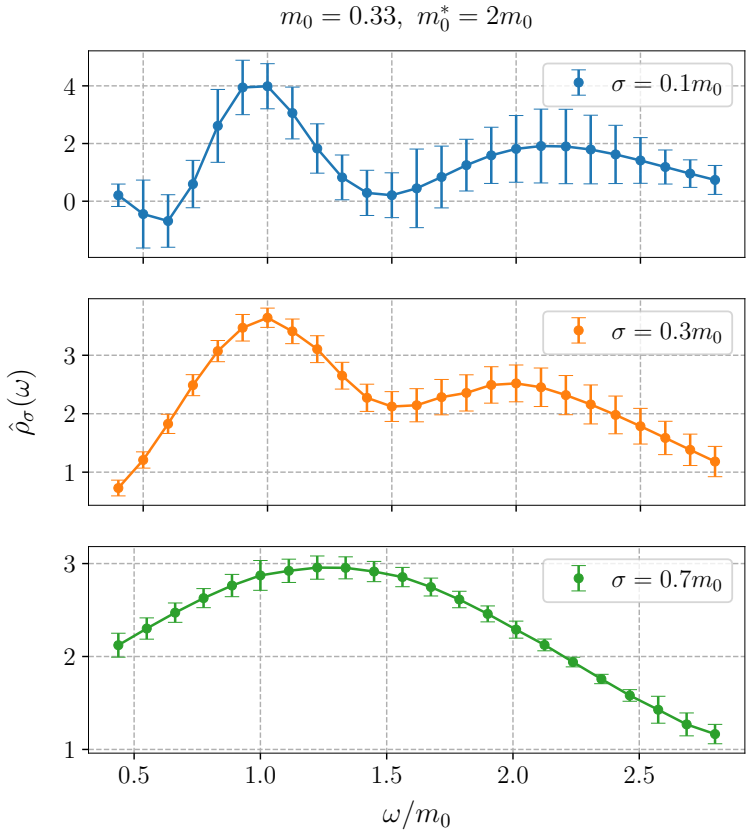

Figure 5.5. Reconstruction of spectral densities for synthetic data with $m_0^* = 2m_0$. Panels correspond to $\sigma = 0.1m_0$, $0.3m_0$, and $0.7m_0$ (top to bottom).

correlation functions, where we assume an exponential functional form $\sim \exp(-m_0 t)$ with a ground state $am_0 = 0.33$, and an excited state contribution $\sim \exp(-m_0^* t)$, where $m_0^* = 2m_0$. The reconstructed spectral density, $\hat{\rho}_\sigma(E)$, is shown for three representative smearing radii: $\sigma = 0.1m_0$, $0.3m_0$, and $0.7m_0$. For the smallest radius, $\sigma = 0.1m_0$, the reconstruction deteriorates significantly for energies $E/m_0 \gtrsim 1.0$, leading to the loss of excited states amidst systematic errors. Conversely, a large radius, $\sigma = 0.7m_0$, causes the two peaks to merge entirely, on one hand, keeping statistical and systematic errors moderate, but on the other hand, effectively hindering the resolution of different energy peaks. An intermediate choice of $\sigma = 0.3m_0$ strikes a balance: the reconstruction successfully distinguishes the two peaks while maintaining control over both statistical and systematic uncertainties.

This approach ensures accurate reconstructions while maintaining control over both statistical and systematic uncertainties.

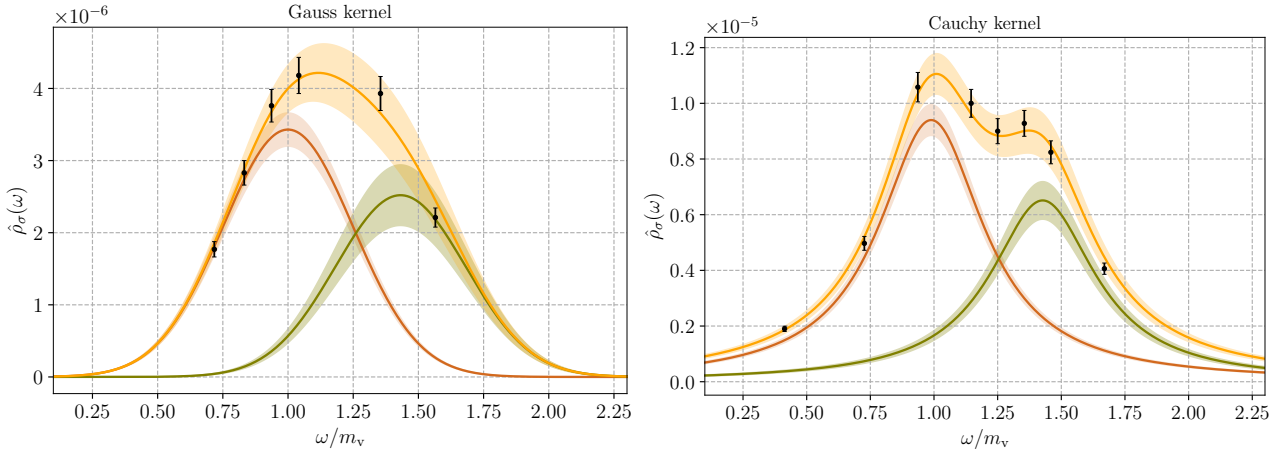

Figure 5.6. Spectral density reconstruction in the v channel from ensemble M2 ($N_t = 64$). Black points denote the reconstructed spectral density $\hat{\rho}_\sigma(\omega)$, while the yellow curve represents the fit function $f_\sigma^{(2)}(E)$ as in Eq. (3.5.19). The red and green lines correspond to the ground and first excited states, $\Delta_\sigma(E - E_0)$ and $\Delta_\sigma(E - E_1)$, respectively. Gaussian kernels are used for the left panel, and Cauchy kernels for the right, with smearing radius $\sigma = 0.25\, m_\mathrm{v}$ and Wuppertal smearing ($N_\mathrm{source} = 0$, $N_\mathrm{sink} = 40$). The left panel fit yields $\chi^2/\mathrm{d.o.f.} = 1.6$ with $aE_0 = 0.6511(32)$, $aE_1 = 0.932(11)$, and amplitudes $\mathcal{A}_1 = 3.73(23) \times 10^{-6}$, $\mathcal{A}_2 = 2.52(52) \times 10^{-6}$. The right panel fit yields $\chi^2/\mathrm{d.o.f.} = 1.1$ with $aE_0 = 0.6442(37)$, $aE_1 = 0.929(12)$, and amplitudes $\mathcal{A}_1 = 2.33(12) \times 10^{-6}$, $\mathcal{A}_2 = 1.63(16) \times 10^{-6}$. The mass m_v is obtained from GEVP analysis.

5.2.3 Fitting procedure and cross-checks: spectra

The spectral densities corresponding to two-point correlation functions can be fitted by minimising the correlated χ^2 functional as described in Eq. (3.4.11), for both smearing kernels in Eq. (5.2.1) and (5.2.2). As mentioned in Sec. 3.5, E_n represents the eigenvalues of the finite-volume Hamiltonian. Moreover, the number of peaks fitted k is determined a posteriori.

Figure 5.6 illustrates the comparison of spectral reconstructions for the v channel (Table 3.1) using both Gaussian and Cauchy kernels. Despite the difference in the spectral shapes, the peak positions agree within statistical uncertainties. Employing both Gaussian and Cauchy smearing kernels provides a valuable consistency check associated with this choice in determining the n^th energy level:

$$\sigma_\mathrm{sys}(aE_n) = |aE_{n,\,\mathrm{Gauss}} - aE_{n,\,\mathrm{Cauchy}}|. \tag{5.2.3}$$

whereas for chimera baryons overlap factors:

$$\sigma_\mathrm{sys}(K_n) = \left|K_{n,\mathrm{Gauss}} - K_{n,\mathrm{Cauchy}}\right| . \tag{5.2.4}$$

To check for robustness against the contamination of further excited states, fits are also repeated with $k+1$ peaks. Fit results may be affected by contributions from additional states not included in the model. To assess the stability of the extracted parameters for the first k

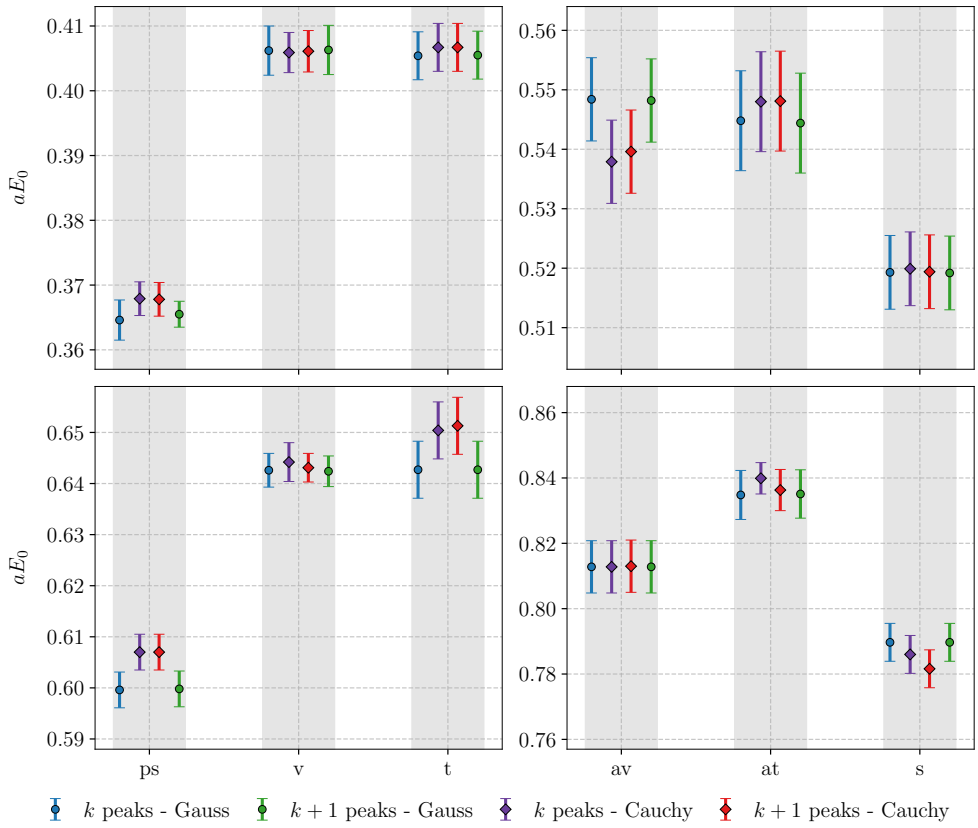

Figure 5.7. Evaluation of the ground-state energy level for ensemble M2. Results for each channel are shown by comparing fits with k and $k+1$ peaks, using both Gaussian and Cauchy kernels. Additional details are given in Tab. F.4. The offset between data points for the same mesonic channel is applied for clarity.

states, we repeat the fit with an extended model that includes $k+1$ peaks (both for Gaussian and Cauchy cases) in Eq. (3.5.18). This procedure allows us to test for contamination from excited states. If the parameters associated with the target states remain stable and the chi-square does not deteriorate significantly, we regard the original estimate as reliable. An analysis of the possible effects arising from kernel choice and excited-state contamination is presented in Figs. 5.7 and 5.8. It should be noted that due to the limitations of smearing and its deterioration at high energies, only a limited number of states can be reliably accessed.

5.2.4 Extraction of matrix elements and overlap factors from spectral density fits

As illustrated in Eq. (3.5.19) and the subsequent discussion, fitting spectral densities enables the determination of both the energy levels, aE_n, and the matrix elements (or overlap factors) of the interpolating operators involved in the spectral reconstruction. The amplitudes of the fitted functions $f^{(k)}(E)$ encode the matrix elements $\langle 0|\mathcal{O}(0)|e_n\rangle$ and overlap factors K_n. To

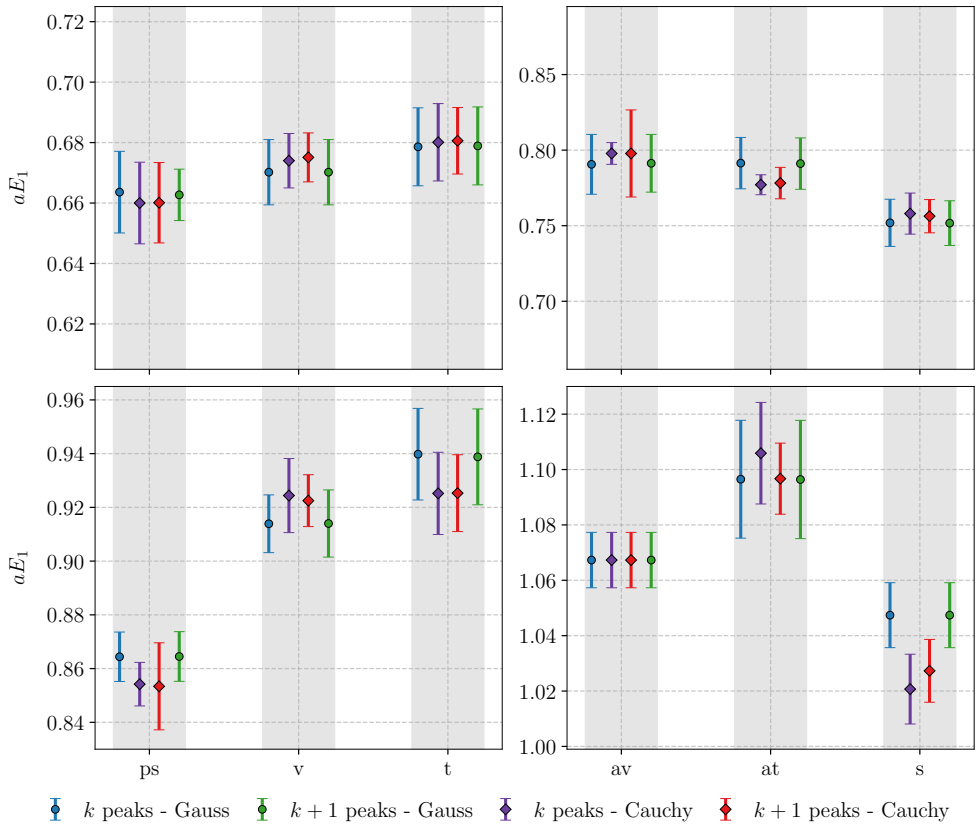

Figure 5.8. Evaluation of the first excited energy level for ensemble M2. For each channel, we compare results obtained by fitting with k and $k+1$ peaks, using Gaussian and Cauchy kernels. Further details are available in Tab. F.5. The offset between data points in the same mesonic channel is applied for visual clarity.

extract this information, we use the technique described in Sec. 3.5, denoted by a simultaneous fitting procedure between two spectral densities deriving from the same hadronic channel with different levels of Wuppertal smearings.

An example of this fitting procedure is shown in Fig. 5.9, where the ground state peak is fitted for a meson operator. The matrix element, $\langle 0|\mathcal{O}(0)|e_0\rangle$, (or the overlap factor K_0 for chimera baryons) is extracted from the fit, as depicted in the right panel.

The principles of spectroscopy apply here as well: no dependence on the choice of smearing kernel Δ_σ is expected. To cross-check this fact, we compare results obtained using Gaussian and Cauchy kernels. This effect is then estimated for mesons as:

$$\sigma_{\text{sys}}(\langle 0|\mathcal{O}(0)|e_n\rangle) = |\langle 0|\mathcal{O}(0)|e_n\rangle_{\text{Gauss}} - \langle 0|\mathcal{O}(0)|e_n\rangle_{\text{Cauchy}}|, \tag{5.2.5}$$

and for chimera baryons as:

$$\sigma_{\text{sys}}(K_n) = \left|K_{n,\text{Gauss}} - K_{n,\text{Cauchy}}\right| . \tag{5.2.6}$$

As for the spectrum case in Sec. 5.2.3, these effects are found to be negligible when compared to the statistical errors associated with the matrix elements and overlap factors.

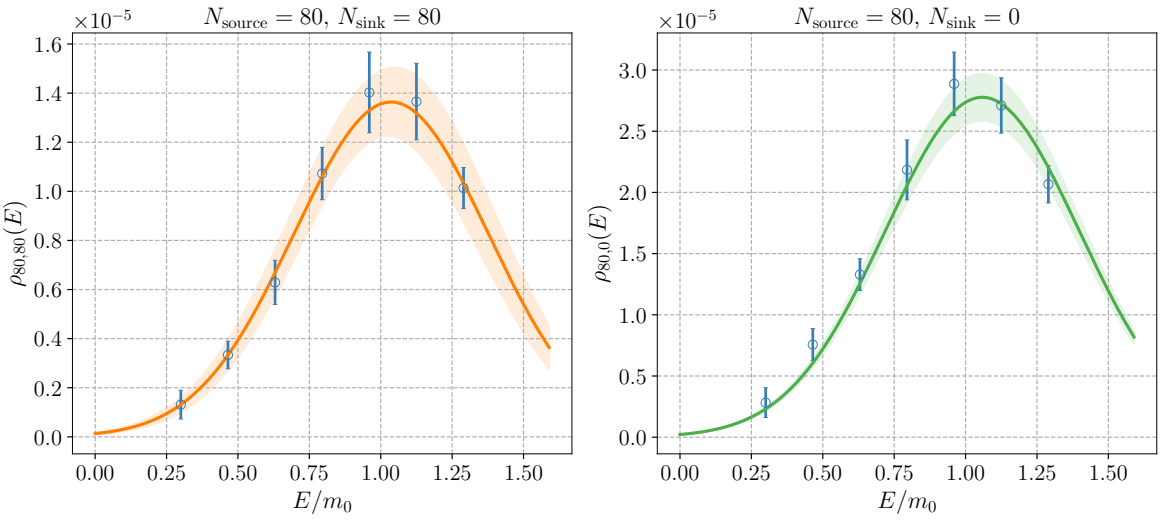

Figure 5.9. Simultaneous fitting procedure for the ground state peak of a vector meson operator in the fundamental representation (ensemble M1). The Gaussian kernel with $\sigma/m_0 = 0.33$ is used. The extracted matrix element $\langle 0|\mathcal{O}(0)|e_0\rangle$ is shown in the right panel.

5.2.5 The effect of APE and Wuppertal smearing on spectral densities

Considering Eq. (3.5.19), one can express the spectral densities in terms of the smearing kernels in correspondence with each eigenvalue of the spectrum for a determined set of quantum numbers.

Disentangling the spectrum in lattice gauge theory can be challenging due to the closeness of energy levels and the potential dominance of certain states, leading to discrepancies in matrix elements and overlap factors for different states. This difficulty also affects two-point correlation functions, distorting their large-t behaviour and compromising multi-exponential fits to effective mass plateaus. Noticing how Eq. (3.4.25) is written, this issue is mitigated by combining APE and Wuppertal smearing, which enhances the overlap of relevant states with the interpolating operator, reducing contributions from undesired states.

The effect of smearing optimisation is illustrated in Fig. 5.10, where the left panel shows the effective mass and the right panel displays the reconstructed spectral density for the optimal smearing parameters. As shown in Tab. 5.2, cases A to F represent reasonable smearing choices that yield comparable amplitudes for the ground and first excited states, resulting in accurate spectroscopy. Over-smearing (case G) or under-smearing (case H) lead to inaccurate energy levels, due to larger amplitude discrepancies.

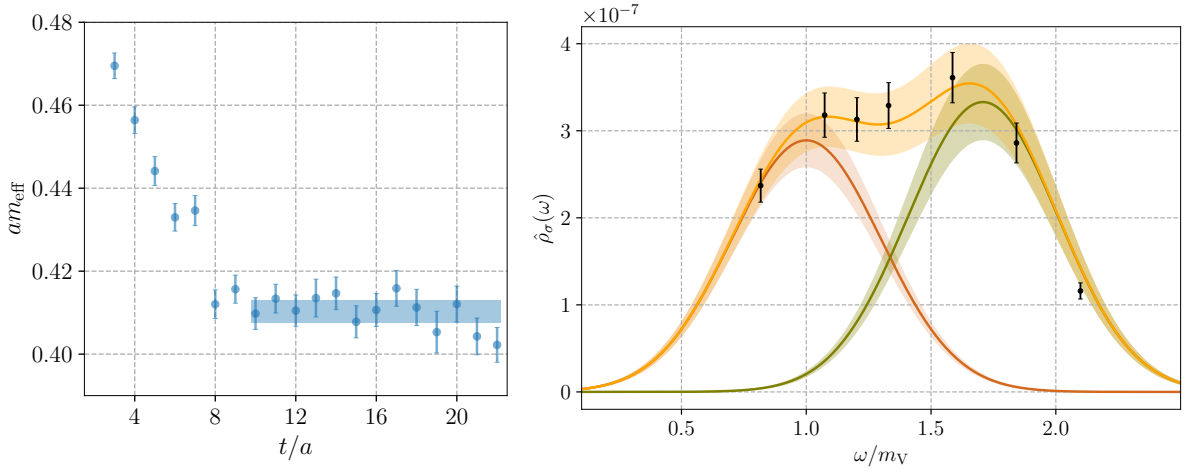

Figure 5.10. Illustration of a high-quality plateau and fit achieved with optimised APE and Wuppertal smearing. The vector channel correlator from ensemble M1 is obtained using APE smearing ($N_{\mathrm{APE}} = 50$, $\alpha_{\mathrm{APE}} = 0.4$) combined with Wuppertal smearing ($N_{\mathrm{source}} = 80$, $N_{\mathrm{sink}} = 40$, $\varepsilon_{\mathrm{f}} = 0.12$). Shown are the effective mass (left) and the spectral density reconstructed via a Gaussian kernel with $\sigma = 0.30\, m_{\mathrm{V}}$ (right). Fitted masses are $aE_0 = 0.4098(25)$ and $aE_1 = 0.700(26)$.

The results confirm that smearing increases the ground state overlap while suppressing excited state contributions, as expected from Eq. (3.5.19). In fact, smearing the operators enhances their projection onto the ground state and suppresses overlap with excited states. As a result, the ratio $\mathcal{A}_2/\mathcal{A}_1$ of Tab. 5.2 is reduced with increased smearing. Moreover, in line with Eq. (3.4.25), smearing leads to the emergence of longer and more stable effective-mass plateaux for the ground state.

Table 5.2. Effect of APE and Wuppertal smearing on spectroscopy results for ensemble M1 in the V channel. The table shows various smearing parameters and their impact on the relative amplitudes $\mathcal{A}_2/\mathcal{A}_1$ and energy levels aE_0 and aE_1.

Case	α_{APE}	ε_{f}	N_{source}	N_{sink}	$\mathcal{A}_2/\mathcal{A}_1$	aE_0	aE_1
A	0.4	0.12	80	20	1.32(19)	0.4144(50)	0.692(27)
B	0.4	0.12	80	40	1.15(11)	0.4139(49)	0.702(19)
C	0.4	0.12	80	80	0.75(15)	0.4131(52)	0.699(22)
D	0.4	0.12	40	80	1.24(18)	0.4132(43)	0.694(27)
E	0.4	0.12	20	80	1.80(28)	0.4148(51)	0.714(23)
F	0.4	0.24	90	30	1.01(20)	0.4148(52)	0.698(19)
G	0.4	0.4	170	170	0.63(11)	0.4113(82)	0.717(33)
H	0.4	0.05	20	20	2.28(27)	0.4136(74)	0.705(32)
I	0.0	0.12	80	40	1.27(11)	0.4154(73)	0.698(32)

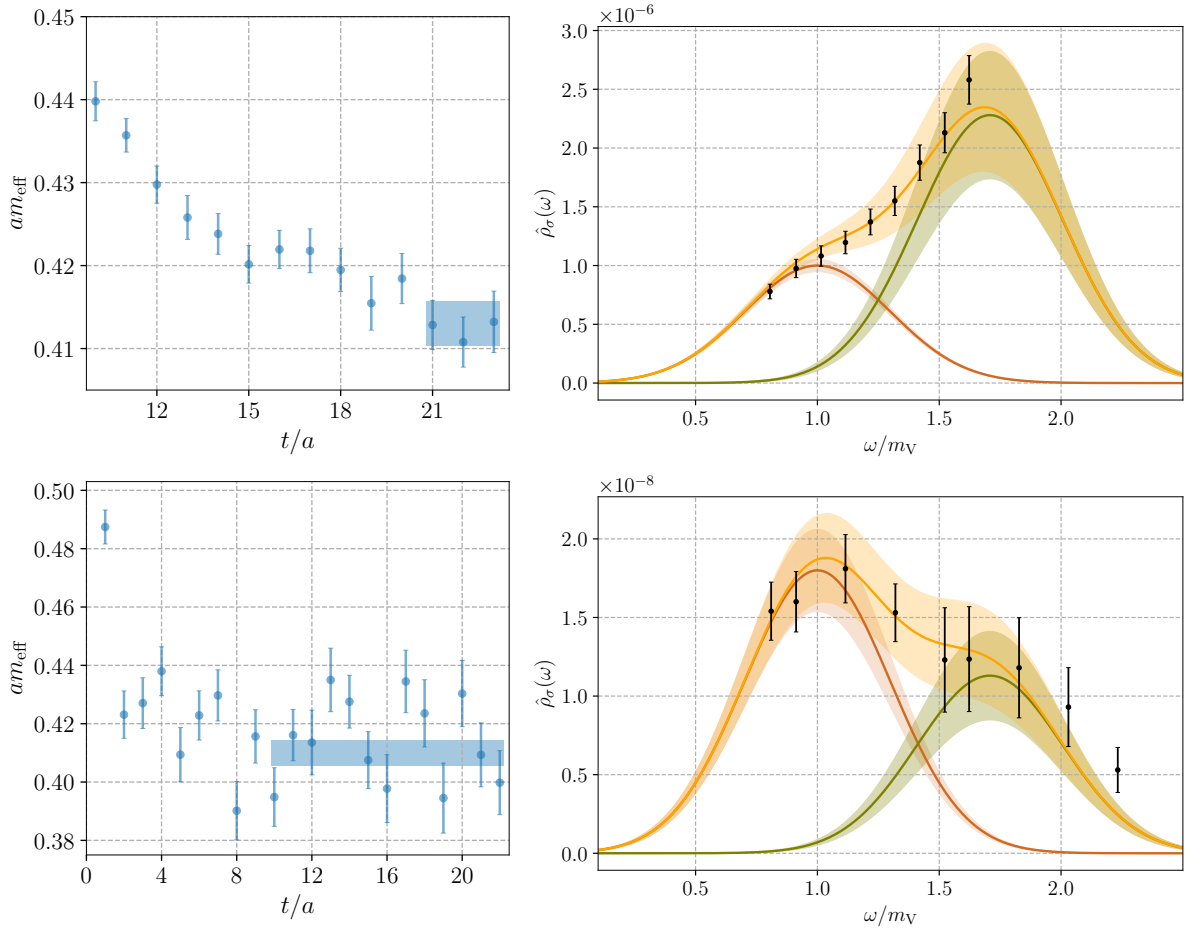

Figure 5.11. The V channel for ensemble M1. Top: effective mass and spectral density with APE smearing (N_{APE} = 50, α_{APE} = 0.4) and Wuppertal smearing (N_{source} = 20, N_{sink} = 20, ε_{f} = 0.05). Bottom: same with stronger Wuppertal smearing (N_{source} = 170, N_{sink} = 170, ε_{f} = 0.90). Fit results for top: $aE_0 = 0.4166(74)$, $aE_1 = 0.705(32)$. Bottom: $aE_0 = 0.4113(82)$, $aE_1 = 0.717(33)$.

We present in Fig. 5.11 two examples where suboptimal choices of smearing parameters lead to less accurate results, corresponding to cases G and H in Tab. 5.2. In the top panels, a minimal amount of Wuppertal smearing is applied to the two-point correlation functions, resulting in a very short or virtually absent effective mass plateau, severely limiting the resolution of the spectral density. On the other hand, excessive Wuppertal smearing, shown in the bottom panels of Fig. 5.11, also leads to undesirable outcomes: the effective mass plateau disappears entirely, and the plot becomes dominated by uncontrolled systematics, further degrading the quality of the spectral density reconstruction.

To highlight this issue more clearly, we show in Fig. 5.12 the scenario where no APE or Wuppertal smearing is applied. In this case, the effective mass plateau is short, leading to unreliable effective mass fits. This serves as a strong example of why point sources can be problematic for reliable reconstructions. In such cases, a larger smearing radius for the spectral density, σ, is necessary compared to the scenarios considered above. Furthermore,

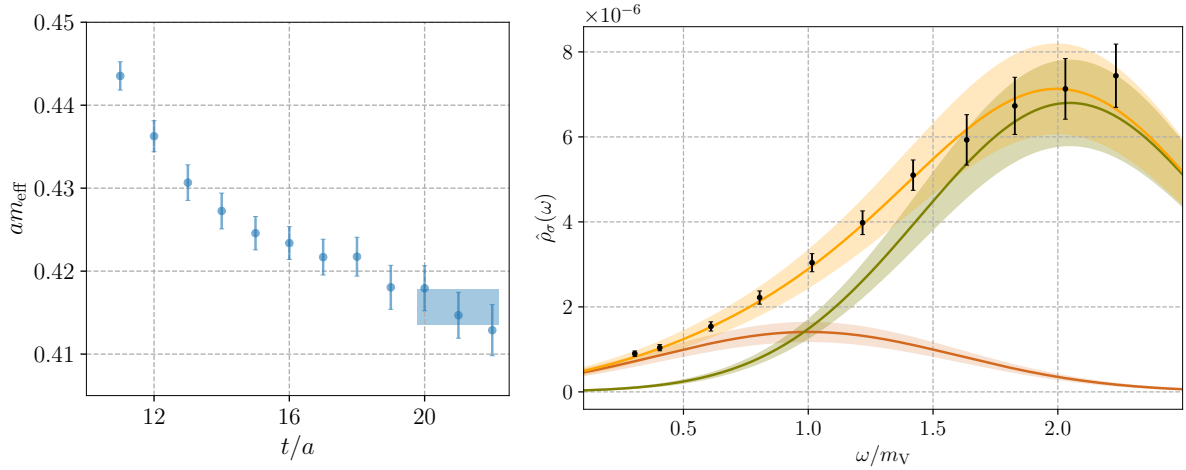

Figure 5.12. The vector channel in ensemble M1 yields masses from the GEVP analysis of $m_{\text{V}} = 0.4098(25)$ and $m^*_{\text{V}} = 0.700(26)$. Spectral density reconstruction without APE or Wuppertal smearing uses a smearing radius of $\sigma = 0.60\, m_{\text{V}}$. An example of optimal smearing (APE and Wuppertal) is shown in Fig. 5.10, while the case without APE smearing is illustrated in Fig. 5.13. Black points indicate the reconstructed spectral density $\hat{\rho}_\sigma(\omega)$; the yellow curve corresponds to the fit function $f^{(2)}_\sigma(E)$ from Eq. (3.5.19). The red and green curves represent the ground state $\Delta_\sigma(E - E_0)$ and first excited state $\Delta_\sigma(E - E_1)$, respectively. Fit results include amplitudes $\mathcal{A}_1 = 1.41(22) \times 10^{-6}$, $\mathcal{A}_2 = 6(1) \times 10^{-6}$, energy levels $aE_0 = 0.413(11)$ and $aE_1 = 0.839(77)$, with a reduced chi-square of $\chi^2/N_{\text{d.o.f.}} = 0.80$.

the difference in peak heights is considerable, all contributing to the degradation of the signal.

In Fig. 5.13, we revisit the same reconstruction shown in Fig. 5.10, but this time without applying APE smearing. By comparing the effective mass plateaux from the left panels of Figs. 5.10 and 5.13 (cases B and I), we observe how APE smearing influences both the effective mass plots and the spectroscopy. APE smearing works by averaging out ultraviolet fluctuations in the gauge links, and in its absence, the spectral density fits degrade at higher energy values, as shown in the right panels. Thus, applying APE smearing to the two-point correlation functions helps widen the energy window for spectral reconstruction.

5.2.6 Dependence on the time extent of spectral densities

The reconstructed smearing kernel, denoted as $\bar{\Delta}_\sigma(E, \omega)$, is defined by a finite summation over the temporal index $\tau \equiv t/a$, where the summand involves the function $b(a\tau, E)$, as outlined in Eq. (3.5.10). This sum is subject to precision limitations due to the finite lattice size, with the temporal index τ constrained by the condition $\tau_{\max} \leq N_t/2$, where N_t is the temporal extent of the lattice.

In the case of $\lambda = 0$, the sum converges to the true kernel in the infinite time extent limit, as discussed in Ref. [218]. For non-zero $\lambda > 0$, by increasing N_t, the reconstruction of

the kernel is expected to have the potential to improve as the set of basis functions expands, possibly allowing for smaller values of λ, and thus reducing the bias in the reconstructed spectrum.

To investigate this behaviour, we compare the spectral reconstruction on lattices with different temporal extents, N_t, while holding all other parameters constant. Specifically, we focus on ensembles M1, M2, and M3, with N_t values of 48, 64, and 96, respectively, and focus on the high-energy region of the spectrum.

The first comparison is presented in Fig. 5.15, where we show the reconstructed Gaussian kernel, $\bar{\Delta}_\sigma(E,\omega)$, at $\omega/m_{\mathrm{V}} = 1.8$ for all three ensembles. The maximum value of $\tau_{\max}$, corresponding to $\tau_{\max} = N_t/2$, is used in this reconstruction. For the lattice with the smallest time extent ($N_t = 48$), the reconstructed kernel deviates significantly from the target kernel, $\Delta_\sigma(E,\omega)$, leading to increased systematic uncertainties. This is in agreement with the observations made in Fig. 5.4. On the other hand, for the largest time extent ($N_t = 96$), the reconstructed kernel exhibits significantly smaller deviations from the exact one, reflecting a more accurate reconstruction.

The impact of increasing N_t is further demonstrated by the improved quality of spectral density fits, which can capture higher-energy measurements and a broader range of excited states. This improvement is exemplified in Fig. 5.15 for the PS meson channel across time

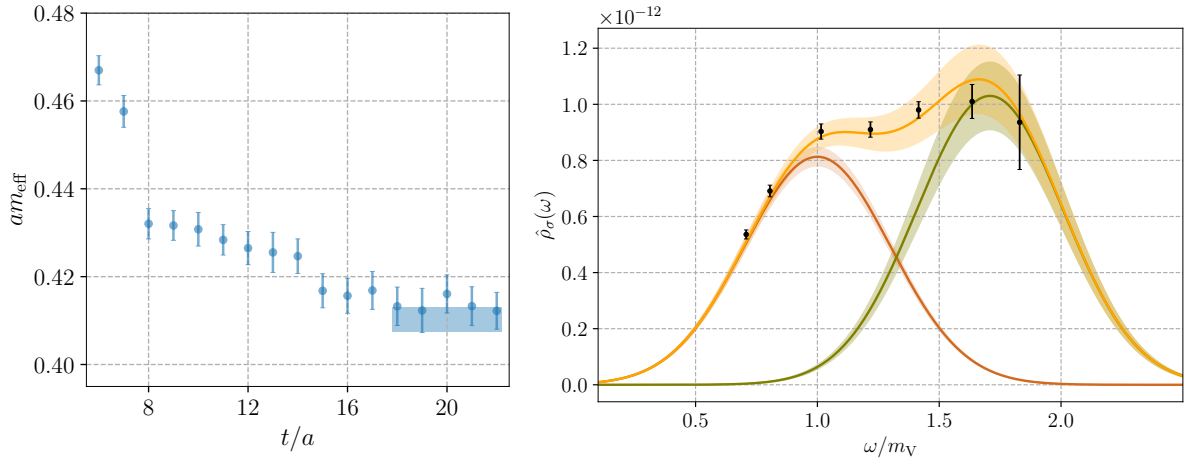

Figure 5.13. In the vector channel of ensemble M1, the GEVP analysis yields masses $m_{\mathrm{V}} = 0.4098(25)$ and $m^*_{\mathrm{V}} = 0.700(26)$. No APE smearing was applied; Wuppertal smearing used $N_{\mathrm{source}} = 80$ steps at the source and $N_{\mathrm{sink}} = 40$ steps at the sink, with a step size of $\varepsilon_{\mathrm{f}} = 0.12$. An example of the optimal combination of APE and Wuppertal smearing is presented in Fig. 5.10. Spectral density reconstruction was performed with a smearing radius $\sigma = 0.30\, m_{\mathrm{V}}$. The black points denote the reconstructed spectral density $\hat{\rho}_\sigma(\omega)$, the yellow curve represents the fitted function $f^{(2)}_\sigma(E)$ (Eq. (3.5.19)), while the red and green curves correspond to the ground state $\Delta_\sigma(E - E_0)$ and first excited state $\Delta_\sigma(E - E_1)$, respectively. The fit yields amplitudes $\mathcal{A}_1 = 8.13(32) \times 10^{-13}$, $\mathcal{A}_2 = 1.03(12) \times 10^{-12}$, energy levels $aE_0 = 0.4154(73)$ and $aE_1 = 0.698(32)$, with a reduced chi-square of $\chi^2/N_{\mathrm{d.o.f.}} = 1.3$.

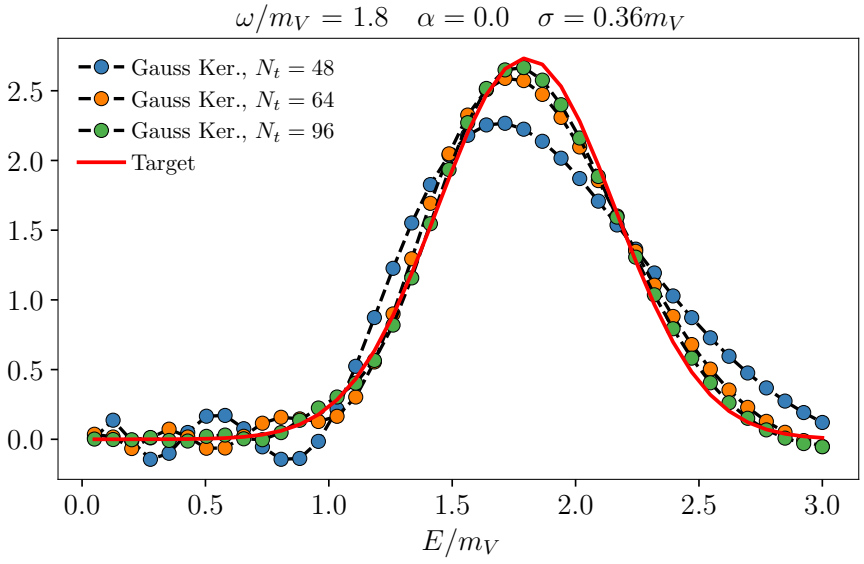

Figure 5.14. Reconstructed spectral densities with Gaussian kernels at $\omega/m_{\mathrm{V}} = 1.8$, shown for ensembles M1, M2, and M3, which have temporal extents $N_t = 48$, 64, and 96, respectively. The mass m_{V} corresponds to the vector channel ground state in ensemble M3, obtained via the GEVP analysis.

extents $N_t = 48$, 64, and 96. At higher energies, the reconstructed spectrum becomes more stable, and additional excited states can be identified. Notably, the positions of the first two peaks in the spectral function show agreement within statistical errors and exhibit negligible dependence on N_t. The energy levels from ensembles M1, M2, and M3 are presented in Fig. 5.16, in the form $[aE_n - \sigma_{aE_n}, aE_n + \sigma_{aE_n}]$, where σ_{aE_n} represents the uncertainty in the n^{th} energy level.

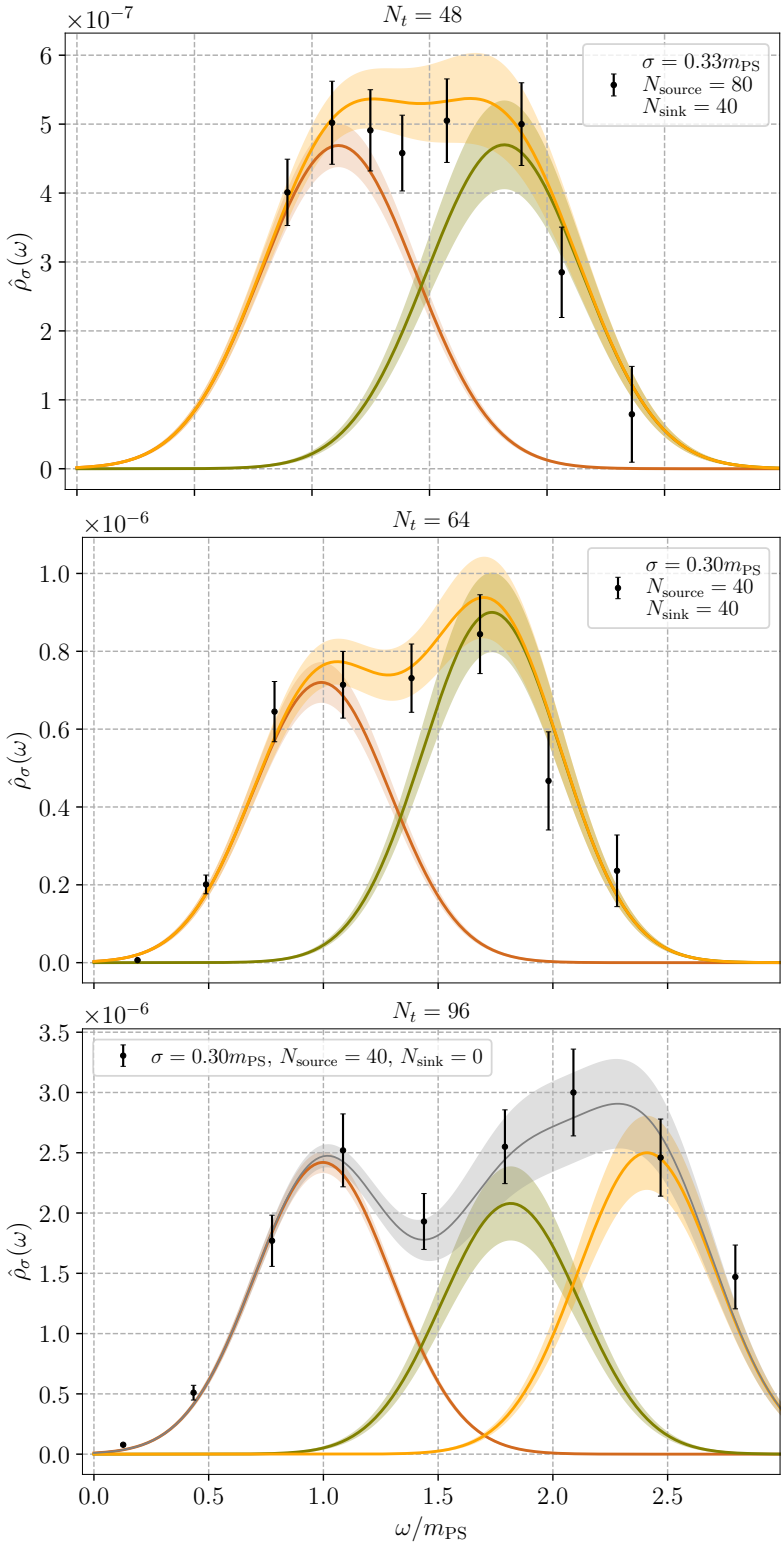

Figure 5.15. Spectral densities reconstructed in the pseudoscalar meson channel using Gaussian kernels. Correlation functions are obtained with APE smearing ($N_{\mathrm{APE}} = 50$, $\alpha_{\mathrm{APE}} = 0.4$), and the ground state mass m_{PS} is extracted via the GEVP at the largest temporal extent. Black points show the reconstructed spectral density $\hat{\rho}_\sigma(\omega)$.Top panel: Ensemble M1 ($N_t = 48$) with Wuppertal smearing step size $\varepsilon_{\mathrm{f}} = 0.18$. The yellow curve represents the fit $f_\sigma^{(2)}(E)$ (Eq. (3.5.19)), with red and green curves indicating the ground and first excited states $\Delta_\sigma(E - E_0)$ and $\Delta_\sigma(E - E_1)$. Middle panel: Ensemble M2 ($N_t = 64$), with Wuppertal step size $\varepsilon_{\mathrm{as}} = 0.20$. Curves correspond as above. Bottom panel: Ensemble M3 ($N_t = 96$), Wuppertal step size $\varepsilon_{\mathrm{as}} = 0.20$. The grey curve shows the fit $f_\sigma^{(3)}(E)$, with red, green, and yellow lines marking the ground, first, and second excited states $\Delta_\sigma(E - E_0)$, $\Delta_\sigma(E - E_1)$, and $\Delta_\sigma(E - E_2)$.

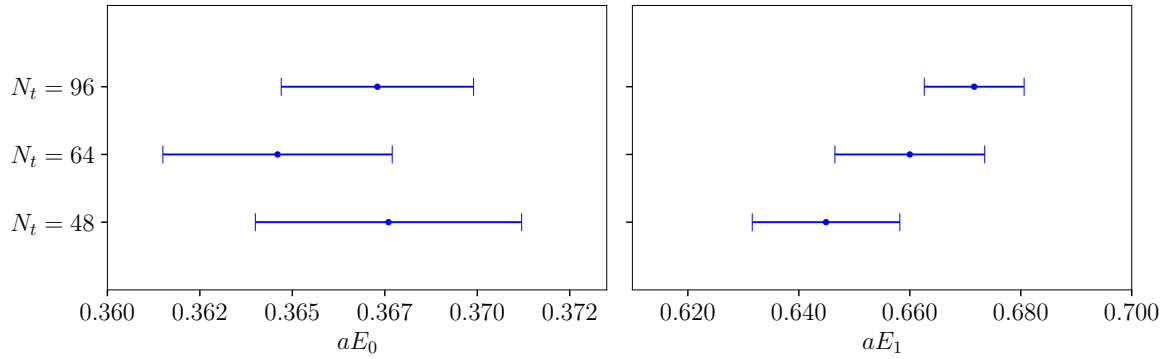

Figure 5.16. Summary of spectroscopy results from Fig. 5.15, displaying the ground and first excited state energies. Each marker indicates the central value of the corresponding energy level, with error bars representing the associated uncertainties. Slight vertical offsets have been applied to the points to enhance visual distinction.

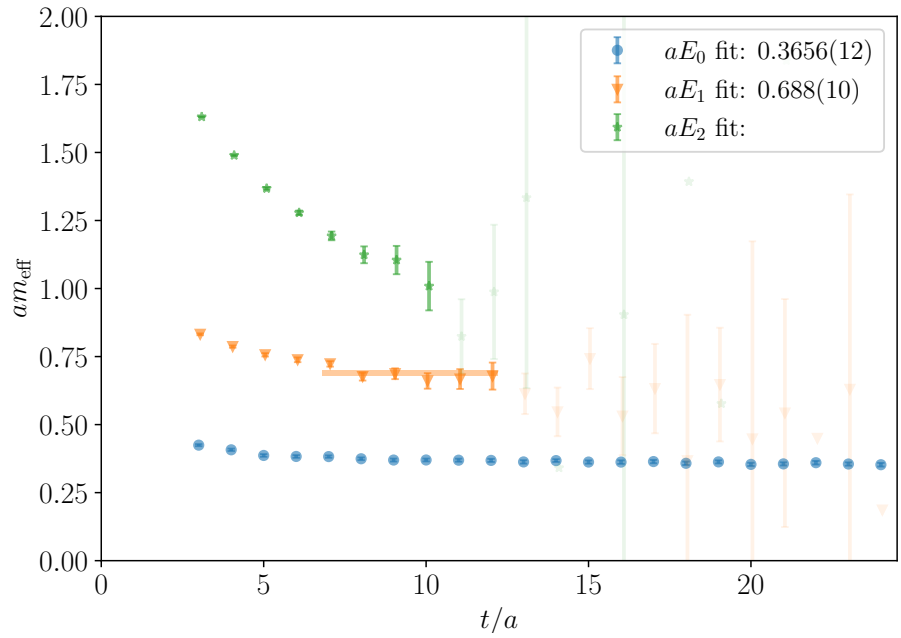

Figure 5.17. Effective mass plateaux, am_{eff}, extracted in the pseudoscalar channel for ensemble M2 (N_t = 64). The plateaux are determined via the GEVP method applied to a nine-correlator basis, as defined in Eq. (3.4.21). The analysis explores different levels of Wuppertal smearing, with N = 0, 40, and 80 iterations at both source and sink, using fixed parameters ε_{as} = 0.10, α_{APE} = 0.4, and N_{APE} = 50.

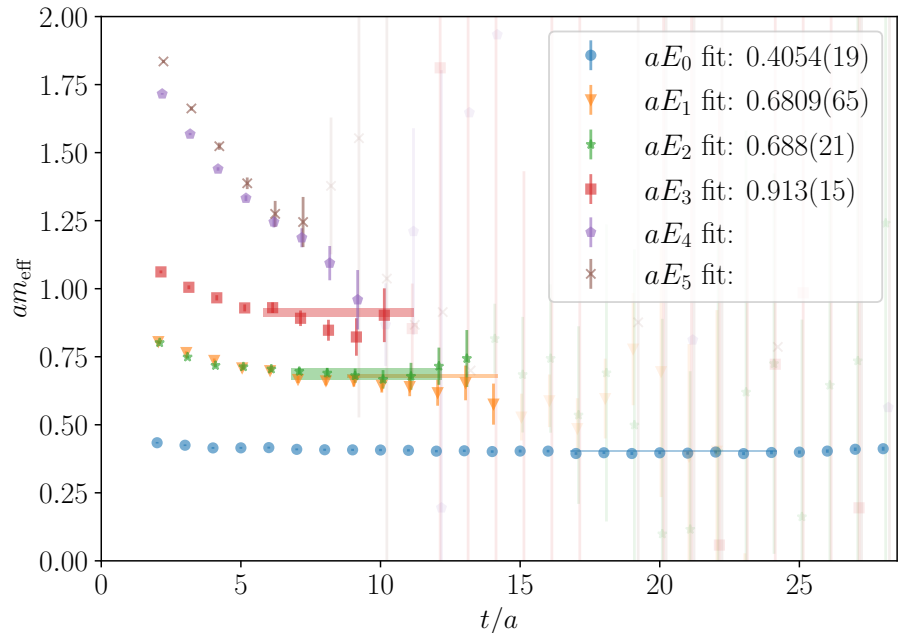

Figure 5.18. Effective mass plateaux, am_{eff}, for the combined vector (V) and tensor (T) channels in ensemble M2 (N_t = 64). These plateaux are extracted using the GEVP approach applied to a basis of thirty-six correlators, as detailed in Eq. (3.4.22). When multiple plateau candidates arise due to degeneracy, the energy level with the lowest statistical uncertainty is chosen. Accordingly, the first excited state is identified with aE_1 rather than aE_2 in this analysis.

5.3 Comparisons with GEVP and correlation function fitting

In this section, we report our numerical findings, including precise determinations of masses and matrix elements, and provide a critical comparison with previous studies. We begin by extracting the meson spectrum using both a variational approach and spectral density reconstructions on the ensembles M1–M5. We then present results for the chimera baryon mass spectrum, as well as matrix element calculations for both meson and chimera baryon channels.

5.3.1 Spectroscopy results

This section presents the spectroscopy numerical results obtained using the HLT method, compared with those from the GEVP analysis for consistency. Figures 5.17 and 5.18 showcase two representative GEVP computations: one using a nine-element variational basis (Eq. (3.4.21)) and another incorporating V and T channels (Eq. (3.4.22)). Both examples reveal sufficient signal-to-noise ratios to extract the ground and first excited states with smaller bases, while the cross-channel analysis enables access to further excited states.

Figure 5.19 displays representative results in the meson and chimera baryons spectra, by showing the tensor meson channel for all ensembles (Tab. 5.1), and the chimera baryons $\Sigma^{*,+}_{\mathrm{CB}}$ channel, both expressed in Wilson flow units, $\hat{m} \equiv w_0 \cdot m$. Shading and horizontal offsets distinguish ensembles M1–M3, while larger offsets and hatched patterns highlight M4 and M5. Colour blocks represent combined statistical and systematic uncertainties, including the variation effects of smearing kernels (Gaussian and Cauchy) and the number of peaks (k, $k+1$) in spectral density fits. Figure 5.20 extends this analysis to the full meson spectrum, using consistent colours for identical channels across fermion representations (fundamental and antisymmetric).

Numerical results for the ground, first, and second excited states are listed in Tabs. F.1–F.15. These tables detail the smearing levels, k-peak fits (using both Gaussian and Cauchy kernels), and corresponding GEVP results, presented in lattice units with Wilson flow unit conversions available in Tab. 5.1. Longer temporal extents (N_t) show a general trend of improvement, as evident from the ensembles M1–M3.

For all the ensembles M1-M5, the spectral density method shows a general agreement with GEVP results across all meson channels. While ground-state uncertainties are slightly larger for spectral density fits (consistently with Ref. [227]), excited-state extractions remain competitive. Notably, spectral density fits require only a single correlator, compared to the nine or thirty-six correlators used in GEVP analysis, highlighting potential efficiency gains for future studies.

A similar analysis was performed for chimera baryons. Using spin- and parity-projected operators (Tab. 3.2, Eq. (3.4.6)), we computed correlation functions, reconstructed spectral

densities, and fitted them. The GEVP analysis followed the same method as for mesons, with a nine-element variational basis ($N_{\text{source}}, N_{\text{sink}} = 0, 40, 80$). Results for chimera baryons (Tabs. F.16–F.30) include k- and $k+1$-peak fits (Gaussian and Cauchy) and GEVP results, extending to ground, first, and second excited states.

For chimera baryons, ensembles M1–M3 exhibit improved precision with increased N_t, as expected from the HLT method. Longer temporal lattices enable more accurate spectral density reconstruction and reduce uncertainties. The four energy estimates from spectral density fits show minimal discrepancies and align well with GEVP results. Figure 5.19 makes the improvement visual with N_t with representative channels: T for mesons and $\Sigma^{*,+}_{\text{CB}}$ for baryons.

Finally, Fig. 5.20 combines results for mesons and chimera baryons across all ensembles. Six colours represent distinct non-singlet meson channels, matched across fermion representations, while six additional colours distinguish chimera baryon channels. Statistical and systematic uncertainties, including excited-state contamination and smearing kernel variations, are represented by the vertical extents of the colour blocks.

5.3.2 Matrix elements and overlap factors results

The determination of matrix elements and overlap factors is carried out following the approach detailed in Secs. 3.4.2 and 5.2.4, combining the use of correlation function analysis and spectral density amplitude fits. These methods are applied to calculate the matrix elements associated with the interpolating operators listed in Tab. 3.1 for mesons and the overlap factors corresponding to the operators in Tab. 3.2 for chimera baryons. After extracting the bare matrix elements and overlap factors, normalisation is performed using the renormalisation constants specified in Eqs. (3.4.30) and (3.4.40). The final normalised results are presented in Tabs. F.31–F.35 for the mesonic channels and Tabs. F.36–F.40 for chimera baryons.

The tables show results obtained from two complementary methods: the spectral density fitting approach (outlined in Sec. 5.2.4) and traditional correlation function fitting described in Sec. 3.4.2. Specifically, they include values from Gaussian kernel fits (a^2c_0-G for mesons, a^3K_0-G for chimera baryons), Cauchy kernel fits (a^2c_0-C for mesons, a^3K_0-C for chimera baryons), and two-point correlation function-based fits. The matrix elements and overlap factors show no significant sensitivity to the choice of smearing kernel, with Gaussian and Cauchy fits yielding consistent results. This agreement between fits provides an estimate of systematic uncertainties, calculated as described in Eq. (5.2.5). These effects are generally comparable to or smaller than the statistical errors.

Overall, the results demonstrate agreement between the spectral density and correlation function fitting methods, validating the spectral density approach. For ensembles M1 through

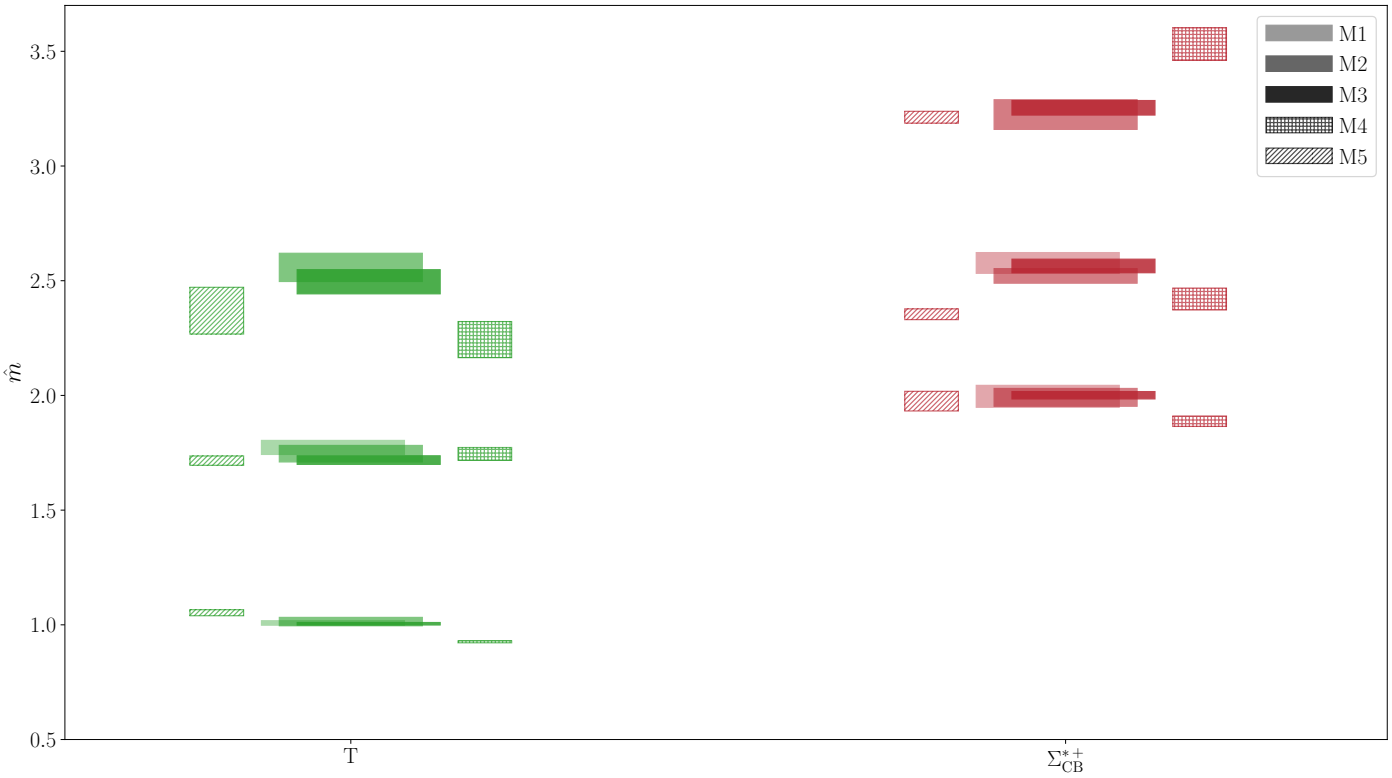

Figure 5.19. Spectrum of mesons and chimera baryons for the representative channels T and $\Sigma^{*,+}_{\mathrm{CB}}$ across ensembles M1 through M5, as defined in Tab. 5.1. Masses are extracted from fits to the reconstructed spectral densities. For each channel, we present a tower of states—ground, first, and, where available, second excited states—expressed in Wilson flow units as $\hat{m} \equiv w_0 \cdot m$. Each coloured block represents the central value (block midpoint), with total uncertainties (statistical and systematic combined in quadrature) indicated by the block height. Small horizontal displacements separate results from different ensembles for clarity. Solid fill denotes data from ensemble M3, while hollow or patterned blocks correspond to M4 and M5.

M5, a clear consistency is observed across all analysed channels. This is expected, given that the primary difference between these ensembles lies in their temporal extent, N_t. Such uniformity is evident in the mesonic matrix elements shown in Tabs. F.31–F.33 and the chimera baryon overlap factors detailed in Tabs. F.36–F.38.

The ground-state results for mesons and baryons are presented in Figs. 5.21 and 5.22, respectively, to help visualisation. As observed for the masses, the measurements of both meson and chimera baryon observables obtained on ensembles M1–M3—differing only in the temporal extent of the lattice—are generally consistent and show a general trend of improvement with increasing temporal extent N_t.

Matrix elements and overlap factors are expressed in Wilson flow units, defined as $\hat{c}_0 \equiv w_0^2 \cdot c_0$ and $\hat{K}_0 \equiv w_0^3 \cdot K_0$. Although systematic uncertainties are smaller than the statistical

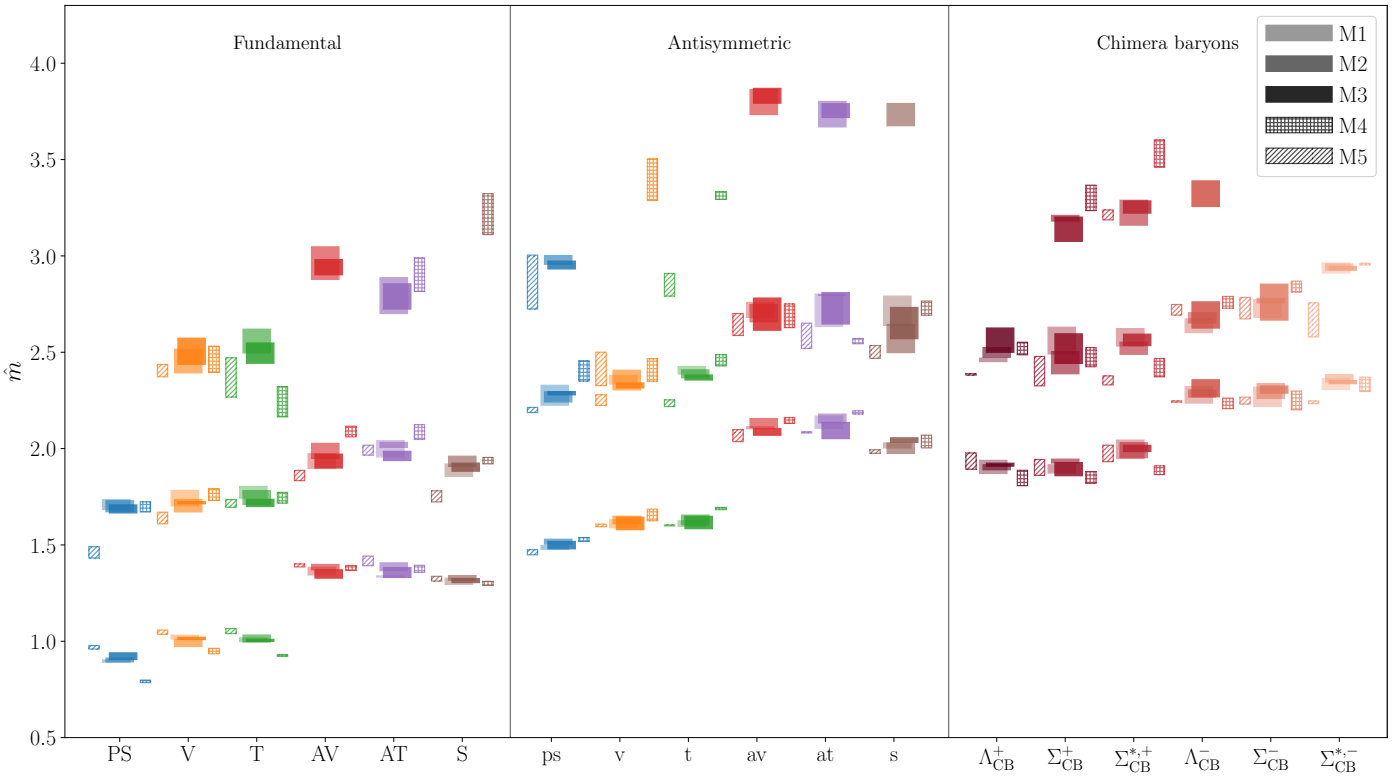

Figure 5.20. Mass spectrum of mesons and chimera baryons across all ensembles listed in Tab. 5.1. Mesonic states are shown for fermions in both the fundamental and antisymmetric representations, with masses extracted via fits to the reconstructed spectral densities. For each channel, we display the lowest-lying states—ground, first, and, when available, second excitations—expressed in Wilson flow units as $\hat{m} \equiv w_0 \cdot m$. The central value of each state corresponds to the midpoint of the coloured block, while the block height reflects the combined statistical and systematic uncertainties (added in quadrature). Horizontal displacements are introduced for visual separation of ensembles. Ensembles M1, M2, and M3 (which differ only in temporal extent: N_t = 48, 64, and 96, respectively) are identified using shaded versions of the same base colours. Ensembles M4 and M5, which also differ in bare parameters, are represented by unfilled or patterned blocks. The increasing temporal extent from M1 to M3 leads to progressively reduced uncertainties in the extracted masses. Six distinct colours are used to label the various meson channels; for operators built with the same gamma structure but different fermion representations, the same colour is used. An additional six colours identify the chimera baryon channels, grouped by parity.

ones, we conservatively combine them in quadrature. The systematic effects account for contributions from excited-state contamination and the choice of smearing kernel. To estimate these, we consider the spread among lattice results obtained using k- and $(k{+}1)$-peak Gaussian and Cauchy fits (k-G, $(k{+}1)$-G, k-C, $(k{+}1)$-C), taking the maximal variation as the systematic uncertainty.

Due to the limited set of available ensembles, we are not in a position to perform a continuum extrapolation. As a result, our results are expected to be affected by lattice

discretisation artefacts. Despite this limitation, some noteworthy qualitative patterns emerge.

In the meson sector, we observe that the matrix elements $\hat{c}_0$ in the pseudoscalar channel are systematically smaller than those in the vector and axial-vector channels. Additionally, we find that $\hat{c}_0$ tends to be larger in the antisymmetric representation than in the fundamental one.

In the case of chimera baryons, we find that the ground-state overlap factors $\hat{K}_0$ for the Λ_{CB} states are smaller than those for the Σ_{CB} and Σ^*_{CB} states, which appear to have comparable magnitudes. Moreover, odd-parity states generally exhibit smaller overlap factors than their even-parity counterparts.

It is instructive to place our results in the broader context of related theories. In particular, we consider overlap factors relevant for proton decay in QCD [269], as well as for partial top compositeness in a $SU(4)$ gauge theory featuring $N_{\mathrm{f}} = 2$ fermions in the fundamental representation and $N_{\mathrm{as}} = 2$ in the two-index antisymmetric representation [270]. In both cases, a key dimensionless quantity is the ratio K_0/f_{PS}^3.

The corresponding values reported in the literature are:[3]

$$\left(\frac{K_0}{f_{\mathrm{PS}}^3}\right)_{\mathrm{QCD}} \sim 20\,, \qquad \text{and} \qquad \left(\frac{K_0}{f_{\mathrm{PS}}^3}\right)_{SU(4)} \sim 3\,. \tag{5.3.1}$$

In our case, the results for the Λ_{CB} and Σ_{CB} channels are fairly consistent across all ensembles (M1–M5). Averaging over these, we obtain:

$$\left(\frac{K_{\Lambda_+,0}}{f_{\mathrm{PS}}^3}\right) \sim 6\,, \qquad \text{and} \qquad \left(\frac{K_{\Sigma_+,0}}{f_{\mathrm{PS}}^3}\right) \sim 25\,. \tag{5.3.2}$$

While our results are obtained without performing a continuum extrapolation and with renormalisation matched at the cutoff scale, it is nonetheless reassuring that the extracted values for the Λ and Σ chimera baryons are broadly consistent—at the level of order-of-magnitude estimates—with those reported in the literature.

We further note that Ref. [270] adopts a normalisation for the overlap factors based on the decay constant of mesons composed of antisymmetric-representation fermions. This choice is appropriate for the composite Higgs model (CHM) framework considered there [271]. In contrast, the CHM scenarios explored in Refs. [140, 181]—which are more directly related to

[3] In both references, the decay constant is normalised according to the convention $F_\pi = F_{\mathrm{PS}} \simeq 130$ MeV. To align with our convention, where $f_\pi \simeq 93$ MeV, we rescale the corresponding QCD results. In the case of the $SU(4)$ theory, we use the decay constant associated with mesons formed from fermions in the fundamental representation. Another point to bear in mind is that our overlap factors are renormalised at the scale $\mu = 1/a$, which differs when varying the lattice spacing, whereas the QCD results are renormalised at a fixed scale of $\mu = 2$ GeV. Owing to the logarithmic nature of the renormalisation group evolution, this scale mismatch is not expected to substantially affect the validity of the comparison at the level of order-of-magnitude estimates.

Table 5.3. Results for the quantities s_0, s_1, and s_2—as defined in the main text—are presented for all ensembles and both meson species. These values are obtained by combining our most precise lattice measurements. Uncertainties reflect both statistical fluctuations and systematic effects, added in quadrature. Deviations from the idealised limits $s_1 = 0$ and $s_2 = 0$ arise due to approximations involved in the continuum and chiral extrapolations, as well as incomplete isolation of the ground state contributions.

Meson	Ensemble	s_0	s_1	s_2
(f)-type	M1	0.298(4)	-0.008(19)	0.005(44)
(f)-type	M2	0.253(5)	-0.149(32)	-0.310(78)
(f)-type	M3	0.257(15)	-0.156(47)	-0.270(73)
(f)-type	M4	0.220(9)	-0.245(31)	-0.384(55)
(f)-type	M5	0.192(4)	-0.629(25)	-1.561(68)
(as)-type	M1	0.220(4)	-0.116(19)	0.213(27)
(as)-type	M2	0.204(3)	-0.193(21)	0.103(34)
(as)-type	M3	0.206(5)	-0.194(30)	0.151(40)
(as)-type	M4	0.229(6)	-0.137(23)	0.205(26)
(as)-type	M5	0.197(5)	-0.206(23)	0.097(37)

our setup—feature a Higgs sector arising from fermions in the fundamental representation. Since we consistently find $f_{\rm PS} < f_{\rm ps}$ across our ensembles, our computed values of $K_0/f_{\rm PS}^3$ are correspondingly enhanced compared to those of Ref. [270].

Moreover, it is still an open question whether the chimera baryon state playing a central role in the top partial compositeness mechanism is identified with the Σ rather than the Λ. It would be of extreme interest to target this question and to test the robustness of our conclusions through future high-precision studies including continuum-limit extrapolations.

Another simplified yet illustrative exercise can be performed. This is aimed at assessing the current level of precision of our lattice measurements and highlighting the potential of the methodology developed in this work for future high-precision studies.

To this end, we define the following three quantities, adopting the normalisation conventions of Ref. [259] for mesons composed of (f)-type fermions:

$$s_0 \equiv 4\pi \left(\frac{\hat{f}_{\rm V}^2}{\hat{m}_{\rm V}^2} - \frac{\hat{f}_{\rm AV}^2}{\hat{m}_{\rm AV}^2} \right), \tag{5.3.3}$$

$$s_1 \equiv 1 - \frac{\hat{f}_{\rm AV}^2 + \hat{f}_{\rm PS}^2}{\hat{f}_{\rm V}^2}, \tag{5.3.4}$$

$$s_2 \equiv 1 - \frac{\hat{m}_{\rm AV}^2 \hat{f}_{\rm AV}^2}{\hat{m}_{\rm V}^2 \hat{f}_{\rm V}^2}, \tag{5.3.5}$$

with analogous definitions holding for mesons composed of (as)-type fermions. Among these,

the quantities s_1 and s_2 are directly related to the Weinberg sum rules [272], while s_0 is associated with the Peskin–Takeuchi S parameter [188].

In the chiral and continuum limit, and assuming that the right-hand sides of these definitions include contributions from the full tower of vector and axial-vector resonances, the Weinberg sum rules imply $s_1 = 0 = s_2$. Furthermore, if the electroweak symmetry group $SU(2)_L \times U(1)_Y$ is embedded in the global symmetry of the strong sector in such a way that electroweak symmetry breaking occurs analogously to the Standard Model, then s_0 serves as a measure of new physics contributions to isospin-breaking effects. Current bounds from electroweak precision observables constrain this parameter to satisfy $s_0 = S < 0.4$ at the 3σ confidence level.

In this study, all measurements were performed at finite fermion mass and nonzero lattice spacing. Moreover, decay constants were extracted only for the ground-state mesons. These simplifications potentially introduce significant systematic uncertainties. Nevertheless, we present in Tab. 5.3 the computed values of s_0, s_1, and s_2 for both (f)-type and (as)-type fermions, across all available ensembles.

While the results for s_1 and s_2 are not compatible with zero, consistently with the presence of systematic effects. However, their central values are found to be roughly one order of magnitude smaller than those obtained in the quenched approximation reported in Ref. [259]. This observation highlights the sensitivity of these quantities to the inclusion of dynamical fermions and demonstrates their potential as diagnostic tools for probing the dynamics of the underlying theory.

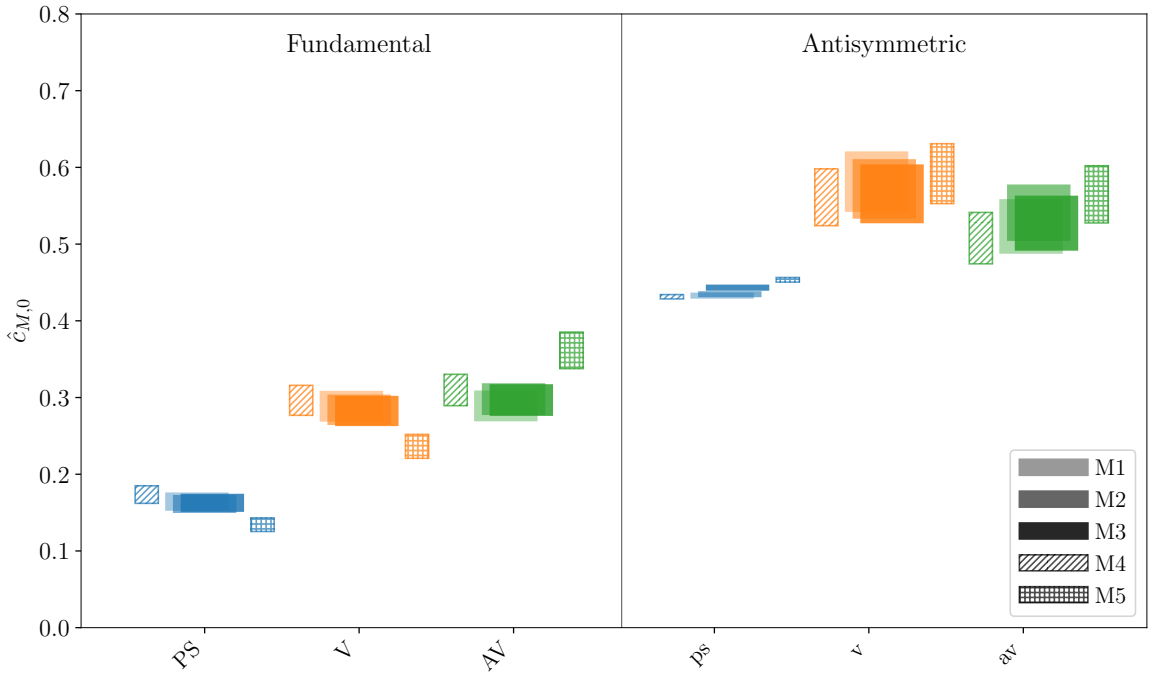

Figure 5.21. Ground-state matrix elements for flavoured mesons, defined as $\hat{c}_0 \equiv w_0^2\langle 0|\mathcal{O}^M|e_0\rangle$, are shown for all ensembles listed in Tab. 5.1. These values are extracted from fits to the reconstructed spectral densities, and are presented in units of the Wilson flow scale w_0. Each coloured block represents one measurement: the midpoint corresponds to the central value, while the height encodes the total uncertainty—combining statistical and systematic errors in quadrature. To enhance readability, horizontal displacements are applied to separate data from different ensembles. Ensembles M1, M2, and M3 (which vary only in temporal extent: N_t = 48, 64, and 96, respectively) are shown with progressively darker shadings of the same base colour. Ensembles M4 and M5, which differ additionally in bare parameters, are indicated with patterned, unfilled blocks.

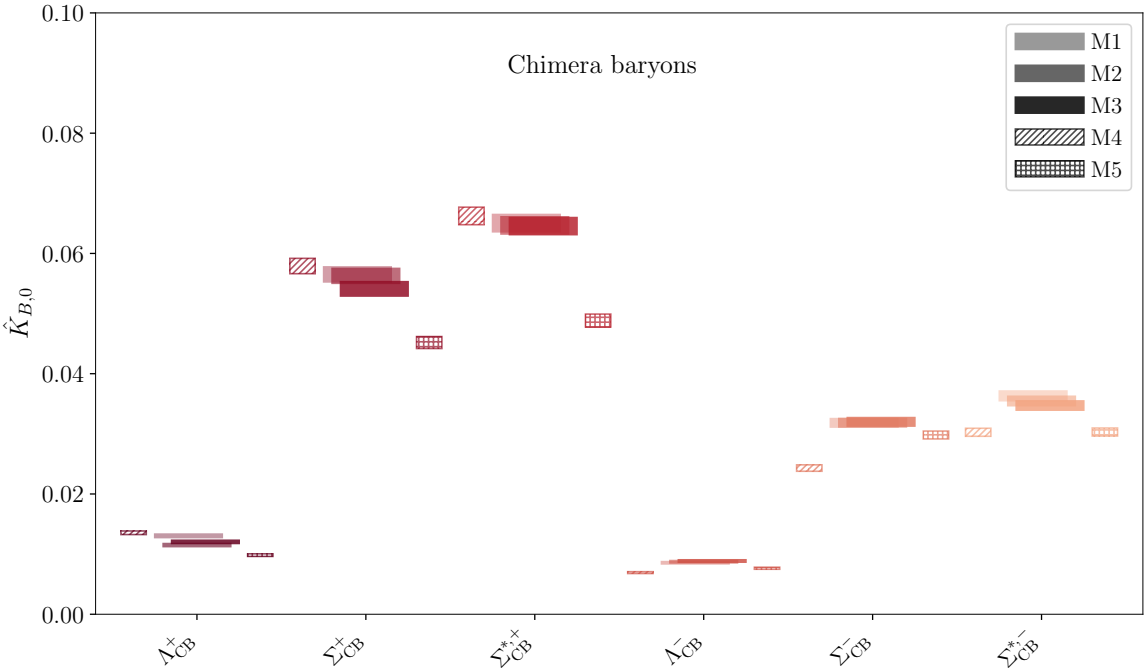

Figure 5.22. Overlap factors for chimera baryons, defined as $\hat{K}_0 \equiv w_0^3 \cdot K_0$, are presented for all ensembles listed in Tab. 5.1. The values are determined through fits to the reconstructed spectral densities and expressed in units of the Wilson flow scale, w_0. Each coloured block denotes a measured overlap factor: the central value corresponds to the midpoint of the block, while the height reflects the combined statistical and systematic uncertainty, added in quadrature. To aid visual separation, results from different ensembles are offset horizontally. Shading variations of the same colour distinguish ensembles that differ only in their temporal extent (N_t = 48, 64, and 96 for M1, M2, and M3), while patterned, unfilled blocks are used for M4 and M5, which also differ in bare parameters.

Chapter 6

Conclusions

This thesis has presented a non-perturbative study of strongly coupled gauge theories based on symplectic gauge groups, primarily $Sp(4)$, with dynamical fermions in both the fundamental and two-index antisymmetric representations. The motivation for such a study originates from the growing interest in these theories as ultraviolet completions of Composite Higgs Models [158–160], and their increasing physical relevance in the literature. The work combines theoretical foundations with advanced numerical simulations. At the core of this research lies the hypothesis that the Higgs boson is not an elementary scalar, but a bound state emerging from new strong dynamics. Symplectic gauge theories, in particular $Sp(4)$ with appropriate fermion content, naturally realise global symmetry breaking patterns such as $SU(4)/Sp(4)$, which yield the correct number of pseudo-Nambu-Goldstone bosons to accommodate a composite Higgs doublet. Moreover, by including additional fermionic fields (e.g. fermions in the two-index antisymmetric representation of $Sp(4)$), the framework allows for partial top compositeness mechanisms [271, 273–318] that can explain the top quark's large mass through the formation of baryon-like top partners.

A technical achievement of this thesis is the extension and customisation of the `GRID` software library [145–147] to handle symplectic gauge groups, $Sp(2N)$, with multiple fermionic representations. This required substantial algorithmic work, as described in Chapter 4, including implementing the generation of random Lie-algebra valued $\mathfrak{sp}(2N)$ conjugate momenta and projection algorithms, supporting HMC and RHMC evolution for mixed representation fermions and benchmarking performance and correctness on GPU architectures. These developments constitute a reusable and scalable computational framework for future lattice studies of symplectic gauge theories. The correctness of the implementation is verified through several tests presented in this thesis.

A central focus is given to the application of spectral density reconstruction techniques, notably the Hansen-Lupo-Tantalo (HLT) method [218, 227, 319–321], to extract physical information from Euclidean correlators. These methods are shown to efficiently reconstruct multi-state contributions from correlators using inverse Laplace transforms. Moreover, they

provide robust estimates for ground and excited state spectra, and they offer alternative paths to compute matrix elements and decay constants with control over systematics. This work demonstrates that the spectral density approach is not only feasible for $Sp(2N)$ theories, but also competitive with traditional GEVP-based methods [207]. Extensive comparisons are made between the results obtained from both methods for mesons and chimera baryons, showing agreement in findings (see tables in Appendix F). The thesis also addresses in Chapter 5 practical considerations such as the impact of different correlator smearing techniques (APE and Wuppertal), smearing kernel types (Gaussian vs. Cauchy), and more. Systematic uncertainties are rigorously quantified, reinforcing the reliability of the extracted observables. The numerical simulations are performed across a range of ensembles with varying lattice volumes, fermion masses, and temporal extents. An original first one-loop perturbative computation of the matching coefficients for the $Sp(2N)$ chimera baryons overlap factors is presented in Appendix D.

This thesis makes several methodological contributions that will be of use to the lattice community:

- A software for running symplectic gauge theories simulations (`GRID` framework) and a validated pipeline for implementing new gauge groups and fermion representations in modern lattice codes.
- Implementation of an open-source code to find spectral densities using the HLT method (`LSDensities` software package).
- A detailed workflow for spectral density fitting, including discussions about kernel choice and numerical stability considerations.
- A systematic comparative analysis of traditional GEVP fits and spectral density reconstruction.

The validation of `GRID` for $Sp(2N)$ and our spectral densities findings for this class of gauge theories subjects open multiple settings for future investigation:

- Spectral density methodology: inspect further methodological improvements for the spectral density techniques and for hadronic observables extrapolations.
- Continuum and chiral extrapolations: the encouraging results from the meson and chimera baryons matrix elements in mixed-representation theories motivate further numerical investigations, including continuum and chiral extrapolations of observables for the models under consideration and related ones.

- Phenomenology studies: the matrix elements results, once extrapolated to the continuum limit, can be directly integrated into low-energy effective models of composite Higgs physics [270]. This is relevant to pursue further phenomenology studies, since chimera baryon matrix elements provide critical inputs for estimating partial compositeness couplings.

- Large-N and universal dynamics: extending the framework to $Sp(6)$ and $Sp(8)$ will allow tests of large-N scaling laws and comparisons with $SU(N)$ theories [13, 322]. This can provide information about universal features of non-Abelian gauge theories.

- Finite temperature studies, phase transitions and chemical potential: exploring the thermal phase structure of $Sp(2N)$ theories, including possible deconfinement and chiral transitions, could be crucial for cosmological implications of Beyond Standard Model models [229, 245].

- Glueballs studies in $Sp(2N)$ gauge theories and their potential role as composite dark matter candidates [229, 323, 324]. Non-perturbative investigations of the glueball spectrum and its phenomenological implications in dark sector models.

Appendix A

Generators of the $Sp(4)$ algebra in GRID

Let T^a_{f} denote the generators of the Lie algebra of $Sp(2N)$ in the fundamental representation. These generators are implemented in GRID as Hermitian matrices, adhering to the block structure described in Eq. (2.3.19). Their normalisation satisfies:

$$\mathrm{Tr}\left(T^a_{\mathrm{f}} T^b_{\mathrm{f}}\right) = \frac{\delta^{ab}}{2} \,. \tag{A.0.1}$$

As shown in Ref. [178], the implementation of T^a_{f}, with $a = 1, \ldots, 2N^2+N$, in GRID follows these conventions:

1. Off-diagonal Generators ($2N^2$ total): for the first $N(N-1)/2$ generators:

$$T^a_{\mathrm{f}\,i,j} = T^a_{\mathrm{f}\,j,i} = -T^a_{\mathrm{f}\,i+N,j+N} = -T^a_{\mathrm{f}\,j+N,i+N} = \frac{1}{2\sqrt{2}} \,, \tag{A.0.2}$$

with $i = 1, \ldots, N-1$ and $i < j \leq N$. For the next $N(N-1)/2$ generators:

$$T^a_{\mathrm{f}\,i,j} = -T^a_{\mathrm{f}\,j,i} = T^a_{\mathrm{f}\,i+N,j+N} = -T^a_{\mathrm{f}\,j+N,i+N} = \frac{i}{2\sqrt{2}} \,, \tag{A.0.3}$$

with the same index ranges.

2. Mixed Generators ($N(N-1)$ total): for the first $N(N-1)/2$:

$$T^a_{\mathrm{f}\,i,j+N} = T^a_{\mathrm{f}\,j,i+N} = T^a_{\mathrm{f}\,i+N,j} = T^a_{\mathrm{f}\,j+N,i} = \frac{1}{2\sqrt{2}} \,, \tag{A.0.4}$$

with $i = 1, \ldots, N-1$ and $i < j \leq N-1$. For the next $N(N-1)/2$:

$$T^a_{\mathrm{f}\,i,j+N} = T^a_{\mathrm{f}\,j,i+N} = -T^a_{\mathrm{f}\,i+N,j} = -T^a_{\mathrm{f}\,j+N,i} = \frac{i}{2\sqrt{2}} \,. \tag{A.0.5}$$

3. Diagonal Generators ($2N$ total): - For the first N:

$$T^a_{\mathrm{f}\,i,i+N} = T^a_{\mathrm{f}\,i+N,i} = \frac{1}{2}\,, \tag{A.0.6}$$

where $i = 1, \ldots, N$. For the next N:

$$T^a_{\mathrm{f}\,i,i+N} = -T^a_{\mathrm{f}\,i+N,i} = \frac{i}{2}\,. \tag{A.0.7}$$

4. Cartan Subalgebra Generators (N total): the diagonal elements are:

$$(T^a_{\mathrm{f}})_{i,i} = -(T^a_{\mathrm{f}})_{i+N,i+N} = \frac{1}{2}\,, \tag{A.0.8}$$

with $i = 1, \ldots, N$.

For $2N = 4$, an explicit representation of the generators in the fundamental representation is given by:

$$\begin{aligned}
T^1_{\mathrm{f}} &= \frac{1}{2\sqrt{2}}\begin{pmatrix} 0 & 1 & 0 & 0 \\ 1 & 0 & 0 & 0 \\ 0 & 0 & 0 & -1 \\ 0 & 0 & -1 & 0 \end{pmatrix} & T^2_{\mathrm{f}} &= \frac{1}{2\sqrt{2}}\begin{pmatrix} 0 & i & 0 & 0 \\ -i & 0 & 0 & 0 \\ 0 & 0 & 0 & i \\ 0 & 0 & -i & 0 \end{pmatrix} \\
T^3_{\mathrm{f}} &= \frac{1}{2\sqrt{2}}\begin{pmatrix} 0 & 0 & 0 & 1 \\ 0 & 0 & 1 & 0 \\ 0 & 1 & 0 & 0 \\ 1 & 0 & 0 & 0 \end{pmatrix} & T^4_{\mathrm{f}} &= \frac{1}{2\sqrt{2}}\begin{pmatrix} 0 & 0 & 0 & i \\ 0 & 0 & i & 0 \\ 0 & -i & 0 & 0 \\ -i & 0 & 0 & 0 \end{pmatrix} \\
T^5_{\mathrm{f}} &= \frac{1}{2}\begin{pmatrix} 0 & 0 & 1 & 0 \\ 0 & 0 & 0 & 0 \\ 1 & 0 & 0 & 0 \\ 0 & 0 & 0 & 0 \end{pmatrix} & T^6_{\mathrm{f}} &= \frac{1}{2}\begin{pmatrix} 0 & 0 & 0 & 0 \\ 0 & 0 & 0 & 1 \\ 0 & 0 & 0 & 0 \\ 0 & 1 & 0 & 0 \end{pmatrix} \\
T^7_{\mathrm{f}} &= \frac{1}{2}\begin{pmatrix} 0 & 0 & i & 0 \\ 0 & 0 & 0 & 0 \\ -i & 0 & 0 & 0 \\ 0 & 0 & 0 & 0 \end{pmatrix} & T^8_{\mathrm{f}} &= \frac{1}{2}\begin{pmatrix} 0 & 0 & 0 & 0 \\ 0 & 0 & 0 & i \\ 0 & 0 & 0 & 0 \\ 0 & -i & 0 & 0 \end{pmatrix} \\
T^9_{\mathrm{f}} &= \frac{1}{2}\begin{pmatrix} 1 & 0 & 0 & 0 \\ 0 & 0 & 0 & 0 \\ 0 & 0 & -1 & 0 \\ 0 & 0 & 0 & 0 \end{pmatrix} & T^{10}_{\mathrm{f}} &= \frac{1}{2}\begin{pmatrix} 0 & 0 & 0 & 0 \\ 0 & 1 & 0 & 0 \\ 0 & 0 & 0 & 0 \\ 0 & 0 & 0 & -1 \end{pmatrix}
\end{aligned} \tag{A.0.9}$$

The orthonormal basis used to find the 2-index antisymmetric generators can be written

explicitly, and they are the same as Ref. [16]:

$$
\begin{aligned}
e^{(12)} &= \frac{1}{\sqrt{2}}\begin{pmatrix} 0 & -1 & 0 & 0 \\ 1 & 0 & 0 & 0 \\ 0 & 0 & 0 & 0 \\ 0 & 0 & 0 & 0 \end{pmatrix}, \; e^{(23)} = \frac{1}{\sqrt{2}}\begin{pmatrix} 0 & 0 & 0 & 0 \\ 0 & 0 & -1 & 0 \\ 0 & 1 & 0 & 0 \\ 0 & 0 & 0 & 0 \end{pmatrix}, \; e^{(14)} = \frac{1}{\sqrt{2}}\begin{pmatrix} 0 & 0 & 0 & -1 \\ 0 & 0 & 0 & 0 \\ 0 & 0 & 0 & 0 \\ 1 & 0 & 0 & 0 \end{pmatrix}, \\
e^{(24)} &= \frac{1}{2}\begin{pmatrix} 0 & 0 & 1 & 0 \\ 0 & 0 & 0 & -1 \\ -1 & 0 & 0 & 0 \\ 0 & 1 & 0 & 0 \end{pmatrix}, \; e^{(34)} = \frac{1}{\sqrt{2}}\begin{pmatrix} 0 & 0 & 0 & 0 \\ 0 & 0 & 0 & 0 \\ 0 & 0 & 0 & -1 \\ 0 & 0 & 1 & 0 \end{pmatrix}.
\end{aligned}
\tag{A.0.10}
$$

Appendix B

$SU(4)$ algebra generators

In the CHM context, we build a model based on the $SU(4)/Sp(4)$ coset. In order to discuss the embedding within the Standard Model, we borrow notations for the $SU(4)$ choice of generators from Ref. [189]. By imposing the normalization $\mathrm{Tr}\, T_{\mathrm{f}}^a T_{\mathrm{f}}^b = \frac{1}{2}\delta^{ab}$, we write the 15 generators as follows.

$$
\begin{aligned}
T_{\mathrm{f}}^1 &= \frac{1}{2\sqrt{2}}\begin{pmatrix} 0&1&0&0\\ 1&0&0&0\\ 0&0&0&1\\ 0&0&1&0 \end{pmatrix}, \quad T_{\mathrm{f}}^2 = \frac{1}{2\sqrt{2}}\begin{pmatrix} 0&-i&0&0\\ i&0&0&0\\ 0&0&0&i\\ 0&0&-i&0 \end{pmatrix}, \quad T_{\mathrm{f}}^3 = \frac{1}{2\sqrt{2}}\begin{pmatrix} 1&0&0&0\\ 0&-1&0&0\\ 0&0&1&0\\ 0&0&0&-1 \end{pmatrix},\\
T_{\mathrm{f}}^4 &= \frac{1}{2\sqrt{2}}\begin{pmatrix} 0&0&0&-i\\ 0&0&i&0\\ 0&-i&0&0\\ i&0&0&0 \end{pmatrix}, \quad T_{\mathrm{f}}^5 = \frac{1}{2\sqrt{2}}\begin{pmatrix} 0&0&0&1\\ 0&0&-1&0\\ 0&-1&0&0\\ 1&0&0&0 \end{pmatrix}, \quad T_{\mathrm{f}}^6 = \frac{1}{2\sqrt{2}}\begin{pmatrix} 0&0&-i&0\\ 0&0&0&-i\\ i&0&0&0\\ 0&i&0&0 \end{pmatrix},\\
T_{\mathrm{f}}^7 &= \frac{1}{2\sqrt{2}}\begin{pmatrix} 0&0&0&-i\\ 0&0&-i&0\\ 0&i&0&0\\ i&0&0&0 \end{pmatrix}, \quad T_{\mathrm{f}}^8 = \frac{1}{2\sqrt{2}}\begin{pmatrix} 0&-i&0&0\\ i&0&0&0\\ 0&0&0&-i\\ 0&0&i&0 \end{pmatrix}, \quad T_{\mathrm{f}}^9 = \frac{1}{2\sqrt{2}}\begin{pmatrix} 0&0&-i&0\\ 0&0&0&i\\ i&0&0&0\\ 0&-i&0&0 \end{pmatrix},\\
T_{\mathrm{f}}^{10} &= \frac{1}{2}\begin{pmatrix} 0&0&1&0\\ 0&0&0&0\\ 1&0&0&0\\ 0&0&0&0 \end{pmatrix}, \quad T_{\mathrm{f}}^{11} = \frac{1}{2\sqrt{2}}\begin{pmatrix} 0&0&0&1\\ 0&0&1&0\\ 0&1&0&0\\ 1&0&0&0 \end{pmatrix}, \quad T_{\mathrm{f}}^{12} = \frac{1}{2}\begin{pmatrix} 0&0&0&0\\ 0&0&0&1\\ 0&0&0&0\\ 0&1&0&0 \end{pmatrix},\\
T_{\mathrm{f}}^{13} &= \frac{1}{2\sqrt{2}}\begin{pmatrix} 0&1&0&0\\ 1&0&0&0\\ 0&0&0&-1\\ 0&0&-1&0 \end{pmatrix}, \quad T_{\mathrm{f}}^{14} = \frac{1}{2\sqrt{2}}\begin{pmatrix} 1&0&0&0\\ 0&-1&0&0\\ 0&0&-1&0\\ 0&0&0&1 \end{pmatrix}, \quad T_{\mathrm{f}}^{15} = \frac{1}{2\sqrt{2}}\begin{pmatrix} 1&0&0&0\\ 0&1&0&0\\ 0&0&-1&0\\ 0&0&0&-1 \end{pmatrix}.
\end{aligned}
\tag{B.0.1}
$$

Among these, T_{f}^a with $a = 6, \ldots, 15$ are the subset of generators of $Sp(4)$.

Appendix C

Correlation functions smearing techniques

To improve ground-state extraction from two-point correlation functions in lattice simulations, it is common to apply a combination of APE [212, 213] and Wuppertal [209–211] smearing techniques. APE smearing acts on the gauge links to suppress ultraviolet fluctuations, while Wuppertal smearing modifies fermion sources and sinks to increase overlap with the ground state and reduce excited-state contamination. When used together, these techniques help improve signal quality, allowing the effective mass plateau to emerge earlier in Euclidean time and enabling better control over systematic uncertainties from fitting procedures.

Wuppertal smearing: To enhance the ground-state projection of fermionic sources and sinks, Wuppertal smearing replaces point sources with spatially extended ones via a discretised diffusion process. Starting from a localized source $q_{\mathrm{R}}^{(0)}(x) = \delta_{x,0}$, the smeared field at iteration $n+1$ is given by

$$q_{\mathrm{R}}^{(n+1)}(x) = \frac{1}{1+6\varepsilon_{\mathrm{R}}}\left[q_{\mathrm{R}}^{(n)}(x) + \varepsilon_{\mathrm{R}} \sum_{\hat{\mu}} U_{\mu}(x) q_{\mathrm{R}}^{(n)}(x+\hat{\mu})\right], \tag{C.0.1}$$

where ε_{R} is the smearing step size. After N_{source} iterations, the resulting extended source is used to solve the equation for the Green function associated with the Dirac operator of a point source and sink:

$$\sum_{y,\beta,b} D^{\mathrm{R}}_{a\alpha,b\beta}(x,y)\, S^{b\beta}_{\mathrm{R},c\gamma}(y,0) = \delta_{x,0}\,\delta_{\alpha\gamma}\,\delta_{ac}, \tag{C.0.2}$$

where D^{R} is the Wilson-Dirac operator in representation R, with colour indices a, b, c and spinor indices α, β, γ. The solution $S_{\mathrm{R}}(y,0)$ represents the point-to-all quark propagator. The same procedure is applied to the sink, with no additional inversions required. This procedure is then supported by APE smearing to smoothen the gauge links into consideration.

APE smearing: The APE smearing procedure iteratively smooths the gauge links by averaging each link with its surrounding staples, defined as

$$S_\mu(x) \equiv \sum_{\pm\nu\neq\mu} U_\nu(x)\, U_\mu(x+\hat{\nu})\, U_\nu^\dagger(x+\hat{\mu})\,.$$

The updated (smeared) link at iteration m, denoted $U_\mu^{(m)}(x)$, is computed via

$$U_\mu^{(m)}(x) = \mathcal{P}\left[(1-\alpha_{\rm APE})U_\mu^{(m-1)}(x) + \frac{\alpha_{\rm APE}}{6} S_\mu^{(m-1)}(x)\right], \tag{C.0.3}$$

with initial condition $U_\mu^{(0)} = U_\mu$. Here, $\alpha_{\rm APE}$ is the smearing parameter, $N_{\rm APE}$ is the number of iterations, and $\mathcal{P}$ denotes a projection back onto the gauge group, ensuring that the smeared links remain valid elements of the group manifold.

Let us consider, as an illustrative example, a generic meson two-point correlator can be expressed as

$$C(t) = \left\langle \sum_{\vec{x}} \mathrm{Tr}\left[\Gamma\, S_{\rm R}(x,0)\, \bar{\Gamma}\, S_{\rm R}(x,0)\right]\right\rangle, \tag{C.0.4}$$

with Dirac structures Γ and $\bar{\Gamma} \equiv \gamma^0\Gamma^\dagger\gamma^0$.

Once Wuppertal smearing is applied, the correlator is modified to use the smeared propagators:

$$C_{N_{\rm source},N_{\rm sink}}(t) = \left\langle \sum_{\vec{x}} \mathrm{Tr}\left[\Gamma\, S^{\rm R}_{(N_{\rm source},N_{\rm sink})}(x,0)\, \bar{\Gamma}\, S^{\rm R}_{(N_{\rm source},N_{\rm sink})}(x,0)\right]\right\rangle. \tag{C.0.5}$$

where the propagator $S^{\rm R}_{(N_{\rm source},N_{\rm sink})}(x,0)$ presents smearing at both the source and the sink. and the three parameters that define Wuppertal smearing, $\varepsilon_{\rm R}$, $N_{\rm source}$, and $N_{\rm sink}$, are tuned to optimise overlap with the desired state and minimise noise.

All correlation functions involving APE and Wuppertal smearing are computed using the `HiRep` code [200, 266, 267].

Appendix D

Renormalisation of chimera baryons matrix elements

As devised in early studies [214, 215, 325], the renormalisation of operators using Wilson fermions involves the computation of Feynman diagrams results in the continuum and on the lattice. Here, we present both the calculations.

Computation in the continuum theory

The operators that we consider, associated with chimera baryons is:

$$O^{\mu}(x) = \left\{\left[Q^{a}_{1\,\alpha}\Gamma_1^{\alpha\beta}Q^{b}_{2\,\beta}\right]\Omega_{ad}\Omega^{bc}\Gamma_2^{\mu\gamma}\psi^{cd}_{\gamma}\right\}(x)\,. \tag{D.0.1}$$

where throughout the appendix roman letters indicate colour indices, whereas greek letters indicate spin indices. In this case, we will consider, $\Gamma_2^{\mu\gamma} = \mathbb{I}^{\mu\gamma}$. Q_1, Q_2 are fundamental fermions and ψ are 2-index antisymmetric ones. In order to renormalise this operator, we introduce the 4-point function

$$\mathcal{G}^{\mu\alpha\beta\gamma}(x, x_1, x_2, x_3) = \left\langle O^{\mu}(x)\psi^{\alpha}_{cd}(x_3)\,Q^{\beta}_{1\,a}(x_2)\,Q^{\gamma}_{2\,b}(x_3)\right\rangle [\mathrm{CM}]^{abcd}\,. \tag{D.0.2}$$

The colour matrix [CM] can be added to fix the colour structure of the external legs. This trick is not a mandatory step, but it can be useful, and we proceed to use it.
We will fix, at the end, the colour structure with

$$[\mathrm{CM}]_{abcd} = \frac{1}{N}\Omega_{ad}\Omega_{bc}\,. \tag{D.0.3}$$

Let us define

$$\Gamma^{\mu\mu'\alpha\beta}_{\{a:\}}(x, x_1 \ldots x_3) = \left\langle O^{\mu}(x)\psi^{\mu'}_{cd}(x_3)\,Q^{\alpha}_{1\,a}(x_2)Q^{\beta}_{2,b}(x_1)\right\rangle_{\text{amputated}}\,, \tag{D.0.4}$$

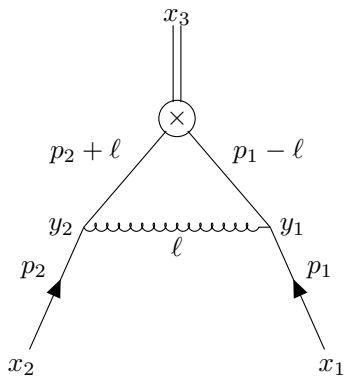

Figure D.1. Diagram A. One-loop Feynman diagram showing a gluon exchange between two fundamental fermion legs. The vertex ⊗ indicates the presence of the Γ operators coming from Eq. (D.0.1).

$\{a:\}$ denotes the colour indices which we can fix later.

The following terms in the Lagrangian are relevant at 1-loop:

$$\mathcal{L}(x) \supset -\sum_{f=1}^{N_{\rm f}} g\bar{Q}^f_a \gamma^\mu A^b_\mu T^b_{{\rm f}\,ac} Q^f_c(x) \equiv \mathcal{L}^{\phi\phi A}\,, \tag{D.0.5}$$

$$\mathcal{L}(x) \supset -2\sum_{f=1}^{N_{\rm as}} g\bar{\psi}^f_{(ab)} \gamma^\mu A^c_\mu T^c_{{\rm as}\,(ab)(de)} \psi^f_{(de)}(x) \equiv \mathcal{L}^{\psi\psi A}\,, \tag{D.0.6}$$

where $T_{\rm f}$, $T_{\rm as}$ are generators of the $Sp(4)$ algebra in fundamental and 2-index antisymmetric representations, respectively.
By performing the 1-loop expansion, from the $\mathcal{L}^{\phi\phi A}\times\mathcal{L}^{\phi\phi A}$ term, we get the Feynman diagram in Fig. D.1.

The quantities p_1 and p_2 are the fundamental fermions external momenta, and the corresponding Wick contractions are:

$$\mathcal{I}^{\mu_1\mu_2\alpha'\beta'\,a'b'c'd'}_{A\,f_1,f_2}(p_1,p_2) = 2(-i)^3\left(-\frac{g^2}{2}\right)(\mathbb{I})^{\mu_1\mu_2}\,\xi^{a'b'c'd'}_A \tag{D.0.7}$$

$$\int \frac{d^dl}{(2\pi)^d}\left[\gamma^T_\sigma S^T_{f_2}(p_2+l)\,\Gamma^T_1 S_{f_1}(p_1-l)\,\gamma_\sigma\right]^{\alpha'\beta'} D(l)\,, \tag{D.0.8}$$

where the factor 2 comes from the multiplicity of contraction of ϕ at y_1 or y_2, the colour

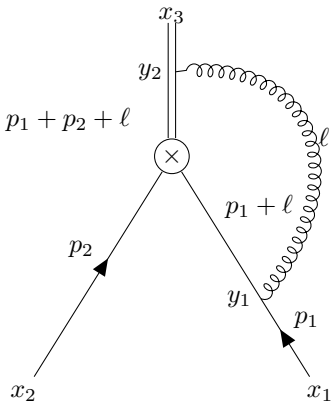

Figure D.2. Diagram B. One-loop Feynman diagram showing a gluon exchange between one fundamental fermion leg and a 2-index antisymmetric one. The vertex ⊗ indicates the presence of the Γ operators coming from Eq. (D.0.1). A "Diagram C" is obtained by exchanging the two fundamental fermion-legs.

factor (saturated by the the colour matrix [CM]) is

$$\xi_A \equiv [\mathrm{CM}]_{a'b'c'd'}\, \xi_A^{a'b'c'd'} = \left[\frac{1}{N}\Omega_{b'c'}\Omega_{a'd'}\right]\left[\Omega_{ad}\Omega_{bc}T_{\mathrm{f}}^{aa'}\cdot T_{\mathrm{f}}^{bb'}\delta^{(cd)(cd')}\right], \tag{D.0.9}$$

$S(p)$ is the fermionic propagator, and it is defined as

$$S(p) = \delta^{ab}\cdot\frac{-i\gamma_\mu p_\mu + m_0}{p_\mu^2 + m_0^2}, \tag{D.0.10}$$

and the gauge field propagator (in Feynman gauge) is defined

$$D_{\mu\nu}^{ab}(l) = \frac{\delta^{ab}}{l^2}\delta_{\mu\nu}\,. \tag{D.0.11}$$

(we will also denote $D(l) \equiv 1/l^2$).
From the expansion term $\mathcal{L}^{\phi\phi A}\times\mathcal{L}^{\psi\psi A}$, one gets the Feynman diagram in Fig. D.2 and the Wick contractions are

$$\mathcal{I}_{B\,f_1}^{\mu_1\mu_2\alpha'\beta'\,a'b'c'd'}(p_1,p_2) = -ig^2\xi_B^{a'b'c'd'}\int\frac{d^dl}{(2\pi)^d}\left[\gamma_\sigma^T S_{f_1}^T(p_1+l)\,\Gamma_1\right]^{\alpha'\beta'}\left[W(p_1+p_2+l)\,\gamma_\sigma\right]^{\mu_1\mu_2}D(l)\,, \tag{D.0.12}$$

where $W(p_1+p_2+l)$ is the propagator for 2-index antisymmetric fermions. The colour factor

(saturated by the colour matrix [CM]) is

$$\xi_B \equiv [\mathrm{CM}]_{a'b'c'd'}\, \xi_B^{a'b'c'd'} = [\frac{1}{N}\Omega_{b'c'}\Omega_{a'd'}][\Omega_{ad}\Omega_{bc}T_{\mathrm{f}}^{aa'}\cdot T_{\mathrm{as}}^{(cd)(c'd')}\delta^{bb'}]\,, \tag{D.0.13}$$

and

$$\mathcal{I}_{C,\,f_1}^{\mu_1\mu_2\alpha'\beta'\,a'b'c'd'}(p_1,p_2) = \mathcal{I}_{B,\,f_2}^{\mu_1\mu_2\alpha'\beta'\,b'a'c'd'}(p_2,p_1)\,. \tag{D.0.14}$$

At one-loop level, also the self-energy corrections at order $\mathcal{O}(g^2)$ require particular care, and the computation for the matching between continuum and lattice results can be found in Ref. [325]. Those results are reported and used at the end of this discussion. Any other Feynman diagram at one-loop order is irrelevant for the renormalisation under consideration. Let us consider external momenta[1], $p_1, p_2 \to 0$. We adopt the $\overline{\mathrm{MS}}$ renormalisation scheme, implemented via naive dimensional regularisation (NDR), as our working prescription.[2]

For diagram A, the structure of the numerator of Eq. (D.0.7) (assuming, for simplicity, zero masses $m_1 = m_2 = 0$) is

$$\mathrm{num}_A\,[\Gamma_1] = -ig^2\xi_A\cdot\left\{\gamma_\sigma^T\gamma_{\mu_2}^T\Gamma_1^T\gamma_{\mu_1}\gamma_\sigma\right\}(+l)^{\mu_2}\,(-l)^{\mu_1}\ . \tag{D.0.15}$$

We consider the operators

$$\Gamma_1 = \{\mathcal{C}\gamma_5, \mathcal{C}\gamma_\alpha\}\ , \tag{D.0.16}$$

and we use the conventions $\mathcal{C}^2 = \mathbb{I}$, $\mathcal{C}^\dagger = -\mathcal{C}$, $\mathcal{C}^T = -\mathcal{C}$ and the commutation rule $\mathcal{C}\gamma_\mu\mathcal{C}^{-1} = -\gamma_\mu^T \Rightarrow \gamma_\mu^T\mathcal{C} = -\mathcal{C}\gamma_\mu$ and $\gamma_5^T = \gamma_5$. After anticommutations of gamma matrices, we get

$$\mathrm{num}_A\,[\mathcal{C}\gamma_5] = -ig^2\xi_A\cdot\left\{\gamma_\sigma^T\gamma_{\mu_2}^T\gamma_5^T\mathcal{C}^T\gamma_{\mu_1}\gamma_\sigma\right\}(+l)^{\mu_2}\,(-l)^{\mu_1} = \tag{D.0.17}$$

$$= +ig^2\xi_A\mathcal{C}\gamma_5\left\{-l^2 d\right\} = ig^2\xi_A\mathcal{C}\gamma_5\{l^2(2\epsilon-4)\}\,. \tag{D.0.18}$$

From diagram B, we can write the numerator of the integral in Eq. (D.0.12) as follows:

$$\mathrm{num}_B\,[\mathcal{C}\gamma_5] = ig^2\xi_B\mathcal{C}\gamma_5\left\{(2\varepsilon-4)l^2\right\}\ , \tag{D.0.19}$$

$$\mathrm{num}_C\,[\mathcal{C}\gamma_5] = \mathrm{num}_B\,[\mathcal{C}\gamma_5] \tag{D.0.20}$$

For the second operator, $\Gamma_1 = \mathcal{C}\gamma_\alpha$, one can write the numerators using FORM [331],

[1] The computation at finite momenta can be performed following the same steps, and it produces the same results, modulo IR terms, coming from the triangle integral [326], $T(p_1, p_1+p_2, 0) \sim \Delta^{\mathrm{IR}}(p_1,p_2)$, that can be treated separately [327] and are irrelevant for the purposes of our matching between two different UV regulations.

[2] While the divergent part of the one-loop correction for the local operator is scheme-independent, the finite part generally depends on the renormalisation scheme. In this work, we use the $\overline{\mathrm{MS}}$ scheme. An alternative is the Breitenlohner–Maison–'t Hooft–Veltman (BMHV) scheme [328–330], which maintains consistency in d dimensions by modifying the treatment of γ_5.

a symbolic manipulation system designed for high-performance algebraic computations in quantum field theory,

$$\mathrm{num}_A\left[\mathcal{C}\gamma_\alpha\right] = -ig^2\xi_A\cdot\left\{\gamma_\sigma^T\gamma_{\mu_2}\gamma_\alpha^T\mathcal{C}^T\gamma_{\mu_1}\gamma_\sigma\right\}. \tag{D.0.21}$$

As we work using dimensional regularisation [332], we use the following identity under $\int d^4l$,

$$d = (4-2\varepsilon) \quad \text{with} \quad \epsilon\to 0\,, \tag{D.0.22}$$

And therefore, we get the numerators

$$\mathrm{num}_A\left[\mathcal{C}\gamma_\alpha\right] = ig^2\xi_A\mathcal{C}\gamma_\alpha\left\{l^2\left(1-\frac{3\varepsilon}{2}\right)\right\}, \tag{D.0.23}$$

$$\mathrm{num}_B[\mathcal{C}\gamma_\alpha] = ig^2\xi_B\mathcal{C}\gamma_\alpha\left\{l^2\left(\frac{3\epsilon}{2}-1\right)\right\}. \tag{D.0.24}$$

We can write these results in terms of scalar one-loop integral [333] ("Bubble integral", B) (for a more recent reference [326]):

$$\begin{aligned}
\mathcal{I}_A[\mathcal{C}\gamma_5] &= ig^2\xi_A\mathcal{C}\gamma_5\left\{(2\epsilon-4)B\left(\lambda\right)\right\},\\
\mathcal{I}_B[\mathcal{C}\gamma_5] &= ig^2\xi_B\mathcal{C}\gamma_5\left\{(2\epsilon-4)B\left(\lambda\right)\right\},\\
\mathcal{I}_C[\mathcal{C}\gamma_5] &= ig^2\xi_B\mathcal{C}\gamma_5\left\{(2\epsilon-4)B\left(\lambda\right)\right\},
\end{aligned} \tag{D.0.25}$$

where we insert λ an infrared regulator (a "gluon mass") in the gluon propagator and

$$\begin{aligned}
B\left(\lambda\right) &= \int\frac{d^dl}{(2\pi)^d}\frac{1}{l^2\left(l+\lambda\right)^2},\\
\mu^{4-d}B(\lambda) &= \frac{i}{16\pi^2}\left[\frac{1}{\varepsilon}+2+\log 4\pi-\gamma_E+\log\left(\frac{\mu^2}{\lambda^2}\right)+\mathcal{O}(\epsilon)\right],
\end{aligned} \tag{D.0.26}$$

μ is a scale introduced so that the integrals preserve their natural dimensions, and $\gamma_E\approx 0.57721$ is the Euler-Mascheroni constant.

We therefore obtain

$$\begin{aligned}
\mathcal{I}_A\left[\mathcal{C}\gamma_5\right] &= ig^2\xi_A\mathcal{C}\gamma_5\left\{(2\epsilon-4)B\left(\lambda\right)\right\}\\
&= +\frac{g^2\xi_A}{16\pi^2}\mathcal{C}\gamma_5\left\{6+4\log\left[\frac{\mu^2}{\lambda^2}\right]+4\left[\frac{1}{\epsilon}+\log 4\pi-\gamma_E\right]\right\},
\end{aligned}$$

$$\begin{aligned}
\mathcal{I}_{B+C}\left[\mathcal{C}\gamma_5\right] &= ig^2\xi_B\mathcal{C}\gamma_5\{(4-2\epsilon)\left(B\left(\lambda\right)+B\left(\lambda\right)\right)\\
&= \frac{g^2}{16\pi^2}\xi_B\mathcal{C}\gamma_5\left\{+12+4\log\left(\frac{\mu^2}{\lambda^2}\right)+4\log\left(\frac{\mu^2}{\lambda^2}\right)+8\left[\frac{1}{\epsilon}+\log 4\pi-\gamma_E\right]\right\},
\end{aligned}$$

$$\mathcal{I}_A\left[\mathcal{C}\gamma_\alpha\right] = ig^2\xi_A\mathcal{C}\gamma_\alpha\left\{\left(1-\frac{3\epsilon}{2}\right)B\left(\lambda\right)\right\} =$$
$$= +\frac{g^2\xi_A}{16\pi^2}\mathcal{C}\gamma_\alpha\left\{-\frac{1}{2}+\log\left[\frac{\mu^2}{\lambda^2}\right]-\left[\frac{1}{\epsilon}+\log 4\pi-\gamma_E\right]\right\},$$
$$\mathcal{I}_{B+C}\left[\mathcal{C}\gamma_\alpha\right] = \frac{g^2}{16\pi^2}\xi_B\mathcal{C}\gamma_\alpha\left\{1+\log\left(\frac{\mu^2}{\lambda^2}\right)+\log\left(\frac{\mu^2}{\lambda^2}\right)+2\left[\frac{1}{\epsilon}+\log 4\pi-\gamma_E\right]\right\}.$$

Putting all together, we can summarise the results in the continuum:

$$\boxed{\begin{aligned}\mathcal{I}\left[\mathcal{C}\gamma_5\right] =& \frac{g^2}{16\pi^2}\left(\mathcal{C}\gamma_5\right)\left\{\xi_A\left[6+4\log\frac{\mu^2}{\lambda^2}+4\delta_{\overline{\text{MS}}}\right]+\right.\\ &\left.\xi_B\left[12+8\log\frac{\mu^2}{\lambda^2}+8\delta_{\overline{\text{MS}}}\right]\right\}\end{aligned}} \tag{D.0.27}$$

and

$$\boxed{\begin{aligned}\mathcal{I}\left[\mathcal{C}\gamma_\alpha\right] =& \frac{g^2}{16\pi^2}\left(\mathcal{C}\gamma_\alpha\right)\left\{\xi_A\left[-\frac{1}{2}-\log\frac{\mu^2}{\lambda^2}-\delta_{\overline{\text{MS}}}\right]+\right.\\ &\left.\xi_B\left[1+2\log\frac{\mu^2}{\lambda^2}+2\delta_{\overline{\text{MS}}}\right]\right\}\end{aligned}} \tag{D.0.28}$$

where

$$\delta_{\overline{\text{MS}}} = \frac{1}{\epsilon}+\log 4\pi-\gamma_E\,, \tag{D.0.29}$$

is the $1/\epsilon$ pole part that one removes in $\overline{\text{MS}}$ scheme. The finite parts for these results depend on the renormalisation scheme one employs, whereas the divergences are scheme-independent.

Lattice computation

For the computations in lattice perturbation theory, following Ref. [334], let us define:

$$S_\mu(p) = \sin\left(ap_\mu\right), \quad C_\mu(p) = \cos\left(ap_\mu\right), \quad \int_l \equiv \int_{-\pi/2}^{\pi/2}\frac{d^4l}{(2\pi)^4}\,, \tag{D.0.30}$$

and the fermion-gluon lines one-vertex Feynman rule [334],

$$\left[V_{\text{R}}\right]^a_{\mu,bc}\left(p,p'\right) = -g\left(T^a_{\text{R}}\right)_{bc}\left\{i\gamma_\mu C_\mu\left(\frac{p+p'}{2}\right)+S_\mu\left(\frac{p+p'}{2}\right)\right\}. \tag{D.0.31}$$

On the lattice, one can write fermion and gluon propagators as follows:

$$D^{ab}_{\mu\nu}(k) = \frac{\delta_{\mu\nu}\delta^{ab}}{\frac{4}{a^4}\sum_\lambda \sin^2\left(\frac{ak_\lambda}{2}\right)}\,, \tag{D.0.32}$$

and

$$S(p) = a\delta^{ab}\frac{-i\sum_\mu \gamma_\mu S_\mu(p) + 2\sum_\mu S_\mu(p/2)S_\mu(p/2)}{\sum_\mu S_\mu(p)S_\mu(p) + 4\left[\sum_\mu S_\mu(p/2)S_\mu(p/2)\right]^2}\,. \tag{D.0.33}$$

From the expansions at one-loop of the lattice actions, in our case, the same Feynman diagrams as D.1 and D.2 are found on the lattice, and the integrals considered are

$$\begin{aligned} L_A[\Gamma] &= \int_l \left[V_\sigma^T\,(p_2, p_2+l)\,S_{f_2}^T(p+e)\Gamma_1^T S_{f_1}\,(p_2-l)\,V_\sigma\,(p_1-l,p_1)\right] D(l)\,,\\ L_B[\Gamma] &= \int_l \left[V_\sigma^T\,(p_1, p_1+l)\,S_{f_1}^T\,(p_1+l)\,\Gamma_1\right]\cdot\left[W\,(p_1+p_2+l)\cdot V_\sigma\,(p_1+p_1+l, p_1+p_2)\right] D(l)\,. \end{aligned} \tag{D.0.34}$$

Expanding Eqs. (D.0.30), (D.0.31), (D.0.32) and (D.0.33) around $ap = 0$,

$$\begin{aligned} \sin\left[a\left(p+\frac{l}{2}\right)\right] &= S_\mu\left(\frac{l}{2}\right) + ap_\mu S_\mu\left(\frac{l}{2}\right) + O(ap)\,,\\ \cos\left[a\left(p+\frac{l}{2}\right)\right] &= S_\mu\left(\frac{l}{2}\right) - ap_\mu S_\mu\left(\frac{l}{2}\right) + O(ap)\,,\\ V(p,p+l) &= gT_R\left[-i\gamma_\mu C_\mu\left(\frac{l}{2}\right) - S_\mu\left(\frac{l}{2}\right)\right] + O(ap)\,,\\ S(p+l) &= a\frac{-i\gamma_\mu S_\mu(p+l) + 2S_\mu\left(\frac{p+l}{2}\right)S_\mu\left(\frac{p+l}{2}\right)}{S_\mu(p+l)S_\mu(p+l) + 4\left[S_\mu\left(\frac{p+l}{2}\right)S_\mu\left(\frac{p+l}{2}\right)\right]^2}\\ &= a\frac{-i\gamma_\mu S_\mu(l) + 2S_\mu\left(\frac{l}{2}\right)S_\mu\left(\frac{l}{2}\right)}{S_\mu(l)S_\mu(l) + 4\left(S_\mu\left(\frac{l}{2}\right)S_\mu\left(\frac{l}{2}\right)\right]^2} + O(ap)\,. \end{aligned} \tag{D.0.35}$$

We can then express the integrals in Eq. (D.0.34) to the order in $\mathcal{O}(ap)$:

$$\begin{aligned} L_A[\Gamma] = g^2\xi_A \int_l &\left[-i\gamma_\sigma^T C_\sigma\left(\frac{l}{2}\right) - S_\sigma\left(\frac{l}{2}\right)\right]\frac{-i\gamma_\mu S_\mu(l) + 2\Delta(l)}{G(l)+4\Delta(l)^2}\\ &\Gamma_1^T\frac{i\gamma_\nu S_\nu(l) + 2\Delta(l)}{G(l)+4\Delta(l)^2}\quad\left[-i\gamma_\sigma C_\sigma\left(\frac{l}{2}\right) + S_\sigma\left(\frac{l}{2}\right)\right],\\ L_B[\Gamma] = g^2\xi_B \int_l &\left[-i\gamma_\sigma^T C_\sigma\left(\frac{l}{2}\right) - S_\sigma\left(\frac{l}{2}\right)\right]\frac{-i\gamma_\mu^T S_\mu(l) + 2\Delta(l)}{G(l)+4\Delta(l)^2}\Gamma_1\\ &\frac{-i\gamma_\nu S_\nu(l) + 2\Delta(l)}{G(l)+4\Delta(l)^2}\left[-i\gamma_\sigma C_\sigma\left(\frac{l}{2}\right) - S_\sigma\left(\frac{l}{2}\right)\right]. \end{aligned} \tag{D.0.36}$$

We adopt the definitions:

$$\begin{aligned} &\Delta(l) = \textstyle\sum_\mu \sin\left(\frac{al_\mu}{2}\right)\sin\left(a\frac{l_\mu}{2}\right),\quad H(l) = \textstyle\sum_\mu \sin(al_\mu)\sin(al_\mu)\,,\\ &G(l) = H(l) + 4\Delta^2(l),\qquad\qquad \Theta(l) = \textstyle\sum_\mu S_\mu^2(l)S_\mu^2\left(\frac{l}{2}\right). \end{aligned} \tag{D.0.37}$$

Using FORM, the numerators can be rewritten in the following forms

$$\mathrm{num}_A\left[\mathcal{C}\gamma_5\right] = g^2\xi_A\mathcal{C}\gamma_5\left\{4H(l)+16\Delta^2(l)\right\}, \tag{D.0.38}$$

$$\mathrm{num}_B\left[\mathcal{C}\gamma_5\right] = \mathrm{num}_C\left[\mathcal{C}\gamma_5\right] = g^2\xi_B\mathcal{C}\gamma_5\left\{4H(l)+2\Delta(l)H(l)-16\Delta^2(l)+8\Delta^3(l)\right\}, \tag{D.0.39}$$

$$\mathrm{num}_A\left[\mathcal{C}\gamma_\alpha\right] = g^2\xi_B\mathcal{C}\gamma_a\left\{-H(l)-\frac{3}{2}\Delta(l)H(l)+\Theta(l)-8\Delta^2(l)-2\Delta^3(l)\right\}, \tag{D.0.40}$$

$$\mathrm{num}_B\left[\mathcal{C}\gamma_\alpha\right] = \mathrm{num}_C\left[\mathcal{C}\gamma_\alpha\right] = g^2\xi_B C\gamma_\alpha\left\{H(l)+\frac{5}{2}\Delta(l)H(l)-\Theta(l)-8\Delta(l)^2+6\Delta^3(l)\right\}. \tag{D.0.41}$$

The following integrals appear,

$$\begin{aligned}
\widetilde{T}^{(n)} &= \int_{-\pi}^{\pi}\frac{d^4l}{(2\pi)^n}\frac{H(l)\cdot\Delta^n(l)}{4G(l)^2\left[\Delta(l)+a^2\lambda^2\right]} \quad n\geq 0\,,\\
T^{(n)} &= \int_{-\pi}^{\pi}\frac{d^n\ell}{(2\pi)^a}\frac{\Delta^n(l)}{4G(l)^2\left[\Delta(l)+a^2\lambda^2\right]} \quad n\geq 1\,,\\
P &= \int_{-\pi}^{\pi}\frac{d^4l}{(2\pi)^a}\frac{\Theta(l)}{4G(l)^2\left[\Delta(l)+a^2\lambda^2\right]}\,.
\end{aligned} \tag{D.0.42}$$

where λ is an infrared regulator (a "gluon mass") that one inserts in the gluon propagator in Eq. (D.0.32) to regulate divergences and isolate logarithmic divergent terms.
$\widetilde{T}^{(0)}$ and $T^{(1)}$ are divergent as $a\to 0$. It is a standard trick in the literature [334] to perform the following split in order to isolate the $a\to 0$ divergence:

$$\int_{hypercube} f(a) = \int_{hypercube} f(a) - \int_{4-sphere,|r|<1} f(a) + \int_{4-sphere,|r|<1} f(a)\,, \tag{D.0.43}$$

and the first two terms in the sum are finite as $a\to 0$.

Let us study the integrands as $a\to 0$

$$\begin{aligned}
H(l) &= \sum_\alpha \sin^2\left(l_\alpha a\right) \to l_\alpha l^\alpha a^2 = a^2l^2\,,\\
\Delta(l) &= \sum_\alpha \sin\left(\frac{l_\alpha a}{2}\right)\sin\left(\frac{l_\alpha a}{2}\right) \to a^2l^2/4\,,\\
G(l) &\to a^2 l_\alpha l^\alpha + \frac{1}{4}\left(a^2 l_\alpha l^\alpha\right)^2 = a^2l^2 + a^4l^4/4 \sim a^2l^2 + \mathcal{O}\left(l^2\right)\,,\\
G(l)^2 &\to a^4l^4 + \frac{1}{2}a^6l^6 + \frac{1}{16}a^8l^8 \sim a^4l^4 + \mathcal{O}\left(l^4\right)\,.
\end{aligned} \tag{D.0.44}$$

Then, for $T^{(0)}$, we can capture the divergence by adding and subtracting

$$\lim_{a\to 0}\int_{4-sphere}\frac{d^4l}{(2\pi)^4}\frac{H(l)}{4G(l)^2\left[\Delta(l)+\frac{a^2\lambda^2}{4}\right]} = \int_{4-sphere}\frac{d^4l}{(2\pi)^4}\frac{1}{l^2\left(l^2+a^2\lambda^2\right)}\,. \tag{D.0.45}$$

While for T^1 it is 1/4 of it. Let us compute this integral. Recall that

$$\begin{aligned} &d(4-sphere) = r^{d-1}\sin^{d-2}\theta_1\sin^{d-3}\theta_2\ldots\sin\theta_{d-2}\,dr d\theta_1\ldots d\theta_{d-1}\,,\\ &\int_{4-sphere}\frac{d^4l}{(2\pi)^4}\frac{1}{l^2\left(l^2+a^2\lambda^2\right)} = \frac{2\pi^2}{(2\pi)^4}\int_0^1 dr\frac{r^3}{r^2\left(r^2+a^2\lambda^2\right)} = \\ &= \frac{1}{8\pi^2}\int_0^1 dr\frac{r}{r^2+a^2\lambda^2} = \frac{1}{8\pi^2}\frac{1}{2}\log\left(r^2+a^2\lambda^2\right)\Big|_0^1 \end{aligned} \tag{D.0.46}$$

$$\Rightarrow \widetilde{T}^{(0)}_{\Theta} = -\frac{1}{16\pi^2}\log\left(a^2\lambda^2\right)\,, \tag{D.0.47}$$

and this is one of the aforementioned logarithmic divergent terms isolated through the infrared regulator, λ.

The rest of the integrals are finite and can be computed numerically. We use multidimensional integrals evaluation Vegas package [335] and the result is:

$$\widetilde{T}^{(0)} - \widetilde{T}^{(0)}_{\Theta} = \int_{-\pi}^{\pi}\frac{d^4l}{(2\pi)^4}\left[\frac{H(l)}{4G(l)^2\Delta(l)} - \frac{\theta\left(1-|l|^2\right)}{l^4}\right] = 0.005617(3)\,. \tag{D.0.48}$$

The full result for this diagram reads

$$\begin{aligned} \mathcal{L}_A\left[\mathcal{C}\gamma_5\right] &= g^2\xi_A\mathcal{C}\gamma_5\left[4\widetilde{T}^{(0)}+16T^{(2)}\right] = g^2\xi_A\mathcal{C}\gamma_5\left[4\left(\widetilde{T}^{(0)}-\widetilde{T}^{(0)}_{\Theta}\right)+4\widetilde{T}^{(0)}_{\Theta}+16T^{(2)}\right]\\ &= g^2\xi_A\mathcal{C}\gamma_5\frac{1}{4\pi^2}\left[-\log\left(a^2\lambda^2\right)+2.9352(6)\right]\\ &= \frac{g^2}{16\pi^2}\xi_A\mathcal{C}\gamma_5\left[-4\log\left(a^2\lambda^2\right)+11.748(2)\right]\,. \end{aligned} \tag{D.0.49}$$

We similarly evaluate B and C

$$\begin{aligned} &\mathrm{num}_B\left[\mathcal{C}\gamma_5\right] = \mathrm{num}_C\left[\mathcal{C}\gamma_5\right] = g^2\xi_B\mathcal{C}\gamma_5\left(4H(l)+2\Delta(l)H(l)-16\Delta^2(l)+8\Delta^3(l)\right)\\ &L_B+L_C = g^2\xi_B\mathcal{C}\gamma_5\left(8\widetilde{T}^{(0)}+4\widetilde{T}^{(1)}-32T^{(2)}+16T^{(3)}\right)\\ &= g^2\xi_B\mathcal{C}\gamma_5\left(-\frac{1}{2\pi^2}\log\left(a^2\lambda^2\right)+8\left(\widetilde{T}^{(0)}-\widetilde{T}^{(0)}_{\Theta}\right)+4\widetilde{T}^{(1)}-32T^{(2)}+16T^{(3)}\right) \end{aligned} \tag{D.0.50}$$

$$= g^2\xi_B\mathcal{C}\gamma^5\frac{1}{16\pi^2}\left(-8\log\left(a^2\lambda^2\right)+4.206(5)\right)\,. \tag{D.0.51}$$

The lattice result for $\Gamma_1 = \mathcal{C}\gamma_5$ is:

$$\boxed{L[\mathcal{C}\gamma_5] = \frac{g^2}{16\pi^2}\mathcal{C}\gamma_5\left\{-4\xi_A\log\left(a^2\lambda^2\right)+\xi_A 11.748-8\xi_B\log\left(a^2\lambda^2\right)+\xi_B 4.206\right\}} \tag{D.0.52}$$

For $\Gamma = \mathcal{C}\gamma_\alpha$,

$$\begin{aligned} L_A[\mathcal{C}\gamma_\alpha] &= g^2\xi_A\mathcal{C}\gamma_\alpha\left\{-\widetilde{T}^{(0)} - \frac{3}{2}\widetilde{T}^{(1)} + P - 8T^{(2)} - 2T^{(3)}\right\} \\ &= g^2\xi_A\mathcal{C}\gamma_\alpha\left\{-\left(\widetilde{T}^{(0)} - \widetilde{T}^{(0)}_\Theta\right) - \widetilde{T}^{(0)}_\Theta - \frac{3}{2}\widetilde{T}^{(1)} + P - 8T^{(2)} - 2T^{(3)}\right\} \\ &= \frac{g^2}{16\pi^2}\mathcal{C}\gamma_\alpha\xi_A\left\{+\log\left(a^2\lambda^2\right) - 7.2644(11)\right\} \end{aligned} \tag{D.0.53}$$

$$\begin{aligned} &L_{B+C}[\mathcal{C}\gamma_\alpha] = g^2\xi_B\mathcal{C}\gamma_\alpha\left\{2\widetilde{T}^{(0)} + 5\widetilde{T}^{(1)} - 2P - 16T^{(2)} + 12T^{(3)}\right\} = \\ &= \frac{g^2}{16\pi^2}\xi_B\mathcal{C}\gamma_\alpha\left\{-2\log\left(a^2\lambda^2\right) + 4.8870(16)\right\} \end{aligned} \tag{D.0.54}$$

As in the continuum theory case, the divergent terms are independent of the regularisation scheme, whereas the finite terms depend on the specific scheme employed.

Results

Subtracting between the continuum (Eqs. (D.0.27) and (D.0.28)) and lattice results (Eq. (D.0.52), Eq. (D.0.53) and (D.0.54)), and removing the UV-logarithmic divergences in the continuum and on the lattice:

$$\Delta_\Gamma[\mathcal{C}\gamma_5] = \mathcal{I}[\mathcal{C}\gamma_5] - L[\mathcal{C}\gamma_5] = \tag{D.0.55}$$

$$= -\xi_A 5.748(2) + \xi_B 7.794(5) + 8\xi_A\log(a\mu) + 16\xi_B\log(a\mu)\,. \tag{D.0.56}$$

Then

$$\Delta_\Gamma[\mathcal{C}\gamma_\alpha] = \mathcal{I}[\mathcal{C}\gamma_\alpha] - L[\mathcal{C}\gamma_\alpha] = \tag{D.0.57}$$

$$= \xi_A 6.724(1) - \xi_B 3.887(2) - 2\xi_A\log(a\mu) + 4\xi_B\log(a\mu)\,. \tag{D.0.58}$$

Let us finally give an explicit expression for the colour factor. We assume that the colour structure of the fermion legs is the same as the one of the operator. We can compute the colour factors for the diagrams A and B:

$$\xi_A = C_\mathrm{f} \quad \xi_B = C_\mathrm{f}\,(2 - N)\,. \tag{D.0.59}$$

Therefore, using a common choice for the renormalisation scale ($\mu = 1/a$), we find

$$\begin{aligned} \Delta_\Gamma[\mathcal{C}\gamma_5] &= C_\mathrm{f}\left\{-5.748(2) - (N-2)\,7.794(5)\right\}\,, \\ \Delta_\Gamma[\mathcal{C}\gamma_\alpha] &= C_\mathrm{f}\left\{6.724(1) + (N-2)\,3.887(2)\right\}\,, \end{aligned} \tag{D.0.60}$$

using $N = 4$, $C_f = 5/4$ for $Sp(4)$,

$$\begin{aligned} \Delta_\Gamma[\mathcal{C}\gamma_5] &= -26.670(13)\,, \\ \Delta_\Gamma\left[\mathcal{C}\gamma_\alpha\right] &= 18.123(5)\,. \end{aligned} \tag{D.0.61}$$

Using the $\overline{\text{MS}}$ renormalisation scheme and following Ref. [334], we get at order $\mathcal{O}\left(g^2\right)$, the following conversion factor:

$$\Gamma_{\overline{\text{MS}}} = \left\{1 + \frac{\tilde{g}^2}{16\pi^2}\left(\left[C_f + \frac{1}{2}C_{as}\right]\Delta_{\Sigma_1} + \Delta_\Gamma\right)\right\}\Gamma_{\text{lattice}} \tag{D.0.62}$$

$$\Delta_\Gamma\left[\mathcal{C}\gamma_5\right] = -26.670(13) \tag{D.0.63}$$

$$\Delta_\Gamma\left[\mathcal{C}\gamma_\alpha\right] = 18.123(5) \tag{D.0.64}$$

$$\Delta_{\Sigma_1} = -12.82 \tag{D.0.65}$$

The self-energy contribution to the conversion factor, Δ_{Σ_1}, is taken from Ref. [214]. The coupling used in Eq. (D.0.62) is defined through a mean field treatment of the link variable, which effectively absorbs the contributions of tadpole diagrams. In this approach, the improved coupling is given by $\tilde{g}^2 = g^2/\langle P\rangle$, where $\langle P\rangle$ is the average plaquette value and g denotes the bare gauge coupling.

Appendix E

Formulas used in `LSDensities`

In this appendix, we show details of our implementation of the HLT method. Let us assume $a = 1$ to simplify the notation. As described in Chapter 3, the functional $W[\vec{g}]$ in Eq. (3.5.13) consists of two parts: the systematic-error functional $A[\vec{g}]/A_0$ and the statistical-error functional B/B_{norm}. The minimisation of $W[\vec{g}]$ equals to solving the linear system

$$\vec{g} = \left(\mathtt{S} + \frac{\lambda A_0}{B_{\text{norm}}}\,\mathtt{B}\right)^{-1} \vec{\mathtt{f}}\,. \tag{E.0.1}$$

where B_{norm} is defined below Eq. (3.5.13). The matrix $\mathtt{S}$ descends from minimising in $A[\vec{g}]/A_0$ the contribution quadratic in $\vec{g}$. Its matrix elements can always be expressed as follows

$$\begin{aligned}\mathtt{S}_{tr} &= \int_{E_{\min}}^{\infty} dE e^{\alpha E}\, b(t+1,E)\, b(r+1,E) = \\ &= \frac{e^{E_{\min}(\alpha-r-t-2)}}{t+r+2-\alpha} + \frac{e^{E_{\min}(\alpha+r+t+2-2T)}}{2T-t-r-2-\alpha} + \frac{e^{E_{\min}(\alpha+r-t-T)}}{T+t-r-\alpha} + \frac{e^{E_{\min}(\alpha-r+t-T)}}{T-t+r-\alpha}\,,\end{aligned} \tag{E.0.2}$$

where $b(t,E)$ are the functions defined in Eq. (3.5.2), where $\mathtt{S}$ is a $t_{\max} \times t_{\max}$ matrix.
The error functional $B[\vec{g}]/B_{\text{norm}}$ contributes another functional quadratic part in $\vec{g}$, minimised by

$$\mathtt{B}_{tr} = \text{Cov}_{tr}\,. \tag{E.0.3}$$

The vector $\vec{f}$ appears due to the minimisation of terms linear in $\vec{g}$ inside $A[\vec{g}]/A_0$. Its entries are defined to coincide with f_{t+1}, where

$$f_t(\omega) = \int_{E_{\min}}^{\infty} dE\; \Delta_\sigma(E,\omega)\, e^{\alpha E}\, b(t,E)\,. \tag{E.0.4}$$

For a Gaussian kernel, $A_0(\omega)$ and the entries $f_{t+1}(\omega)$ from Eq. (E.0.4) are calculable:

$$A_0(\omega) \equiv A[0](\omega) = \int_{E_{\min}}^{\infty} dE\, e^{\alpha E}\left[\Delta_\sigma^{(1)}(E,\omega)\right]^2 = \frac{\text{Erf}\left(\frac{\omega - E_{\min} + \alpha\sigma^2/2}{\sigma}\right) + 1}{\sigma\sqrt{\pi}\left(\text{Erf}\left(\frac{\omega}{\sqrt{2}\sigma}\right) + 1\right)^2}\, e^{\alpha\omega + \alpha^2\sigma^2/4}\,, \tag{E.0.5}$$

and

$$\tilde{f}_t(\omega) = \int_{E_{\min}}^{\infty} dE\, \Delta_\sigma^{(1)}(E,\omega)\, e^{(-t+\alpha)E} = \frac{e^{\frac{\sigma^2}{2}(\alpha-t)^2} e^{(\alpha-t)\omega} \left\{1 - \mathrm{Erf}\left[\frac{E_{\min}-\omega+\sigma^2(t-\alpha)}{\sqrt{2}\sigma}\right]\right\}}{1 + \mathrm{Erf}\left[\frac{\omega}{\sigma\sqrt{2}}\right]}\,, \quad \text{(E.0.6)}$$

respectively, with

$$f_t(\omega) = \tilde{f}_t(\omega) + \tilde{f}_{T-t}(\omega)\,. \quad \text{(E.0.7)}$$

For the Cauchy kernel, the integrals have to be computed numerically.

Appendix F

Tables for spectral density findings

In this appendix, we present the tables containing the relevant results of this thesis, obtained through spectral density investigations. The results are computed for the meson spectrum in consideration (Tab. 3.1) and the baryon one (Tab. 3.2). The renormalised matrix elements and overlap factors are also reported.

Table F.1. Ground-state meson masses extracted from ensemble M1 are summarised using different spectral reconstruction strategies. Each entry corresponds to a specific mesonic channel C. The mass am_C is obtained from a Generalised Eigenvalue Problem (GEVP) analysis. We report results from spectral density fits using both Gaussian and Cauchy kernel bases: a k-G fit employs a sum of k Gaussian functions, while a $(k+1)$-G fit adds one more Gaussian component. Similarly, k-C and $(k+1)$-C refer to fits using Cauchy functions. The smearing radii used for each reconstruction are denoted by σ_G (Gaussian) and σ_C (Cauchy). Wuppertal smearing is applied with $N_{\text{source}} = 80$ steps at the source and no smearing at the sink ($N_{\text{sink}} = 0$).

C	k	aE_0 k-G	aE_0 $(k+1)$-G	aE_0 k-C	aE_0 $(k+1)$-C	am_C	σ_G/m_C	σ_C/m_C
PS	2	0.3545(30)	0.3546(18)	0.3543(18)	0.3543(18)	0.35435(11)	0.33	0.32
V	3	0.3999(32)	0.3996(31)	0.3994(32)	0.4006(31)	0.4018(14)	0.3	0.22
T	3	0.4003(29)	0.4003(29)	0.4018(30)	0.4021(31)	0.4016(15)	0.3	0.3
AV	2	0.5340(43)	0.5345(45)	0.5345(45)	0.53420(80)	0.5357(36)	0.2	0.18
AT	2	0.5215(28)	0.5217(31)	0.5260(50)	0.5246(41)	0.5246(69)	0.18	0.2
S	2	0.5171(46)	0.5167(46)	0.5198(33)	0.5165(51)	0.5147(42)	0.2	0.2
ps	3	0.5882(53)	0.5844(54)	0.5846(23)	0.5858(11)	0.58529(86)	0.18	0.2
v	2	0.6441(12)	0.6431(12)	0.6454(12)	0.6456(22)	0.64459(86)	0.2	0.26
t	2	0.6540(16)	0.6545(26)	0.6442(28)	0.6445(13)	0.64465(93)	0.2	0.26
av	2	0.8283(75)	0.8285(75)	0.8202(37)	0.8201(38)	0.8283(48)	0.2	0.18
at	3	0.8477(42)	0.8477(38)	0.8387(63)	0.8389(62)	0.8423(43)	0.18	0.18
s	3	0.7947(66)	0.7946(67)	0.7855(42)	0.7867(42)	0.7923(25)	0.18	0.2

Table F.2. First excited state meson masses extracted from ensemble M1 are summarised using different spectral reconstruction strategies. Each entry corresponds to a specific mesonic channel C. The mass am_C is obtained from a Generalised Eigenvalue Problem (GEVP) analysis. We report results from spectral density fits using both Gaussian and Cauchy kernel bases: a k-G fit employs a sum of k Gaussian functions, while a $(k+1)$-G fit adds one more Gaussian component. Similarly, k-C and $(k+1)$-C refer to fits using Cauchy functions. The smearing radii used for each reconstruction are denoted by σ_G (Gaussian) and σ_C (Cauchy). Wuppertal smearing is applied with $N_{\text{source}} = 80$ steps at the source and no smearing at the sink ($N_{\text{sink}} = 0$).

C	k	aE_1 k-G	aE_1 $(k+1)$-G	aE_1 k-C	aE_1 $(k+1)$-C	am_C	σ_G/m_C	σ_C/m_C
PS	2	0.6723(42)	0.6792(72)	0.6721(40)	0.6718(40)	0.6745(94)	0.33	0.32
V	3	0.704(14)	0.703(14)	0.705(13)	0.714(12)	0.7027(86)	0.3	0.22
T	3	0.696(18)	0.696(18)	0.695(17)	0.6951(19)	0.696(11)	0.3	0.3
AV	2	0.715(13)	0.706(13)	0.707(11)	0.702(11)	0.702(38)	0.2	0.18
AT	2	0.701(14)	0.691(14)	0.714(21)	0.709(14)	0.704(21)	0.18	0.2
S	2	0.741(17)	0.740(17)	0.737(13)	0.737(13)	0.722(30)	0.2	0.2
ps	3	0.927(13)	0.927(11)	0.913(18)	0.912(17)	0.914(11)	0.18	0.2
v	2	0.9370(41)	0.9370(41)	0.9383(68)	0.9375(66)	0.9495(72)	0.2	0.26
t	2	0.948(21)	0.947(22)	0.9303(10)	0.9303(13)	0.9426(86)	0.2	0.26
av	2	1.092(31)	1.092(31)	1.099(29)	1.084(22)	1.093(13)	0.2	0.18
at	3	1.107(11)	1.119(10)	1.106(24)	1.106(26)	1.098(28)	0.18	0.18
s	3	1.062(11)	1.061(14)	1.064(12)	1.068(13)	1.065(25)	0.18	0.2

Table F.3. Second excited state meson masses extracted from ensemble M1 are summarised using different spectral reconstruction strategies. Each entry corresponds to a specific mesonic channel C. The mass am_C is obtained from a Generalised Eigenvalue Problem (GEVP) analysis. We report results from spectral density fits using both Gaussian and Cauchy kernel bases: a k-G fit employs a sum of k Gaussian functions, while a $(k+1)$-G fit adds one more Gaussian component. Similarly, k-C and $(k+1)$-C refer to fits using Cauchy functions. The smearing radii used for each reconstruction are denoted by σ_G (Gaussian) and σ_C (Cauchy). Wuppertal smearing is applied with $N_{\text{source}} = 80$ steps at the source and no smearing at the sink ($N_{\text{sink}} = 0$).

C	k	aE_2 k-G	aE_2 $(k+1)$-G	aE_2 k-C	aE_2 $(k+1)$-C	am_C	σ_G/m_C	σ_C/m_C
PS	2	-	-	-	-	1.074(79)	0.33	0.32
V	3	0.983(31)	0.987(31)	0.992(29)	0.984(30)	1.002(93)	0.3	0.22
T	3	0.970(29)	0.960(29)	0.961(28)	0.973(30)	0.947(93)	0.3	0.3
AV	2	-	-	-	-	-	0.2	0.18
AT	2	-	-	-	-	-	0.18	0.2
S	2	-	-	-	-	-	0.2	0.2
ps	3	1.217(29)	1.224(30)	1.224(47)	1.250(45)	1.210(53)	0.18	0.2
v	2	-	-	-	-	-	0.2	0.26
t	2	-	-	-	-	-	0.2	0.26
av	2	-	-	-	-	-	0.2	0.18
at	3	1.400(41)	1.401(44)	1.418(41)	1.4280(45)	1.463(50)	0.18	0.18
s	3	1.383(48)	1.389(49)	1.381(39)	1.382(40)	1.389(39)	0.18	0.2

Table F.4. Ground-state meson masses extracted from ensemble M2 are summarised using different spectral reconstruction strategies. Each entry corresponds to a specific mesonic channel C. The mass am_C is obtained from a Generalised Eigenvalue Problem (GEVP) analysis. We report results from spectral density fits using both Gaussian and Cauchy kernel bases: a k-G fit employs a sum of k Gaussian functions, while a $(k+1)$-G fit adds one more Gaussian component. Similarly, k-C and $(k+1)$-C refer to fits using Cauchy functions. The smearing radii used for each reconstruction are denoted by σ_G (Gaussian) and σ_C (Cauchy). Wuppertal smearing is applied with $N_{\text{source}} = 80$ steps at the source and no smearing at the sink ($N_{\text{sink}} = 0$)..

C	k	aE_0 k-G	aE_0 $(k+1)$-G	aE_0 k-C	aE_0 $(k+1)$-C	am_C	σ_G/m_C	σ_C/m_C
PS	2	0.3557(25)	0.3559(21)	0.3555(17)	0.3559(15)	0.35593(88)	0.35	0.3
V	3	0.3968(20)	0.3963(13)	0.3963(23)	0.3960(80)	0.3964(13)	0.28	0.33
T	3	0.3957(33)	0.3967(24)	0.3950(40)	0.3960(30)	0.3965(14)	0.23	0.23
AV	3	0.5431(44)	0.5433(44)	0.5421(13)	0.5442(11)	0.5431(36)	0.3	0.18
AT	3	0.5494(26)	0.5493(27)	0.5453(27)	0.5512(50)	0.5426(32)	0.3	0.2
S	2	0.5250(47)	0.5246(40)	0.5250(14)	0.5250(22)	0.5245(31)	0.3	0.2
ps	3	0.5932(11)	0.5939(12)	0.5931(22)	0.5932(22)	0.59399(62)	0.18	0.18
v	2	0.63840(90)	0.63840(90)	0.63840(90)	0.63840(90)	0.6380(10)	0.2	0.2
t	2	0.6384(12)	0.6367(14)	0.6378(10)	0.6379(10)	0.6375(11)	0.2	0.2
av	3	0.8346(80)	0.8366(76)	0.8363(80)	0.8369(22)	0.8349(35)	0.18	0.18
at	3	0.8442(48)	0.8450(48)	0.8440(41)	0.8430(43)	0.8440(39)	0.18	0.23
s	3	0.7966(55)	0.7987(56)	0.79010(99)	0.7900(10)	0.7984(33)	0.18	0.18

Table F.5. First excited state meson masses extracted from ensemble M2 are summarised using different spectral reconstruction strategies. Each entry corresponds to a specific mesonic channel C. The mass am_C is obtained from a Generalised Eigenvalue Problem (GEVP) analysis. We report results from spectral density fits using both Gaussian and Cauchy kernel bases: a k-G fit employs a sum of k Gaussian functions, while a $(k+1)$-G fit adds one more Gaussian component. Similarly, k-C and $(k+1)$-C refer to fits using Cauchy functions. The smearing radii used for each reconstruction are denoted by σ_G (Gaussian) and σ_C (Cauchy). Wuppertal smearing is applied with $N_{\text{source}} = 80$ steps at the source and no smearing at the sink ($N_{\text{sink}} = 0$).

C	k	aE_1 k-G	aE_1 $(k+1)$-G	aE_1 k-C	aE_1 $(k+1)$-C	am_C	σ_G/m_C	σ_C/m_C
PS	2	0.6781(11)	0.6794(58)	0.6721(54)	0.6789(51)	0.6764(68)	0.35	0.3
V	3	0.6685(89)	0.6674(50)	0.6699(68)	0.667(10)	0.668(17)	0.28	0.33
T	3	0.6928(94)	0.695(13)	0.7047(87)	0.704(11)	0.682(12)	0.23	0.23
AV	3	0.7806(90)	0.7803(68)	0.795(15)	0.794(15)	0.791(10)	0.3	0.18
AT	3	0.797(10)	0.797(10)	0.797(17)	0.7984(92)	0.808(12)	0.3	0.2
S	2	0.766(12)	0.7698(99)	0.770(11)	0.765(13)	0.765(13)	0.3	0.2
ps	3	0.905(11)	0.905(10)	0.9003(90)	0.9036(80)	0.908(11)	0.18	0.18
v	2	0.9199(63)	0.9196(36)	0.94520(10)	0.9444(34)	0.9310(93)	0.2	0.2
t	2	0.929(23)	0.926(23)	0.9421(36)	0.9422(28)	0.930(11)	0.2	0.2
av	3	1.052(22)	1.048(14)	1.063(23)	1.059(18)	1.054(20)	0.18	0.18
at	3	1.081(22)	1.084(23)	1.081(34)	1.0816(53)	1.119(54)	0.18	0.23
s	3	1.020(29)	1.020(30)	1.0090(70)	1.022(15)	1.032(39)	0.18	0.18

Table F.6. Second excited state meson masses extracted from ensemble M2 are summarised using different spectral reconstruction strategies. Each entry corresponds to a specific mesonic channel C. The mass am_C is obtained from a Generalised Eigenvalue Problem (GEVP) analysis. We report results from spectral density fits using both Gaussian and Cauchy kernel bases: a k-G fit employs a sum of k Gaussian functions, while a $(k+1)$-G fit adds one more Gaussian component. Similarly, k-C and $(k+1)$-C refer to fits using Cauchy functions. The smearing radii used for each reconstruction are denoted by σ_G (Gaussian) and σ_C (Cauchy). Wuppertal smearing is applied with $N_{\text{source}} = 80$ steps at the source and no smearing at the sink ($N_{\text{sink}} = 0$).

C	k	aE_2 k-G	aE_2 $(k+1)$-G	aE_2 k-C	aE_2 $(k+1)$-C	am_C	σ_G/m_C	σ_C/m_C
PS	2	-	-	-	-	-	0.35	0.3
V	3	0.960(22)	0.975(21)	0.978(29)	0.969(18)	-	0.28	0.33
T	3	0.979(35)	0.970(40)	0.960(30)	0.973(26)	-	0.23	0.23
AV	3	1.171(23)	1.172(22)	1.172(19)	1.180(21)	-	0.3	0.18
AT	3	1.0589(22)	1.0563(98)	1.057(15)	1.054(15)	-	0.3	0.2
S	2	-	-	-	-	-	0.3	0.2
ps	3	1.256(11)	1.253(20)	1.248(36)	1.258(56)	1.261(36)	0.18	0.18
v	2	-	-	-	-	-	0.2	0.2
t	2	-	-	-	-	-	0.2	0.2
av	3	1.424(50)	1.424(40)	1.435(47)	1.429(51)	-	0.18	0.18
at	3	1.387(10)	1.3856(88)	1.385(24)	1.382(28)	-	0.18	0.23
s	3	1.355(65)	1.360(69)	1.362(43)	1.360(49)	-	0.18	0.18

Table F.7. Ground-state meson masses extracted from ensemble M3 are summarised using different spectral reconstruction strategies. Each entry corresponds to a specific mesonic channel C. The mass am_C is obtained from a Generalised Eigenvalue Problem (GEVP) analysis. We report results from spectral density fits using both Gaussian and Cauchy kernel bases: a k-G fit employs a sum of k Gaussian functions, while a $(k+1)$-G fit adds one more Gaussian component. Similarly, k-C and $(k+1)$-C refer to fits using Cauchy functions. The smearing radii used for each reconstruction are denoted by σ_G (Gaussian) and σ_C (Cauchy). Wuppertal smearing is applied with $N_{\text{source}} = 80$ steps at the source and no smearing at the sink ($N_{\text{sink}} = 0$).

C	k	aE_0 k-G	aE_0 $(k+1)$-G	aE_0 k-C	aE_0 $(k+1)$-C	am_C	σ_G/m_C	σ_C/m_C
PS	2	0.3639(31)	0.3625(27)	0.3629(12)	0.3628(11)	0.36239(72)	0.3	0.27
V	3	0.4010(50)	0.4000(20)	0.4017(24)	0.4017(23)	0.40267(81)	0.28	0.25
T	3	0.3996(13)	0.3999(18)	0.4013(27)	0.4010(25)	0.40244(86)	0.33	0.28
AV	3	0.5391(51)	0.5387(51)	0.5444(22)	0.5426(39)	0.5396(30)	0.28	0.32
AT	3	0.5422(23)	0.5421(24)	0.5441(26)	0.5447(21)	0.5433(29)	0.3	0.18
S	2	0.5137(36)	0.5142(31)	0.5191(31)	0.5196(20)	0.5159(31)	0.3	0.24
ps	3	0.59920(44)	0.59940(50)	0.59973(20)	0.59960(44)	0.59975(41)	0.23	0.22
v	2	0.6454(15)	0.6454(12)	0.6425(25)	0.6499(39)	0.64543(78)	0.24	0.25
t	2	0.6461(12)	0.64620(80)	0.6469(11)	0.64660(90)	0.6469(11)	0.28	0.28
av	3	0.8371(76)	0.8364(78)	0.8335(32)	0.8357(10)	0.8353(49)	0.18	0.25
at	3	0.8337(37)	0.8322(50)	0.8387(10)	0.8388(11)	0.8376(42)	0.25	0.25
s	3	0.8026(42)	0.8036(39)	0.8016(46)	0.8026(14)	0.8021(42)	0.23	0.23

Table F.8. First excited state meson masses extracted from ensemble M3 are summarised using different spectral reconstruction strategies. Each entry corresponds to a specific mesonic channel C. The mass am_C is obtained from a Generalised Eigenvalue Problem (GEVP) analysis. We report results from spectral density fits using both Gaussian and Cauchy kernel bases: a k-G fit employs a sum of k Gaussian functions, while a $(k+1)$-G fit adds one more Gaussian component. Similarly, k-C and $(k+1)$-C refer to fits using Cauchy functions. The smearing radii used for each reconstruction are denoted by σ_G (Gaussian) and σ_C (Cauchy). Wuppertal smearing is applied with $N_{\text{source}} = 80$ steps at the source and no smearing at the sink ($N_{\text{sink}} = 0$).

C	k	aE_1 k-G	aE_1 $(k+1)$-G	aE_1 k-C	aE_1 $(k+1)$-C	am_C	σ_G/m_C	σ_C/m_C
PS	2	0.6558(34)	0.6549(74)	0.657(13)	0.656(13)	0.6569(73)	0.3	0.27
V	3	0.683(16)	0.66190(80)	0.689(14)	0.688(12)	0.6894(55)	0.28	0.25
T	3	0.694(13)	0.693(14)	0.693(11)	0.693(10)	0.6892(66)	0.33	0.28
AV	3	0.7668(40)	0.7668(20)	0.7679(68)	0.7679(55)	0.7775(78)	0.28	0.32
AT	3	0.7878(96)	0.7871(30)	0.7754(14)	0.7761(38)	0.7883(90)	0.3	0.18
S	2	0.7627(43)	0.7651(85)	0.7634(79)	0.7640(90)	0.7651(94)	0.3	0.24
ps	3	0.914(11)	0.908(11)	0.917(11)	0.909(11)	0.9172(35)	0.23	0.22
v	2	0.923(15)	0.932(13)	0.9253(85)	0.933(15)	0.9364(69)	0.24	0.25
t	2	0.932(21)	0.935(11)	0.921(13)	0.933(13)	0.9335(85)	0.28	0.28
av	3	1.076(27)	1.077(28)	1.0679(66)	1.082(11)	1.0887(70)	0.18	0.25
at	3	1.099(26)	1.096(26)	1.0922(99)	1.082(17)	1.0966(95)	0.25	0.25
s	3	1.071(10)	1.077(10)	1.072(16)	1.0719(80)	1.0631(78)	0.23	0.23

Table F.9. Second excited state meson masses extracted from ensemble M3 are summarised using different spectral reconstruction strategies. Each entry corresponds to a specific mesonic channel C. The mass am_C is obtained from a Generalised Eigenvalue Problem (GEVP) analysis. We report results from spectral density fits using both Gaussian and Cauchy kernel bases: a k-G fit employs a sum of k Gaussian functions, while a $(k+1)$-G fit adds one more Gaussian component. Similarly, k-C and $(k+1)$-C refer to fits using Cauchy functions. The smearing radii used for each reconstruction are denoted by σ_G (Gaussian) and σ_C (Cauchy). Wuppertal smearing is applied with $N_{\text{source}} = 80$ steps at the source and no smearing at the sink ($N_{\text{sink}} = 0$).

C	k	aE_2 k-G	aE_2 $(k+1)$-G	aE_2 k-C	aE_2 $(k+1)$-C	am_C	σ_G/m_C	σ_C/m_C
PS	2	-	-	-	-	-	0.3	0.27
V	3	0.970(25)	0.961(26)	0.969(28)	0.973(24)	0.961(34)	0.28	0.25
T	3	0.971(40)	0.964(41)	0.977(18)	0.966(13)	0.962(38)	0.33	0.28
AV	3	1.151(52)	1.165(55)	1.161(25)	1.148(14)	-	0.28	0.32
AT	3	1.046(19)	1.041(16)	1.041(17)	1.0346(67)	-	0.3	0.18
S	2	-	-	-	-	-	0.3	0.24
ps	3	1.240(37)	1.239(39)	1.249(43)	1.239(39)	1.262(23)	0.23	0.22
v	2	-	-	-	-	-	0.24	0.25
t	2	-	-	-	-	-	0.28	0.28
av	3	1.420(36)	1.422(35)	1.420(36)	1.410(33)	-	0.18	0.25
at	3	1.403(26)	1.406(24)	1.406(34)	1.406(24)	-	0.25	0.25
s	3	1.386(21)	1.387(22)	1.387(28)	1.373(44)	-	0.23	0.23

Table F.10. Ground-state meson masses extracted from ensemble M4 are summarised using different spectral reconstruction strategies. Each entry corresponds to a specific mesonic channel C. The mass am_C is obtained from a Generalised Eigenvalue Problem (GEVP) analysis. We report results from spectral density fits using both Gaussian and Cauchy kernel bases: a k-G fit employs a sum of k Gaussian functions, while a $(k+1)$-G fit adds one more Gaussian component. Similarly, k-C and $(k+1)$-C refer to fits using Cauchy functions. The smearing radii used for each reconstruction are denoted by σ_G (Gaussian) and σ_C (Cauchy). Wuppertal smearing is applied with $N_{\text{source}} = 80$ steps at the source and no smearing at the sink ($N_{\text{sink}} = 0$).

C	k	aE_0 k-G	aE_0 $(k+1)$-G	aE_0 k-C	aE_0 $(k+1)$-C	am_C	σ_G/m_C	σ_C/m_C
PS	2	0.4065(35)	0.4068(30)	0.4063(29)	0.4060(24)	0.4080(12)	0.3	0.3
V	3	0.4469(15)	0.4469(15)	0.4480(37)	0.4483(36)	0.4471(16)	0.3	0.27
T	3	0.4407(11)	0.4437(60)	0.4420(80)	0.4419(45)	0.4411(11)	0.25	0.25
AV	2	0.5876(40)	0.5889(80)	0.5902(57)	0.5865(34)	0.5889(37)	0.25	0.25
AT	2	0.5909(23)	0.5920(27)	0.59110(80)	0.5916(44)	0.5931(37)	0.25	0.25
S	2	0.5660(41)	0.5660(36)	0.5664(56)	0.5695(30)	0.5644(43)	0.25	0.3
ps	3	0.6234(12)	0.6236(10)	0.62312(72)	0.62340(75)	0.62367(46)	0.24	0.24
v	3	0.6695(46)	0.6694(46)	0.6690(10)	0.6980(10)	0.66991(61)	0.23	0.2
t	3	0.6702(11)	0.6673(40)	0.6696(57)	0.6692(50)	0.66985(64)	0.23	0.25
av	2	0.8602(42)	0.8651(22)	0.8642(22)	0.8645(32)	0.8654(34)	0.2	0.2
at	2	0.8768(61)	0.8736(79)	0.8727(20)	0.8718(32)	0.8717(61)	0.25	0.25
s	2	0.8332(32)	0.8323(23)	0.8312(31)	0.8323(63)	0.8308(30)	0.24	0.2

Table F.11. First excited state meson masses extracted from ensemble M4 are summarised using different spectral reconstruction strategies. Each entry corresponds to a specific mesonic channel C. The mass am_C is obtained from a Generalised Eigenvalue Problem (GEVP) analysis. We report results from spectral density fits using both Gaussian and Cauchy kernel bases: a k-G fit employs a sum of k Gaussian functions, while a $(k+1)$-G fit adds one more Gaussian component. Similarly, k-C and $(k+1)$-C refer to fits using Cauchy functions. The smearing radii used for each reconstruction are denoted by σ_G (Gaussian) and σ_C (Cauchy). Wuppertal smearing is applied with $N_{\text{source}} = 80$ steps at the source and no smearing at the sink ($N_{\text{sink}} = 0$).

C	k	aE_1 k-G	aE_1 $(k+1)$-G	aE_1 k-C	aE_1 $(k+1)$-C	am_C	σ_G/m_C	σ_C/m_C
PS	2	0.6034(93)	0.610(23)	0.614(15)	0.615(14)	0.613(23)	0.3	0.3
V	3	0.712(15)	0.712(15)	0.727(11)	0.728(11)	0.701(15)	0.3	0.27
T	3	0.7389(73)	0.7389(72)	0.7299(58)	0.7337(54)	0.7306(98)	0.25	0.25
AV	2	0.786(12)	0.7777(33)	0.7836(71)	0.7874(77)	0.780(26)	0.25	0.25
AT	2	0.837(16)	0.838(10)	0.8289(21)	0.834(13)	0.843(14)	0.25	0.25
S	2	0.7450(47)	0.7419(95)	0.731(17)	0.734(21)	-	0.25	0.3
ps	3	0.930(18)	0.930(19)	0.934(17)	0.931(14)	0.942(11)	0.24	0.24
v	3	0.9607(35)	0.9610(44)	0.9672(68)	0.974(17)	0.964(13)	0.23	0.2
t	3	0.965(26)	0.968(23)	0.956(21)	0.960(24)	0.956(16)	0.23	0.25
av	2	1.101(16)	1.104(12)	1.106(14)	1.106(11)	1.115(24)	0.2	0.2
at	2	1.1035(99)	1.106(13)	1.106(14)	1.1029(70)	1.104(41)	0.25	0.25
s	2	1.093(14)	1.093(14)	1.0920(52)	1.089(21)	1.070(28)	0.24	0.2

Table F.12. Second excited state meson masses extracted from ensemble M4 are summarised using different spectral reconstruction strategies. Each entry corresponds to a specific mesonic channel C. The mass am_C is obtained from a Generalised Eigenvalue Problem (GEVP) analysis. We report results from spectral density fits using both Gaussian and Cauchy kernel bases: a k-G fit employs a sum of k Gaussian functions, while a $(k+1)$-G fit adds one more Gaussian component. Similarly, k-C and $(k+1)$-C refer to fits using Cauchy functions. The smearing radii used for each reconstruction are denoted by σ_G (Gaussian) and σ_C (Cauchy). Wuppertal smearing is applied with $N_{\text{source}} = 80$ steps at the source and no smearing at the sink ($N_{\text{sink}} = 0$).

C	k	aE_2 k-G	aE_2 $(k+1)$-G	aE_2 k-C	aE_2 $(k+1)$-C	am_C	σ_G/m_C	σ_C/m_C
PS	2	-	-	-	-	-	0.3	0.3
V	3	0.986(44)	0.986(44)	0.996(40)	1.010(32)	0.975(47)	0.3	0.27
T	3	1.000(33)	0.997(33)	1.002(38)	1.003(32)	1.001(45)	0.25	0.25
AV	2	-	-	-	-	-	0.25	0.25
AT	2	-	-	-	-	-	0.25	0.25
S	2	-	-	-	-	-	0.25	0.3
ps	3	1.198(39)	1.192(45)	1.161(38)	1.174(40)	1.181(56)	0.24	0.24
v	3	1.192(39)	1.195(39)	1.205(13)	1.2067(97)	1.209(56)	0.23	0.2
t	3	1.208(18)	1.206(21)	1.192(40)	1.190(20)	1.193(75)	0.23	0.25
av	2	-	-	-	-	-	0.2	0.2
at	2	-	-	-	-	-	0.25	0.25
s	2	-	-	-	-	-	0.24	0.2

Table F.13. Ground-state meson masses extracted from ensemble M5 are summarised using different spectral reconstruction strategies. Each entry corresponds to a specific mesonic channel C. The mass am_C is obtained from a Generalised Eigenvalue Problem (GEVP) analysis. We report results from spectral density fits using both Gaussian and Cauchy kernel bases: a k-G fit employs a sum of k Gaussian functions, while a $(k+1)$-G fit adds one more Gaussian component. Similarly, k-C and $(k+1)$-C refer to fits using Cauchy functions. The smearing radii used for each reconstruction are denoted by σ_G (Gaussian) and σ_C (Cauchy). Wuppertal smearing is applied with $N_{\text{source}} = 80$ steps at the source and no smearing at the sink ($N_{\text{sink}} = 0$).

C	k	aE_0 k-G	aE_0 $(k+1)$-G	aE_0 k-C	aE_0 $(k+1)$-C	am_C	σ_G/m_C	σ_C/m_C
PS	2	0.29393(40)	0.29370(43)	0.29380(60)	0.29399(20)	0.29393(60)	0.25	0.25
V	3	0.3357(32)	0.3357(12)	0.3364(17)	0.3354(20)	0.3362(14)	0.3	0.3
T	3	0.3425(24)	0.3411(32)	0.3421(32)	0.3411(23)	0.3418(11)	0.3	0.3
AV	3	0.50890(80)	0.5089(19)	0.50800(70)	0.5084(44)	0.5079(39)	0.25	0.2
AT	3	0.5079(13)	0.50700(10)	0.5079(32)	0.5079(32)	0.5066(49)	0.2	0.2
S	3	0.4772(47)	0.4776(48)	0.4764(21)	0.4787(44)	0.4785(49)	0.25	0.25
ps	2	0.57261(53)	0.57233(63)	0.57232(62)	0.57240(80)	0.57249(63)	0.2	0.2
v	3	0.6207(17)	0.6207(17)	0.6200(15)	0.62010(90)	0.62071(84)	0.2	0.25
t	3	0.6209(38)	0.6201(30)	0.6204(13)	0.6204(15)	0.62072(90)	0.2	0.25
av	2	0.8007(74)	0.7980(79)	0.7982(46)	0.7977(48)	0.7986(43)	0.2	0.2
at	2	0.8027(65)	0.8022(65)	0.8031(81)	0.8022(41)	0.8050(65)	0.2	0.2
s	2	0.7633(66)	0.7630(65)	0.7625(69)	0.7606(65)	0.7644(32)	0.2	0.2

Table F.14. First excited state meson masses extracted from ensemble M5 are summarised using different spectral reconstruction strategies. Each entry corresponds to a specific mesonic channel C. The mass am_C is obtained from a Generalised Eigenvalue Problem (GEVP) analysis. We report results from spectral density fits using both Gaussian and Cauchy kernel bases: a k-G fit employs a sum of k Gaussian functions, while a $(k+1)$-G fit adds one more Gaussian component. Similarly, k-C and $(k+1)$-C refer to fits using Cauchy functions. The smearing radii used for each reconstruction are denoted by σ_G (Gaussian) and σ_C (Cauchy). Wuppertal smearing is applied with $N_{\text{source}} = 80$ steps at the source and no smearing at the sink ($N_{\text{sink}} = 0$).

C	k	aE_1 k-G	aE_1 $(k+1)$-G	aE_1 k-C	aE_1 $(k+1)$-C	am_C	σ_G/m_C	σ_C/m_C
PS	2	0.6354(82)	0.6343(95)	0.631(10)	0.6305(79)	0.6303(92)	0.25	0.25
V	3	0.653(12)	0.652(17)	0.6535(95)	0.6553(87)	0.650(16)	0.3	0.3
T	3	0.647(11)	0.649(13)	0.640(12)	0.652(13)	0.649(10)	0.3	0.3
AV	3	0.7763(72)	0.7686(73)	0.777(15)	0.777(15)	0.7750(68)	0.25	0.2
AT	3	0.783(18)	0.783(11)	0.788(14)	0.788(13)	0.7779(83)	0.2	0.2
S	3	0.732(19)	0.731(19)	0.726(11)	0.7229(97)	0.728(13)	0.25	0.25
ps	2	0.8894(77)	0.8854(74)	0.8859(10)	0.8859(20)	0.8844(64)	0.2	0.2
v	3	0.896(10)	0.907(11)	0.9084(79)	0.904(17)	0.906(10)	0.2	0.25
t	3	0.9087(51)	0.9063(64)	0.9127(35)	0.9127(35)	0.899(12)	0.2	0.25
av	2	0.978(27)	0.985(28)	0.965(28)	0.975(28)	0.979(27)	0.2	0.2
at	2	0.974(44)	0.977(32)	0.967(48)	0.974(34)	0.937(54)	0.2	0.2
s	2	1.029(14)	1.030(11)	1.030(11)	1.025(25)	1.017(16)	0.2	0.2

Table F.15. Second excited state meson masses extracted from ensemble M5 are summarised using different spectral reconstruction strategies. Each entry corresponds to a specific mesonic channel C. The mass am_C is obtained from a Generalised Eigenvalue Problem (GEVP) analysis. We report results from spectral density fits using both Gaussian and Cauchy kernel bases: a k-G fit employs a sum of k Gaussian functions, while a $(k+1)$-G fit adds one more Gaussian component. Similarly, k-C and $(k+1)$-C refer to fits using Cauchy functions. The smearing radii used for each reconstruction are denoted by σ_G (Gaussian) and σ_C (Cauchy). Wuppertal smearing is applied with $N_{\text{source}} = 80$ steps at the source and no smearing at the sink ($N_{\text{sink}} = 0$).

C	k	aE_2 k-G	aE_2 $(k+1)$-G	aE_2 k-C	aE_2 $(k+1)$-C	am_C	σ_G/m_C	σ_C/m_C
PS	2	-	-	-	-	-	0.25	0.25
V	3	0.902(21)	0.901(22)	0.902(32)	0.905(26)	0.900(46)	0.3	0.3
T	3	0.861(16)	0.848(17)	0.849(32)	0.849(30)	0.840(71)	0.3	0.3
AV	3	1.082(44)	1.084(42)	1.074(53)	1.086(58)	-	0.25	0.2
AT	3	1.084(46)	1.092(44)	1.0714(62)	1.0872(66)	1.08(14)	0.2	0.2
S	3	1.202(52)	1.200(52)	1.212(42)	1.214(40)	1.192(35)	0.25	0.25
ps	2	-	-	-	-	-	0.2	0.2
v	3	1.204(23)	1.194(23)	1.189(42)	1.181(42)	1.185(44)	0.2	0.25
t	3	1.209(20)	1.209(30)	1.196(44)	1.192(42)	1.212(52)	0.2	0.25
av	2	-	-	-	-	-	0.2	0.2
at	2	-	-	-	-	-	0.2	0.2
s	2	-	-	-	-	-	0.2	0.2

Table F.16. Results for the ground state masses of chimera baryons in ensemble M1, obtained via spectral density reconstructions. Each row corresponds to a baryon channel C, with am_C denoting the excited-state energy extracted from the GEVP procedure. To model the spectral features, we perform fits using both Gaussian and Cauchy kernels: a k-G fit includes k Gaussian terms, while a $(k+1)$-G fit adds an additional one; similarly, k-C and $(k+1)$-C refer to fits using k and $k+1$ Cauchy components, respectively. The smearing widths employed in these fits are denoted by σ_G for the Gaussian basis and σ_C for the Cauchy basis. Wuppertal smearing is applied at the source with $N_{\text{source}} = 80$ steps, while the sink remains unsmeared ($N_{\text{sink}} = 0$).

C	k	aE_0 k-G	aE_0 $(k+1)$-G	aE_0 k-C	aE_0 $(k+1)$-C	am_C	σ_G/m_C	σ_C/m_C
Λ^+_{CB}	2	0.7663(21)	0.7663(21)	0.7677(22)	0.7687(29)	0.7684(28)	0.32	0.32
Σ^+_{CB}	3	0.7556(21)	0.7556(21)	0.7583(23)	0.7578(28)	0.7576(19)	0.3	0.3
Σ^{*+}_{CB}	3	0.7949(63)	0.7849(64)	0.7814(61)	0.7849(64)	0.7840(28)	0.2	0.2
Λ^-_{CB}	2	0.8938(73)	0.8988(73)	0.8933(43)	0.8959(20)	0.8973(61)	0.22	0.22
Σ^-_{CB}	2	0.9059(53)	0.9078(53)	0.9078(53)	0.9058(53)	0.9092(74)	0.18	0.18
Σ^{*-}_{CB}	2	0.9053(25)	0.9074(27)	0.9031(74)	0.9091(74)	0.9075(70)	0.2	0.2

Table F.17. Results for the first excited state masses of chimera baryons in ensemble M1, obtained via spectral density reconstructions. Each row corresponds to a baryon channel C, with am_C denoting the excited-state energy extracted from the GEVP procedure. To model the spectral features, we perform fits using both Gaussian and Cauchy kernels: a k-G fit includes k Gaussian terms, while a $(k+1)$-G fit adds an additional one; similarly, k-C and $(k+1)$-C refer to fits using k and $k+1$ Cauchy components, respectively. The smearing widths employed in these fits are denoted by σ_G for the Gaussian basis and σ_C for the Cauchy basis. Wuppertal smearing is applied at the source with $N_{\text{source}} = 80$ steps, while the sink remains unsmeared ($N_{\text{sink}} = 0$).

C	k	aE_1 k-G	aE_1 $(k+1)$-G	aE_1 k-C	aE_1 $(k+1)$-C	am_C	σ_G/m_C	σ_C/m_C
Λ^+_{CB}	2	0.996(10)	0.995(11)	0.996(12)	0.997(10)	0.995(12)	0.32	0.32
Σ^+_{CB}	3	0.9984(77)	0.9954(73)	0.9930(99)	0.9930(99)	0.9979(96)	0.3	0.3
Σ^{*+}_{CB}	3	1.031(11)	1.032(11)	1.025(10)	1.025(10)	1.0265(95)	0.2	0.2
Λ^-_{CB}	2	1.025(11)	1.023(11)	1.026(21)	1.021(35)	-	0.22	0.22
Σ^-_{CB}	2	1.133(32)	1.143(37)	1.124(11)	1.124(11)	1.102(29)	0.18	0.18
Σ^{*-}_{CB}	2	1.055(18)	1.075(17)	1.077(11)	1.051(24)	1.062(31)	0.2	0.2

Table F.18. Results for the second excited state masses of chimera baryons in ensemble M1, obtained via spectral density reconstructions. Each row corresponds to a baryon channel C, with am_C denoting the excited-state energy extracted from the GEVP procedure. To model the spectral features, we perform fits using both Gaussian and Cauchy kernels: a k-G fit includes k Gaussian terms, while a $(k+1)$-G fit adds an additional one; similarly, k-C and $(k+1)$-C refer to fits using k and $k+1$ Cauchy components, respectively. The smearing widths employed in these fits are denoted by σ_G for the Gaussian basis and σ_C for the Cauchy basis. Wuppertal smearing is applied at the source with $N_{\text{source}} = 80$ steps, while the sink remains unsmeared ($N_{\text{sink}} = 0$).

C	k	aE_2 k-G	aE_2 $(k+1)$-G	aE_2 k-C	aE_2 $(k+1)$-C	am_C	σ_G/m_C	σ_C/m_C
Λ^+_{CB}	2	-	-	-	-	1.326(54)	0.32	0.32
Σ^+_{CB}	3	1.286(34)	1.291(32)	1.296(44)	1.292(54)	1.342(38)	0.3	0.3
Σ^{*+}_{CB}	3	1.266(36)	1.276(38)	1.268(39)	1.261(42)	1.266(36)	0.2	0.2
Λ^-_{CB}	2	-	-	-	-	-	0.22	0.22
Σ^-_{CB}	2	-	-	-	-	-	0.18	0.18
Σ^{*-}_{CB}	2	-	-	-	-	-	0.2	0.2

Table F.19. Results for the ground-state masses of chimera baryons in ensemble M2, obtained via spectral density reconstructions. Each row corresponds to a baryon channel C, with am_C denoting the excited-state energy extracted from the GEVP procedure. To model the spectral features, we perform fits using both Gaussian and Cauchy kernels: a k-G fit includes k Gaussian terms, while a $(k+1)$-G fit adds an additional one; similarly, k-C and $(k+1)$-C refer to fits using k and $k+1$ Cauchy components, respectively. The smearing widths employed in these fits are denoted by σ_G for the Gaussian basis and σ_C for the Cauchy basis. Wuppertal smearing is applied at the source with $N_{\text{source}} = 80$ steps, while the sink remains unsmeared ($N_{\text{sink}} = 0$).

C	k	aE_0 k-G	aE_0 $(k+1)$-G	aE_0 k-C	aE_0 $(k+1)$-C	am_C	σ_G/m_C	σ_C/m_C
Λ^+_{CB}	2	0.7584(60)	0.7574(60)	0.7577(26)	0.7543(40)	0.7596(32)	0.3	0.3
Σ^+_{CB}	3	0.7585(20)	0.7585(20)	0.7572(25)	0.7587(18)	0.7595(20)	0.23	0.23
Σ^{*+}_{CB}	2	0.7731(29)	0.7750(25)	0.7748(23)	0.7754(18)	0.7748(27)	0.2	0.2
Λ^-_{CB}	2	0.9221(74)	0.9221(74)	0.9039(72)	0.9139(72)	0.9134(90)	0.33	0.33
Σ^-_{CB}	2	0.9124(65)	0.9140(73)	0.9253(22)	0.9240(37)	0.920(14)	0.18	0.18
Σ^{*-}_{CB}	2	0.9220(24)	0.9219(16)	0.9217(74)	0.9222(21)	0.926(11)	0.2	0.2

Table F.20. Results for the first excited-state masses of chimera baryons in ensemble M2, obtained via spectral density reconstructions. Each row corresponds to a baryon channel C, with am_C denoting the excited-state energy extracted from the GEVP procedure. To model the spectral features, we perform fits using both Gaussian and Cauchy kernels: a k-G fit includes k Gaussian terms, while a $(k+1)$-G fit adds an additional one; similarly, k-C and $(k+1)$-C refer to fits using k and $k+1$ Cauchy components, respectively. The smearing widths employed in these fits are denoted by σ_G for the Gaussian basis and σ_C for the Cauchy basis. Wuppertal smearing is applied at the source with $N_{\text{source}} = 80$ steps, while the sink remains unsmeared ($N_{\text{sink}} = 0$).

C	k	aE_1 k-G	aE_1 $(k+1)$-G	aE_1 k-C	aE_1 $(k+1)$-C	am_C	σ_G/m_C	σ_C/m_C
Λ^+_{CB}	2	0.9967(99)	0.9967(99)	0.9968(66)	0.9967(99)	1.006(25)	0.3	0.3
Σ^+_{CB}	3	0.9922(99)	0.9922(99)	0.9923(53)	0.9922(99)	0.978(19)	0.23	0.23
Σ^{*+}_{CB}	2	1.0288(42)	1.027(10)	1.017(29)	1.022(22)	0.990(27)	0.2	0.2
Λ^-_{CB}	2	1.084(11)	1.084(11)	1.077(11)	1.0779(87)	-	0.33	0.33
Σ^-_{CB}	2	1.089(15)	1.087(15)	1.0802(80)	1.0806(83)	1.073(27)	0.18	0.18
Σ^{*-}_{CB}	2	1.136(35)	1.135(35)	1.151(11)	1.148(19)	1.176(55)	0.2	0.2

Table F.21. Results for the second excited-state masses of chimera baryons in ensemble M2, obtained via spectral density reconstructions. Each row corresponds to a baryon channel C, with am_C denoting the excited-state energy extracted from the GEVP procedure. To model the spectral features, we perform fits using both Gaussian and Cauchy kernels: a k-G fit includes k Gaussian terms, while a $(k+1)$-G fit adds an additional one; similarly, k-C and $(k+1)$-C refer to fits using k and $k+1$ Cauchy components, respectively. The smearing widths employed in these fits are denoted by σ_G for the Gaussian basis and σ_C for the Cauchy basis. Wuppertal smearing is applied at the source with $N_{\text{source}} = 80$ steps, while the sink remains unsmeared ($N_{\text{sink}} = 0$).

C	k	aE_2 k-G	aE_2 $(k+1)$-G	aE_2 k-C	aE_2 $(k+1)$-C	am_C	σ_G/m_C	σ_C/m_C
Λ^+_{CB}	2	-	-	-	-	-	0.3	0.3
Σ^+_{CB}	3	1.245(25)	1.245(25)	1.270(18)	1.269(18)	1.308(56)	0.23	0.23
Σ^{*+}_{CB}	2	-	-	-	-	-	0.2	0.2
Λ^-_{CB}	2	-	-	-	-	-	0.33	0.33
Σ^-_{CB}	2	-	-	-	-	-	0.18	0.18
Σ^{*-}_{CB}	2	-	-	-	-	-	0.2	0.2

Table F.22. Results for the ground-state masses of chimera baryons in ensemble M3, obtained via spectral density reconstructions. Each row corresponds to a baryon channel C, with am_C denoting the excited-state energy extracted from the GEVP procedure. To model the spectral features, we perform fits using both Gaussian and Cauchy kernels: a k-G fit includes k Gaussian terms, while a $(k+1)$-G fit adds an additional one; similarly, k-C and $(k+1)$-C refer to fits using k and $k+1$ Cauchy components, respectively. The smearing widths employed in these fits are denoted by σ_G for the Gaussian basis and σ_C for the Cauchy basis. Wuppertal smearing is applied at the source with $N_{\text{source}} = 80$ steps, while the sink remains unsmeared ($N_{\text{sink}} = 0$).

C	k	aE_0 k-G	aE_0 $(k+1)$-G	aE_0 k-C	aE_0 $(k+1)$-C	am_C	σ_G/m_C	σ_C/m_C
Λ^+_{CB}	2	0.7664(31)	0.7664(31)	0.7646(11)	0.7666(11)	0.7649(24)	0.27	0.27
Σ^+_{CB}	3	0.7525(61)	0.7545(61)	0.7555(61)	0.7543(20)	0.7557(38)	0.28	0.28
Σ^{*+}_{CB}	3	0.7860(78)	0.7836(77)	0.7828(63)	0.7866(21)	0.7848(22)	0.18	0.18
Λ^-_{CB}	3	0.9277(15)	0.9275(19)	0.9279(20)	0.9282(44)	0.9244(52)	0.25	0.25
Σ^-_{CB}	2	0.9215(85)	0.9214(87)	0.9300(74)	0.9293(66)	0.9229(92)	0.32	0.32
Σ^{*-}_{CB}	2	0.9382(35)	0.9377(64)	0.9422(75)	0.9417(75)	0.9375(67)	0.24	0.24

Table F.23. Results for the first excited state masses of chimera baryons in ensemble M3, obtained via spectral density reconstructions. Each row corresponds to a baryon channel C, with am_C denoting the excited-state energy extracted from the GEVP procedure. To model the spectral features, we perform fits using both Gaussian and Cauchy kernels: a k-G fit includes k Gaussian terms, while a $(k+1)$-G fit adds an additional one; similarly, k-C and $(k+1)$-C refer to fits using k and $k+1$ Cauchy components, respectively. The smearing widths employed in these fits are denoted by σ_G for the Gaussian basis and σ_C for the Cauchy basis. Wuppertal smearing is applied at the source with $N_{\text{source}} = 80$ steps, while the sink remains unsmeared ($N_{\text{sink}} = 0$).

C	k	aE_1 k-G	aE_1 $(k+1)$-G	aE_1 k-C	aE_1 $(k+1)$-C	am_C	σ_G/m_C	σ_C/m_C
Λ^+_{CB}	2	1.0298(92)	1.0289(93)	1.0271(92)	1.0279(98)	1.0220(59)	0.27	0.27
Σ^+_{CB}	3	0.9960(50)	0.9953(30)	0.9952(54)	0.9965(57)	1.0110(89)	0.28	0.28
Σ^{*+}_{CB}	3	1.004(24)	1.009(29)	0.997(10)	0.997(10)	1.013(11)	0.18	0.18
Λ^-_{CB}	3	1.0991(84)	1.0918(86)	1.094(11)	1.094(11)	1.107(16)	0.25	0.25
Σ^-_{CB}	2	1.124(11)	1.114(11)	1.126(23)	1.120(17)	1.133(15)	0.32	0.32
Σ^{*-}_{CB}	2	1.1784(96)	1.189(10)	1.176(10)	1.171(13)	1.1840(69)	0.24	0.24

Table F.24. Results for the second excited state masses of chimera baryons in ensemble M3, obtained via spectral density reconstructions. Each row corresponds to a baryon channel C, with am_C denoting the excited-state energy extracted from the GEVP procedure. To model the spectral features, we perform fits using both Gaussian and Cauchy kernels: a k-G fit includes k Gaussian terms, while a $(k+1)$-G fit adds an additional one; similarly, k-C and $(k+1)$-C refer to fits using k and $k+1$ Cauchy components, respectively. The smearing widths employed in these fits are denoted by σ_G for the Gaussian basis and σ_C for the Cauchy basis. Wuppertal smearing is applied at the source with $N_{\text{source}} = 80$ steps, while the sink remains unsmeared ($N_{\text{sink}} = 0$).

C	k	aE_2 k-G	aE_2 $(k+1)$-G	aE_2 k-C	aE_2 $(k+1)$-C	am_C	σ_G/m_C	σ_C/m_C
Λ^+_{CB}	2	-	-	-	-	1.308(50)	0.27	0.27
Σ^+_{CB}	3	1.239(10)	1.239(12)	1.222(20)	1.244(17)	1.213(64)	0.28	0.28
Σ^{*+}_{CB}	3	1.280(20)	1.270(21)	1.259(26)	1.279(26)	1.269(33)	0.18	0.18
Λ^-_{CB}	3	1.2831(25)	1.2830(25)	1.298(22)	1.293(23)	1.284(89)	0.25	0.25
Σ^-_{CB}	2	-	-	-	-	-	0.32	0.32
Σ^{*-}_{CB}	2	-	-	-	-	-	0.24	0.24

Table F.25. Results for the ground-state masses of chimera baryons in ensemble M4, obtained via spectral density reconstructions. Each row corresponds to a baryon channel C, with am_C denoting the excited-state energy extracted from the GEVP procedure. To model the spectral features, we perform fits using both Gaussian and Cauchy kernels: a k-G fit includes k Gaussian terms, while a $(k+1)$-G fit adds an additional one; similarly, k-C and $(k+1)$-C refer to fits using k and $k+1$ Cauchy components, respectively. The smearing widths employed in these fits are denoted by σ_G for the Gaussian basis and σ_C for the Cauchy basis. Wuppertal smearing is applied at the source with $N_{\text{source}} = 80$ steps, while the sink remains unsmeared ($N_{\text{sink}} = 0$).

C	k	aE_0 k-G	aE_0 $(k+1)$-G	aE_0 k-C	aE_0 $(k+1)$-C	am_C	σ_G/m_C	σ_C/m_C
Λ^+_{CB}	2	0.8246(24)	0.8247(24)	0.8245(27)	0.8248(18)	0.8260(15)	0.3	0.3
Σ^+_{CB}	2	0.8107(25)	0.8106(28)	0.8111(66)	0.8111(66)	0.8122(14)	0.25	0.25
Σ^{*+}_{CB}	2	0.8424(68)	0.8454(68)	0.8424(68)	0.8424(68)	0.8433(20)	0.25	0.25
Λ^-_{CB}	2	0.951(11)	0.955(12)	0.955(18)	0.955(12)	0.958(14)	0.27	0.27
Σ^-_{CB}	2	0.9537(79)	0.9537(79)	0.9529(42)	0.9533(44)	0.9598(88)	0.25	0.25
Σ^{*-}_{CB}	2	0.9566(89)	0.9566(89)	0.9566(52)	0.9558(78)	0.954(12)	0.3	0.3

Table F.26. Results for the first excited state masses of chimera baryons in ensemble M4, obtained via spectral density reconstructions. Each row corresponds to a baryon channel C, with am_C denoting the excited-state energy extracted from the GEVP procedure. To model the spectral features, we perform fits using both Gaussian and Cauchy kernels: a k-G fit includes k Gaussian terms, while a $(k+1)$-G fit adds an additional one; similarly, k-C and $(k+1)$-C refer to fits using k and $k+1$ Cauchy components, respectively. The smearing widths employed in these fits are denoted by σ_G for the Gaussian basis and σ_C for the Cauchy basis. Wuppertal smearing is applied at the source with $N_{\text{source}} = 80$ steps, while the sink remains unsmeared ($N_{\text{sink}} = 0$).

C	k	aE_1 k-G	aE_1 $(k+1)$-G	aE_1 k-C	aE_1 $(k+1)$-C	am_C	σ_G/m_C	σ_C/m_C
Λ^+_{CB}	2	1.024(10)	1.025(10)	1.035(11)	1.035(10)	1.022(18)	0.3	0.3
Σ^+_{CB}	2	0.995(11)	0.975(11)	0.993(29)	0.984(31)	0.998(18)	0.25	0.25
Σ^{*+}_{CB}	2	1.013(14)	1.003(11)	1.020(10)	1.020(10)	1.010(18)	0.25	0.25
Λ^-_{CB}	2	1.168(23)	1.178(23)	1.182(12)	1.172(12)	1.171(15)	0.27	0.27
Σ^-_{CB}	2	1.194(36)	1.189(38)	1.181(17)	1.181(16)	1.173(20)	0.25	0.25
Σ^{*-}_{CB}	2	1.154(18)	1.144(16)	1.142(24)	1.153(12)	1.144(43)	0.3	0.3

Table F.27. Results for the second excited state masses of chimera baryons in ensemble M4, obtained via spectral density reconstructions. Each row corresponds to a baryon channel C, with am_C denoting the excited-state energy extracted from the GEVP procedure. To model the spectral features, we perform fits using both Gaussian and Cauchy kernels: a k-G fit includes k Gaussian terms, while a $(k+1)$-G fit adds an additional one; similarly, k-C and $(k+1)$-C refer to fits using k and $k+1$ Cauchy components, respectively. The smearing widths employed in these fits are denoted by σ_G for the Gaussian basis and σ_C for the Cauchy basis. Wuppertal smearing is applied at the source with $N_{\text{source}} = 80$ steps, while the sink remains unsmeared ($N_{\text{sink}} = 0$).

C	k	aE_2 k-G	aE_2 $(k+1)$-G	aE_2 k-C	aE_2 $(k+1)$-C	am_C	σ_G/m_C	σ_C/m_C
Λ^+_{CB}	2	-	-	-	-	1.375(62)	0.3	0.3
Σ^+_{CB}	2	-	-	-	-	-	0.25	0.25
Σ^{*+}_{CB}	2	-	-	-	-	1.330(35)	0.25	0.25
Λ^-_{CB}	2	-	-	-	-	-	0.27	0.27
Σ^-_{CB}	2	-	-	-	-	-	0.25	0.25
Σ^{*-}_{CB}	2	-	-	-	-	-	0.3	0.3

Table F.28. Results for the ground-state masses of chimera baryons in ensemble M5, obtained via spectral density reconstructions. Each row corresponds to a baryon channel C, with am_C denoting the excited-state energy extracted from the GEVP procedure. To model the spectral features, we perform fits using both Gaussian and Cauchy kernels: a k-G fit includes k Gaussian terms, while a $(k+1)$-G fit adds an additional one; similarly, k-C and $(k+1)$-C refer to fits using k and $k+1$ Cauchy components, respectively. The smearing widths employed in these fits are denoted by σ_G for the Gaussian basis and σ_C for the Cauchy basis. Wuppertal smearing is applied at the source with $N_{\text{source}} = 80$ steps, while the sink remains unsmeared ($N_{\text{sink}} = 0$).

C	k	aE_0 k-G	aE_0 $(k+1)$-G	aE_0 k-C	aE_0 $(k+1)$-C	am_C	σ_G/m_C	σ_C/m_C
Λ^+_{CB}	2	0.6971(55)	0.6971(55)	0.6949(56)	0.6949(56)	0.6929(22)	0.25	0.25
Σ^+_{CB}	3	0.6872(54)	0.6872(54)	0.6808(55)	0.6808(55)	0.6827(22)	0.3	0.3
Σ^{*+}_{CB}	2	0.7064(66)	0.7063(66)	0.7061(57)	0.7061(57)	0.7065(28)	0.2	0.2
Λ^-_{CB}	3	0.8367(57)	0.8366(52)	0.8375(69)	0.8375(69)	0.8383(73)	0.3	0.3
Σ^-_{CB}	2	0.8366(98)	0.8366(97)	0.8377(88)	0.8390(83)	0.8444(90)	0.2	0.2
Σ^{*-}_{CB}	2	0.8597(58)	0.8595(65)	0.8538(54)	0.8553(56)	0.8577(85)	0.25	0.25

Table F.29. Results for the first excited state masses of chimera baryons in ensemble M5, obtained via spectral density reconstructions. Each row corresponds to a baryon channel C, with am_C denoting the excited-state energy extracted from the GEVP procedure. To model the spectral features, we perform fits using both Gaussian and Cauchy kernels: a k-G fit includes k Gaussian terms, while a $(k+1)$-G fit adds an additional one; similarly, k-C and $(k+1)$-C refer to fits using k and $k+1$ Cauchy components, respectively. The smearing widths employed in these fits are denoted by σ_G for the Gaussian basis and σ_C for the Cauchy basis. Wuppertal smearing is applied at the source with $N_{\text{source}} = 80$ steps, while the sink remains unsmeared ($N_{\text{sink}} = 0$).

C	k	aE_1 k-G	aE_1 $(k+1)$-G	aE_1 k-C	aE_1 $(k+1)$-C	am_C	σ_G/m_C	σ_C/m_C
Λ^+_{CB}	2	0.9469(94)	0.9469(94)	0.943(13)	0.9469(94)	0.951(17)	0.25	0.25
Σ^+_{CB}	3	0.9064(97)	0.9166(91)	0.9158(96)	0.916(12)	0.907(21)	0.3	0.3
Σ^{*+}_{CB}	2	0.9176(96)	0.9177(87)	0.9177(91)	0.9179(97)	0.913(22)	0.2	0.2
Λ^-_{CB}	3	1.041(11)	1.041(11)	1.057(10)	1.057(10)	1.043(20)	0.3	0.3
Σ^-_{CB}	2	1.051(10)	1.059(10)	1.0410(85)	1.045(16)	1.037(20)	0.2	0.2
Σ^{*-}_{CB}	2	1.109(11)	1.098(23)	1.109(11)	1.108(22)	1.115(12)	0.25	0.25

Table F.30. Results for the second excited state masses of chimera baryons in ensemble M5, obtained via spectral density reconstructions. Each row corresponds to a baryon channel C, with am_C denoting the excited-state energy extracted from the GEVP procedure. To model the spectral features, we perform fits using both Gaussian and Cauchy kernels: a k-G fit includes k Gaussian terms, while a $(k+1)$-G fit adds an additional one; similarly, k-C and $(k+1)$-C refer to fits using k and $k+1$ Cauchy components, respectively. The smearing widths employed in these fits are denoted by σ_G for the Gaussian basis and σ_C for the Cauchy basis. Wuppertal smearing is applied at the source with $N_{\text{source}} = 80$ steps, while the sink remains unsmeared ($N_{\text{sink}} = 0$).

C	k	aE_2 k-G	aE_2 $(k+1)$-G	aE_2 k-C	aE_2 $(k+1)$-C	am_C	σ_G/m_C	σ_C/m_C
Λ^+_{CB}	2	-	-	-	-	1.286(34)	0.25	0.25
Σ^+_{CB}	3	1.240(25)	1.242(25)	1.214(24)	1.214(24)	1.203(44)	0.3	0.3
Σ^{*+}_{CB}	2	-	-	-	-	1.289(34)	0.2	0.2
Λ^-_{CB}	3	1.052(25)	1.053(21)	1.042(21)	1.043(21)	1.106(58)	0.3	0.3
Σ^-_{CB}	2	-	-	-	-	1.060(35)	0.2	0.2
Σ^{*-}_{CB}	2	-	-	-	-	-	0.25	0.25

Table F.31. Extracted matrix elements for mesonic channels in ensemble M1, determined through spectral density fits. Each row corresponds to a meson type C, with c_0 representing the ground-state matrix element obtained from correlation function analysis. We employ two fitting strategies based on different kernel choices: Gaussian (G) and Cauchy (C) bases. The associated energy resolution scales are denoted by σ_G for Gaussian fits and σ_C for Cauchy fits.

C	a^2c_0-G	a^2c_0-C	a^2c_0(corr.)	σ_G/m_C	σ_C/m_C
PS	0.0259(4)	0.0259(4)	0.0262(4)	0.33	0.32
V	0.0454(8)	0.0454(8)	0.0446(6)	0.3	0.22
AV	0.0454(7)	0.0454(7)	0.0446(19)	0.2	0.18
ps	0.0680(13)	0.0680(14)	0.0689(16)	0.33	0.32
v	0.0914(22)	0.0914(24)	0.0930(26)	0.3	0.22
av	0.0822(16)	0.0822(17)	0.0825(33)	0.2	0.18

Table F.32. Extracted matrix elements for mesonic channels in ensemble M2, determined through spectral density fits. Each row corresponds to a meson type C, with c_0 representing the ground-state matrix element obtained from correlation function analysis. We employ two fitting strategies based on different kernel choices: Gaussian (G) and Cauchy (C) bases. The associated energy resolution scales are denoted by σ_G for Gaussian fits and σ_C for Cauchy fits.

C	a^2c_0-G	a^2c_0-C	a^2c_0(corr.)	σ_G/m_C	σ_C/m_C
PS	0.0252(4)	0.0252(4)	0.0249(4)	0.35	0.3
V	0.0444(7)	0.0444(8)	0.0435(6)	0.28	0.33
AV	0.0466(7)	0.0466(8)	0.0479(28)	0.3	0.18
ps	0.0679(13)	0.0679(14)	0.0682(18)	0.35	0.3
v	0.0894(22)	0.0894(24)	0.0862(34)	0.28	0.33
av	0.0845(16)	0.0845(18)	0.0848(38)	0.3	0.18

Table F.33. Extracted matrix elements for mesonic channels in ensemble M3, determined through spectral density fits. Each row corresponds to a meson type C, with c_0 representing the ground-state matrix element obtained from correlation function analysis. We employ two fitting strategies based on different kernel choices: Gaussian (G) and Cauchy (C) bases. The associated energy resolution scales are denoted by σ_G for Gaussian fits and σ_C for Cauchy fits.

C	a^2c_0-G	a^2c_0-C	a^2c_0(corr.)	σ_G/m_C	σ_C/m_C
PS	0.0256(4)	0.0256(4)	0.0256(5)	0.3	0.27
V	0.0443(7)	0.0443(8)	0.0417(21)	0.28	0.25
AV	0.0466(7)	0.0466(8)	0.0469(16)	0.28	0.32
ps	0.0695(13)	0.0695(14)	0.0697(20)	0.3	0.27
v	0.0887(22)	0.0886(24)	0.0900(33)	0.28	0.25
av	0.0827(16)	0.0827(17)	0.0830(46)	0.28	0.32

Table F.34. Extracted matrix elements for mesonic channels in ensemble M4, determined through spectral density fits. Each row corresponds to a meson type C, with c_0 representing the ground-state matrix element obtained from correlation function analysis. We employ two fitting strategies based on different kernel choices: Gaussian (G) and Cauchy (C) bases. The associated energy resolution scales are denoted by σ_G for Gaussian fits and σ_C for Cauchy fits.

C	a^2c_0-G	a^2c_0-C	a^2c_0(corr.)	σ_G/m_C	σ_C/m_C
PS	0.0310(5)	0.0310(5)	0.0309(7)	0.3	0.3
V	0.0529(9)	0.0529(10)	0.0477(16)	0.3	0.27
AV	0.0553(8)	0.0553(9)	0.0561(12)	0.25	0.25
ps	0.0770(15)	0.0770(16)	0.0770(22)	0.3	0.3
v	0.1003(24)	0.1003(27)	0.1019(36)	0.3	0.27
av	0.0906(17)	0.0906(19)	0.0908(26)	0.25	0.25

Table F.35. Extracted matrix elements for mesonic channels in ensemble M5, determined through spectral density fits. Each row corresponds to a meson type C, with c_0 representing the ground-state matrix element obtained from correlation function analysis. We employ two fitting strategies based on different kernel choices: Gaussian (G) and Cauchy (C) bases. The associated energy resolution scales are denoted by σ_G for Gaussian fits and σ_C for Cauchy fits.

C	a^2c_0-G	a^2c_0-C	a^2c_0(corr.)	σ_G/m_C	σ_C/m_C
PS	0.0185(3)	0.0185(3)	0.0190(4)	0.25	0.25
V	0.0325(5)	0.0325(6)	0.0301(8)	0.3	0.3
AV	0.0498(7)	0.0498(8)	0.0506(11)	0.25	0.2
ps	0.0625(12)	0.0625(13)	0.0628(18)	0.25	0.25
v	0.0814(20)	0.0814(22)	0.0825(20)	0.3	0.3
av	0.0778(15)	0.0778(16)	0.0784(36)	0.25	0.2

Table F.36. Overlap factors for chimera baryons in ensemble M1, extracted from fits to the spectral density. Each entry corresponds to a baryon channel C, with K_0 denoting the ground-state overlap obtained from the correlator analysis. Two types of kernel functions are used for the reconstruction: Gaussian (G) and Cauchy (C), with smearing widths indicated by σ_G and σ_C, respectively.

C	a^3K_0-G	a^3K_0-C	a^3K_0(corr.)	σ_G/m_C	σ_C/m_C
Λ^+_{CB}	0.000813(11)	0.000812(12)	0.000813(11)	0.32	0.32
Σ^+_{CB}	0.003523(15)	0.003527(17)	0.003527(14)	0.3	0.3
$\Sigma^{*+}_{\mathrm{CB}}$	0.004054(18)	0.004062(19)	0.004058(18)	0.2	0.2
Λ^-_{CB}	0.000533(8)	0.000533(8)	0.000534(10)	0.22	0.22
Σ^-_{CB}	0.001984(9)	0.001984(9)	0.001986(23)	0.18	0.18
$\Sigma^{*-}_{\mathrm{CB}}$	0.002264(10)	0.002267(10)	0.002265(16)	0.2	0.2

Table F.37. Overlap factors for chimera baryons in ensemble M2, extracted from fits to the spectral density. Each entry corresponds to a baryon channel C, with K_0 denoting the ground-state overlap obtained from the correlator analysis. Two types of kernel functions are used for the reconstruction: Gaussian (G) and Cauchy (C), with smearing widths indicated by σ_G and σ_C, respectively.

C	a^3K_0-G	a^3K_0-C	a^3K_0(corr.)	σ_G/m_C	σ_C/m_C
Λ^+_{CB}	0.000711(10)	0.000711(11)	0.000709(20)	0.3	0.3
Σ^+_{CB}	0.003476(15)	0.003473(16)	0.003476(12)	0.23	0.23
$\Sigma^{*+}_{\mathrm{CB}}$	0.003994(17)	0.003990(19)	0.003994(17)	0.2	0.2
Λ^-_{CB}	0.000540(8)	0.000540(8)	0.000540(14)	0.33	0.33
Σ^-_{CB}	0.001968(9)	0.001968(9)	0.001971(33)	0.18	0.18
$\Sigma^{*-}_{\mathrm{CB}}$	0.002192(9)	0.002192(10)	0.002193(25)	0.2	0.2

Table F.38. Overlap factors for chimera baryons in ensemble M3, extracted from fits to the spectral density. Each entry corresponds to a baryon channel C, with K_0 denoting the ground-state overlap obtained from the correlator analysis. Two types of kernel functions are used for the reconstruction: Gaussian (G) and Cauchy (C), with smearing widths indicated by σ_G and σ_C, respectively.

C	a^3K_0-G	a^3K_0-C	a^3K_0(corr.)	σ_G/m_C	σ_C/m_C
Λ^+_{CB}	0.000748(10)	0.000748(11)	0.000749(13)	0.27	0.27
Σ^+_{CB}	0.003362(15)	0.003359(16)	0.003362(12)	0.28	0.28
$\Sigma^{*+}_{\mathrm{CB}}$	0.004012(17)	0.004012(19)	0.004017(13)	0.18	0.18
Λ^-_{CB}	0.000550(8)	0.000550(9)	0.000550(9)	0.25	0.25
Σ^-_{CB}	0.001989(9)	0.001986(9)	0.001989(15)	0.32	0.32
$\Sigma^{*-}_{\mathrm{CB}}$	0.002158(9)	0.002158(10)	0.002159(25)	0.24	0.24

Table F.39. Overlap factors for chimera baryons in ensemble M4, extracted from fits to the spectral density. Each entry corresponds to a baryon channel C, with K_0 denoting the ground-state overlap obtained from the correlator analysis. Two types of kernel functions are used for the reconstruction: Gaussian (G) and Cauchy (C), with smearing widths indicated by σ_G and σ_C, respectively.

C	a^3K_0-G	a^3K_0-C	a^3K_0(corr.)	σ_G/m_C	σ_C/m_C
Λ^+_{CB}	0.001022(15)	0.001022(16)	0.001022(8)	0.3	0.3
Σ^+_{CB}	0.004365(19)	0.004362(20)	0.004362(12)	0.25	0.25
$\Sigma^{*+}_{\mathrm{CB}}$	0.004993(21)	0.004993(23)	0.004999(19)	0.25	0.25
Λ^-_{CB}	0.000522(8)	0.000522(8)	0.000522(22)	0.27	0.27
Σ^-_{CB}	0.001833(8)	0.001833(9)	0.001835(34)	0.25	0.25
$\Sigma^{*-}_{\mathrm{CB}}$	0.002281(10)	0.002280(11)	0.002281(32)	0.3	0.3

Table F.40. Overlap factors for chimera baryons in ensemble M5, extracted from fits to the spectral density. Each entry corresponds to a baryon channel C, with K_0 denoting the ground-state overlap obtained from the correlator analysis. Two types of kernel functions are used for the reconstruction: Gaussian (G) and Cauchy (C), with smearing widths indicated by σ_G and σ_C, respectively.

C	a^3K_0-G	a^3K_0-C	a^3K_0(corr.)	σ_G/m_C	σ_C/m_C
Λ^+_{CB}	0.000503(7)	0.000503(8)	0.000503(11)	0.25	0.25
Σ^+_{CB}	0.002312(10)	0.002312(11)	0.002312(13)	0.3	0.3
$\Sigma^{*+}_{\mathrm{CB}}$	0.002498(11)	0.002498(12)	0.002498(18)	0.2	0.2
Λ^-_{CB}	0.000392(6)	0.000392(6)	0.000392(16)	0.3	0.3
Σ^-_{CB}	0.001525(7)	0.001525(7)	0.001525(22)	0.2	0.2
$\Sigma^{*-}_{\mathrm{CB}}$	0.001551(7)	0.001553(7)	0.001553(31)	0.25	0.25

Bibliography

[1] E. Bennett, P. A. Boyle, L. D. Debbio, N. Forzano, D. K. Hong, J.-W. Lee, J. Lenz, C.-J. D. Lin, B. Lucini, A. Lupo, M. Piai, and D. Vadacchino, "Symplectic lattice gauge theories on grid: approaching the conformal window—data release." doi:10.5281/zenodo.8136452.

[2] E. Bennett, P. A. Boyle, L. D. Debbio, N. Forzano, D. K. Hong, J.-W. Lee, J. Lenz, C.-J. D. Lin, B. Lucini, A. Lupo, M. Piai, and D. Vadacchino, "Symplectic lattice gauge theories on grid: approaching the conformal window—analysis code." doi:10.5281/zenodo.8136514.

[3] E. Bennett, L. D. Debbio, N. Forzano, R. Hill, D. K. Hong, H. Hsiao, J.-W. Lee, C.-J. D. Lin, B. Lucini, A. Lupo, M. Piai, D. Vadacchino, and F. Zierler, *Meson spectroscopy from spectral densities in lattice gauge theories - data release*, 2024. doi:10.5281/zenodo.11048346.

[4] E. Bennett, L. D. Debbio, N. Forzano, R. Hill, D. K. Hong, H. Hsiao, J.-W. Lee, C.-J. D. Lin, B. Lucini, A. Lupo, M. Piai, D. Vadacchino, and F. Zierler, *Meson spectroscopy from spectral densities in lattice gauge theories - analysis code*, 2024. doi:10.5281/zenodo.11048300.

[5] E. Bennett, L. D. Debbio, N. Forzano, R. Hill, D. K. Hong, H. Hsiao, J.-W. Lee, C.-J. D. Lin, B. Lucini, A. Lupo, M. Piai, D. Vadacchino, and F. Zierler, *Chimera baryons and mesons on the lattice: a spectral density analysis - data release*, 2025. doi:10.5281/zenodo.15804848.

[6] E. Bennett, L. D. Debbio, N. Forzano, R. Hill, D. K. Hong, H. Hsiao, J.-W. Lee, C.-J. D. Lin, B. Lucini, A. Lupo, M. Piai, D. Vadacchino, and F. Zierler, *Chimera baryons and mesons on the lattice: a spectral density analysis - analysis code*, 2025. doi:10.5281/zenodo.15804889.

[7] K. G. Wilson, *Confinement of Quarks*, *Phys. Rev. D* **10** (1974) 2445–2459.

[8] E. Bennett, D. K. Hong, J.-W. Lee, C. J. D. Lin, B. Lucini, M. Piai, and D. Vadacchino, *Sp(4) gauge theory on the lattice: towards SU(4)/Sp(4) composite Higgs (and beyond)*, *JHEP* **03** (2018) 185, [arXiv:1712.04220].

[9] J.-W. Lee, E. Bennett, D. K. Hong, C. J. D. Lin, B. Lucini, M. Piai, and D. Vadacchino, *Progress in the lattice simulations of Sp(2N) gauge theories*, *PoS* **LATTICE2018** (2018) 192, [arXiv:1811.00276].

[10] E. Bennett, D. K. Hong, J.-W. Lee, C. J. D. Lin, B. Lucini, M. Piai, and D. Vadacchino, *Sp(4) gauge theories on the lattice: $N_f = 2$ dynamical fundamental fermions*, *JHEP* **12** (2019) 053, [arXiv:1909.12662].

[11] E. Bennett, D. K. Hong, J.-W. Lee, C.-J. D. Lin, B. Lucini, M. Mesiti, M. Piai, J. Rantaharju, and D. Vadacchino, *Sp*(4) *gauge theories on the lattice: quenched fundamental and antisymmetric fermions*, *Phys. Rev. D* **101** (2020), no. 7 074516, [arXiv:1912.06505].

[12] E. Bennett, J. Holligan, D. K. Hong, J.-W. Lee, C. J. D. Lin, B. Lucini, M. Piai, and D. Vadacchino, *Color dependence of tensor and scalar glueball masses in Yang-Mills theories*, *Phys. Rev. D* **102** (2020), no. 1 011501, [arXiv:2004.11063].

[13] E. Bennett, J. Holligan, D. K. Hong, J.-W. Lee, C. J. D. Lin, B. Lucini, M. Piai, and D. Vadacchino, *Glueballs and strings in $Sp(2N)$ Yang-Mills theories*, *Phys. Rev. D* **103** (2021), no. 5 054509, [arXiv:2010.15781].

[14] B. Lucini, E. Bennett, J. Holligan, D. K. Hong, H. Hsiao, J.-W. Lee, C. J. D. Lin, M. Mesiti, M. Piai, and D. Vadacchino, *Sp(4) gauge theories and beyond the standard model physics*, *EPJ Web Conf.* **258** (2022) 08003, [arXiv:2111.12125].

[15] E. Bennett, J. Holligan, D. K. Hong, H. Hsiao, J.-W. Lee, C. J. D. Lin, B. Lucini, M. Mesiti, M. Piai, and D. Vadacchino, *Progress in $Sp(2N)$ lattice gauge theories*, *PoS* **LATTICE2021** (2022) 308, [arXiv:2111.14544].

[16] E. Bennett, D. K. Hong, H. Hsiao, J.-W. Lee, C. J. D. Lin, B. Lucini, M. Mesiti, M. Piai, and D. Vadacchino, *Lattice studies of the Sp(4) gauge theory with two fundamental and three antisymmetric Dirac fermions*, *Phys. Rev. D* **106** (2022), no. 1 014501, [arXiv:2202.05516].

[17] E. Bennett, D. K. Hong, J.-W. Lee, C. J. D. Lin, B. Lucini, M. Piai, and D. Vadacchino, *Color dependence of the topological susceptibility in Yang-Mills theories*, *Phys. Lett. B* **835** (2022) 137504, [arXiv:2205.09254].

[18] E. Bennett, D. K. Hong, J.-W. Lee, C. J. D. Lin, B. Lucini, M. Piai, and D. Vadacchino, *Sp(2N) Yang-Mills theories on the lattice: Scale setting and topology*, *Phys. Rev. D* **106** (2022), no. 9 094503, [arXiv:2205.09364].

[19] E. Bennett, D. K. Hong, H. Hsiao, J. W. Lee, C. J. D. Lin, B. Lucini, M. Piai, and D. Vadacchino, "Sp(4) theories on the lattice: dynamical antisymmetric fermions." in preparation.

[20] J.-W. Lee, E. Bennett, D. K. Hong, H. Hsiao, C. J. D. Lin, B. Lucini, M. Piai, and D. Vadacchino, *Spectroscopy of $sp(4)$ lattice gauge theory with $n_f = 3$ antisymmetric fermions*, 2022.

[21] H. Hsiao, E. Bennett, D. K. Hong, J.-W. Lee, C. J. D. Lin, B. Lucini, M. Piai, and D. Vadacchino, *Spectroscopy of chimera baryons in a $Sp(4)$ lattice gauge theory*, *PoS* **LATTICE2022** (2022) 211, [arXiv:2211.03955].

[22] E. Bennett, H. Hsiao, J.-W. Lee, B. Lucini, A. Maas, M. Piai, and F. Zierler, *Singlets in gauge theories with fundamental matter*, *Phys. Rev. D* **109** (2024), no. 3 034504, [arXiv:2304.07191].

[23] A. Maas and F. Zierler, *Strong isospin breaking in $\boldsymbol{Sp(4)}$ gauge theory*, *PoS* **LATTICE2021** (2022) 130, [arXiv:2109.14377].

[24] F. Zierler and A. Maas, *$Sp(4)$ SIMP Dark Matter on the Lattice*, *PoS* **LHCP2021** (2021) 162.

[25] S. Kulkarni, A. Maas, S. Mee, M. Nikolic, J. Pradler, and F. Zierler, *Low-energy effective description of dark $Sp(4)$ theories*, *SciPost Phys.* **14** (2023) 044, [arXiv:2202.05191].

[26] E. Bennett, J. Holligan, D. K. Hong, H. Hsiao, J.-W. Lee, C. J. D. Lin, B. Lucini, M. Mesiti, M. Piai, and D. Vadacchino, *Sp(2N) Lattice Gauge Theories and Extensions of the Standard Model of Particle Physics*, *Universe* **9** (2023), no. 5 236, [arXiv:2304.01070].

[27] B. Lucini and M. Teper, *Su(n) gauge theories in four-dimensions: Exploring the approach to n = infinity*, *JHEP* **06** (2001). doi:10.1088/1126-6708/2001/06/050. 050 [arXiv:hep-lat/0103027 [hep-lat]].

[28] B. Lucini, M. Teper, and U. Wenger, *Glueballs and k-strings in su(n) gauge theories: Calculations with improved operators*, *JHEP* **06** (2004). doi:10.1088/1126-6708/2004/06/012. 012 [arXiv:hep-lat/0404008 [hep-lat]].

[29] B. Lucini, A. Rago, and E. Rinaldi, *Glueball masses in the large N limit*, *JHEP* **08** (2010) 119, [arXiv:1007.3879].

[30] B. Lucini and M. Panero, *Su(n) gauge theories at large n*, *Phys. Rept.* **526** (2013) 93–163. doi:10.1016/j.physrep.2013.01.001. [arXiv:1210.4997 [hep-th]].

[31] A. Athenodorou, R. Lau, and M. Teper, *On the weak n -dependence of so(n) and su(n) gauge theories in 2+1 dimensions*, *Phys. Lett. B* **749** (2015) 448–453. doi:10.1016/j.physletb.2015.08.023. [arXiv:1504.08126 [hep-lat]].

[32] R. Lau and M. Teper, *So(n) gauge theories in 2 + 1 dimensions: glueball spectra and confinement*, *JHEP* **10** (2017). doi:10.1007/JHEP10(2017)022. 022 [arXiv:1701.06941 [hep-lat]].

[33] P. Hernández and F. Romero-López, *The large n_c limit of qcd on the lattice*, *Eur. Phys. J. A* **57** (2021), no. 2 52. doi:10.1140/epja/s10050-021-00374-2. [arXiv:2012.03331 [hep-lat]].

[34] A. Athenodorou and M. Teper, *Su(n) gauge theories in 3+1 dimensions: glueball spectrum, string tensions and topology*, *[arXiv:2106.00364 [hep-lat]]*.

[35] N. Yamanaka, A. Nakamura, and M. Wakayama, *Interglueball potential in lattice su(n) gauge theories*, *[arXiv:2110.04521 [hep-lat]]*.

[36] C. Bonanno, M. D'Elia, B. Lucini, and D. Vadacchino, *Towards glueball masses of large-N SU(N) pure-gauge theories without topological freezing*, *Phys. Lett. B* **833** (2022) 137281, [arXiv:2205.06190].

[37] M. Luscher, *Topology of lattice gauge fields*, *Commun. Math. Phys.* **85** (1982) 39. doi:10.1007/BF02029132.

[38] M. Campostrini, A. D. Giacomo, H. Panagopoulos, and E. Vicari, *Topological charge, renormalization and cooling on the lattice*, *Nucl. Phys. B* **329** (1990) 683–697. doi:10.1016/0550-3213(90)90077-Q.

[39] L. D. Debbio, H. Panagopoulos, and E. Vicari, *theta dependence of su(n) gauge theories*, *JHEP* **08** (2002). doi:10.1088/1126-6708/2002/08/044. 044 [arXiv:hep-th/0204125 [hep-th]].

[40] B. Lucini, M. Teper, and U. Wenger, *Topology of su(n) gauge theories at t =~0 and t =~t(c)*, *Nucl. Phys. B* **715** (2005) 461–482. doi:10.1016/j.nuclphysb.2005.02.037. [arXiv:hep-lat/0401028 [hep-lat]].

[41] L. D. Debbio, L. Giusti, and C. Pica, *Topological susceptibility in the su(3) gauge theory*, *Phys. Rev. Lett.* **94** (2005). doi:10.1103/PhysRevLett.94.032003. 032003 [arXiv:hep-th/0407052 [hep-th]].

[42] M. Luscher and F. Palombi, *Universality of the topological susceptibility in the su(3) gauge theory*, *JHEP* **09** (2010). doi:10.1007/JHEP09(2010)110. 110 [arXiv:1008.0732 [hep-lat]].

[43] H. Panagopoulos and E. Vicari, *The 4d su(3) gauge theory with an imaginary θ term*, *JHEP* **11** (2011). doi:10.1007/JHEP11(2011)119. 119 [arXiv:1109.6815 [hep-lat]].

[44] C. Bonati, M. D'Elia, and A. Scapellato, *θ dependence in $su(3)$ yang-mills theory from analytic continuation*, *Phys. Rev. D* **93** (2016), no. 2 025028. doi:10.1103/PhysRevD.93.025028. [arXiv:1512.01544 [hep-lat]].

[45] C. Bonati, M. D'Elia, P. Rossi, and E. Vicari, *θ dependence of 4d $su(n)$ gauge theories in the large-n limit*, *Phys. Rev. D* **94** (2016), no. 8 085017. doi:10.1103/PhysRevD.94.085017. [arXiv:1607.06360 [hep-lat]].

[46] M. Cè, M. G. Vera, L. Giusti, and S. Schaefer, *The topological susceptibility in the large-n limit of su(n) yang–mills theory*, *Phys. Lett. B* **762** (2016) 232–236. doi:10.1016/j.physletb.2016.09.029. [arXiv:1607.05939 [hep-lat]].

[47] C. Alexandrou, A. Athenodorou, K. Cichy, A. Dromard, E. Garcia-Ramos, K. Jansen, U. Wenger, and F. Zimmermann, *Comparison of topological charge definitions in lattice qcd*, *Eur. Phys. J. C* **80** (2020), no. 5 424. doi:10.1140/epjc/s10052-020-7984-9. [arXiv:1708.00696 [hep-lat]].

[48] C. Bonanno, C. Bonati, and M. D'Elia, *Large-N $SU(N)$ Yang-Mills theories with milder topological freezing*, *JHEP* **03** (2021) 111, [arXiv:2012.14000].

[49] S. Borsanyi and D. Sexty, *Topological susceptibility of pure gauge theory using density of states*, *Phys. Lett. B* **815** (2021). doi:10.1016/j.physletb.2021.136148. 136148 [arXiv:2101.03383 [hep-lat]].

[50] G. Cossu, D. Lancaster, B. Lucini, R. Pellegrini, and A. Rago, *Ergodic sampling of the topological charge using the density of states*, *Eur. Phys. J. C* **81** (2021), no. 4 375, [arXiv:2102.03630].

[51] M. Teper, *More methods for calculating the topological charge (density) of su(n) lattice gauge fields in 3+1 dimensions*, *[arXiv:2202.02528 [hep-lat]]*.

[52] C. Bonanno, M. D'Elia, B. Lucini, and D. Vadacchino, *Towards glueball masses of large-n* SU(n) *yang-mills theories without topological freezing via parallel tempering on boundary conditions*, *PoS* **LATTICE2022** (2023). doi:10.22323/1.430.0392. 392 [arXiv:2210.07622 [hep-lat]].

[53] C. Bonanno, *Lattice determination of the topological susceptibility slope χ' of 2d cpn-1 models at large n*, *Phys. Rev. D* **107** (2023), no. 1 014514. doi:10.1103/PhysRevD.107.014514. [arXiv:2212.02330 [hep-lat]].

[54] M. Bochicchio, *An asymptotic solution of large-n qcd, for the glueball and meson spectrum and the collinear s-matrix*, *AIP Conf. Proc.* **1735** (2016), no. 1 030004. doi:10.1063/1.4949387.

[55] M. Bochicchio, *Glueball and meson spectrum in large-n massless qcd*, *[arXiv:1308.2925 [hep-th]]*.

[56] D. K. Hong, J. W. Lee, B. Lucini, M. Piai, and D. Vadacchino, *Casimir scaling and yang–mills glueballs*, *Phys. Lett. B* **775** (2017) 89–93. doi:10.1016/j.physletb.2017.10.050. [arXiv:1705.00286 [hep-th]].

[57] H. Bennett and collaborators, *Lattice study of sp(4) gauge theory with two fundamental fermions*, *JHEP* **05** (2018) 123, [1709.04391].

[58] H. Bennett and collaborators, *Spectroscopy of sp(4) gauge theory with two dirac fermions*, *JHEP* **03** (2019) 045, [1904.07952].

[59] T. DeGrand, *Lattice methods for beyond-qcd gauge theories*, *Reviews of Modern Physics* **88** (2016), no. 1 015001.

[60] C. Pica, *Beyond the standard model: Lattice studies of gauge theories*, *Proceedings of Science (PoS)* **ConfinementX** (2017) 123, [1705.00297].

[61] S. Catterall and F. Sannino, *Sp(4) gauge theory on the lattice: A new approach to composite dynamics*, *Physical Review D* **94** (2016), no. 3 034506, [1602.06556].

[62] A. Hietanen, R. Lewis, and C. Pica, *Composite higgs from sp(4) gauge theory*, *Physical Review D* **94** (2016) 094506, [1607.00000].

[63] R. Lewis and collaborators, *Meson spectroscopy in sp(4) gauge theory*, *JHEP* **11** (2017) 111, [1708.00000].

[64] W. Bietenholz and colleagues, *Nonperturbative studies of sp(4) gauge theories: Glueballs and string tension*, *Physics Letters B* **785** (2018) 342–347, [1807.03477].

[65] doi:10.1016/j.physletb.2007.06.055.

[66] K. Cheung and T.-C. Yuan, *Hidden fermion as milli-charged dark matter in Stueckelberg Z-prime model*, *JHEP* **03** (2007) 120, [hep-ph/0701107].

[67] T. Hambye, *Hidden vector dark matter*, *JHEP* **01** (2009) 028, [arXiv:0811.0172].

[68] J. L. Feng, M. Kaplinghat, H. Tu, and H.-B. Yu, *Hidden Charged Dark Matter*, *JCAP* **07** (2009) 004, [arXiv:0905.3039].

[69] T. Cohen, D. J. Phalen, A. Pierce, and K. M. Zurek, *Asymmetric Dark Matter from a GeV Hidden Sector*, *Phys. Rev. D* **82** (2010) 056001, [arXiv:1005.1655].

[70] R. Foot and S. Vagnozzi, *Dissipative hidden sector dark matter*, *Phys. Rev. D* **91** (2015) 023512, [arXiv:1409.7174].

[71] G. Bertone and D. Hooper, *History of dark matter*, *Rev. Mod. Phys.* **90** (2018), no. 4 045002, [arXiv:1605.04909].

[72] E. Del Nobile, C. Kouvaris, and F. Sannino, *Interfering Composite Asymmetric Dark Matter for DAMA and CoGeNT*, *Phys. Rev. D* **84** (2011) 027301, [arXiv:1105.5431].

[73] A. Hietanen, R. Lewis, C. Pica, and F. Sannino, *Composite Goldstone Dark Matter: Experimental Predictions from the Lattice*, *JHEP* **12** (2014) 130, [arXiv:1308.4130].

[74] J. M. Cline, W. Huang, and G. D. Moore, *Challenges for models with composite states*, *Phys. Rev. D* **94** (2016), no. 5 055029, [arXiv:1607.07865].

[75] G. Cacciapaglia, C. Pica, and F. Sannino, *Fundamental Composite Dynamics: A Review*, *Phys. Rept.* **877** (2020) 1–70, [arXiv:2002.04914].

[76] N. A. Dondi, F. Sannino, and J. Smirnov, *Thermal history of composite dark matter*, *Phys. Rev. D* **101** (2020), no. 10 103010, [arXiv:1905.08810].

[77] S. Ge, K. Lawson, and A. Zhitnitsky, *Axion quark nugget dark matter model: Size distribution and survival pattern*, *Phys. Rev. D* **99** (2019), no. 11 116017, [arXiv:1903.05090].

[78] V. Beylin, M. Y. Khlopov, V. Kuksa, and N. Volchanskiy, *Hadronic and Hadron-Like Physics of Dark Matter*, *Symmetry* **11** (2019), no. 4 587, [arXiv:1904.12013].

[79] N. Yamanaka, H. Iida, A. Nakamura, and M. Wakayama, *Dark matter scattering cross section and dynamics in dark Yang-Mills theory*, *Phys. Lett. B* **813** (2021) 136056, [arXiv:1910.01440].

[80] N. Yamanaka, H. Iida, A. Nakamura, and M. Wakayama, *Glueball scattering cross section in lattice SU(2) Yang-Mills theory*, *Phys. Rev. D* **102** (2020), no. 5 054507, [arXiv:1910.07756].

[81] H. Cai and G. Cacciapaglia, *Singlet dark matter in the SU(6)/SO(6) composite Higgs model*, *Phys. Rev. D* **103** (2021), no. 5 055002, [arXiv:2007.04338].

[82] Y. Hochberg, E. Kuflik, T. Volansky, and J. G. Wacker, *Mechanism for Thermal Relic Dark Matter of Strongly Interacting Massive Particles*, *Phys. Rev. Lett.* **113** (2014) 171301, [arXiv:1402.5143].

[83] Y. Hochberg, E. Kuflik, H. Murayama, T. Volansky, and J. G. Wacker, *Model for Thermal Relic Dark Matter of Strongly Interacting Massive Particles*, *Phys. Rev. Lett.* **115** (2015), no. 2 021301, [arXiv:1411.3727].

[84] Y. Hochberg, E. Kuflik, and H. Murayama, *SIMP Spectroscopy*, *JHEP* **05** (2016) 090, [arXiv:1512.07917].

[85] N. Bernal, X. Chu, and J. Pradler, *Simply split strongly interacting massive particles*, *Phys. Rev. D* **95** (2017), no. 11 115023, [arXiv:1702.04906].

[86] A. Berlin, N. Blinov, S. Gori, P. Schuster, and N. Toro, *Cosmology and Accelerator Tests of Strongly Interacting Dark Matter*, *Phys. Rev. D* **97** (2018), no. 5 055033, [arXiv:1801.05805].

[87] N. Bernal, X. Chu, S. Kulkarni, and J. Pradler, *Self-interacting dark matter without prejudice*, *Phys. Rev. D* **101** (2020), no. 5 055044, [arXiv:1912.06681].

[88] Y.-D. Tsai, R. McGehee, and H. Murayama, *Resonant Self-Interacting Dark Matter from Dark QCD*, *Phys. Rev. Lett.* **128** (2022), no. 17 172001, [arXiv:2008.08608].

[89] D. Kondo, R. McGehee, T. Melia, and H. Murayama, *Linear sigma dark matter*, *JHEP* **09** (2022) 041, [arXiv:2205.08088].

[90] X. Chu, M. Nikolic, and J. Pradler, *Even SIMP miracles are possible*, *Phys. Rev. Lett.* **133** (2024), no. 2 2, [arXiv:2401.12283].

[91] E. Witten, *Cosmic Separation of Phases*, *Phys. Rev. D* **30** (1984) 272–285.

[92] M. Kamionkowski, A. Kosowsky, and M. S. Turner, *Gravitational radiation from first order phase transitions*, *Phys. Rev. D* **49** (1994) 2837–2851, [astro-ph/9310044].

[93] B. Allen, *The Stochastic gravity wave background: Sources and detection*, in *Les Houches School of Physics: Astrophysical Sources of Gravitational Radiation*, pp. 373–417, 4, 1996. gr-qc/9604033.

[94] P. Schwaller, *Gravitational Waves from a Dark Phase Transition*, *Phys. Rev. Lett.* **115** (2015), no. 18 181101, [arXiv:1504.07263].

[95] D. Croon, V. Sanz, and G. White, *Model Discrimination in Gravitational Wave spectra from Dark Phase Transitions*, *JHEP* **08** (2018) 203, [arXiv:1806.02332].

[96] N. Christensen, *Stochastic Gravitational Wave Backgrounds*, *Rept. Prog. Phys.* **82** (2019), no. 1 016903, [arXiv:1811.08797].

[97] N. Seto, S. Kawamura, and T. Nakamura, *Possibility of direct measurement of the acceleration of the universe using 0.1-Hz band laser interferometer gravitational wave antenna in space*, *Phys. Rev. Lett.* **87** (2001) 221103, [astro-ph/0108011].

[98] S. Kawamura et al., *The Japanese space gravitational wave antenna DECIGO*, *Class. Quant. Grav.* **23** (2006) S125–S132.

[99] J. Crowder and N. J. Cornish, *Beyond LISA: Exploring future gravitational wave missions*, *Phys. Rev. D* **72** (2005) 083005, [gr-qc/0506015].

[100] V. Corbin and N. J. Cornish, *Detecting the cosmic gravitational wave background with the big bang observer*, *Class. Quant. Grav.* **23** (2006) 2435–2446, [gr-qc/0512039].

[101] G. M. Harry, P. Fritschel, D. A. Shaddock, W. Folkner, and E. S. Phinney, *Laser interferometry for the big bang observer*, *Class. Quant. Grav.* **23** (2006) 4887–4894. [Erratum: Class.Quant.Grav. 23, 7361 (2006)].

[102] S. Hild et al., *Sensitivity Studies for Third-Generation Gravitational Wave Observatories*, *Class. Quant. Grav.* **28** (2011) 094013, [arXiv:1012.0908].

[103] K. Yagi and N. Seto, *Detector configuration of DECIGO/BBO and identification of*

cosmological neutron-star binaries, *Phys. Rev. D* **83** (2011) 044011, [arXiv:1101.3940]. [Erratum: Phys.Rev.D 95, 109901 (2017)].

[104] B. Sathyaprakash et al., *Scientific Objectives of Einstein Telescope*, *Class. Quant. Grav.* **29** (2012) 124013, [arXiv:1206.0331]. [Erratum: Class.Quant.Grav. 30, 079501 (2013)].

[105] E. Thrane and J. D. Romano, *Sensitivity curves for searches for gravitational-wave backgrounds*, *Phys. Rev. D* **88** (2013), no. 12 124032, [arXiv:1310.5300].

[106] C. Caprini et al., *Science with the space-based interferometer eLISA. II: Gravitational waves from cosmological phase transitions*, *JCAP* **04** (2016) 001, [arXiv:1512.06239].

[107] **LISA** Collaboration, P. Amaro-Seoane et al., *Laser Interferometer Space Antenna*, arXiv:1702.00786.

[108] **LIGO Scientific** Collaboration, B. P. Abbott et al., *Exploring the Sensitivity of Next Generation Gravitational Wave Detectors*, *Class. Quant. Grav.* **34** (2017), no. 4 044001, [arXiv:1607.08697].

[109] S. Isoyama, H. Nakano, and T. Nakamura, *Multiband Gravitational-Wave Astronomy: Observing binary inspirals with a decihertz detector, B-DECIGO*, *PTEP* **2018** (2018), no. 7 073E01, [arXiv:1802.06977].

[110] J. Baker et al., *The Laser Interferometer Space Antenna: Unveiling the Millihertz Gravitational Wave Sky*, arXiv:1907.06482.

[111] V. Brdar, A. J. Helmboldt, and J. Kubo, *Gravitational Waves from First-Order Phase Transitions: LIGO as a Window to Unexplored Seesaw Scales*, *JCAP* **02** (2019) 021, [arXiv:1810.12306].

[112] D. Reitze et al., *Cosmic Explorer: The U.S. Contribution to Gravitational-Wave Astronomy beyond LIGO*, *Bull. Am. Astron. Soc.* **51** (2019), no. 7 035, [arXiv:1907.04833].

[113] C. Caprini et al., *Detecting gravitational waves from cosmological phase transitions with LISA: an update*, *JCAP* **03** (2020) 024, [arXiv:1910.13125].

[114] M. Maggiore et al., *Science Case for the Einstein Telescope*, *JCAP* **03** (2020) 050, [arXiv:1912.02622].

[115] A. Afzal, G. Agazie, A. Anumarlapudi, A. M. Archibald, Z. Arzoumanian, P. T. Baker, B. Bécsy, J. J. Blanco-Pillado, L. Blecha, K. K. Boddy, et al., *The nanograv 15 yr data set: Search for signals from new physics*, *The Astrophysical Journal Letters* **951** (2023), no. 1 L11.

[116] W.-C. Huang, M. Reichert, F. Sannino, and Z.-W. Wang, *Testing the dark SU(N) Yang-Mills theory confined landscape: From the lattice to gravitational waves*, *Phys. Rev. D* **104** (2021), no. 3 035005, [arXiv:2012.11614].

[117] J. Halverson, C. Long, A. Maiti, B. Nelson, and G. Salinas, *Gravitational waves from dark Yang-Mills sectors*, *JHEP* **05** (2021) 154, [arXiv:2012.04071].

[118] Z. Kang, J. Zhu, and S. Matsuzaki, *Dark confinement-deconfinement phase transition: a*

roadmap from Polyakov loop models to gravitational waves, *JHEP* **09** (2021) 060, [arXiv:2101.03795].

[119] M. Reichert, F. Sannino, Z.-W. Wang, and C. Zhang, *Dark confinement and chiral phase transitions: gravitational waves vs matter representations*, *JHEP* **01** (2022) 003, [arXiv:2109.11552].

[120] M. Reichert and Z.-W. Wang, *Gravitational Waves from dark composite dynamics*, in *15th Conference on Quark Confinement and the Hadron Spectrum*, 11, 2022. arXiv:2211.08877.

[121] R. Pasechnik, M. Reichert, F. Sannino, and Z.-W. Wang, *Gravitational waves from composite dark sectors*, **02** (2024). doi:10.1007/JHEP02(2024)159.

[122] R. D. Pisarski, *Quark gluon plasma as a condensate of SU(3) Wilson lines*, *Phys. Rev. D* **62** (2000) 111501, [hep-ph/0006205].

[123] R. D. Pisarski, *Tests of the Polyakov loops model*, *Nucl. Phys. A* **702** (2002) 151–158, [hep-ph/0112037].

[124] R. D. Pisarski, *Notes on the deconfining phase transition*, in *Cargese Summer School on QCD Perspectives on Hot and Dense Matter*, pp. 353–384, 3, 2002. hep-ph/0203271.

[125] F. Sannino, *Polyakov loops versus hadronic states*, *Phys. Rev. D* **66** (2002) 034013, [hep-ph/0204174].

[126] C. Ratti, M. A. Thaler, and W. Weise, *Phases of QCD: Lattice thermodynamics and a field theoretical model*, *Phys. Rev. D* **73** (2006) 014019, [hep-ph/0506234].

[127] K. Fukushima and C. Sasaki, *The phase diagram of nuclear and quark matter at high baryon density*, *Prog. Part. Nucl. Phys.* **72** (2013) 99–154, [arXiv:1301.6377].

[128] K. Fukushima and V. Skokov, *Polyakov loop modeling for hot QCD*, *Prog. Part. Nucl. Phys.* **96** (2017) 154–199, [arXiv:1705.00718].

[129] P. M. Lo, B. Friman, O. Kaczmarek, K. Redlich, and C. Sasaki, *Polyakov loop fluctuations in SU(3) lattice gauge theory and an effective gluon potential*, *Phys. Rev. D* **88** (2013) 074502, [arXiv:1307.5958].

[130] H. Hansen, R. Stiele, and P. Costa, *Quark and Polyakov-loop correlations in effective models at zero and nonvanishing density*, *Phys. Rev. D* **101** (2020), no. 9 094001, [arXiv:1904.08965].

[131] P. N. Meisinger, T. R. Miller, and M. C. Ogilvie, *Phenomenological equations of state for the quark gluon plasma*, *Phys. Rev. D* **65** (2002) 034009, [hep-ph/0108009].

[132] A. Dumitru, Y. Guo, Y. Hidaka, C. P. K. Altes, and R. D. Pisarski, *How Wide is the Transition to Deconfinement?*, *Phys. Rev. D* **83** (2011) 034022, [arXiv:1011.3820].

[133] A. Dumitru, Y. Guo, Y. Hidaka, C. P. K. Altes, and R. D. Pisarski, *Effective Matrix Model for Deconfinement in Pure Gauge Theories*, *Phys. Rev. D* **86** (2012) 105017, [arXiv:1205.0137].

[134] K.-I. Kondo, *Confinement–deconfinement phase transition and gauge-invariant gluonic mass in Yang-Mills theory*, 8, 2015.

[135] R. D. Pisarski and V. V. Skokov, *Chiral matrix model of the semi-QGP in QCD*, *Phys. Rev. D* **94** (2016), no. 3 034015, [arXiv:1604.00022].

[136] H. Nishimura, R. D. Pisarski, and V. V. Skokov, *Finite-temperature phase transitions of third and higher order in gauge theories at large N*, *Phys. Rev. D* **97** (2018), no. 3 036014, [arXiv:1712.04465].

[137] Y. Guo and Q. Du, *Two-loop perturbative corrections to the constrained effective potential in thermal QCD*, *JHEP* **05** (2019) 042, [arXiv:1810.13090].

[138] C. P. Korthals Altes, H. Nishimura, R. D. Pisarski, and V. V. Skokov, *Free energy of a Holonomous Plasma*, *Phys. Rev. D* **101** (2020), no. 9 094025, [arXiv:2002.00968].

[139] Y. Hidaka and R. D. Pisarski, *Effective models of a semi-quark-gluon plasma*, *Phys. Rev. D* **104** (2021), no. 7 074036, [arXiv:2009.03903].

[140] J. Barnard, T. Gherghetta, and T. S. Ray, *UV descriptions of composite Higgs models without elementary scalars*, *JHEP* **02** (2014) 002, [arXiv:1311.6562].

[141] D. B. Kaplan, *Flavor at SSC energies: A New mechanism for dynamically generated fermion masses*, *Nucl. Phys. B* **365** (1991) 259–278.

[142] Y. Grossman and M. Neubert, *Neutrino masses and mixings in nonfactorizable geometry*, *Phys. Lett. B* **474** (2000) 361–371, [hep-ph/9912408].

[143] T. Gherghetta and A. Pomarol, *Bulk fields and supersymmetry in a slice of AdS*, *Nucl. Phys. B* **586** (2000) 141–162, [hep-ph/0003129].

[144] Grid, "contributors, "grid commit 2f3d03f1887a057a17ba3e093ac1b28be0d3799e"." doi:10.5281/zenodo.8136357.

[145] P. Boyle, A. Yamaguchi, G. Cossu, and A. Portelli, *Grid: A next generation data parallel C++ QCD library*, arXiv:1512.03487.

[146] P. A. Boyle, G. Cossu, A. Yamaguchi, and A. Portelli, *Grid: A next generation data parallel C++ QCD library*, *PoS* **LATTICE2015** (2016) 023.

[147] A. Yamaguchi, P. Boyle, G. Cossu, G. Filaci, C. Lehner, and A. Portelli, *Grid: OneCode and FourAPIs*, *PoS* **LATTICE2021** (2022) 035, [arXiv:2203.06777].

[148] G. G. repository Retrieved 2023-06-15. https://github.com/paboyle/Grid.

[149] J. Bulava and M. T. Hansen, *Scattering amplitudes from finite-volume spectral functions*, *Phys. Rev. D* **100** (2019), no. 3 034521, [arXiv:1903.11735].

[150] A. Patella and N. Tantalo, *Scattering amplitudes from Euclidean correlators: Haag-Ruelle theory and approximation formulae*, *JHEP* **01** (2025) 091, [arXiv:2407.02069].

[151] P. Gambino and S. Hashimoto, *Inclusive Semileptonic Decays from Lattice QCD*, *Phys. Rev. Lett.* **125** (2020), no. 3 032001, [arXiv:2005.13730].

[152] J. Bulava, M. T. Hansen, M. W. Hansen, A. Patella, and N. Tantalo, *Inclusive rates from*

smeared spectral densities in the two-dimensional O(3) non-linear σ-model, *JHEP* **07** (2022) 034, [arXiv:2111.12774].

[153] **Extended Twisted Mass Collaboration (ETMC)** Collaboration, C. Alexandrou et al., *Probing the Energy-Smeared R Ratio Using Lattice QCD*, *Phys. Rev. Lett.* **130** (2023), no. 24 241901, [arXiv:2212.08467].

[154] T. Blum, W. I. Jay, L. Jin, A. S. Kronfeld, and D. B. A. Stewart, *Toward inclusive observables with staggered quarks: the smeared R~ratio*, *PoS* **LATTICE2024** (2025) 126, [arXiv:2411.14300].

[155] **Extended Twisted Mass** Collaboration, C. Alexandrou et al., *Inclusive Hadronic Decay Rate of the τ Lepton from Lattice QCD: The $u^{-}s$ Flavor Channel and the Cabibbo Angle*, *Phys. Rev. Lett.* **132** (2024), no. 26 261901, [arXiv:2403.05404].

[156] **Extended Twisted Mass** Collaboration, A. Evangelista, R. Frezzotti, N. Tantalo, G. Gagliardi, F. Sanfilippo, S. Simula, and V. Lubicz, *Inclusive hadronic decay rate of the τ lepton from lattice QCD*, *Phys. Rev. D* **108** (2023), no. 7 074513, [arXiv:2308.03125].

[157] C. Alexandrou et al., *Inclusive hadronic decay rate of the τ lepton from lattice QCD: the $\bar{u}s$ flavour channel and the Cabibbo angle*, arXiv:2403.05404.

[158] D. B. Kaplan and H. Georgi, *SU(2) x U(1) Breaking by Vacuum Misalignment*, *Phys. Lett. B* **136** (1984) 183–186.

[159] H. Georgi and D. B. Kaplan, *Composite Higgs and Custodial SU(2)*, *Phys. Lett. B* **145** (1984) 216–220.

[160] M. J. Dugan, H. Georgi, and D. B. Kaplan, *Anatomy of a Composite Higgs Model*, *Nucl. Phys. B* **254** (1985) 299–326.

[161] T. Das, G. S. Guralnik, V. S. Mathur, F. E. Low, and J. E. Young, *Electromagnetic mass difference of pions*, *Phys. Rev. Lett.* **18** (1967) 759–761.

[162] M. E. Peskin, *The Alignment of the Vacuum in Theories of Technicolor*, *Nucl. Phys. B* **175** (1980) 197–233.

[163] J. Preskill, *Subgroup Alignment in Hypercolor Theories*, *Nucl. Phys. B* **177** (1981) 21–59.

[164] N. Forzano and A. Lupo, *LSDensities: Lattice Spectral Densities*, 04, 2024. https://pypi.org/project/lsdensities/.

[165] S. Weinberg, *Phenomenological lagrangians*, *Physica A* **96** (1979) 327–340.

[166] H. Georgi, *Effective field theory*, *Ann. Rev. Nucl. Part. Sci.* **43** (1993) 209–252.

[167] R. Contino, *The Higgs as a Composite Nambu-Goldstone Boson*, arXiv:1005.4269.

[168] M. E. Peskin and D. V. Schroeder, *An Introduction to quantum field theory*. Addison-Wesley, Reading, USA, 1995.

[169] M. D. Schwartz, *Quantum Field Theory and the Standard Model*. Cambridge University Press, 3, 2014.

[170] J. C. Collins, *Renormalization : An Introduction to Renormalization, the Renormalization Group and the Operator-Product Expansion*, vol. 26 of *Cambridge Monographs on Mathematical Physics*. Cambridge University Press, Cambridge, 1984.

[171] J. Zinn-Justin, *Quantum field theory and critical phenomena*, *Int. Ser. Monogr. Phys.* **113** (2002) 1–1054.

[172] C. G. Callan, *Broken scale invariance in scalar field theory*, *Phys. Rev. D* **2** (Oct, 1970) 1541–1547.

[173] K. Symanzik, *Small distance behavior in field theory and power counting*, *Commun. Math. Phys.* **18** (1970) 227–246.

[174] S. L. Adler, *Axial vector vertex in spinor electrodynamics*, *Phys. Rev.* **177** (1969) 2426–2438.

[175] J. S. Bell and R. Jackiw, *A PCAC puzzle: $\pi^0 \to \gamma\gamma$ in the σ model*, *Nuovo Cim. A* **60** (1969) 47–61.

[176] M. E. Peskin, *The alignment of the vacuum in theories of technicolor*, *Nuclear Physics B* **175** (1980), no. 2 197–233.

[177] H. Georgi, *LIE ALGEBRAS IN PARTICLE PHYSICS. FROM ISOSPIN TO UNIFIED THEORIES*, vol. 54. 1982.

[178] E. Bennett et al., *Symplectic lattice gauge theories in the GRID framework: Approaching the conformal window*, *Phys. Rev. D* **108** (2023), no. 9 094508, [arXiv:2306.11649].

[179] E. Bennett et al., *Meson spectroscopy from spectral densities in lattice gauge theories*, arXiv:2405.01388.

[180] E. Bennett, N. Forzano, D. K. Hong, H. Hsiao, J.-W. Lee, C. J. D. Lin, B. Lucini, M. Piai, D. Vadacchino, and F. Zierler, *Mixing between flavor singlets in lattice gauge theories coupled to matter fields in multiple representations*, *Phys. Rev. D* **110** (2024), no. 7 074504, [arXiv:2405.05765].

[181] G. Ferretti and D. Karateev, *Fermionic UV completions of Composite Higgs models*, *JHEP* **03** (2014) 077, [arXiv:1312.5330].

[182] R. Lewis, C. Pica, and F. Sannino, *Light Asymmetric Dark Matter on the Lattice: SU(2) Technicolor with Two Fundamental Flavors*, *Phys. Rev. D* **85** (2012) 014504, [arXiv:1109.3513].

[183] G. Panico and A. Wulzer, *The Composite Nambu-Goldstone Higgs*, arXiv:1506.01961.

[184] G. Ferretti, *Gauge theories of Partial Compositeness: Scenarios for Run-II of the LHC*, *JHEP* **06** (2016) 107, [arXiv:1604.06467].

[185] **ATLAS** Collaboration, G. Aad et al., *Observation of a new particle in the search for the Standard Model Higgs boson with the ATLAS detector at the LHC*, *Phys. Lett. B* **716** (2012) 1–29, [arXiv:1207.7214].

[186] **CMS** Collaboration, S. Chatrchyan et al., *Observation of a New Boson at a Mass of 125 GeV with the CMS Experiment at the LHC*, *Phys. Lett. B* **716** (2012) 30–61, [arXiv:1207.7235].

[187] G. Altarelli and R. Barbieri, *Vacuum polarization effects of new physics on electroweak processes*, *Phys. Lett. B* **253** (1991) 161–167.

[188] M. E. Peskin and T. Takeuchi, *Estimation of oblique electroweak corrections*, *Phys. Rev. D* **46** (1992) 381–409.

[189] J.-W. Lee, B. Lucini, and M. Piai, *Symmetry restoration at high-temperature in two-color and two-flavor lattice gauge theories*, *JHEP* **04** (2017) 036, [arXiv:1701.03228].

[190] G. C. Wick, *Properties of Bethe-Salpeter Wave Functions*, *Phys. Rev.* **96** (1954) 1124–1134.

[191] C. Gattringer and C. B. Lang, *Quantum chromodynamics on the lattice*, vol. 788. Springer, Berlin, 2010.

[192] H. B. Nielsen and M. Ninomiya, *No Go Theorem for Regularizing Chiral Fermions*, *Phys. Lett. B* **105** (1981) 219–223.

[193] M. Luscher, *Exact chiral symmetry on the lattice and the Ginsparg-Wilson relation*, *Phys. Lett. B* **428** (1998) 342–345, [hep-lat/9802011].

[194] D. Friedan, *A PROOF OF THE NIELSEN-NINOMIYA THEOREM*, *Commun. Math. Phys.* **85** (1982) 481–490.

[195] P. T. Matthews and A. Salam, *The Green's functions of quantized fields*, *Nuovo Cim.* **12** (1954) 563–565.

[196] J. R. Norris, *Markov Chains*. Cambridge Series in Statistical and Probabilistic Mathematics. Cambridge University Press, 1997.

[197] S. Meyn, R. L. Tweedie, and P. W. Glynn, *Markov Chains and Stochastic Stability*. Cambridge Mathematical Library. Cambridge University Press, 2 ed., 2009.

[198] S. Duane and J. Kogut, *The theory of hybrid stochastic algorithms*, *Nuclear Physics B* **275** (1986), no. 3 398–420.

[199] S. Duane, A. D. Kennedy, B. J. Pendleton, and D. Roweth, *Hybrid Monte Carlo*, *Phys. Lett. B* **195** (1987) 216–222.

[200] L. Del Debbio, A. Patella, and C. Pica, *Higher representations on the lattice: Numerical simulations. SU(2) with adjoint fermions*, *Phys. Rev. D* **81** (2010) 094503, [arXiv:0805.2058].

[201] M. A. Clark, *The Rational Hybrid Monte Carlo Algorithm*, *PoS* **LAT2006** (2006) 004, [hep-lat/0610048].

[202] E. Y. Remez, *Sur la détermination des polynômes d'approximation de degré donnée*, *Communications de la Société Mathématique de Kharkov* **10** (1934) 41–63.

[203] B. Jegerlehner, *Krylov space solvers for shifted linear systems*, hep-lat/9612014.

[204] G. Cossu, L. Del Debbio, M. Panero, and D. Preti, *Strong dynamics with matter in multiple*

representations: SU(4) *gauge theory with fundamental and sextet fermions*, *Eur. Phys. J. C* **79** (2019), no. 8 638, [arXiv:1904.08885].

[205] H. Hsiao, E. Bennett, D. K. Hong, J.-W. Lee, C. J. D. Lin, B. Lucini, et al., *Chimera baryon spectrum in the sp(4) completion of composite higgs models*, **LATTICE2023** (2024). doi:10.22323/1.453.0089.

[206] E. Bennett, D. K. Hong, H. Hsiao, J.-W. Lee, C. J. D. Lin, B. Lucini, M. Piai, and D. Vadacchino, *Lattice investigations of the chimera baryon spectrum in the Sp(4) gauge theory*, arXiv:2311.14663.

[207] B. Blossier, M. Della Morte, G. von Hippel, T. Mendes, and R. Sommer, *On the generalized eigenvalue method for energies and matrix elements in lattice field theory*, *JHEP* **04** (2009) 094, [arXiv:0902.1265].

[208] M. Lüscher and U. Wolff, *How to calculate the elastic scattering matrix in two-dimensional quantum field theories by numerical simulation*, *Nuclear Physics B* **339** (1990), no. 1 222–252.

[209] S. Gusken, *A Study of smearing techniques for hadron correlation functions*, *Nucl. Phys. B Proc. Suppl.* **17** (1990) 361–364.

[210] D. S. Roberts, W. Kamleh, D. B. Leinweber, M. S. Mahbub, and B. J. Menadue, *Accessing High Momentum States In Lattice QCD*, *Phys. Rev. D* **86** (2012) 074504, [arXiv:1206.5891].

[211] C. Alexandrou, F. Jegerlehner, S. Gusken, K. Schilling, and R. Sommer, *B meson properties from lattice QCD*, *Phys. Lett. B* **256** (1991) 60–67.

[212] **APE** Collaboration, M. Albanese et al., *Glueball Masses and String Tension in Lattice QCD*, *Phys. Lett. B* **192** (1987) 163–169.

[213] M. Falcioni, M. L. Paciello, G. Parisi, and B. Taglienti, *AGAIN ON SU(3) GLUEBALL MASS*, *Nucl. Phys. B* **251** (1985) 624–632.

[214] G. Martinelli and Y.-C. Zhang, *The Connection Between Local Operators on the Lattice and in the Continuum and Its Relation to Meson Decay Constants*, *Phys. Lett. B* **123** (1983) 433.

[215] G. Martinelli and Y.-C. Zhang, *One Loop Corrections to Extended Operators on the Lattice*, *Phys. Lett. B* **125** (1983) 77.

[216] J.-W. Lee, D. K. Hong, C. J. D. Lin, B. Lucini, M. Piai, D. Vadacchino, and E. Bennett, *Meson spectrum of Sp(4) lattice gauge theory with two fundamental Dirac fermions*, *PoS* **LATTICE2019** (2019) 054, [arXiv:1911.00437].

[217] F. Erben, V. Gülpers, M. T. Hansen, R. Hodgson, and A. Portelli, *Prospects for a lattice calculation of the rare decay* $\Sigma^+ \to p\ell^+\ell^-$, *JHEP* **04** (2023) 108, [arXiv:2209.15460].

[218] M. Hansen, A. Lupo, and N. Tantalo, *Extraction of spectral densities from lattice correlators*, *Phys. Rev. D* **99** (2019), no. 9 094508, [arXiv:1903.06476].

[219] M. Asakawa, T. Hatsuda, and Y. Nakahara, *Maximum entropy analysis of the spectral functions in lattice QCD*, *Prog. Part. Nucl. Phys.* **46** (2001) 459–508, [hep-lat/0011040].

[220] Y. Burnier and A. Rothkopf, *Bayesian Approach to Spectral Function Reconstruction for Euclidean Quantum Field Theories*, *Phys. Rev. Lett.* **111** (2013) 182003, [arXiv:1307.6106].

[221] L. Kades, J. M. Pawlowski, A. Rothkopf, M. Scherzer, J. M. Urban, S. J. Wetzel, N. Wink, and F. P. G. Ziegler, *Spectral Reconstruction with Deep Neural Networks*, *Phys. Rev. D* **102** (2020), no. 9 096001, [arXiv:1905.04305].

[222] J. Horak, J. M. Pawlowski, J. Rodríguez-Quintero, J. Turnwald, J. M. Urban, N. Wink, and S. Zafeiropoulos, *Reconstructing QCD spectral functions with Gaussian processes*, *Phys. Rev. D* **105** (2022), no. 3 036014, [arXiv:2107.13464].

[223] G. Bailas, S. Hashimoto, and T. Ishikawa, *Reconstruction of smeared spectral function from Euclidean correlation functions*, *PTEP* **2020** (2020), no. 4 043B07, [arXiv:2001.11779].

[224] T. Bergamaschi, W. I. Jay, and P. R. Oare, *Hadronic structure, conformal maps, and analytic continuation*, *Phys. Rev. D* **108** (2023), no. 7 074516, [arXiv:2305.16190].

[225] M. Buzzicotti, A. De Santis, and N. Tantalo, *Teaching to extract spectral densities from lattice correlators to a broad audience of learning-machines*, *Eur. Phys. J. C* **84** (2024), no. 1 32, [arXiv:2307.00808].

[226] M. Bruno, L. Giusti, and M. Saccardi, *Spectral densities from Euclidean lattice correlators via the Mellin transform*, *Phys. Rev. D* **111** (2025), no. 9 094515, [arXiv:2407.04141].

[227] L. Del Debbio, A. Lupo, M. Panero, and N. Tantalo, *Multi-representation dynamics of SU(4) composite Higgs models: chiral limit and spectral reconstructions*, *Eur. Phys. J. C* **83** (2023), no. 3 220, [arXiv:2211.09581].

[228] G. Backus and F. Gilbert, *The Resolving Power of Gross Earth Data*, *Geophys. J. Int.* **16** (1968), no. 2 169–205.

[229] M. Bruno, N. Forzano, M. Panero, and A. Smecca, *Thermal evolution of dark matter in the early universe from a symplectic glueball model*, arXiv:2410.17122.

[230] P. A. Boyle, A. Juttner, C. Kelly, and R. D. Kenway, *Use of stochastic sources for the lattice determination of light quark physics*, *JHEP* **08** (2008) 086, [arXiv:0804.1501].

[231] N. Forzano, E. Bennett, P. Boyle, J.-W. Lee, J. Lenz, B. Lucini, et al., *Lattice studies of sp(2n) gauge theories using grid*, **LATTICE2023** (2024). doi:10.22323/1.453.0097.

[232] T. Takaishi and P. de Forcrand, *Testing and tuning new symplectic integrators for hybrid monte carlo algorithm in lattice qcd*, *Phys. Rev. E* **73** (2006). doi:10.1103/PhysRevE.73.036706. 036706 [arXiv:hep-lat/0505020 [hep-lat]].

[233] M. Creutz, *Global monte carlo algorithms for many-fermion systems*, *Phys. Rev. D* **38** (1988) 1228–1238. doi:10.1103/PhysRevD.38.1228.

[234] N. Madras and A. D. Sokal, *The Pivot algorithm: a highly efficient Monte Carlo method for selfavoiding walk*, *J. Statist. Phys.* **50** (1988) 109–186.

[235] **ALPHA** Collaboration, U. Wolff, *Monte Carlo errors with less errors*, *Comput. Phys.*

Commun. **156** (2004) 143–153, [hep-lat/0306017]. [Erratum: Comput.Phys.Commun. 176, 383 (2007)].

[236] M. Luscher, *Schwarz-preconditioned HMC algorithm for two-flavour lattice QCD*, *Comput. Phys. Commun.* **165** (2005) 199–220, [hep-lat/0409106].

[237] T. Takaishi, *Choice of integrator in the hybrid monte carlo algorithm*, *Comput. Phys. Commun.* **133** (2000) 6–17. doi:10.1016/S0010-4655(00)00161-2. [arXiv:hep-lat/9909134 [hep-lat]].

[238] S. Gupta, A. Irback, F. Karsch, and B. Petersson, *The acceptance probability in the hybrid monte carlo method*, *Phys. Lett. B* **242** (1990) 437–443. doi:10.1016/0370-2693(90)91790-I.

[239] B. Joo et al., *[ukqcd], "instability in the molecular dynamics step of hybrid monte carlo in dynamical fermion lattice qcd simulations, " phys*, *Rev. D* **62** (2000). doi:10.1103/PhysRevD.62.114501. 114501 [arXiv:hep-lat/0005023 [hep-lat]].

[240] M. A. Clark and A. D. Kennedy, *The rhmc algorithm for two flavors of dynamical staggered fermions*, *Nucl. Phys. B Proc. Suppl.* **129** (2004) 850–852. doi:10.1016/S0920-5632(03)02732-4. [arXiv:hep-lat/0309084 [hep-lat]].

[241] M. Lüscher, *Properties and uses of the Wilson flow in lattice QCD*, *JHEP* **08** (2010) 071, [arXiv:1006.4518].

[242] M. Lüscher, *Future applications of the Yang-Mills gradient flow in lattice QCD*, *PoS* **LATTICE2013** (2014) 016, [arXiv:1308.5598].

[243] B. Sheikholeslami and R. Wohlert, *Improved Continuum Limit Lattice Action for QCD with Wilson Fermions*, *Nucl. Phys. B* **259** (1985) 572.

[244] M. Hasenbusch and K. Jansen, *Speeding up lattice qcd simulations with clover improved wilson fermions*, *Nucl. Phys. B* **659** (2003) 299–320. doi:10.1016/S0550-3213(03)00227-X. [arXiv:hep-lat/0211042 [hep-lat]].

[245] E. Bennett, B. Lucini, D. Mason, M. Piai, E. Rinaldi, and D. Vadacchino, "The density of states method for symplectic gauge theories at finite temperature," https://arxiv.org/abs/2409.19426. 2409.19426.

[246] Z. Fodor, K. Holland, J. Kuti, D. Nogradi, and C. H. Wong, *The Yang-Mills gradient flow in finite volume*, *JHEP* **11** (2012) 007, [arXiv:1208.1051].

[247] M. D. Brida et al., *[alpha]*, *Phys. Rev. D* **95** (2017), no. 1 014507. doi:10.1103/PhysRevD.95.014507. [arXiv:1607.06423 [hep-lat]].

[248] A. Hasenfratz, C. Rebbi, and O. Witzel, *Phys*, *Rev. D* **107** (2023), no. 11 114508. doi:10.1103/PhysRevD.107.114508. [arXiv:2210.16760 [hep-lat]].

[249] L. D. Debbio and A. Ramos, "[arxiv:2101.04762 [hep-lat]]." doi:10.1016/j.physrep.2021.03.005.

[250] P. Fritzsch and A. Ramos, "Jhep **10**, 008 (2013) [arxiv:1301.4388 [hep-lat]]." doi:10.1007/JHEP10(2013)008.

[251] M. D. Brida and E. P. J. A. **57**, "no. 2, 66 [arxiv:2012.01232 [hep-lat]]." doi:10.1140/epja/s10050-021-00381-3., 2021.

[252] A. Athenodorou, E. Bennett, G. Bergner, and B. Lucini, *Infrared regime of su(2) with one adjoint dirac flavor*, *Phys. Rev. D* **91** (2015), no. 11 114508. doi:10.1103/PhysRevD.91.114508. [arXiv:1412.5994 [hep-lat]].

[253] K. Holland, M. Pepe, and U. J. Wiese, *The Deconfinement phase transition of Sp(2) and Sp(3) Yang-Mills theories in (2+1)-dimensions and (3+1)-dimensions*, *Nucl. Phys. B* **694** (2004) 35–58, [hep-lat/0312022].

[254] J. J. M. Verbaarschot, *The spectrum of the qcd dirac operator and chiral random matrix theory: The threefold way*, *Phys. Rev. Lett.* **72** (1994) 2531–2533. doi:10.1103/PhysRevLett.72.2531. [arXiv:hep-th/9401059 [hep-th]].

[255] J. J. M. Verbaarschot and T. Wettig, *Random matrix theory and chiral symmetry in qcd*, *Ann. Rev. Nucl. Part. Sci.* **50** (2000) 343–410. doi:10.1146/annurev.nucl.50.1.343. [arXiv:hep-ph/0003017 [hep-ph]].

[256] T. Banks and A. Casher, *Chiral symmetry breaking in confining theories*, *Nucl. Phys. B* **169** (1980) 103–125. doi:10.1016/0550-3213(80)90255-2.

[257] N. Forzano et al., *Progress on the spectroscopy of lattice gauge theories using spectral densities*, *PoS* **LATTICE2024** (2025) 137, [arXiv:2410.11386].

[258] Bennett et al., *Chimera baryons and mesons on the lattice: a spectral density analysis*, arXiv:2506.19804.

[259] E. Bennett, J. Holligan, D. K. Hong, J.-W. Lee, C. J. D. Lin, B. Lucini, M. Piai, and D. Vadacchino, *On the spectrum of mesons in quenched $Sp(2N)$ gauge theories*, arXiv:2312.08465.

[260] J. Pomper and S. Kulkarni, *Low energy effective theories of composite dark matter with real representations*, arXiv:2402.04176.

[261] M. A. Clark and A. D. Kennedy, *Accelerating dynamical fermion computations using the rational hybrid Monte Carlo (RHMC) algorithm with multiple pseudofermion fields*, *Phys. Rev. Lett.* **98** (2007) 051601, [hep-lat/0608015].

[262] S. Hands, I. Montvay, S. Morrison, M. Oevers, L. Scorzato, and J. Skullerud, *Numerical study of dense adjoint matter in two color QCD*, *Eur. Phys. J. C* **17** (2000) 285–302, [hep-lat/0006018].

[263] G. P. Lepage and P. B. Mackenzie, *On the viability of lattice perturbation theory*, *Phys. Rev. D* **48** (1993) 2250–2264, [hep-lat/9209022].

[264] **BMW** Collaboration, S. Borsanyi et al., *High-precision scale setting in lattice QCD*, *JHEP* **09** (2012) 010, [arXiv:1203.4469].

[265] E. Bennett, D. K. Hong, H. Hsiao, J.-W. Lee, C. J. D. Lin, B. Lucini, et al., "Meson

spectroscopy in the $Sp(4)$ gauge theory with three antisymmetric fermions,." https://arxiv.org/abs/2412.01170. 2412.01170.

[266] "GitHub - claudiopica/HiRep: HiRep repository — github.com." https://github.com/claudiopica/HiRep.

[267] "GitHub - sa2c/HiRep: HiRep repository — github.com." https://github.com/sa2c/HiRep.

[268] "GitHub - RJHudspith/GLU: GaugeLinkUtility repository — github.com." https://github.com/RJHudspith/GLU.

[269] Y. Aoki, T. Izubuchi, E. Shintani, and A. Soni, *Improved lattice computation of proton decay matrix elements*, *Phys. Rev. D* **96** (2017), no. 1 014506, [arXiv:1705.01338].

[270] V. Ayyar, T. DeGrand, D. C. Hackett, W. I. Jay, E. T. Neil, Y. Shamir, and B. Svetitsky, *Partial compositeness and baryon matrix elements on the lattice*, *Phys. Rev. D* **99** (2019), no. 9 094502, [arXiv:1812.02727].

[271] G. Cacciapaglia, H. Cai, A. Deandrea, and A. Kushwaha, *Composite Higgs and Dark Matter Model in SU(6)/SO(6)*, *JHEP* **10** (2019) 035, [arXiv:1904.09301].

[272] S. Weinberg, *Precise relations between the spectra of vector and axial vector mesons*, *Phys. Rev. Lett.* **18** (1967) 507–509.

[273] E. Katz, A. E. Nelson, and D. G. E. Walker, *The Intermediate Higgs*, *JHEP* **08** (2005) 074, [hep-ph/0504252].

[274] R. Barbieri, B. Bellazzini, V. S. Rychkov, and A. Varagnolo, *The Higgs boson from an extended symmetry*, *Phys. Rev. D* **76** (2007) 115008, [arXiv:0706.0432].

[275] P. Lodone, *Vector-like quarks in a 'composite' Higgs model*, *JHEP* **12** (2008) 029, [arXiv:0806.1472].

[276] B. Gripaios, A. Pomarol, F. Riva, and J. Serra, *Beyond the Minimal Composite Higgs Model*, *JHEP* **04** (2009) 070, [arXiv:0902.1483].

[277] J. Mrazek, A. Pomarol, R. Rattazzi, M. Redi, J. Serra, and A. Wulzer, *The Other Natural Two Higgs Doublet Model*, *Nucl. Phys. B* **853** (2011) 1–48, [arXiv:1105.5403].

[278] D. Marzocca, M. Serone, and J. Shu, *General Composite Higgs Models*, *JHEP* **08** (2012) 013, [arXiv:1205.0770].

[279] C. Grojean, O. Matsedonskyi, and G. Panico, *Light top partners and precision physics*, *JHEP* **10** (2013) 160, [arXiv:1306.4655].

[280] G. Cacciapaglia and F. Sannino, *Fundamental Composite (Goldstone) Higgs Dynamics*, *JHEP* **04** (2014) 111, [arXiv:1402.0233].

[281] G. Ferretti, *UV Completions of Partial Compositeness: The Case for a SU(4) Gauge Group*, *JHEP* **06** (2014) 142, [arXiv:1404.7137].

[282] A. Arbey, G. Cacciapaglia, H. Cai, A. Deandrea, S. Le Corre, and F. Sannino, *Fundamental*

Composite Electroweak Dynamics: Status at the LHC, *Phys. Rev. D* **95** (2017), no. 1 015028, [arXiv:1502.04718].

[283] G. Cacciapaglia, H. Cai, A. Deandrea, T. Flacke, S. J. Lee, and A. Parolini, *Composite scalars at the LHC: the Higgs, the Sextet and the Octet*, *JHEP* **11** (2015) 201, [arXiv:1507.02283].

[284] L. Vecchi, *A dangerous irrelevant UV-completion of the composite Higgs*, *JHEP* **02** (2017) 094, [arXiv:1506.00623].

[285] T. Ma and G. Cacciapaglia, *Fundamental Composite 2HDM: SU(N) with 4 flavours*, *JHEP* **03** (2016) 211, [arXiv:1508.07014].

[286] F. Feruglio, B. Gavela, K. Kanshin, P. A. N. Machado, S. Rigolin, and S. Saa, *The minimal linear sigma model for the Goldstone Higgs*, *JHEP* **06** (2016) 038, [arXiv:1603.05668].

[287] T. DeGrand, M. Golterman, E. T. Neil, and Y. Shamir, *One-loop Chiral Perturbation Theory with two fermion representations*, *Phys. Rev. D* **94** (2016), no. 2 025020, [arXiv:1605.07738].

[288] S. Fichet, G. von Gersdorff, E. Pontón, and R. Rosenfeld, *The Excitation of the Global Symmetry-Breaking Vacuum in Composite Higgs Models*, *JHEP* **09** (2016) 158, [arXiv:1607.03125].

[289] J. Galloway, A. L. Kagan, and A. Martin, *A UV complete partially composite-pNGB Higgs*, *Phys. Rev. D* **95** (2017), no. 3 035038, [arXiv:1609.05883].

[290] A. Agugliaro, O. Antipin, D. Becciolini, S. De Curtis, and M. Redi, *UV complete composite Higgs models*, *Phys. Rev. D* **95** (2017), no. 3 035019, [arXiv:1609.07122].

[291] A. Belyaev, G. Cacciapaglia, H. Cai, G. Ferretti, T. Flacke, A. Parolini, and H. Serodio, *Di-boson signatures as Standard Candles for Partial Compositeness*, *JHEP* **01** (2017) 094, [arXiv:1610.06591]. [Erratum: JHEP 12, 088 (2017)].

[292] C. Csaki, T. Ma, and J. Shu, *Maximally Symmetric Composite Higgs Models*, *Phys. Rev. Lett.* **119** (2017), no. 13 131803, [arXiv:1702.00405].

[293] M. Chala, G. Durieux, C. Grojean, L. de Lima, and O. Matsedonskyi, *Minimally extended SILH*, *JHEP* **06** (2017) 088, [arXiv:1703.10624].

[294] M. Golterman and Y. Shamir, *Effective potential in ultraviolet completions for composite Higgs models*, *Phys. Rev. D* **97** (2018), no. 9 095005, [arXiv:1707.06033].

[295] C. Csáki, T. Ma, and J. Shu, *Trigonometric Parity for Composite Higgs Models*, *Phys. Rev. Lett.* **121** (2018), no. 23 231801, [arXiv:1709.08636].

[296] T. Alanne, D. Buarque Franzosi, and M. T. Frandsen, *A partially composite Goldstone Higgs*, *Phys. Rev. D* **96** (2017), no. 9 095012, [arXiv:1709.10473].

[297] T. Alanne, D. Buarque Franzosi, M. T. Frandsen, M. L. A. Kristensen, A. Meroni, and M. Rosenlyst, *Partially composite Higgs models: Phenomenology and RG analysis*, *JHEP* **01** (2018) 051, [arXiv:1711.10410].

[298] F. Sannino, P. Stangl, D. M. Straub, and A. E. Thomsen, *Flavor Physics and Flavor*

Anomalies in Minimal Fundamental Partial Compositeness, *Phys. Rev. D* **97** (2018), no. 11 115046, [arXiv:1712.07646].

[299] T. Alanne, N. Bizot, G. Cacciapaglia, and F. Sannino, *Classification of NLO operators for composite Higgs models*, *Phys. Rev. D* **97** (2018), no. 7 075028, [arXiv:1801.05444].

[300] N. Bizot, G. Cacciapaglia, and T. Flacke, *Common exotic decays of top partners*, *JHEP* **06** (2018) 065, [arXiv:1803.00021].

[301] C. Cai, G. Cacciapaglia, and H.-H. Zhang, *Vacuum alignment in a composite 2HDM*, *JHEP* **01** (2019) 130, [arXiv:1805.07619].

[302] A. Agugliaro, G. Cacciapaglia, A. Deandrea, and S. De Curtis, *Vacuum misalignment and pattern of scalar masses in the SU(5)/SO(5) composite Higgs model*, *JHEP* **02** (2019) 089, [arXiv:1808.10175].

[303] G. Cacciapaglia, T. Ma, S. Vatani, and Y. Wu, *Towards a fundamental safe theory of composite Higgs and Dark Matter*, *Eur. Phys. J. C* **80** (2020), no. 11 1088, [arXiv:1812.04005].

[304] D. Buarque Franzosi, G. Cacciapaglia, and A. Deandrea, *Sigma-assisted low scale composite Goldstone–Higgs*, *Eur. Phys. J. C* **80** (2020), no. 1 28, [arXiv:1809.09146].

[305] H. Gertov, A. E. Nelson, A. Perko, and D. G. E. Walker, *Lattice-Friendly Gauge Completion of a Composite Higgs with Top Partners*, *JHEP* **02** (2019) 181, [arXiv:1901.10456].

[306] V. Ayyar, M. F. Golterman, D. C. Hackett, W. Jay, E. T. Neil, Y. Shamir, and B. Svetitsky, *Radiative Contribution to the Composite-Higgs Potential in a Two-Representation Lattice Model*, *Phys. Rev. D* **99** (2019), no. 9 094504, [arXiv:1903.02535].

[307] D. Buarque Franzosi and G. Ferretti, *Anomalous dimensions of potential top-partners*, *SciPost Phys.* **7** (2019), no. 3 027, [arXiv:1905.08273].

[308] G. Cacciapaglia, S. Vatani, and C. Zhang, *Composite Higgs Meets Planck Scale: Partial Compositeness from Partial Unification*, *Phys. Lett. B* **815** (2021) 136177, [arXiv:1911.05454].

[309] G. Cacciapaglia, A. Deandrea, T. Flacke, and A. M. Iyer, *Gluon-Photon Signatures for color octet at the LHC (and beyond)*, *JHEP* **05** (2020) 027, [arXiv:2002.01474].

[310] T. Appelquist, J. Ingoldby, and M. Piai, *Nearly Conformal Composite Higgs Model*, *Phys. Rev. Lett.* **126** (2021), no. 19 191804, [arXiv:2012.09698].

[311] Z.-Y. Dong, C.-S. Guan, T. Ma, J. Shu, and X. Xue, *UV completed composite Higgs model with heavy composite partners*, *Phys. Rev. D* **104** (2021), no. 3 035013, [arXiv:2011.09460].

[312] G. Cacciapaglia, T. Flacke, M. Kunkel, and W. Porod, *Phenomenology of unusual top partners in composite Higgs models*, *JHEP* **02** (2022) 208, [arXiv:2112.00019].

[313] A. Banerjee, D. B. Franzosi, and G. Ferretti, *Modelling vector-like quarks in partial compositeness framework*, *JHEP* **03** (2022) 200, [arXiv:2202.00037].

[314] G. Ferretti, *Compositeness above the electroweak scale and a proposed test at lhcb*, *EPJ Web Conf* **258** (2022) 08002. doi:10.1051/epjconf/202225808002.

[315] H. Cai and G. Cacciapaglia, *Partial compositeness under precision scrutiny*, *JHEP* **12** (2022) 104, [arXiv:2208.04290].

[316] T. Appelquist, J. Ingoldby, and M. Piai, *Composite two-Higgs doublet model from dilaton effective field theory*, *Nucl. Phys. B* **983** (2022) 115930, [arXiv:2205.03320].

[317] G. Cacciapaglia, A. Deandrea, M. Kunkel, and W. Porod, *Coloured spin-1 states in composite Higgs models*, *JHEP* **06** (2024) 092, [arXiv:2404.02198].

[318] A. Banerjee, E. Bergeaas Kuutmann, V. Ellajosyula, R. Enberg, G. Ferretti, and L. Panizzi, *Vector-like quarks: Status and new directions at the LHC*, *SciPost Phys. Core* **7** (2024) 079, [arXiv:2406.09193].

[319] A. Lupo, L. Del Debbio, M. Panero, and N. Tantalo, *Fits of finite-volume smeared spectral densities*, *PoS* **LATTICE2022** (2023) 215, [arXiv:2212.08019].

[320] A. Lupo, M. Panero, N. Tantalo, and L. Del Debbio, *Spectral reconstruction in SU(4) gauge theory with fermions in multiple representations*, *PoS* **LATTICE2021** (2022) 092, [arXiv:2112.01158].

[321] A. Lupo, L. Del Debbio, M. Panero, and N. Tantalo, *Bayesian interpretation of Backus-Gilbert methods*, *PoS* **LATTICE2023** (2024) 004, [arXiv:2311.18125].

[322] J. Holligan, E. Bennett, D. K. Hong, J.-W. Lee, C. J. D. Lin, B. Lucini, M. Piai, and D. Vadacchino, *$Sp(2N)$ Yang-Mills towards large N*, *PoS* **LATTICE2019** (2019) 177, [arXiv:1912.09788].

[323] M. E. Machacek, E. D. Carlson, and L. J. Hall, *Selfinteracting dark matter: An alternative scenario?*, in *16th Texas Symposium on Relativistic Astrophysics and 3rd Particles, Strings, and Cosmology Symposium*, pp. 681–685, 12, 1992.

[324] A. E. Faraggi and M. Pospelov, *Selfinteracting dark matter from the hidden heterotic string sector*, *Phys.* **16** (2002) 451–461. doi:10.1016/S0927-6505(01)00121-9.

[325] A. Gonzalez Arroyo, F. J. Yndurain, and G. Martinelli, *Computation of the Relation Between the Quark Masses in Lattice Gauge Theories and on the Continuum*, *Phys. Lett. B* **117** (1982) 437. [Erratum: Phys.Lett.B 122, 486 (1983)].

[326] R. K. Ellis and G. Zanderighi, *Scalar one-loop integrals for QCD*, *JHEP* **02** (2008) 002, [arXiv:0712.1851].

[327] V. V. Sudakov, *Vertex Parts at Very High Energies in Quantum Electrodynamics*, *Sov. Phys. JETP* **3** (1956) 65–71.

[328] P. Breitenlohner and D. Maison, *Dimensionally Renormalized Green's Functions for Theories with Massless Particles. 1.*, *Commun. Math. Phys.* **52** (1977) 39.

[329] P. Breitenlohner and D. Maison, *Dimensional Renormalization and the Action Principle*, *Commun. Math. Phys.* **52** (1977) 11–38.

[330] G. 't Hooft and M. J. G. Veltman, *Regularization and Renormalization of Gauge Fields*, *Nucl. Phys. B* **44** (1972) 189–213.

[331] J. Kuipers, T. Ueda, J. Vermaseren, and J. Vollinga, *FORM version 4.0*, *Comput. Phys. Commun.* **184** (2013) 1453–1467, [arXiv:1203.6543].

[332] C. Bollini and J. Giambiagi, *Dimensional renormalization: The number of dimensions as a regularizing parameter*, *Nuovo Cim. B* **12** (1972) 20–26.

[333] G. 't Hooft and M. J. G. Veltman, *Scalar One Loop Integrals*, *Nucl. Phys. B* **153** (1979) 365–401.

[334] S. Capitani, *Lattice perturbation theory*, *Phys. Rept.* **382** (2003) 113–302, [hep-lat/0211036].

[335] P. Lepage, *gplepage/vegas: vegas version 6.2.1*, Feb., 2025.